

# **Additive Manufacturing of Heterogeneous Catalysts: Development of Binder Jetting Printing Strategies for Al<sub>2</sub>O<sub>3</sub>-Supported Catalysts**

Hanh My Bui

Vollständiger Abdruck der von der TUM School of Natural Sciences der Technischen  
Universität München zur Erlangung des akademischen Grades einer

**Doktorin der Ingenieurwissenschaften (Dr.-Ing.)**

genehmigten Dissertation.

Vorsitz: Prof. Dr. Dr. h.c. Bernhard Rieger

Prüfer der Dissertation:

1. Prof. Dr.-Ing. Kai-Olaf Martin Hinrichsen
2. Hon.-Prof. Dr. Richard W. Fischer

Die Dissertation wurde am 21.09.2023 bei der Technischen Universität München eingereicht  
und durch die TUM School of Natural Sciences am 05.12.2023 angenommen.



# Danksagung

Zu allererst bedanke ich mich bei meinem Doktorvater Prof. Dr.-Ing. Kai-Olaf Hinrichsen für die Aufnahme in die Arbeitsgruppe und die Möglichkeit, an einem spannenden Forschungsthema zu arbeiten. Ich danke Ihnen für die Unterstützung und Betreuung, während der Sie mir stets die Freiheit gegeben haben, eigene Themenschwerpunkte zu setzen und danke Ihnen ebenfalls für das entgegengebrachte Vertrauen.

Ich bedanke mich bei Prof. Dr. Richard Fischer, Dr. Markus Tonigold und Dr. Normen Szesni für all die Ideen und Anregungen seitens der Clariant Produkte (Deutschland) GmbH im Rahmen des Projekts 3DKat. Dr. Alexander Seidel danke ich für die Durchführung der katalytischen Tests bei Hydrogenious LOHC Technologies GmbH. Des Weiteren möchte ich mich bei Prof. Dr. Wolfgang Kollenberg, Dr. Dieter Nikolay und allen Mitarbeitern der WZR ceramic solutions GmbH dafür bedanken, mich für einige Wochen in ihr Team aufgenommen zu haben. Die Einblicke in den keramischen 3D-Druck und das Durchführen der ersten Druckversuche in Rheinbach waren für mich sehr wertvoll.

Ein ganz besonderer Dank geht an meinen "Projekt-Buddy" Paula Großmann für die zahlreichen fachlichen und außerfachlichen Gespräche und tägliche/nächtliche Stunden im Labor beim auf-unsere-3D-Drucker-schauen, Messungen durchführen oder Poster/Präsentationen basteln. Ich danke dir für die wirklich tolle und lustige Zusammenarbeit, ich hätte mir bei Weitem keine bessere Projektpartnerin vorstellen können!

Ich danke Maja Lehmann für den regen Austausch über Binder Jetting, Tim Kratky und Prof. Sebastian Günther für die XPS-Expertise, dem Lehrstuhl für Technische Chemie II, v.a. Insu Lee, Rachit Khare, Florian Zahn und Lennart Wahl für die Durchführung und Analyse der XAS-Messungen am DESY, Christoph Gross für die Nutzung seines Reaktors und Jakub Pazdera für die Bereitstellung der TGA. Ebenfalls danke ich Klaus Achterhold für die  $\mu$ CT-Aufnahmen, Anne Berger für die unkomplizierte Durchführung der Quecksilberporosimetriemessungen und Max Hiller für die Unterstützung bei den TPR-Messungen.

Vielen Dank an Thomas Michel und Heidi Holweck, die sich stets um alle bürokratischen Angelegenheiten gekümmert haben. Natürlich bedanke ich mich bei meinen Kollegen am Lehrstuhl, Stefan, Julia, Moritz, Philipp, Sebastian, Johanna, Daniel, Thomas, Tabea, Matthias, Chris, Nini, Heike, Anne, Sebastian und Anna, ohne die ich mir den Alltag am Lehrstuhl mit den zahlreichen Diskussionen und Kaffeepausen nicht vorstellen könnte. Des Weiteren durfte ich einige Studienarbeiten betreuen. Ich möchte Jun Xiang, Rebekah, Son, Steffi, Merle, Noah und Steffen für ihr Interesse am Thema und dem Beitrag zu meiner Promotion danken.

Zuletzt geht mein Dank an meine Familie sowie meine Freunde, die mich durchgehend in meinem Tun unterstützt haben und mir stets zur Seite gestanden haben.

# Abstract

Additive manufacturing (AM) is a rapidly evolving production method, as evidenced by the multitude of printing techniques available today and the swift progression from laboratory-stage processes to market-ready concepts. For many industrial sectors such as aerospace and medical technology, 3D printing has already become an integral part of prototype manufacturing. However, in the chemical industry, especially in catalyst manufacturing, the application of AM is still in its early stages. Considering the objective of developing more resource-efficient chemical processes, 3D printing is gaining increasing attention as an innovative manufacturing technology. It enables the fabrication of catalyst geometries that are unattainable using conventional methods. This thesis explores the potential of the binder jetting (BJ) technology for manufacturing aluminum oxide-based heterogeneous catalysts.

The first part of the thesis focuses on establishing a reproducible printing process for the production of  $\text{Al}_2\text{O}_3$  supports. The material and process development must meet the contrasting requirements of a catalyst support, being mechanically stable while providing high surface area and porosity for subsequent application. Stable test cylinders of 6 mm height and diameter were printed using a compatible combination of transition alumina powder and a water-based ink with colloiddally dispersed boehmite particles. Polyvinylpyrrolidone in powdered form in the print bed was used as a binder, with its complete burnout at 600 °C confirmed through TGA and XRD analysis. The significant decrease in stability after debinding needs to be compensated for by subsequent infiltration with a 20 wt.% aqueous boehmite slurry, followed by calcination. The 3D-printed  $\text{Al}_2\text{O}_3$  supports can be employed in a chemical reactor considering their range of specific surface area, porosity, and side crushing strength.

Printed supports were tested as  $\text{Pt}/\text{Al}_2\text{O}_3$  catalysts for the dehydrogenation of a liquid organic hydrogen carrier (perhydro-dibenzyltoluene). Catalysts printed with the direct ink writing method were used as a comparative system. Both printing methods are suitable for catalyst fabrication, but the products differ in platinum penetration depth, available surface area, and porosity. The metal particle size and dispersion are comparable as well as the catalytic performance in the semi-batch experiment. This underscores the significance of considering the specific potentials of each printing technique.

---

The successful elaboration and application of the powder-based printing process for fabricating support structures provide the groundwork for the further developments of this concept in the second part of this thesis. Because binder jetting is built upon the interplay between powder and ink, these constituents can be modified to formulate diverse strategies for the direct printing of catalysts with an active phase. One strategy involves the fabrication of Ni-Al catalysts for CO<sub>2</sub> methanation using co-precipitated Ni-Al powder for printing. The Ni-Al catalysts with molar Ni/Al ratios ranging from 1/1 to 5/1 exhibit a comparable phase composition, nickel particle size, and dispersion to unshaped catalyst powder. Initial methanation tests in a single pellet string reactor demonstrated significant CO<sub>2</sub> conversions and CH<sub>4</sub> yields.

Another strategy for the production of nickel catalysts involves the printing of Ni(NO<sub>3</sub>)<sub>2</sub>-laden ink onto Al<sub>2</sub>O<sub>3</sub> powder, thereby constituting a simultaneous impregnation and shaping process. Device-specific limitations allow for a maximum nickel loading of approximately 3 wt.%, leading to a high dispersion of nickel. Due to the fine distribution and resulting small metal particles, the calcination process mainly yields nickel aluminate spinel with NiO with a ratio of 3:2, as confirmed by XPS, XAS, and XANES. Furthermore, initial CO<sub>2</sub> methanation tests exhibited catalytic activity in the in-situ impregnated samples, although the reaction rate was relatively low due to the low nickel loading, resulting in the primary product being CO.

# Kurzzusammenfassung

Die additive Fertigung ist ein sich rapide entwickelndes Formgebungsverfahren, was durch die hohe Anzahl an heutzutage verfügbaren Druckverfahren und der schnellen Prozessentwicklung vom Laborstadium zu marktreifen Konzepten deutlich wird. Für viele Industriebereiche wie der Luft- und Raumfahrt als auch der Medizintechnik ist der 3D-Druck bereits fester Bestandteil der Prototypenfertigung. In der chemischen Industrie, besonders im Bereich der Katalysatorherstellung, steht die Anwendung der additiven Fertigung allerdings noch in ihren Anfängen. In Anbetracht des Ziels, ressourcenschonendere chemische Prozesse zu entwickeln, erregt der 3D-Druck als innovative Fertigungstechnologie zunehmendes Interesse. Er ermöglicht die Herstellung von Katalysatorgeometrien, die mit herkömmlichen Verfahren nicht realisierbar sind. In der vorliegenden Arbeit wird das Potential des Pulver-Binder-Verfahrens (Binder Jetting (BJ)) für die Herstellung von aluminiumoxid-basierten heterogenen Katalysatoren untersucht.

Im ersten Teil der Arbeit steht die Etablierung eines reproduzierbaren Druckverfahrens zur Herstellung von  $\text{Al}_2\text{O}_3$ -Trägern im Fokus. Die Material- und Verfahrensentwicklung muss die gegensätzlichen Anforderungen an einen Katalysatorträger erfüllen, mechanisch stabil zu sein und gleichzeitig eine hohe Oberfläche bzw. Porosität für die nachfolgende Nutzung bereitzustellen. Stabile Testzylinder wurden gedruckt, indem eine kompatible Kombination aus Übergangsaluminiumoxidpulver und einer wasserbasierten Tinte mit kolloidal dispergierten Böhmitpartikeln entwickelt wurde. Als Binder dient Polyvinylpyrrolidon in Pulverform im Druckbett, dessen vollständiger Ausbrand bei  $600\text{ }^\circ\text{C}$  mittels TGA und XRD-Analyse bestätigt wurde. Die signifikante Stabilitätsabnahme nach dem Entbindern muss durch nachträgliches Infiltrieren mit einer 20 wt.% wässrigen Böhmit-Slurry und anschließendem Kalzinieren ausgeglichen werden. Die 3D-gedruckten  $\text{Al}_2\text{O}_3$ -Träger können hinsichtlich des Größenbereich der spezifischen Oberfläche, Porosität und Seitendruckfestigkeit in einem chemischen Reaktor verwendet werden.

Gedruckte Träger wurden als Pt/ $\text{Al}_2\text{O}_3$ -Katalysatoren für die Dehydrierung eines flüssigen organischen Wasserstoffträgers (Perhydro-Dibenzyltoluol) getestet. Als Vergleichssystem wurden Katalysatoren, die mit dem Direct Ink Writing-Verfahren hergestellt wurden, herangezogen. Beide Druckmethoden sind für die Herstellung geeignet, unterscheiden sich jedoch in der Eindringtiefe des Platins, nutzbaren Oberfläche und Porosität.

---

Die Metallpartikelgröße und -dispersion sind vergleichbar, ebenso die katalytische Performance im Semibatch-Versuch. Dadurch wird die Relevanz deutlich, die spezifischen Potentiale der einzelnen Druckverfahren zu berücksichtigen.

Die erfolgreiche Ausarbeitung und Anwendung des pulverbasierten Druckverfahrens für das Drucken von Trägerstrukturen bietet die Grundlage für die Weiterentwicklungen dieses Konzepts im zweiten Teil dieser Arbeit. Dadurch, dass BJ auf dem Zusammenspiel zwischen Pulver und Tinte aufbaut, können diese Bestandteile modifiziert werden, um unterschiedliche Strategien für das direkte Verdrucken von Katalysatoren mit aktiver Phase auszuarbeiten. Eine Strategie beinhaltet die Herstellung von Ni-Al-Katalysatoren für die CO<sub>2</sub>-Methanisierung, indem für das Drucken ko-gefälltes Ni-Al-Pulver verwendet wird. Die Ni-Al Katalysatoren mit molaren Ni/Al-Verhältnissen zwischen 1/1 und 5/1 weisen eine vergleichbare Phasenzusammensetzung, Nickelpartikelgröße, Dispersion auf wie ungeformtes Katalysatorpulver. Erste Methanisierungstests in einem Single Pellet String-Reaktor zeigten deutliche CO<sub>2</sub>-Umsätze und CH<sub>4</sub>-Ausbeuten.

Eine weitere Strategie für die Fertigung von Nickelkatalysatoren beinhaltet das Verdrucken von Ni(NO<sub>3</sub>)<sub>2</sub>-haltiger Tinte auf Al<sub>2</sub>O<sub>3</sub>-Pulver, wodurch das Verfahren ein simultanes Imprägnier- und Formgebungsverfahren darstellt. Gerätespezifische Limitierungen lassen eine maximale Nickelbeladung von ca. 3 wt.% zu, was zu einer hohen Nickeldispersion führt. Durch die feine Verteilung und dadurch kleinen Metallpartikel entsteht infolge des Kalzinierprozesses hauptsächlich spinelförmiges Nickelaluminat mit NiO im Verhältnis 3:2, was durch XPS, XAS und XANES besätigt wird. Des Weiteren ergaben erste CO<sub>2</sub>-Methanisierungstests eine katalytische Aktivität der in situ-imprägnierten Proben, wenngleich die Reaktionsgeschwindigkeit aufgrund der niedrigen Nickelbeladung relativ gering war und als Hauptprodukt CO entstand.

# Inhaltsverzeichnis

<b>Abstract</b>	<b>v</b>
<b>Kurzzusammenfassung</b>	<b>vii</b>
<b>1 Introduction</b>	<b>1</b>
1.1 Motivation . . . . .	1
1.2 Outline . . . . .	2
<b>2 Theoretical and Technological Background</b>	<b>5</b>
2.1 Additive Manufacturing . . . . .	5
2.1.1 Binder Jetting Technology . . . . .	7
2.2 Additive Manufacturing and Catalysis . . . . .	10
2.2.1 State of the Art in Catalyst 3D Printing . . . . .	11
2.3 Macroscopic Catalyst Design . . . . .	15
2.3.1 Conventional Catalyst Shaping . . . . .	15
2.3.2 Active Phase Distribution in Catalyst Pellets . . . . .	16
2.4 Investigated Catalytic Reactions . . . . .	18
2.4.1 CO <sub>x</sub> Methanation . . . . .	18
2.4.2 Dehydrogenation of Liquid Organic Hydrogen Carriers . . . . .	21
<b>3 Methodology</b>	<b>25</b>
3.1 Conventional Heterogeneous Catalyst Preparation . . . . .	25
3.1.1 Co-precipitation . . . . .	25
3.1.2 Wet Impregnation . . . . .	26
3.2 Catalyst Preparation Using Binder Jetting . . . . .	26
3.3 Catalyst Material Characterization . . . . .	27
3.3.1 X-ray Powder Diffraction . . . . .	28
3.3.2 X-ray Photoelectron Spectroscopy . . . . .	29
3.3.3 X-ray Absorption Spectroscopy . . . . .	29
3.3.4 N <sub>2</sub> Physisorption . . . . .	31
3.3.5 H <sub>2</sub> Chemisorption . . . . .	33
3.3.6 Thermogravimetric Analysis . . . . .	34

3.3.7	Temperature Programmed Reduction . . . . .	35
3.3.8	Transmission Electron Microscopy . . . . .	36
3.3.9	Inductively Coupled Plasma Optical Emission Spectroscopy . . . . .	36
3.3.10	Laser Diffraction Particle Size Analysis . . . . .	37
3.3.11	Mercury Intrusion Porosimetry . . . . .	38
3.3.12	Uniaxial Compression Test . . . . .	38
<b>4</b>	<b>Development of a Manufacturing Process for Binder Jet 3D Printed Porous Al<sub>2</sub>O<sub>3</sub> Supports Used in Heterogeneous Catalysis</b>	<b>41</b>
4.1	Introduction . . . . .	42
4.1.1	State of Knowledge - 3D Printing of Al <sub>2</sub> O <sub>3</sub> -based Catalysts . . . . .	42
4.1.2	Motivation . . . . .	44
4.2	Materials and methods . . . . .	46
4.2.1	General Process Chain . . . . .	46
4.2.2	Raw Materials . . . . .	47
4.2.3	Characterization and Analysis . . . . .	49
4.3	Results and Discussion . . . . .	52
4.3.1	Raw Materials . . . . .	52
4.3.2	Printed Part Analysis . . . . .	58
4.4	Conclusions . . . . .	72
<b>5</b>	<b>Comparison of Direct Ink Writing and Binder Jetting for Additive Manufacturing of Pt/Al<sub>2</sub>O<sub>3</sub> Catalysts for the Dehydrogenation of Perhydrodibenzyltoluene</b>	<b>75</b>
5.1	Introduction . . . . .	76
5.2	Experimental . . . . .	78
5.2.1	Catalyst Preparation . . . . .	79
5.2.2	Catalyst Characterization . . . . .	82
5.2.3	LOHC Dehydrogenation . . . . .	83
5.3	Results and Discussion . . . . .	85
5.3.1	3D Printed Catalysts . . . . .	85
5.3.2	Calcination Temperature Variation . . . . .	85
5.3.3	Impregnation Time Variation . . . . .	91
5.3.4	Characterization of Catalysts Used for Testing . . . . .	96
5.3.5	Catalytic test . . . . .	97
5.4	Conclusions . . . . .	100
5.5	Supporting Information . . . . .	101
5.5.1	Alumina Phase Determination . . . . .	101
5.5.2	Particle Size of Catalyst Powder for LOHC Dehydrogenation . . . . .	102
5.5.3	Pt Particle Size Distribution by TEM . . . . .	102

<b>6</b>	<b>3D Printed Co-Precipitated Ni-Al CO<sub>2</sub> Methanation Catalysts by Binder Jetting: Fabrication, Characterization and Test in a Single Pellet String Reactor</b>	<b>105</b>
6.1	Introduction . . . . .	106
6.1.1	Additive Manufacturing of Heterogeneous Catalysts . . . . .	107
6.1.2	Single Pellet String Reactor . . . . .	107
6.1.3	Motivation . . . . .	108
6.2	Experimental . . . . .	108
6.2.1	Co-precipitation of Ni-Al Catalyst Precursor . . . . .	108
6.2.2	Catalyst Preparation . . . . .	109
6.2.3	Catalyst Characterization . . . . .	112
6.2.4	Catalytic Test . . . . .	114
6.3	Results and Discussion . . . . .	115
6.3.1	Particle Size Distribution of Printing Powder . . . . .	115
6.3.2	Nickel Loading . . . . .	116
6.3.3	XRD Analysis . . . . .	117
6.3.4	Degree of Reduction . . . . .	122
6.3.5	Sorption Properties . . . . .	123
6.3.6	Mechanical Stability . . . . .	128
6.3.7	Pore Size Analysis . . . . .	129
6.3.8	Catalytic Test in a SPSR . . . . .	132
6.4	Conclusions . . . . .	134
6.5	Supporting Information . . . . .	135
6.5.1	Ni Species in Relation to the Distance from the Pellet Core . . . . .	135
6.5.2	Particle Size Distribution by TEM . . . . .	137
6.5.3	Pore Size Distribution Analysis by Mercury Intrusion Porosimetry . . . . .	138
<b>7</b>	<b>In Situ Impregnated Ni/Al<sub>2</sub>O<sub>3</sub> Catalysts Prepared by Binder Jet 3D Printing Using Nickel Nitrate-containing Ink</b>	<b>139</b>
7.1	Introduction . . . . .	140
7.2	Experimental . . . . .	141
7.2.1	Catalyst Preparation by Binder Jetting with Ni-Containing Ink . . . . .	141
7.2.2	Catalyst Preparation by Wet Impregnation . . . . .	143
7.2.3	Sample Nomenclature . . . . .	143
7.2.4	Catalyst Characterization . . . . .	144
7.3	Results . . . . .	146
7.3.1	Proof of Concept by Preliminary Printing Tests . . . . .	146
7.3.2	XPS Analysis . . . . .	148
7.3.3	Ni K-edge XAS Analysis . . . . .	152
7.3.4	TPR Analysis . . . . .	155

7.4	Conclusion . . . . .	157
7.5	Supporting Information . . . . .	158
7.5.1	Specific Surface Area . . . . .	158
7.5.2	Ni K-edge XAS . . . . .	158
7.5.3	TPR Reference Samples . . . . .	161
7.5.4	Activity Measurements . . . . .	161
<b>8</b>	<b>Summary and Outlook</b>	<b>165</b>
8.1	Summary . . . . .	165
8.2	Outlook . . . . .	167
<b>A</b>	<b>Bibliography</b>	<b>169</b>
	<b>Nomenclature</b>	<b>203</b>
	<b>List of Figures</b>	<b>207</b>
	<b>List of Tables</b>	<b>213</b>
	<b>List of Publications</b>	<b>215</b>

# 1 Introduction

## 1.1 Motivation

Achieving the ideal geometric design of a reactor packing is essential to ensure effective external mass and heat transfer, particularly for exothermal reactions. This involves minimizing pressure loss, short diffusion paths inside the catalyst particle and the availability of active sites for sufficient reactant conversion. Furthermore, these parameters directly correlate with the size of a pellet, specific surface area, pore size distribution, voidage and abrasion resistance of the ceramic material [1, 2]. Therefore, a plethora of studies, particularly fluid dynamic simulations, have covered the influence of catalyst shape in packed beds [3, 4]. Scientific research has notably explored the effect of catalyst shape on systems for methane steam reforming [5–7], hydrolysis of COS and CS<sub>2</sub> in a Claus converter [8], natural gas reforming [9], partial oxidation of methanol [4] or Fischer-Tropsch synthesis for hydrocarbons production from synthesis gas [10]. The examined geometries encompassed simple cylinders, spheres, hollow cylinders, trilobes, quadrilobes, daisy shaped bodies, multi-channel cylinders, multi-channel cubes and monoliths with varying channel geometry. Consensus is evident across all the aforementioned studies, indicating that variation of the catalyst geometry significantly affects the overall performance of a reactor. The conventional methods for shaping catalysts include pelleting, granulation, and extrusion. [11, 12]. Although these methods are well-developed, they generate relatively basic forms that are predominantly modified versions of the standard cylinder or spherical shapes. Therefore, additive manufacturing (AM) of catalysts or their support could unlock new possibilities in the shaping of packings in fixed bed reactors for improved catalytic performance [13].

Additive Manufacturing stands as a pivotal element within the latest industrial revolution, known as Industry 4.0, which unites advanced manufacturing techniques with innovative information technology to revolutionize industrial processes and systems. Within this transformative landscape, AM introduces invaluable components that have the potential to greatly elevate chemical process design, spanning material science, process optimization,

and innovative design methodologies [14, 15]. Nowadays, chemical science and engineering must face challenges regarding process and reactor design in order to transition to more sustainable production. The relevance of 3D printing for structured catalysts emerges from the perspective of advanced manufacturing. This approach enables the creation of intricate custom shapes, leading to the optimization of various factors such as pressure drop, heat and mass transfer capabilities, fluid and particle movement dynamics, along with reaction thermodynamics. Hence, through the utilization of AM, it becomes possible to rapidly manipulate and tailor catalyst performance, reactor design, and overall efficiency to align precisely with the requirements of individual chemical systems [16, 17].

## 1.2 Outline

This work focuses on the utilization of the BJ AM technology to generate active, alumina-based heterogeneous catalysts. Incorporation of active material at different process stages during or after the printing process enables varying catalyst distributions and therefore catalytic properties.

- **Chapter 2** introduces the theoretical background, fundamentals and state of the art on additive manufacturing in the context of heterogeneous catalysis.
- **Chapter 3** describes the basic principles of catalyst synthesis and characterization techniques used in this work.
- **Chapter 4** focuses on the development of a fundamental AM strategy using binder jetting which generates porous alumina catalyst supports for heterogeneous catalysis. The presented 3D printing process steps provide the foundation on which the upcoming BJ catalyst printing strategies are based on.

This chapter is based on: H. M. Bui, R. Fischer, N. Szesni, M. Tonigold, K. Achterhold, F. Pfeiffer, O. Hinrichsen, "Development of a Manufacturing Process for Binder Jet 3D Printed Porous Al<sub>2</sub>O<sub>3</sub> Supports Used in Heterogeneous Catalysis", *Additive Manufacturing*, **2021**, 50, 102498, DOI: 10.1016/j.addma.2021.102498.

- **Chapter 5** compares the two AM techniques direct ink writing (DIW) and binder jetting (BJ) regarding their advantages and drawbacks for the preparation of wet impregnated Pt/Al<sub>2</sub>O<sub>3</sub> catalysts for the dehydrogenation of perhydro-dibenzyltoluene, a liquid organic hydrogen carrier (LOHC). Catalyst characterization and catalytic

testing in a semi-batch reactor setup revealed differing physicochemical properties due to 3D printing while the Pt productivities are similar for both DIW and BJ.

This chapter is based on: H. M. Bui, P. F. Großmann, A. Berger, A. Seidel, M. Tonigold, N. Szesni, R. Fischer, B. Rieger, O. Hinrichsen, "Comparison of Direct Ink Writing and Binder Jetting for additive manufacturing of Pt/Al<sub>2</sub>O<sub>3</sub> catalysts for the dehydrogenation of perhydro-dibenzyltoluene", *Chemical Engineering Journal*, **2023**, 141361, DOI: 10.1016/j.cej.2023.141361.

- **Chapter 6** investigates the fabrication of spherical nickel catalysts by admixing of co-precipitated Ni-Al precursor to the alumina powder bed. Thorough characterization reveals similar catalyst properties compared to conventional Ni-Al catalysts as well as significant CO<sub>2</sub> conversion and CH<sub>4</sub> selectivity during CO<sub>2</sub> methanation tests in a single pellet string reactor (SPSR).

This chapter is based on: H. M. Bui, P. F. Großmann, T. Gros, M. Blum, A. Berger, R. Fischer, N. Szesni, M. Tonigold, O. Hinrichsen, "3D Printed Co-Precipitated Ni-Al CO<sub>2</sub> Methanation Catalysts by Binder Jetting: Fabrication, Characterization and Test in a Single Pellet String Reactor", *Applied Catalysis A: General*, **2022**, 118760, DOI: 10.1016/j.apcata.2022.118760.

- **Chapter 7** focuses on the preparation and characterization of Ni/Al<sub>2</sub>O<sub>3</sub> catalysts by BJ where the Ni precursor Ni(NO<sub>3</sub>)<sub>2</sub> · 6(H<sub>2</sub>O) is incorporated into the aqueous printing liquid, facilitating simultaneous impregnation and shaping of catalysts by 3D printing. Comparison with conventional wet impregnated Ni/Al<sub>2</sub>O<sub>3</sub> catalysts reveals the presence of different Ni species depending on the preparation method and respective post-processing.

This chapter is based on: H. M. Bui, T. Kratky, I. Lee, R. Khare, M. Hiller, S. Wedig, S. Günther, O. Hinrichsen, "In situ impregnated Ni/Al<sub>2</sub>O<sub>3</sub> catalysts prepared by binder jet 3D printing using nickel nitrate-containing ink", *Catalysis Communications*, **2023**, 106738, DOI: 10.1016/j.catcom.2023.106738.



# 2 Theoretical and Technological Background

## 2.1 Additive Manufacturing

In contrast to subtractive and formative manufacturing methods, additive manufacturing is based on a layer-wise building principle which slices an object into layers. Fig. 2.1 visualizes the general AM concept scheme which is universally valid for all of the numerous additive manufacturing techniques. The basic principle of AM is the creation of a physical three-dimensional model by direct conversion of computer-aided design (CAD) data [18].

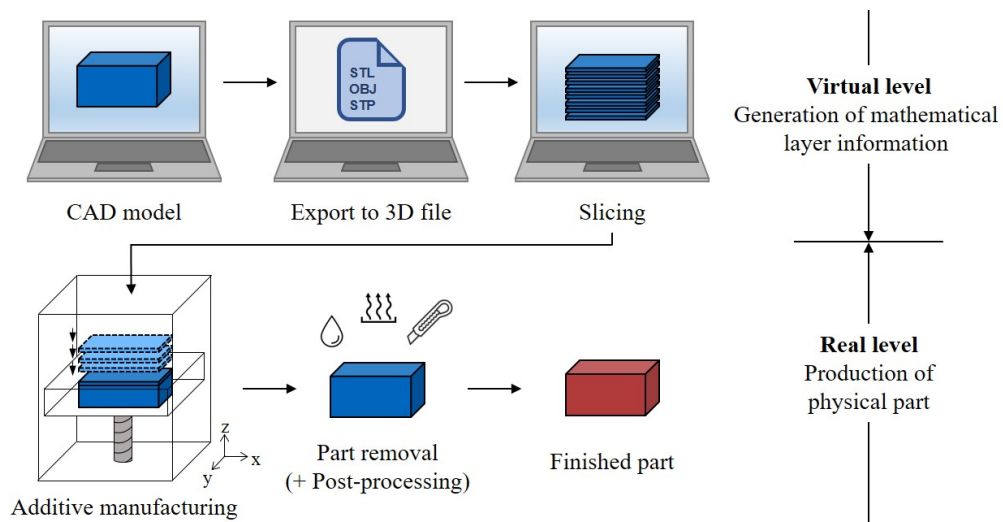


**Figure 2.1:** General concept of additive manufacturing, adapted from [18].

Firstly, a virtual model is created by 3D CAD. Subsequently, the designed model is exported in order to obtain a STL (standard triangle language/standard tessellation language [19]) data set of the part surface which is approximated by triangles. The mathematical generation of layers (of equal thickness) is called slicing. The STL file is then transferred

to the printer together with information regarding tool path generation, machine parameters, part orientation, size, etc. The aforementioned process steps on the virtual level are the basis for the AM process. On the real level, the sliced model is physically printed by joining single cross sections in the  $xy$ -plane with the preceding one in  $z$ -direction. After part removal from the print bed after finishing the print job, post-processing, which comprises any processing steps necessary to obtain a functional part after printing, might be executed. Possible post-processing steps include infiltration, support removal, surface smoothing, coating, painting, sanding, thermal treatment, etc., depending on the used printing technique and the requirements of the technical application. If no more finishing steps are necessary, the 3D printing process is complete.

Since Chuck Hull patented the first 3D printing technology called stereolithography in 1986 [20], 100 different AM machines working with significantly varying fusing mechanisms have been developed and introduced to the market [18]. Fig. 2.2 classifies the most relevant AM technologies according to their used starting material and layer fusing mechanism. The entirety of the machines presented in Fig. 2.2 will not be detailed in

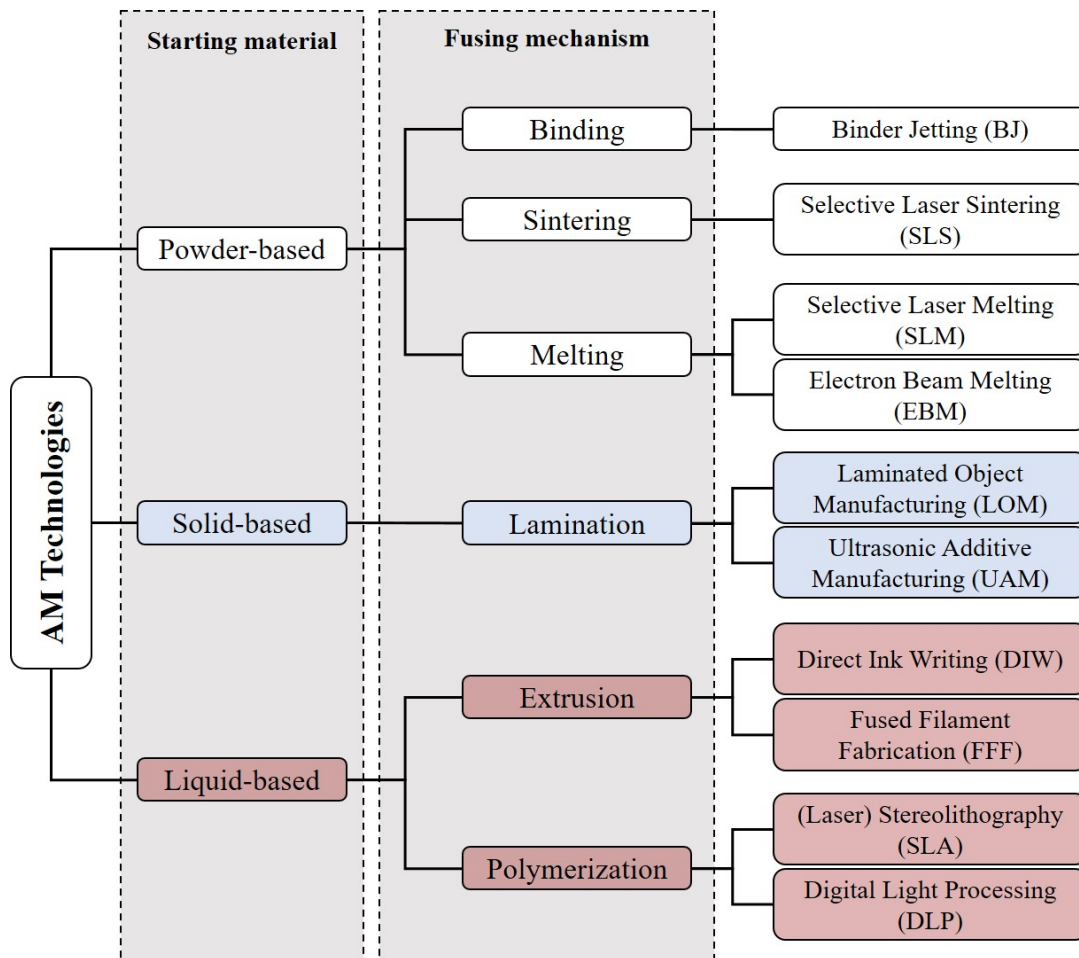
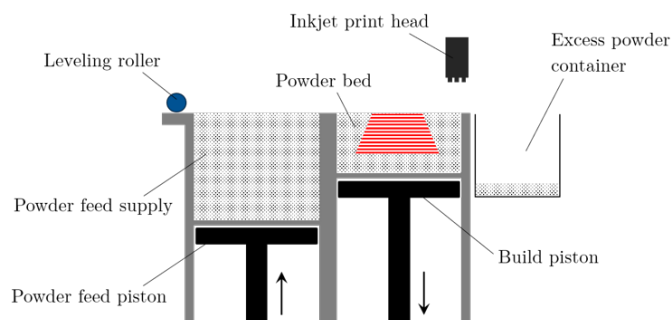


Figure 2.2: Classification of additive manufacturing technologies.

this work. Whether the material feedstock is solid, powdery or liquid, affects how the single layers can be stacked onto each other and connected. Ludwig et al. evaluated the applicability of four different AM techniques for the preparation of  $\text{Al}_2\text{O}_3$  carriers with elevated BET surface area [21]. They identified that stereolithography (SLA), fused filament fabrication (FFF), direct ink writing (DIW) as well as binder jetting (BJ) are suitable for catalyst manufacturing and can possibly generate bodies with high porosity (thus high surface area) and mechanical robustness simultaneously. SLA printers selectively polymerize monomeric liquid precursor layer by layer. The extrusion-based FFF continuously presses a strand of heated thermoplastic material through one or more nozzles and deposits it in a defined path onto the printing platform. In contrast to FFF, DIW involves the extrusion of pastes made from materials such as metals, composites, and ceramics without a temperature-induced phase transition. Since the focus of this work lies on the usage of BJ, chapter 2.1.1 thoroughly details its functional principle.

### 2.1.1 Binder Jetting Technology

In order to satisfy the demand for robust as well as porous catalyst particles, binder jetting is a possible 3D printing method according to Ludwig et al. [21]. Since parts emerge from a powder bed made of loosely cumulated particles, inherently porous particles are generated with this printing method in comparison to other AM methods. A bed of granules or powder is provided which is exposed to an inkjet printhead. The particles are selectively



**Figure 2.3:** Main components of a binder jetting printer.

conglutinated with a liquid binder which is ejected from the printhead in fine droplets that penetrate and simultaneously spread into the powder bed, see Fig. 2.4. After ink deposition, a new powder layer is spread over the preceding one. After layer-wise repetition of the aforementioned steps, a powder bed containing the component arises. Thus, no support structures are necessary as the loose powder surrounding the bound part supports the component, facilitating printing of relatively complex structures. After printing and curing of the binder, if required, the green part must be separated from the surrounding

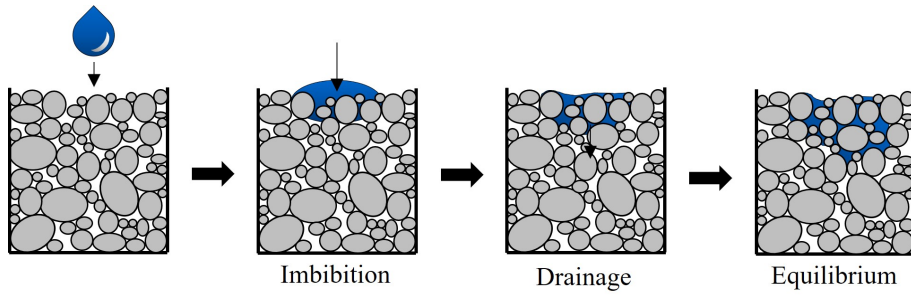


**Figure 2.4:** Binder penetration steps into the powder bed.

powder. The binder which holds together the green part is fully removed in a debinding step which completely burns off all organic and volatile compounds in the binder. Due to the inherent fragility of BJ printed objects induced by a greater amount porosity in contrast to other 3D printing techniques, post-processing by thermal treatment (sintering) and/or infiltration is often necessary to establish sufficient mechanical strength.

**Powder properties** Relevant powder properties are the particle size distribution, surface area and porosity which affect the powder flowability, powder bed density and spreadability. It was investigated that smaller powder particles facilitate the expansion of ink droplets due to smaller interparticle voids, leading to a decreased geometrical accuracy [22]. In general, the usage of smaller particles leads to a increased surface quality of the component, however, at the expense of powder flowability. Larger voids generated by larger powder particles facilitate vertical liquid penetration into the powder bed by increased powder bed permeability [23].

**Ink properties** Ink characteristics are affected by a set of physical parameters, such as the viscosity, surface tension and liquid density. The ink formulation influences the processibility by the printhead and must be adjusted accordingly when new materials are used for binder jet printing. A set of dimensionless numbers containing the Reynolds number  $Re$ , the Weber number  $We$  and the Ohnesorge number  $Oh$  describes the ejectability of a droplet [24]:

$$Re = \frac{u\rho l}{\eta}, \quad (2.1)$$

$$We = \frac{u^2 \rho l}{\sigma}, \quad (2.2)$$

$$Oh = \frac{\sqrt{We}}{Re} = \frac{\eta}{\sqrt{\sigma \rho l}}, \quad (2.3)$$

$$Z = \frac{1}{Oh} \quad (2.4)$$

$u$ ,  $\rho$ ,  $l$ ,  $\eta$ ,  $\sigma$  are the mean jetting velocity, ink density, characteristic length (in most cases the drop diameter), dynamic viscosity, and surface tension, respectively. The inverse  $Oh$  number is defined as  $Z$ . Fig. 2.5 plots the Weber number vs. Reynolds number and visualizes the regimes of droplet behavior valid for drop-on-demand inkjet printheads. Reis and Derby performed numerical simulations of drop formation and proposed that for  $10 > Z > 1$  stable formation is possible, whereas at low values of  $Z$ , ink viscosity is too high and prevents drop generation by viscous dissipation [25]. Fig. 2.5 furthermore illus-

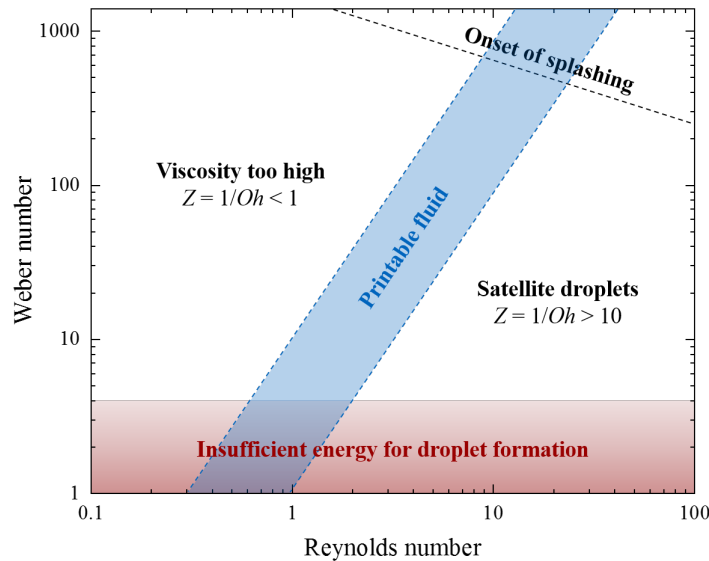


**Figure 2.5:** Regimes of droplet ejectability for a drop on demand printhead, adapted from [26].

trates that at high  $Z$  values ( $Z > 10$ ) the main drop ejected from the nozzle is accompanied by smaller satellite drops, resulting in a decreased feature resolution. Moreover, a region exists where due to a too low  $We$  number, the energy provided is insufficient to form a drop.

**Powder-ink interaction** Ultimately, the interaction between the ink (or binder) and the powder determines the final accuracy and mechanical strength of the green part. The ability of the ink to penetrate and wet the powder bed in terms of binder penetration time and depth defines relevant printer parameters such as the minimal layer thickness which is related to the binder saturation, see Eq. 2.5:

$$\text{Binder saturation} = \frac{\text{Total amount of binder}}{\text{Total pore volume}}. \quad (2.5)$$

An excess amount of binder leads to bleeding of the ink into the surrounding powder, leading to dimensional inaccuracy, while insufficient amounts of ink causes weak layer

cohesion. Binder jetting requires an optimum interaction between the powder and binder in order to form a workable part for further processing. Methods to investigate the penetration characteristics are by sessile drop goniometry [27, 28], X-ray imaging [29] or prediction of the spreading behavior by numerical simulations [30, 31].

## 2.2 Additive Manufacturing and Catalysis

The continuous increase in detailed comprehension of chemical reactions and further development of large-scale chemical processes is depicted by the timeline in Fig. 2.2 which illustrates several crucial milestones in catalysis. The end of the 19th century until the 1920s was marked by the birth of industrial catalysis facilitating the production of basic, bulk inorganic chemicals such as  $\text{H}_2\text{SO}_4$ ,  $\text{NH}_3$  and  $\text{HNO}_3$  for the first time [32, 33]. The emerging transportation industry in the ongoing 20th century drove the need for

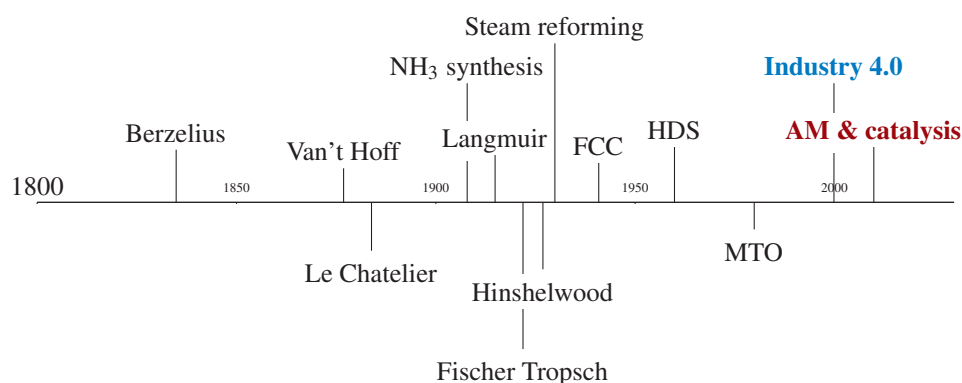


**Figure 2.6:** Temporal evolution and milestones of heterogeneous catalysis.

refined petroleum products so that catalytic fuel processes such as the Fischer-Tropsch process, steam reforming, catalytic cracking (and fluid catalytic cracking (FCC)) produced highly needed fuel feedstock [33]. From the 1960s and still ongoing, environmental (emission) catalysis gains relevance due to awareness of air-born pollutants, resulting in vehicle and stationary engine emission control (hydrodesulfurization (HDS), (Pd) three-way catalyst,  $\text{NO}_x$  reduction). Considering the current concerns regarding environmental protection, "green chemistry" will continuously matter and pose new challenges, e.g. new catalysts and reactor technologies for the synthesis of clean fuel components, further sulfur reduction, reduction of heavy metals from crude oil by (bio-)demetalization, green  $\text{H}_2$  production etc. [34].

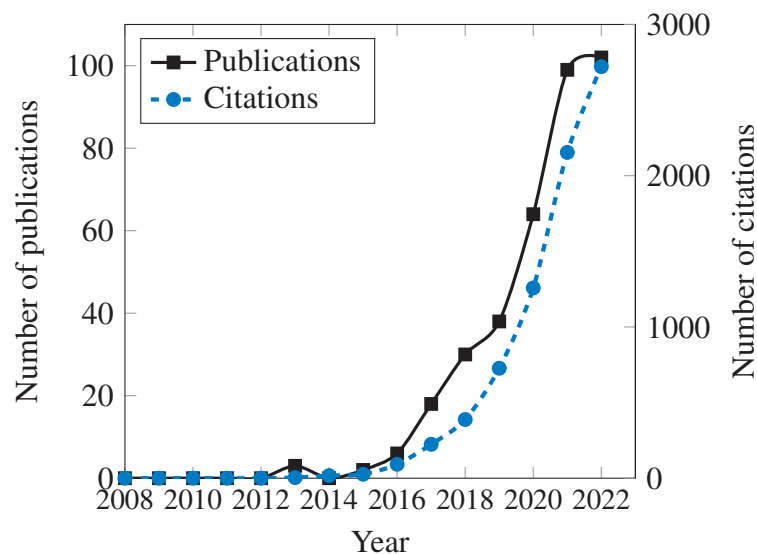


**Figure 2.7:** Development of number of scientific publications and citations for the combined topics of additive manufacturing and catalysis over time (Source: Web of Science [39]).

Since the early 2010s, the term "Industry 4.0" introduces the fourth industrial revolution which encourages the integration of intelligent production systems for enhanced manufacturing efficiency and performance, design flexibility and innovation [14, 35]. Additive manufacturing is an essential element of Industry 4.0 to achieve these goals. While the automotive, aerospace, biomedical industries have quickly adopted AM to reap the benefits of the new manufacturing possibilities [36–38], the chemical industry lags behind due to lack of agility and adaptability [16]. Nevertheless, in the last decade, the combination of AM and heterogeneous catalysis has attracted significant interest which is manifested in the exponential increase in number of scientific publications addressing the combined topics using search key words such as "additive manufacturing", "3D printing", and "catalysis", see Fig. 2.7. The increasing number of published and cited papers emphasizes the growing effort to improve existing catalytic processes using innovative methods and establishing AM as a means to facilitate more sustainable chemical engineering [16].

### 2.2.1 State of the Art in Catalyst 3D Printing

The overall challenge underlying the printing of heterogeneous catalysts is the maintenance of the catalyst particle structure during material preparation to prevent decomposition of the active species as well as maintenance of physicochemical properties such as the pore structure and the specific surface area. Simultaneously, adequate mechanical and thermal stability for usage of printed catalyst particles in a chemical reactor must be ensured. Therefore, feedstock preparation and post-processing steps necessary can

vary drastically depending on the additive manufacturing technique applied for catalyst printing. Although basic processing material processing and post-processing steps can be derived from conventional ceramic 3D printing, differing material requirements for catalysts demand for modification of existing manufacturing protocols.

In recent years, numerous reviews on the application of 3D printing in catalysis or chemistry in general have been published. Most of them provide an overview and a classification of currently used AM techniques for catalytic purposes [40–45]. Current perspectives on (catalytic) process intensification by 3D printing are addressed with reviews by Rosseau et al. [46], McDonough [47], Bracconi [15] and Lawson et al. [48]. Li et al. [49] reviewed 3D printed photocatalytic materials, Alimi et al. assessed future trends of AM for catalysts and other applications in chemistry [50], and Maleki and Bertola [51] present recent advances of inkjet printing for heterogeneous catalysis.

Table 2.1 presents an exhaustive overview of existing scientific studies regarding 3D printing of catalysts, therefore describing the current possibilities using AM in heterogeneous catalysis. First of all, the printing strategies are divided into direct and indirect printing methods. The former method uses the catalyst precursor material as printing feedstock straight away, whereas the latter method uses a polymer 3D printer to generate a sacrificial template which is subsequently filled with liquid or pasty support material. In almost all cases, catalysts with an alumina support were prepared [17, 52–57]. The polymer mold must be removed completely in the end. Since the indirect printing strategy does not require any further AM process development due to usage of a conventional polymer printer, the direct printing method poses significant challenges in respect to raw material requirements and adaptation of the used AM technique for catalytic purposes. Hence, this work will focus on direct 3D printing strategies. Table 2.1 divides printed catalysts into different types of support. Metal monoliths are printed by direct metal laser sintering (DMLS) [58–60] or extrusion-based direct ink writing (DIW, also known as Robocasting) [61, 62] and mostly washcoated with the active component. The resulting specimens are especially attractive for catalytic exhaust gas after-treatment applications. Zeolite catalysts were prepared by DIW using zeolite-containing pastes (e.g. ZSM-5) [63–66] or stereolithography (SLA) where a resin support was printed which was dip coated in  $\text{CuO/CeO}_2$  [67]. Numerous studies fabricated metal oxide-supported catalysts.  $\text{Al}_2\text{O}_3$ -supported structures were most commonly printed, such as  $\text{Ni/Al}_2\text{O}_3$  for  $\text{CO}_2$  methanation [68],  $\text{Pd-Pt/Al}_2\text{O}_3$  [69] and  $\text{Rh/CeO}_2/\text{Al}_2\text{O}_3$  [70] for  $\text{CH}_4$  oxidation, and other catalyst systems for various applications [71–73]. Concerning the direct additive manufacturing of metal oxide-supported catalysts, exclusively DIW was put to use. DIW generates three-dimensional objects by layer-wise extrusion of a viscoelastic ink through a deposition nozzle. Due to its ability to fabricate relatively complex structures and process a wide range and mixture of material classes as long as the precursor ink exhibits adequate rheological properties (e.g. loss and elastic moduli) [74], it is plausible that DIW

garners attention for the manufacturing of monolithic catalyst structures. Additionally, DIW emerged as a printing method for intricate ceramic structures, first patented in 1997 by Cesarano and Calvert [75, 76], so that particular suitability for processing of ceramic/metal oxide feedstock is provided. Chen et al. just recently presented the current progresses of DIW for mass transfer improvement in gas-phase adsorption and catalysis [77] and Großmann et al. investigated the effect of the surface-to-volume ratio on the wet impregnation of DIW printed Pt/Al<sub>2</sub>O<sub>3</sub> monoliths [78], indicating the development process of catalyst printing evolving from feasibility studies to exhaustive parameter studies on the effects on mass and heat transfer.

**Table 2.1:** Literature research of the state of the art on additive manufacturing of heterogeneous catalysts.

Support	Printing technique	Printed structure	Catalyst	Reaction	Reference
Metal oxide / ceramic	DIW	cordierite monolith	BaMn <sub>2</sub> Al <sub>10</sub> O <sub>19</sub> /γ-Al <sub>2</sub> O <sub>3</sub>	CH <sub>4</sub> combustion	[71]
	DIW	Cordierite/α-Al <sub>2</sub> O <sub>3</sub> monolith	Pt/γ-Al <sub>2</sub> O <sub>3</sub> washcoat	CO oxidation	[72]
	DIW	Monolith	Cu/Al <sub>2</sub> O <sub>3</sub>	Ullmann reactions	[73]
	DIW	Monolith	Ni/Al <sub>2</sub> O <sub>3</sub>	CO <sub>2</sub> methanation	[68]
	DIW	SiO <sub>2</sub> monolith	Pd/SiO <sub>2</sub>	1,2,3-triazoles assembly	[79]
	DIW	Cordierite monolith	Doped Pd–Pt/Al <sub>2</sub> O <sub>3</sub> / HY washcoat	CH <sub>4</sub> oxidation	[69]
	DIW	CeO <sub>2</sub> , Al <sub>2</sub> O <sub>3</sub> monolith	Rh/CeO <sub>2</sub> /Al <sub>2</sub> O <sub>3</sub>	Partial CH <sub>4</sub> oxidation	[70]
	DIW	TiO <sub>2</sub> monolith / Au/TiO <sub>2</sub> monolith	Au/TiO <sub>2</sub>	H <sub>2</sub> photoproduction	[80]
	DIW	Fe/SiC monolith	Fe/SiC	Wet peroxide oxidation	[81]
	DIW	α-Al <sub>2</sub> O <sub>3</sub> monolith	α-Al <sub>2</sub> O <sub>3</sub>	Biginelli and Hantzsch reactions	[82]
Metal	DIW	Cu monolith	Ni/Al <sub>2</sub> O <sub>3</sub> washcoat	CO <sub>2</sub> methanation	[61]
	DMLS	Stainless steel monolith	Ni/CeO <sub>2</sub> –ZrO <sub>2</sub> washcoat	CH <sub>4</sub> dry reforming	[58]
	DMLS	Al monolith	Pt	NO oxidation	[59]
	DIW	Ti6Al4V monolith	Fe-ZSM-5	N <sub>2</sub> O decomposition	[62]
	DMLS	Stainless steel monolith	Cu/Zn/Al/Zr	MeOH steam reforming	[60]
Other	DIW	Monolith	ZSM-5	MTO	[63]
	DIW	HZSM-5, HY monolith	SAPO-34	<i>n</i> -hexane cracking	[64]
	DIW	(Doped) ZSM-5 monolith	doped ZSM-5	MTO	[65]
	DIW	Carbon monolith	NiMo/C	CO hydrogenation	[66]
	SLA	Polymer resin monolith	CuO/CeO <sub>2</sub>	Preferential CO oxidation	[67]
Alumina-based	FFF	PLA template	Al <sub>2</sub> O <sub>3</sub>	Tar hydroconversion	[52]
	DLP	Polymeric resin template	Mn/Al <sub>2</sub> O <sub>3</sub>	Oxidative coupling of CH <sub>4</sub>	[53]
	SLA	Polymeric resin template	CuO/CeO <sub>2</sub> /cordierite	CO oxidation	[54]
	DLP	Polymeric resin template	Mn–Na <sub>2</sub> WO <sub>4</sub> /Al <sub>2</sub> O <sub>3</sub>	Oxidative coupling of CH <sub>4</sub>	[55]
	FFF	PLA templates	Ni–Al <sub>2</sub> O <sub>3</sub> /C	Syngas methanation	[17]
	FFF	PLA template	Pd/γ-Al <sub>2</sub> O <sub>3</sub>	Cross-coupling reactions	[56, 57]

Direct printing

Indirect Printing

## 2.3 Macroscopic Catalyst Design

A multitude of parameters must be accounted for regarding heterogeneous catalytic reactor operation in order to achieve optimized reactor performance, e.g. cooling temperature, reactor dimension, feed composition, heat exchange area etc. In addition to the aforementioned variables, catalyst design including the morphology (size, shape, active phase distribution) must be considered prior to reactor design. In academia, research catalysts in form of fine powder are normally used in order to ensure good accessibility of active sites and to avoid heat and mass transfer limitations. However, in industrial reactors, shaped catalyst pellets or structured (monolithic) catalyst packings are used. Different catalyst shapes can be ranked according to their pressure drop: Monolith < rings < pellets < extrudates < powders [12]. The shaping process is a compromise between the minimization of pore diffusion effects (small particles) and pressure drop along the catalyst packing (large particles) [83]. Moreover, technical catalysts should reproduce the performance achieved under laboratory conditions and additionally provide mechanical and chemical stability for implementation in industrial catalytic reactors.

### 2.3.1 Conventional Catalyst Shaping

The two main catalyst manufacturing methods for supported catalysts are (co-)precipitation and impregnation. Oftentimes, more attention is attributed to the chemical composition of a catalyst. Nevertheless, the size and shape of a catalyst are decisive for the avoidance of internal and external mass transport limitations and for heat transfer. Furthermore, surface area, stability towards heat, poisons, variable process conditions and the mechanical robustness are critically affected by catalyst forming [11, 84]. The industrially most commonly used methods to shape precipitates or support material are pelleting, extrusion and granulation. Table 2.2 summarizes the particle sizes producible by each method and the main properties of their output.

**Pelleting** generates relatively dense and therefore mechanically robust cylindrical shapes by compression of dry and free-flowing catalyst powder in a die with a force of 50 to 80 kN. Liquid or solid additives to improve compaction, lubrication or to prevent dust formation can be introduced simultaneously, e.g. water, graphite, talc or waxes [11]. An inexpensive material such as clay is often added as binder. In case migration of sodium from the clay into the catalyst (or ion exchange with other alkali metals in the catalyst) at increased reactor temperature is undesired, alternative binders such as hydrated or hydroxide forms of alumina or silica-alumina can be used [83].

**Table 2.2:** The three most commonly used industrial catalyst shaping methods [83–85].

Shaping method	Size	Properties
Pelleting	3–15 mm	Cylindrical, simple shapes High mechanical strength Porosity (< 30 %) and pore texture hardly controllable
Extrusion	1–30 mm	Broader variety of cylindrical, longer shapes Larger external surface area than by pelleting Flexible porosity (30–60 %)
Granulation	1–20 mm	Only spherical shapes Lower crushing strength than by pelleting/extrusion

A suspension or paste with a high solid content is passed through a profiled die when catalysts are shaped by **extrusion**, the most economic and commonly used forming method for catalysts. The emerging ribbon is either cut to size directly after extrusion or dried and then broken into pieces of adequate length [84]. Thermal treatment in form of calcination or firing transforms the binder to strong, porous matrices of oxidic particles or/and is necessary to burn off organic additives. Since the paste's rheological properties play an important role for the final part stability, shaping agents are added. Besides the aforementioned binders,  $\text{HNO}_3$  and citric acid are admixed to deagglomerate particles. Moreover, porogens such as carbon black and differently shaped or sized starch (corn, rice) generates interparticle porosity [85].

**Granulation** is a size enlargement process which creates roughly spherical catalyst particles. Dry powder is tumbled together with a cohesive liquid binder which is sprayed on in a rotating disc, drum or pan. The granules grow by continued contacting similar to a rolling snowball and eventually reach an equilibrium particle size [86]. Particle size and texture are controlled by the process parameters granulation time, inclination angle of the equipment, stirring speed, type and concentration of binder [85].

### 2.3.2 Active Phase Distribution in Catalyst Pellets

The macroscopic distribution of the active phase within a catalyst pellet influences the catalytic performance as well as reactor design. The Thiele modulus is used to estimate the degree of mass transfer limitations in such a catalyst pellet

$$\phi = \frac{V_p}{A_p} \sqrt{\frac{k}{D_{\text{eff}}}} \quad (2.6)$$

where  $V_p$  is the pellet volume,  $A_p$  is the external surface area of the pellet,  $k$  is the rate constant of the first order reaction and  $D_{\text{eff}}$  denotes the effective diffusion coefficient. Depending on the reaction rate, reaction network (elementary, parallel, consecutive), intraparticle diffusion characteristics or thermal conditions, different metal distributions are preferred, as visualized in Fig. 2.8. A homogeneous catalyst distribution (Fig. 2.8a) is preferential for simple, reversible and relatively slow reactions in the absence of diffusion limitations under isothermal conditions where the reactant is given sufficient time to diffuse to the active sites [87, 88] and the risk of thermal runaway is low. Roth and Reichard [89] reported that an uniform Pt distribution on  $\text{Al}_2\text{O}_3$  improves activity of the dehydrogenation reaction of  $n$ -dodecane to linear dodecenes in comparison to an egg-shell distribution. When dealing with large  $\phi$  (fast reaction, diffusional control), high

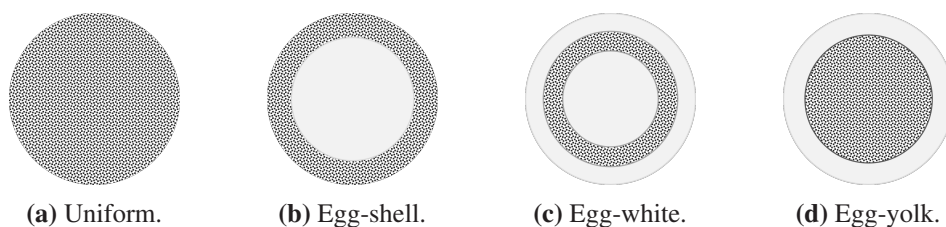


**Figure 2.8:** Different active phase distributions across a spherical catalyst pellet.

catalyst prices or when the intermediate product of a consecutive reaction is desired, an outer distribution (egg-shell, see Fig. 2.8b) is favorable to minimize diffusion resistance under absence of selectivity and poisoning considerations, as outlined by multiple studies [90–95]. An egg-white distribution (Fig. 2.8c) might be useful if the pellet material is either prone to attrition or intrapellet diffusion resistances lead to unfavorable stability characteristics such as isothermal multiplicities, as investigated by Kunimori et al. for the CO oxidation over  $\text{Pt}/\text{Al}_2\text{O}_3$  [96, 97]. If diffusion-limited poisoning occurs in the outer layers of the pellet, the active component may be deposited into the inner layer (egg-yolk distribution, see Fig. 2.8d) so that the inert outer support layer can adsorb the catalyst poison. Fig. 2.9 presents a chart of the preferred active phase distribution based on the Thiele moduli of the main reaction  $\phi_{\text{main}}$  and of the poisoning reaction  $\phi_{\text{poison}}$ .

Varying activity profiles within a catalyst pellet are generated either during shaping or applied on the already shaped support. Deposition of metals on pre-formed carriers is typically achieved by impregnation methods. The adsorption kinetics of the metal precursor on the support depends on their physical and/or chemical interaction, affected by the pH of the impregnation solution [98], isoelectric point [99] of the support surface, salt solution viscosity [100] or usage of additives such as surfactants [101]. Further preparation conditions such as the type of impregnation (capillary/diffusional/melt impregnation [102–104]), contact time between support and metal salt solution [105, 106], aging time and drying conditions [104, 107] affect the final penetration depth and metal coverage.

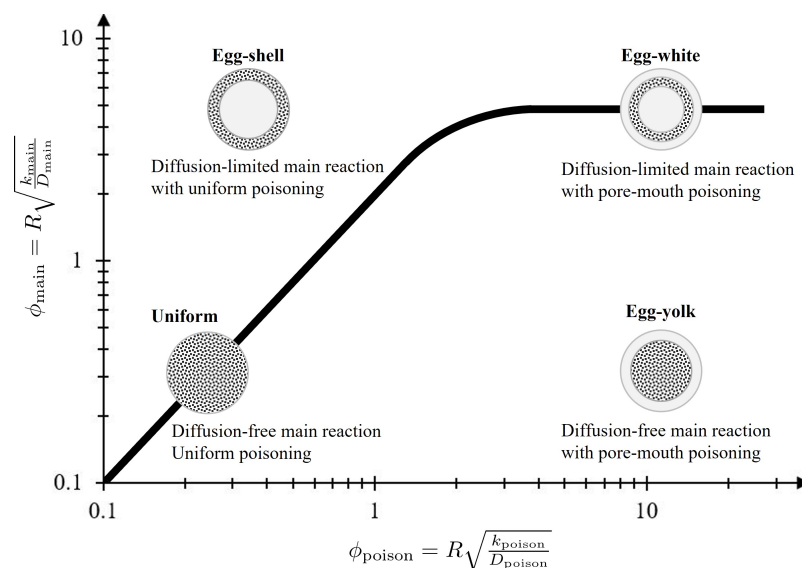


**Figure 2.9:** Catalyst selection in dependence of the Thiele moduli of the main reaction  $\phi_{\text{main}}$  and of the poisoning reaction  $\phi_{\text{poison}}$  where the criterion is the longest catalyst life (effectiveness factor  $\eta \geq 0.4$ ). Based on Becker and Wei [90].

The numerous studies regarding control of the active phase distribution indicate that precise catalyst immobilization presents a challenge. Hence, additive manufacturing poses a profoundly different catalyst preparation strategy concerning the targeted distribution of catalyst precursor compared to the aforementioned traditional impregnation methods by offering alternative pathways for metal deposition.

## 2.4 Investigated Catalytic Reactions

Binder jetting was used to manufacture heterogeneous catalyst geometries for use in various chemical reactions. Nickel catalysts were fabricated for the  $\text{CO}_2$  methanation and  $\text{Pt}/\text{Al}_2\text{O}_3$  catalysts were printed for the hydrogen release reaction of liquid organic hydrogen carriers (LOHC).

### 2.4.1 $\text{CO}_x$ Methanation

Current environmental challenges such as increasing energy consumption and resulting depletion of fossil fuels accompanied by global warming call for economically viable solutions for the utilization of renewable energy. However, the inherent intermittency and uneven geographical distribution of renewably generated power requires efficient and cost-effective storage and transportation of surplus energy. Power-to-gas (PtG) is

one strategy to convert excess electricity (power) from renewable sources into chemical energy (gas) by decentralized sector-coupling. Fig. 2.10 gives a schematic overview of the PtG concept. Water is decomposed into hydrogen and oxygen via electrolysis of water using the excess renewable electricity which preferably stems from wind-, hydro- or solar power plants. The produced green hydrogen is converted to methane in a methanation reactor together with carbon dioxide which is harvested from biomass, biogas or industrial CO<sub>2</sub> waste streams or even carbon air capture. The product gas methane is injected

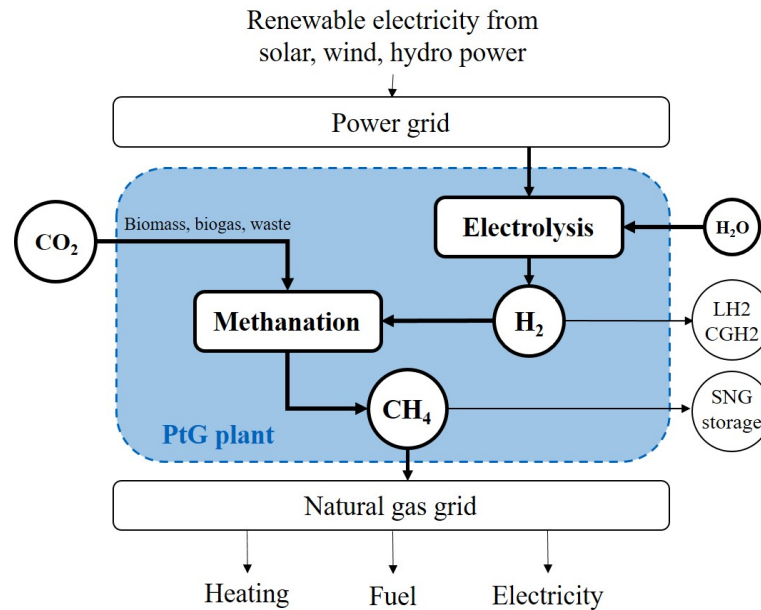


**Figure 2.10:** Schematic overview of the power-to-gas concept.

into the existing gas distribution infrastructure and used in the industrial, transportation, commercial and residential sector as a source for heat, fuel and material feedstock for the chemical industry. Thus, the PtG concept can provide a pathway to balance the energy supply-demand equation.

The effectiveness of a PtG plant depends heavily on the efficiency of the methanation process. The CO<sub>x</sub> methanation process, also known as the Sabatier reaction [108], is described by the CO methanation R1 and CO<sub>2</sub> methanation R2, which is a linear combination of R1 and the reverse water-gas shift reaction R3:



Thermodynamically, CO as well as CO<sub>2</sub> methanation are exothermic and volume contracting reactions. Therefore, elevated pressures and low temperatures generally favor the production of the product gas methane. The typical temperature ranges from 200 to 400 °C. Above 500 °C carbon deposition and mechanical destabilization of the catalyst take place [109]. Ultimately, the optimum operating conditions to achieve the highest possible conversion of carbon oxides, CH<sub>4</sub> selectivity and yield and low carbon deposition depend on the combination of feed gas composition (H<sub>2</sub>/CO, H<sub>2</sub>/CO<sub>2</sub> ratio) [110], initial CH<sub>4</sub> concentration in the gas mixture [109], temperature, pressure, gas hourly space velocity (GHSV) [111] and type of catalyst used.

**Methanation Catalysts** During the last 50 years, a plethora of catalytically active materials have been screened for application in CO<sub>2</sub> methanation [112, 113]. Ru is the most active and selective noble metal at low loadings and temperature due to its ability to dissociate H<sub>2</sub> effectively. Furthermore, Rh and Pd are other thoroughly investigated noble metals for CO<sub>2</sub> methanation. Among the non-noble metals, Ni is the most widely investigated one due to its availability, low price and satisfactory catalytic performance although higher reaction temperatures are necessary compared to noble metal catalysts. Combined with the considerable exothermicity of the methanation reactions R1 and R2, Ni particles are prone to sintering and agglomeration coupled with catalyst deactivation and activity loss [114, 115]. Alternatively, Co is the most active group VIII metal [116–118]. Moreover, Fe-based catalysts pose a lower toxicological concern than nickel and are more economically convenient [119]. Notwithstanding the various investigated metals, the catalyst performance also strongly depends on the properties of the support material. Common supports for the aforementioned metal particles are Al<sub>2</sub>O<sub>3</sub>, zeolites, TiO<sub>2</sub>, SiO<sub>2</sub>, CeO<sub>2</sub>, ZrO<sub>2</sub>, Ce–ZrO<sub>2</sub> [120–122]. Gac et al. investigated the effect of support composition on Ni catalysts for CO<sub>2</sub> methanation and revealed that reducibility, active metal surface area sintering resistance as well as the CO<sub>2</sub> conversion are influenced by the type of support [123]. Lastly, hydrotalcite-derived catalysts promise a combination of high metal loading as well as dispersion while being less prone to sintering. These layered double hydroxides (LDHs) are mixed hydroxides of divalent and trivalent metals in a stacked brucite octahedra configuration with the general structure  $[M_{1-x}^{2+}M_x^{3+}(\text{OH})_2][A^{n-}]_{x/n} \cdot y \text{H}_2\text{O}$  where M<sup>2+</sup> is any divalent metal cation (Ni<sup>2+</sup>, Fe<sup>2+</sup>, Cu<sup>2+</sup>), M<sup>3+</sup> any trivalent metal cation (Al<sup>3+</sup>, Mn<sup>3+</sup>, Sn<sup>3+</sup>), *x* the mole fraction of trivalent cation, A<sup>*n*-</sup> the exchangeable interlayer anion (e.g. CO<sub>3</sub><sup>2-</sup>, Cl<sup>-</sup>) and *y* the amount of crystalline or physisorbed water. Hydrotalcite-derived catalysts offer good CO<sub>2</sub> adsorption and conversion and are easily customizable due to their exchangeable laminate metal ions and interlayer ions [124].

**Reactor Concepts** Main concern of the methanation process is temperature control which directly affects the synthetic natural gas (SNG) quality and the cost-efficiency of the process design. The reaction can be carried out in an *adiabatic fixed-bed reactor*. Due to lack of integrated cooling, high-temperature hot spots and high reactor outlet temperatures occur in this type of reactor. Therefore, established reactor concepts connect two or more adiabatic fixed-bed reactors parallel or serial with intermediate cooling and gas recirculation for temperature control. Commercially available systems were developed by Air Liquide/Lurgi [125], Haldor Topsøe (TREMP process) [126, 127], ICI, Johnson Matthey and MAN among others. Linde developed a *cooled fixed-bed reactor* concept with an integrated heat exchanger and a second adiabatic reactor [128]. In cooled FBRs lower temperature hot spots form with moderate product gas temperatures of about 300 °C. Methanation in *fluidized-bed* [129, 130] and *three-phase* methanation reactors [131] is carried out ideally isothermally at moderate temperatures ensuring complete CO/CO<sub>2</sub> conversion. Drawbacks include limited reaction rates and increased catalyst consumption due to catalyst attrition.

More recent developments focus on (micro-)structured reactors to overcome the hot spot and pressure drop formation in adiabatic fixed-bed reactors [132, 133]. The well-designed internal structure in the form of catalyst-coated packings made of ceramic, metallic or carbon-type support materials promises improved radial heat transport by full access of reactant gas to the catalyst paired with lower pressure drop and mass transfer limitations. Lately, 3D printing comes into focus for the manufacturing of complex geometries for structured reactor internals. AM was applied by González-Castaño et al. to generate novel three-dimensional gyroid-based structured Ru-Ni catalysts which showed enhanced CO<sub>2</sub> conversion [134, 135]. Robocasting/DIW was used by Danaci et al. [61] to print stainless steel and copper structured supports which were subsequently loaded with Ni/Al<sub>2</sub>O<sub>3</sub> catalyst. Middelkoop et al. [68] compared 3D printed monolithic/multi-channel Ni-alumina-based catalysts with their conventionally fabricated counterparts and packed beds and discovered excellent methanation activity.

## 2.4.2 Dehydrogenation of Liquid Organic Hydrogen Carriers

A strategy to store and transport hydrogen yielded from electrolysis, reforming, gasification or pyrolysis is via hydrogenation and dehydrogenation of liquid organic hydrogen carriers (LOHC). Conventional H<sub>2</sub> storage by physical methods include compression (CGH<sub>2</sub>) and liquefaction (LH<sub>2</sub>). However, CGH<sub>2</sub> faces challenges such as safety concerns due to compression between 200 and 700 bar, a relatively low volumetric storage density and the necessity for cylindrical storage vessels. High energy consumption for H<sub>2</sub>

liquefaction to  $-253\text{ }^{\circ}\text{C}$  and loss by evaporation are drawbacks of LH<sub>2</sub> [136]. Hydrogen storage and transport with LOHC is a two-step cycle as detailed in Fig. 2.11 and ultimately enables easy handling and storage of chemically bound hydrogen since LOHC has similar properties to crude oil based liquids and therefore can be handled at ambient conditions using the known infrastructure for fuels such as gasoline and diesel.

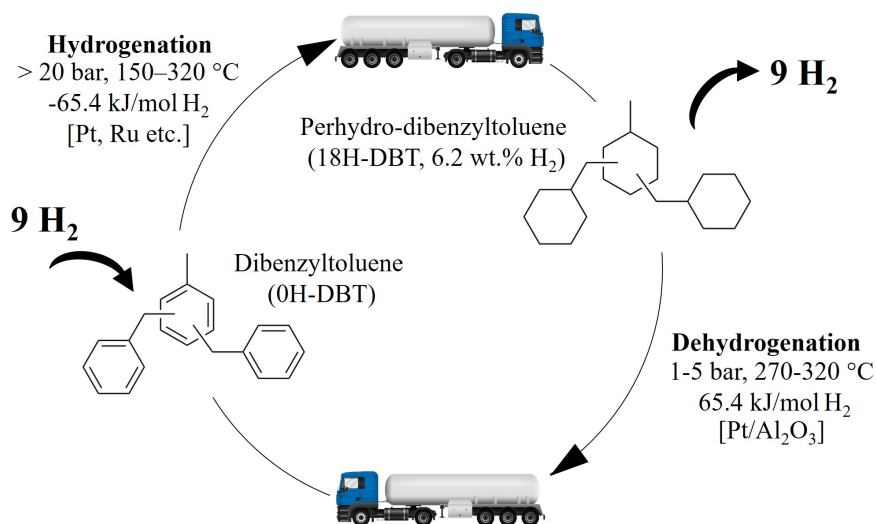


**Figure 2.11:** Schematic LOHC infrastructure using the pair perhydro-dibenzyltoluene / dibenzyltoluene.

- 1.) H<sub>2</sub> is loaded/stored by covalent binding to the hydrogen-lean LOHC molecule. The exothermic catalytic hydrogenation reaction is carried out at elevated H<sub>2</sub> pressure ( $p_{\text{H}_2} > 20\text{ bar}$ ).
- 2.) The loaded LOHC can be transported to a location of demand after hydrogenation. Release of gaseous hydrogen is realized via dehydrogenation of the hydrogen-rich LOHC compound. The endothermic dehydrogenation reaction is carried out close to atmospheric pressure ( $1\text{ bar} < p_{\text{H}_2} < 5\text{ bar}$ ) and elevated temperatures from 200 to 450 °C [137].

**LOHC materials** The prerequisites that a LOHC must meet include having a low melting point to minimize the energy needed for heating during transportation or for utilization in colder climates. Furthermore, the liquids should have a low hazard profile. In the category of aromatic hydrocarbons the following LOHC systems have been investigated and applied so far [138]: toluene / methylcyclohexane, naphthalene / tetralin / decalin, benzyltoluene (H0-BT) / perhydrobenzyltoluene (H12-BT), dibenzyltoluene (H0-DBT) /

perhydro-dibenzyltoluene (H18-DBT). The systems containing benzyltoluene and dibenzyltoluene or mixtures thereof are promising LOHCs due to their attractive property profile. H0-DBT remains liquid between  $-34\text{ }^{\circ}\text{C}$  and  $390\text{ }^{\circ}\text{C}$ , is thermally robust, hardly flammable and has a favorable toxicological profile. Furthermore, H0-DBT has already been in use commercially as a heat transfer oil under the trade name "Marlotherm" for decades and therefore provides industrial acceptance and availability.

Other LOHC systems are *N*-heteroaromatics, including *N*-ethylcarbazole / dodecahydro-*N*-ethylcarbazole, indole / indoline, 1,2,3,4-tetrahydroquinoline / quinolone among others.

**H18-DBT Dehydrogenation Catalysis** Since the LOHC pair H0-DBT/H18-DBT is an inexpensive option and therefore used for the experiments conducted in this work, the focus lies on the dehydrogenation of H18-DBT. In general, common catalysts used for the dehydrogenation of cycloalkanes to their respective aromatic compound are the noble metals Pt and Pd in small quantities supported on porous carriers such as  $\text{Al}_2\text{O}_3$ ,  $\text{SiO}_2$ ,  $\text{TiO}_2$  or  $\text{V}_2\text{O}_5$ . Egg-shell Pt/ $\text{Al}_2\text{O}_3$  is the most thoroughly investigated catalyst system for the dehydrogenation of H18-DBT [139–141]. Various influencing parameters on the dehydrogenation activity have been studied such as the Pt loading [142] and Pt morphology [143, 144]. Moreover, Auer et al. have discovered that modification of Pt/ $\text{Al}_2\text{O}_3$  with a sulfur-containing compound in a distinct molar S/Pt ratio improves the catalytic activity and reduces the formation of side products [145]. Pt/ $\text{CeO}_2$  was synthesized by a combustion method and differences in reaction kinetics were revealed due to differences in metal dispersion and pore size [146]. The dehydrogenation is a liquid-phase reaction. The maximum expansion of the H18-DBT molecule is about 1.4 nm and the average pore size diameter of an alumina-supported catalyst is 10 nm. Therefore, diffusional limitations affect the reaction rate. Auer [147] studied the effect of pore size and concluded that a minimum pore diameter of 28 nm is necessary to minimize diffusional limitations. Further studied catalyst systems are Pt/ $\text{TiO}_2$  [148], Pt/HAP, Pt/SBA–15 and Pt/C [149]. The dehydrogenation reaction is typically carried out at temperatures between  $270\text{ }^{\circ}\text{C}$  and  $320\text{ }^{\circ}\text{C}$ . Interestingly, the hydrogenation reaction can be conducted in the same temperature range.



## 3 Methodology

Basic principles of the utilized preparation and characterization methods are detailed in this chapter. The specific procedures including the experimental parameters are given in the respective chapters.

### 3.1 Conventional Heterogeneous Catalyst Preparation

The conventional catalyst preparation methods co-precipitation and impregnation were utilized in order to synthesize catalytic precursors for further use in 3D printing or for subsequent impregnation of additively manufactured alumina supports.

#### 3.1.1 Co-precipitation

Co-precipitation was used to prepare mixed metal oxide precursor powder which were admixed to the printing feedstock, resulting in the formation of bulk catalysts by 3D printing. In general, co-precipitation involves the mixing of two or more highly soluble metal salts, e.g. nitrates, chlorides, or sulfates with basic reagents such as NaOH,  $\text{Na}_2\text{CO}_3$  or mixtures thereof. The support material can be precipitated simultaneously in one single step [11]. Since the fraction of support can be low, high metal loadings of up to 80 % are attainable in contrast to less than 30 % by impregnation methods. The main processes comprise

- **liquid mixing:** The order in which the reactants are mixed affects the chemical composition as well as the catalyst's structural and textural properties. In a batch-wise operation, forward (base to acid) or reverse (acid to base) precipitation potentially lead to inhomogeneous product mixtures. Therefore, precipitation at a constant pH in a semibatch operation mode by simultaneous addition of acidic metal solution and alkaline precipitation agent is oftentimes preferred to achieve a more homogeneous mixture.

- **nucleation:** the rate of nucleation is mainly dependent on the concentration and temperature, see Eq. 3.1:

$$\frac{dN}{dt} = \beta \exp\left(\frac{-A}{\ln^2 s}\right), \quad (3.1)$$

where  $\beta$  is a pre-exponential term,  $A$  the interfacial energy parameter and  $s$  the supersaturation. A critical extent of supersaturation must be overcome to initiate fast nucleation.

- **crystal growth:** the crystal size is affected by the ratio of the nucleation rate and crystal growth.

Other processes are aggregation and recrystallization (Ostwald ripening) [11]. Subsequent aging, which includes continued stirring of the precipitate in its mother liquor under constant pH and temperature, can significantly change the precipitate's properties by converting the primary amorphous to a crystalline phase, support dissolution/redeposition or counterion displacement [11, 150].

### 3.1.2 Wet Impregnation

Due to its ease of application and the possibility to generate metal gradients, the impregnation method is industrially well-established. During dry or incipient wetness impregnation, the amount of solution is limited to the pore volume so that no excess liquid remains outside the pores, meaning that capillary action draws the solution into the pores. In this work, wet impregnation was applied, which is executed in diffusional conditions by immersing the support in an amount of solution in excess of the support pore volume.

## 3.2 Catalyst Preparation Using Binder Jetting

The custom-built binder jetting printer system used for this study (3d-figo GmbH, Germany) comprised a build platform with the print bed dimensions of  $74 \times 74$  mm and a total print height of 100 mm. The general scheme of the binder jetting printer setup is depicted in Fig. 3.1. Depending on the used catalyst printing strategy, the component of the powder reservoir can vary between metal oxide or catalyst precursor powder among others. All prints were conducted with a print head moving speed of 44.2 mm/s and a counter-rotating leveling roller distributing the fresh powder from the powder feed supply

chamber over to the print bed. The printing liquid reservoir was connected to the drop-on-

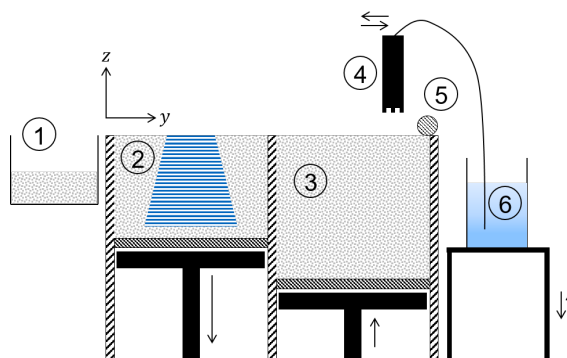


**Figure 3.1:** General scheme of the binder jetting setup with its main components. 1: Excess powder collector, 2: Build platform, 3: Powder supply chamber, 4: Printhead, 5: Spreading roller, 6: Ink supply.

demand (DOD) shear-mode piezo inkjet print head (508GS, Seiko Instruments GmbH, Japan) which conveyed the ink via hydrostatic pressure, while slight underpressure had to be maintained during print jobs by manual height adjustment of the supply tank. The print head is operable with water-based as well as solvent-based inks. Furthermore, it is possible to use particle-loaded ink. All test bodies were printed with a layer thickness of 40  $\mu\text{m}$ . The print head nozzle plate was repeatedly purged and cleaned with distilled water after 40 layers to prevent nozzle clogging during the print job.

The resulting green parts were subsequently cured in a drying oven to set the binder. Thermal treatment follows to remove all containing binder (debinding) and in order to calcine the catalyst precursor. After debinding, post-processing by slurry-infiltration introduces additional particles for part stabilization. The last step comprises another calcination step.

### 3.3 Catalyst Material Characterization

Various characterization techniques were used in this work in order to elucidate material properties such as the elemental composition, reducibility, sorption characteristics, morphology, metal particle size and mechanical stability of the catalyst in its precursor state and after 3D printing.

### 3.3.1 X-ray Powder Diffraction

X-ray powder diffraction (XRD) allows the investigation of catalyst materials in their powdered form, providing information about their crystal structure, phase composition, and crystallite size. When X-rays interact with a crystal, they are diffracted by the crystal lattice structure. The atoms in the crystal cause constructive and destructive interference of the X-ray waves, resulting in a unique diffraction pattern. This pattern contains information about the arrangement of atoms within the crystal. By analyzing the angles and intensities of the diffracted X-rays, the positions of the atoms within the crystal lattice, the unit cell dimensions, and other structural parameters can be determined.

Bragg's law states that when X-rays strike a crystal lattice at a specific angle, constructive interference occurs between the X-ray waves scattered by parallel crystal planes. This constructive interference leads to the formation of reflexes in the XRD pattern. Mathematically, Bragg's law is expressed as:

$$n\lambda = 2d \sin \theta, \quad (3.2)$$

where  $n$  is the order of the diffraction peak,  $\lambda$  is the wavelength of the incident X-rays,  $d$  is the distance between the crystal planes and  $\theta$  is the angle between the incident X-ray beam and the crystal planes.

The Scherrer equation is a widely used equation in XRD to estimate the average particle size of crystalline materials based on the broadening of diffraction peaks. The crystallite size is determined  $d_C$  using the full width at half maximum (FWHM) of a reflex:

$$d_C = \frac{K \cdot \lambda}{\beta \cdot \cos \theta} \quad (3.3)$$

The shape factor  $K$  of the spherical crystallite is typically 0.9 [151],  $\beta$  is the FWHM in radians,  $\lambda$  the wavelength of the X-rays ( $\lambda = 0.15406 \text{ nm}$ ) and  $\theta$  the diffraction angle in radians. It is important to note that in addition to particle size, other factors like strain, microstrain or instrumental effects can also contribute to the broadening of diffraction peaks in XRD patterns. Therefore, the crystallite size determined by the Scherrer equation is a lower bound for the size of the scattering domain and is typically smaller than the particle diameter.

### 3.3.2 X-ray Photoelectron Spectroscopy

X-ray photoelectron spectroscopy (XPS) is a surface characterization technique that uses photoelectrons excited by X-ray radiation (usually Mg K- $\alpha$  or Al K- $\alpha$ ) and released from the material into vacuum, see Fig 3.2. XPS is based on the photoelectric effect, which

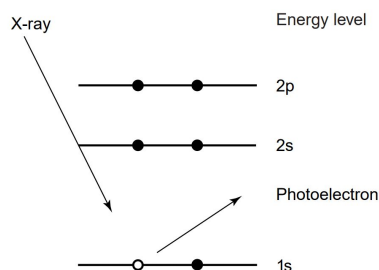


**Figure 3.2:** Diagram of the ejection of a photoelectron from a carbon atom. Reprinted with permission from John Wiley and Sons [152].

states that when soft X-rays of sufficient energy irradiate a material's surface, valence or core electrons are ejected. XPS is a surface-sensitive analysis method with a penetration depth into the sample of 2 to 10 nm. The electrons have a characteristic binding energy  $E_b$  dependent on the element of origin. UHV conditions ( $10^{-9}$  to  $10^{-8}$  Pa) are necessary due to the high surface sensitivity of the measurement. The XPS process is governed by Einstein's relationship

$$E_{\text{kin}} = h\nu - E_b - \phi_{\text{sp}} \quad (3.4)$$

where  $E_{\text{kin}}$  is the measured kinetic energy of the ejected electron with respect to the Fermi level,  $h\nu$  is the photon energy and  $\phi_{\text{sp}}$  is the instrument dependent work function of the spectrometer [152]. Apart from chemical identification, the chemical environment can be deduced from XPS spectra by analyzing the shifts in binding energy according to the atomic environment. Electrons which are excited and escape without loss of energy contribute to the characteristic peaks in the spectrum. Electrons which undergo inelastic scattering contribute to the background of the spectrum. As a result of relaxation after excitation, the ionized atom either undergoes X-ray fluorescence (emission of a X-ray photon) or ejects an Auger electron as a consequence of the XPS process [153].

### 3.3.3 X-ray Absorption Spectroscopy

When light is absorbed through the photoelectric effect at an energy range between 500 eV to 500 keV, an X-ray photon is absorbed by an electron in a tightly bound quantum

core level of an atom. The absorption coefficient  $\mu$  gives the probability that X-rays are absorbed according to Beer's law [154]:

$$I = I_0 e^{-\mu t} \quad (3.5)$$

where  $I_0$  is the incident intensity of the X-ray,  $t$  is the sample thickness and  $I$  is the transmitted intensity through the sample. XAS measures the energy dependence of the absorption coefficient  $\mu(E)$  at and above the absorption edge of a certain element as a function of the X-ray energy  $E$ .  $\mu(E)$  is strongly dependent on the sample density  $\rho$ , the atomic number  $Z$  and atomic mass  $A$ :

$$\mu(E) = \frac{\rho Z^4}{AE^3}. \quad (3.6)$$

An absorption edge is a sharp rise in absorption when the incident X-ray energy equals the binding energy of a core-level electron.

Since hard X-rays penetrate deeply, X-ray absorption spectroscopy (XAS) is a bulk technique. The spectra are linear combinations of all chemical forms of the element contained in the sample. XAS includes two regimes, namely X-ray absorption near-edge structure (XANES) and extended X-ray absorption fine-structure (EXAFS) as detailed in Fig. 3.3. The near-edge XANES gives information about the oxidation state, coordination chem-

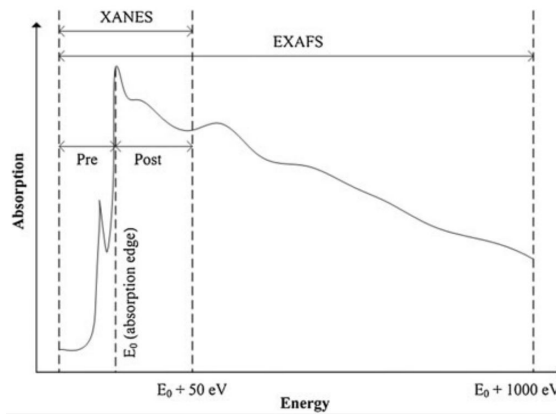


**Figure 3.3:** Exemplary XAS spectrum depicting the XANES and EXAFS regions as well as the pre- and post-absorption edge regions [155].

istry and orbital occupancy of the absorbing atom, while EXAFS elucidates the radial distribution (bond distance and number and type of atomic neighbors). The EXAFS is understood as the wave behavior of the photoelectron during absorption, thus visible as oscillations  $\chi(k)$  which quickly decay with increasing wavenumber  $k$ .

$\mu(E)$  can be measured either in transmission as

$$\mu(E) = \log(I_0/I) \quad (3.7)$$

or in fluorescence as

$$\mu(E) \propto I_f/I_0. \quad (3.8)$$

Transmission measurements can be suitable for concentrated samples whereby the correct sample thickness, uniformity of the sample and a grain size not bigger than the absorption length must be ensured. Fluorescence measurements are better suited for thick samples or samples with a low concentration [154].

### 3.3.4 N<sub>2</sub> Physisorption

Nitrogen physisorption refers to the adsorption of N<sub>2</sub> gas onto the surface of a solid material through weak Van der Waals forces to characterize their porosity and surface area. The measurement is carried out at the temperature of liquid nitrogen (77 K). When carried out discontinuously, successive amounts of adsorptive gas are introduced at a controlled pressure and given time to equilibrate. At each pressure step, the corresponding equilibrium pressure is recorded and correlated to the respective point on the adsorption isotherm. Prior to measurement, sample outgassing must be performed to remove any unwanted species adsorbed on the sample surface. Samples can be degassed using vacuum or under gas flow. Sample elutriation, which mostly affects low-density samples, must be prevented by using an adequate degassing procedure.

For surface area determination, the most widely used procedure is the Brunauer-Emmett-Teller (BET) method which involves the BET theory. It incorporates the Langmuir adsorption isotherm concept regarding the monolayer uptake which assumes homogeneous, independent and energetically equivalent adsorption sites. Furthermore, the Langmuir model assumes a finite number of adsorption sites and reversibility of the adsorption process [156]. The BET theory is an extension of the Langmuir theory but assuming multilayer adsorption. The monolayer volume  $V_{ML}$  is described by the linearized BET equation (see Eq. 3.9),

$$\frac{1}{V_{ads} \cdot \left(\frac{p}{p_0} - 1\right)} = \frac{1}{V_{ML} \cdot C} + \frac{C-1}{V_{ML}} \cdot C \cdot \left(\frac{p}{p_0}\right) \quad (3.9)$$

where  $V_{ads}$  is the volume adsorbed,  $p/p_0$  the relative pressure,  $V_{ML}$  the monolayer volume and  $C$  the BET constant. The specific BET surface area  $S_{BET}$  can be calculated using Eq. 3.10:

$$S_{BET} = \frac{V_{ML} \cdot N_A \cdot \sigma_i}{V_m \cdot m_{cat}} \quad (3.10)$$

$N_A$  denotes the Avogadro constant,  $\sigma_i$  the molecular cross-sectional area of the adsorbate molecule,  $V_m$  the molar volume and  $m_{cat}$  the catalyst mass. The BET equation is only applicable between  $0.05 > p/p_0 > 0.3$  in the region of complete monolayer adsorption [157]. Adsorption isotherms are grouped into six types by IUPAC as shown in Fig. 3.4a.

- **Reversible Type I:** Also termed Langmuir isotherm. Microporous solids with small external surface. Uptake limited by accessible micropore volume.
- **Reversible Type II:** normal S-shaped isotherm attained with nonporous or macroporous samples. Point B indicates the transition from monolayer to multilayer coverage.
- **Reversible Type III:** Convex to the  $p/p_0$  axis. Heat of adsorption is less than the adsorbate heat of liquefaction. Thus, additional adsorption is facilitated.
- **Type IV:** Well-defined mesoporous materials. Hysteresis loop caused by delayed desorption compared to uptake.
- **Type V:** Low adsorbate-adsorbate interactions, porous materials with wide pores. Incomplete monolayer formation.
- **Type VI:** Stepwise multilayer adsorption on an uniform nonporous surface. Each step represents the monolayer uptake for each layer.

Adsorption hysteresis is usually associated with capillary condensation in mesoporous solids and connected to specific pore structures. The IUPAC classifies four different hysteresis loop types (see Fig. 3.4b):

- **Type H1:** Porous materials with cylindrical pore channels or agglomerates of uniform spheres in a regular array, hence narrow pore size distribution.
- **Type H2:** Poorly defined, disordered pore size and shape. Often found in porous adsorbents.
- **Type H3:** No limiting adsorption at high  $p/p_0$ , forced closure of hysteresis loop due to tensile strength effect. Found in aggregates of plate-like particles, slit shaped pores.
- **Type H4:** Associated with narrow slit pores, but including microporosity due to the Type I isotherm character.

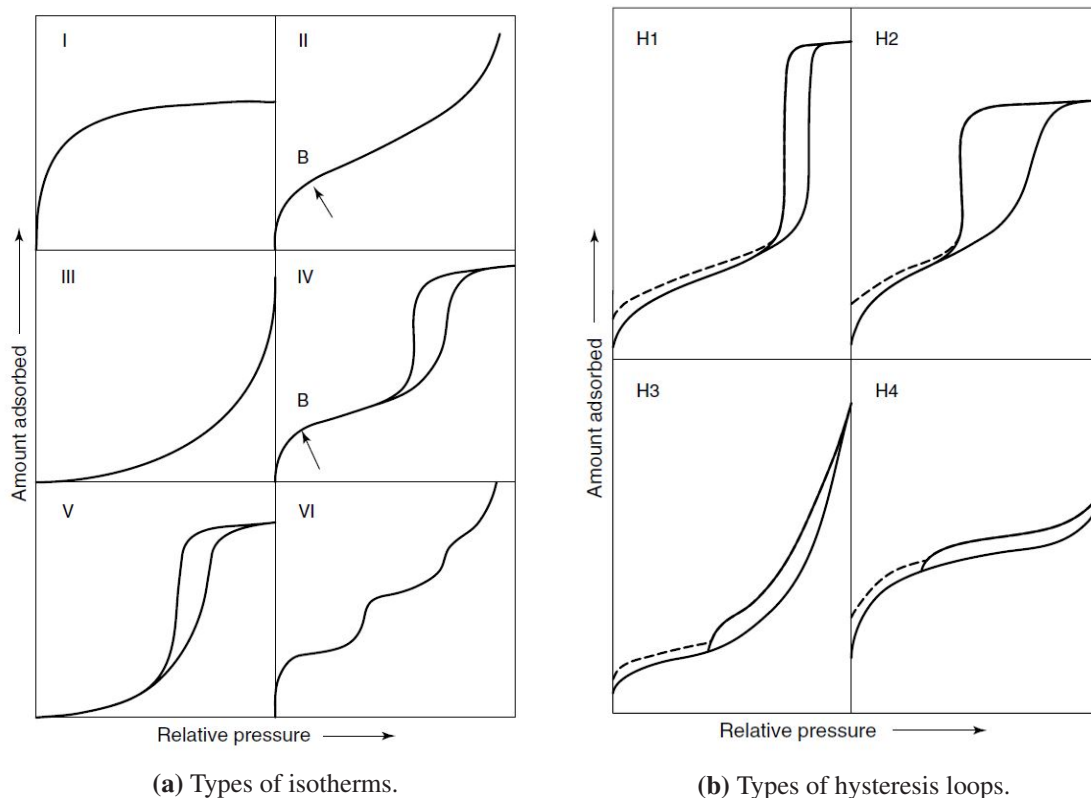


**Figure 3.4:** Gas adsorption data evaluation according to the IUPAC classification. Reprinted with permission from John Wiley & Sons [158].

The pore size distribution of mesopores can be determined iteratively with the Barrett-Joyner-Halenda (BJH) method using the Kelvin equation and assuming cylindrical pore geometry. The method is based on the principle of capillary condensation whereby the pore volume is calculated from the capillary volume upon liquid desorption during a decrease of relative pressure. The area of each pore is a constant and can be calculated from the pore volume. Usually, the desorption branch is used for the BJH method. However, depending on the hysteresis loop, using the desorption branch could be unreliable [158].

### 3.3.5 H<sub>2</sub> Chemisorption

H<sub>2</sub> chemisorption refers to the process by which hydrogen molecules are adsorbed onto the surface of a solid material, forming a chemical bond with the surface atoms. Unlike physisorption, where the bonding is primarily due to weak intermolecular forces, chemisorption involves a stronger interaction and leads to the formation of new chemical species. However, isotherm generation follows a pattern similar to that of physical adsorption isotherms. The aim is to determine the number of active sites present on a given

sample, yielding the metal surface area, metal dispersion on the catalyst surface and the average crystallite size.

Prior to the actual surface characterization, sample-pretreatment includes the steps out-gassing and/or calcination, reduction, inert gas flow to remove the reducing gas and sample cooling to the desired adsorption temperature under inert gas flow. Chemisorption measures the sample's chemisorption capacity at different adsorptive pressures. Subsequently, the monolayer chemisorbed volume  $V_{ML}$  can be estimated. The Extrapolation to  $p = 0$  method requires only the combined (physical/weak and chemical/strong) adsorption isotherm to determine  $V_{ML}$ . Hereby, a straight line is constructed across the high-pressure region of the isotherm and extrapolated to zero pressure. The value of the y-intercept describes  $V_{ML}$ . The molar amount chemisorbed  $n_m$  can be used to calculate the number of surface metal atoms  $N_M$ :

$$N_M = n_m \cdot S \cdot N_A \quad (3.11)$$

where  $S$  is the adsorption stoichiometry. The specific  $H_2$  uptake  $U_{H_2}$  in  $\mu\text{mol/g}$  can be used to calculate the specific metal surface area in  $\text{m}^2/\text{g}$  using the cross-sectional area occupied by a surface atom  $\sigma_M$  and the catalyst mass  $m_{\text{cat}}$ :

$$S_M = \frac{N_M \cdot \sigma_M}{m_{\text{cat}}}. \quad (3.12)$$

The metal dispersion  $D_M$  is defined as the fraction of metal atoms found on the surface of active metal particles expressed as a percentage of all metal atoms present in the sample and is calculated with Eq. 3.13

$$D_M = \frac{U_{H_2} \cdot S \cdot M_M}{w_M} \quad (3.13)$$

where  $M_M$  denotes the molecular weight of the metal and  $w_M$  the metal loading.

### 3.3.6 Thermogravimetric Analysis

Thermogravimetric Analysis (TGA) is used to investigate the changes in mass of a sample as it is subjected to controlled temperature conditions. The instrument consists of a balance or microbalance that measures the weight of the sample, a furnace or heating system that controls the temperature, and a data acquisition system for recording the weight changes. TGA involves measuring the weight of a sample as it is heated or cooled over a defined temperature range, typically in an inert atmosphere. During a TGA experiment, the sample undergoes thermal decomposition, phase transitions, or

other reactions, leading to changes in its mass. The instrument continuously records the sample's weight as a function of temperature or time.

TGA can be used to determine the degree of reduction in a sample by conducting the measurement under hydrogen flow and recording the resulting weight loss. Subsequently, the reduced sample mass is compared with the weight of the unreduced sample. The degree of reduction  $d_{\text{red}}$  is calculated according to the following equation:

$$d_{\text{red}} = \frac{\Delta m_{\text{O}}(t)}{m_{\text{O,initial}}} \quad (3.14)$$

with  $\Delta m_{\text{O}}(t)$  being the weight of removed oxygen at the time  $t$  and  $m_{\text{O,initial}}$  denoting the total weight of removable oxygen [159].

### 3.3.7 Temperature Programmed Reduction

Temperature Programmed Reduction (TPR) is a technique used to study the reduction properties of catalysts or materials by subjecting a sample to a controlled increase in temperature while a reducing gas, such as hydrogen, is passed over it. The temperature is gradually increased, typically at a constant rate, to allow for the observation of different reduction steps that occur at specific temperature ranges. The resulting TPR curve represents the relationship between the degree of reduction and temperature. The location, intensity, and shape of the peaks provide insights into the nature and distribution of the reducible species. Additionally, the temperature at which a peak occurs can indicate the strength of the interaction between the reducing gas and the material. The progress of reduction is monitored by measuring a physical property that changes with the degree of reduction. This property could be the concentration of the reducing gas before and after passing over the sample, or it could be a spectroscopic signal associated with the reduced species. Commonly used techniques include thermal conductivity detection (TCD) and mass spectrometry (MS).

Monti and Baiker [160] conducted parametric sensitivity studies to determine how certain operating variables, such as the  $\text{H}_2$  concentration, flow rate or the amount of sample influence the TPR profile. They defined a characteristic number  $K$  which facilitates the selection of an adequate set of operating variables.

### 3.3.8 Transmission Electron Microscopy

Transmission electron microscopy (TEM) is used to visualize and analyze the atomic-scale arrangement of atoms or nanoparticles, for example the size, shape, distribution, crystal structure or grain boundaries. In a conventional TEM, a thin specimen is irradiated with an electron beam of uniform electron density emitted by an electron gun. This beam is accelerated using a high voltage, usually in the range of 100 to 200 kV. The electrons interact with the specimen by elastic scattering, inelastic scattering, and absorption. A lens system composed of three to eight lenses images the electron-intensity distribution behind the sample onto a fluorescent screen. The transmitted electrons are detected by either a fluorescent screen or a solid-state detector, such as a charge-coupled device (CCD) camera or a scintillator coupled to a photomultiplier tube (PMT). These detectors capture the intensity of the transmitted electrons, and the resulting signal is converted into a visible image or a digital image [161].

The metal dispersion  $D_M$  can be determined using TEM.  $D_M$  is indirectly proportional to the average crystallite size  $d_M$  and is determined according to Eq. 3.15 with the volume of the bulk metal atom  $V_{B,M}$  and the area occupied by one surface atom  $\sigma_M$ . Moreover, the degree of reduction  $d_{red}$  must be considered.

$$D_M = K \cdot \frac{V_{B,M}}{d_M \cdot \sigma_M} \cdot d_{red} = K \cdot \frac{M_M}{d_M \cdot \sigma_M \cdot N_A \cdot \rho_M} \cdot d_{red} \quad (3.15)$$

$V_{B,M}$  can be calculated with the molar mass of the metal  $M_M$ , the Avogadro constant  $N_A$  and the bulk metal density  $\rho_M$ . For spherical particles, the shape factor  $K$  is 6.

### 3.3.9 Inductively Coupled Plasma Optical Emission Spectroscopy

ICP-OES combines the principles of inductively coupled plasma (ICP) and optical emission spectroscopy (OES) to measure the emission of light from excited atoms in the plasma in order to determine the elemental composition of a sample. The plasma is created by ionizing an argon gas using a radiofrequency (RF) coil. The RF coil induces a rapidly oscillating electromagnetic field that ionizes the argon gas, creating a high-energy plasma consisting of charged ions and electrons and a temperature of around 10 000 K. Once introduced into the plasma torch, the high temperature of the plasma atomize the sample. The high-energy environment of the plasma excites the atoms, causing the outermost electrons to move to higher energy levels. As the excited atoms return to their ground state, they emit light in the form of photons. The emitted light consists of characteristic wavelengths or frequencies specific to each element. The emitted light is collected and

directed into a spectrometer which disperses the light into its constituent wavelengths using diffraction gratings or prisms. This separation allows analysis of the individual wavelengths. The dispersed light is then detected using a photomultiplier tube or a CCD camera.

The intensity of the emitted light at specific wavelengths is proportional to the concentration of the corresponding element in the sample. By comparing the observed intensities at specific wavelengths with known standards or calibration curves, the concentration of various elements in the sample can be determined.

### **3.3.10 Laser Diffraction Particle Size Analysis**

The scattering of light is one of the most widely used techniques for measuring the particle size distribution (PSD) of particles. The method involves the analysis of the patterns of scattered light produced when particles of different sizes are exposed to a monochromatic beam of light, typically generated by a helium-neon laser or a diode laser. Since most materials exhibit strong absorption in the infrared and ultraviolet regions, visible light of wavelengths from 350 to 900 nm is used. The scattering intensity is a function of refractive index ratio between the material and its surrounding medium and is inversely proportional to the fourth order of the light wavelength. That means, the shorter the wavelength, the stronger the scattering. The scattered light is collected by a detection system positioned around the sample cell. Subsequently, a series of detectors positioned at various angles relative to the incident laser beam measure the intensity of the scattered light at specific angles.

The analysis software uses an iterative process to fit the scattering data to the theoretical models and calculates the PSD. The scattering pattern is analyzed using mathematical algorithms, such as the Mie theory or Fraunhofer diffraction theory. The result is typically presented as a cumulative or differential particle size distribution graph.

The PSD can be extracted from solid samples dispersed in liquid or as dry powder. In the former case dry powder is suspended in a liquid medium before analysis. The choice of diluent is governed by factors such as solubility, reactivity, suspendibility and end use of the sample material. Furthermore, the color and refractive index of the sample should not be similar to the color of the diluent since the instrument may not be able to see the sample. Physical (e.g. sonication, adjusting the dilution, heat), chemical methods (e.g. wetting agents, surfactants) or a combination of both can aid to achieve a stable dispersion. Dependent on the end use, dry powder suspended in air might be adequate. In

that case, factors to consider are flowability, anti-caking and anti-clogging properties of the powder.

### 3.3.11 Mercury Intrusion Porosimetry

Mercury intrusion porosimetry (MIP) is based on the intrusion of a non-wetting fluid (mercury) into porous structures under increasing pressure. Today, the measurable pore size ranges from 2 nm to 1 mm [162]. If the wetting liquid is non-wetting, meaning a contact angle  $\theta > 90^\circ$ , an external pressure  $p_p$  must be applied to penetrate the pores. Simplified, the pore pressure can be formulated as

$$p_p = \gamma \cdot C \quad (3.16)$$

where  $\gamma$  is the surface tension of mercury and  $C$  is the curvature of the meniscus. Assuming cylindrical pores, the curvature is defined as

$$C = \frac{2 \cos(\theta)}{r} \quad (3.17)$$

where  $r$  is the capillary radius. The combination of Eq. 3.16 and 3.17 gives the Washburn equation [163]. It relates the pore diameter  $d_p$  with the pore pressure  $p_p$ :

$$d_p = -\frac{4 \cdot \gamma_{\text{Hg}} \cdot \cos \theta}{p_p} \quad (3.18)$$

Generally, a surface tension for mercury  $\gamma_{\text{Hg}} = 0.480 \text{ N/m}$  at  $25^\circ \text{C}$  and a contact angle of  $\theta = 140^\circ$  is used for calculations.

The MIP sample is placed into a dilatometer and degassed. A MIP unit is usually composed of a low- and a high-pressure unit. Furthermore, the sample amount is limited by the dilatometer size. It must be considered that MIP can only access pores which are interconnected and accessible from the outside. Moreover, MIP measures the pore entry size so that the ink-bottle effect could lead to an overestimation of small pores and underestimation of big pores.

### 3.3.12 Uniaxial Compression Test

The uniaxial compression test is a method to characterize the (side) crushing strength of a particle, commonly a cylinder. The test specimen is placed between two brackets and is loaded with a continuous load at a certain speed until fracture occurs. Using a cylindrical

test object, the maximum tensile stress is located at the center of the sample, in the plane passing through the upper and lower contacting lines [164]. The maximum side crushing strength  $\sigma_{\text{comp}}$  is given by Timoshenko and Goodier [165]:

$$\sigma_{\text{comp}} = \frac{2F}{\pi dh} \quad (3.19)$$

where  $F$  is the load at failure,  $d$  and  $h$  are the diameter and height of the cylinder.



# 4 Development of a Manufacturing Process for Binder Jet 3D Printed Porous Al<sub>2</sub>O<sub>3</sub> Supports Used in Heterogeneous Catalysis

---

**This chapter was published in similar form in:**

H. M. Bui, R. Fischer, N. Szesni, M. Tonigold, K. Achterhold, F. Pfeiffer, O. Hinrichsen, "Development of a Manufacturing Process for Binder Jet 3D Printed Porous Al<sub>2</sub>O<sub>3</sub> Supports Used in Heterogeneous Catalysis", *Additive Manufacturing*, **2021**, 50, 102498, DOI 10.1016/j.addma.2021.102498.

©2021 Elsevier B.V. All rights reserved.

---

## Abstract

A complete preparation route for the direct 3D printing of Al<sub>2</sub>O<sub>3</sub> supports made from boehmite and bayerite was established using the binder jetting (BJ) technology. The application of the ceramic supports as reactor packing material employed in heterogeneous catalysis requires high porosity but simultaneously a certain robustness which has not been thoroughly investigated for powder-based 3D printing technologies before. With a calcination temperature of only 600 °C, sufficient consolidation by sintering does not occur as it would be the case for conventional BJ procedures so that the post-processing step of ambient slurry infiltration after debinding binds the particles after calcination at relatively low temperatures and significantly stabilizes the alumina framework while keeping the surface area and open porosity at catalytically relevant values of up to 223 m<sup>2</sup>/g and 80 %, respectively. Uniaxial compression tests, density measurements and N<sub>2</sub> physisorption elucidated the chemical composition, size accuracy, shrinkage behavior, side crushing strength, density, porosity and specific surface area of the green body as

well as post-processed parts. Additionally,  $\mu$ CT scans offered a method to analyze the 3D printed character of the alumina carrier structure, effect of post-processing and an alternative way to assess part shrinkage next to size measurement.

## 4.1 Introduction

Additive manufacturing (AM) has established itself as an innovative and economic fabrication technique in many different fields of daily life and research. However, the application of AM in the chemical sciences has not been as intensively investigated in comparison to the automotive [166], aerospace [36] or biomedical [38] fields. The application of AM in catalysis, the driving force of the chemical industry, has only started to be appreciated during the last decade [44], but following the need of chemical process intensification, AM is slowly being incorporated into catalyst development processes.

### 4.1.1 State of Knowledge - 3D Printing of Al<sub>2</sub>O<sub>3</sub>-based Catalysts

The application of AM in heterogeneous catalysis, especially the use of the BJ technology to generate porous ceramic parts, is still in its early stages as an industrial solid catalyst must generally fulfill numerous requirements. The BJ technology generates inherently macroporous parts due to the powder-based working principle. Moreover, the stability of a part correlates directly with its porosity [167] so that studies of printed alumina parts not intended for use in heterogeneous catalysis would aim at high part densities above 90 % as well as a low percentage of porosity [168–171].

Broadly defined, catalysts can either entirely consist of an active material (bulk catalyst) or a metal oxide support (e.g. Al<sub>2</sub>O<sub>3</sub>, TiO<sub>2</sub>, ZrO<sub>2</sub>, SiO<sub>2</sub>) on which the active component is homogeneously dispersed by a coating method of choice (supported catalyst). So far, there are two AM approaches to achieve this.

*Indirect printing* requires a mold, printed with a commercial polymeric 3D printer, therefore making novel material research for catalyst AM unnecessary. After filling the template with a ceramic paste, the mold is thermally treated to burn off the template and consolidate the ceramic support structure. If needed, the catalytic active material is loaded on afterwards. All reported studies on indirect printing have used an Al<sub>2</sub>O<sub>3</sub> paste to generate monolithic support structures, loaded with Mn and Na<sub>2</sub>WO<sub>4</sub> for oxidative coupling of CH<sub>4</sub> [55], Cu/Ceria for CO oxidation [54], Ni for CO methanation reactions

[172] or Pd for several cross-coupling reactions [56]. Indirect printing will not be subject of discussion for this study.

*Direct printing* includes the catalyst or any precursor material within the printing material formulation. Until now, direct ink writing (DIW) is by far the most commonly used technique for catalyst printing, most of them using alumina-based formulations. Successful printing of catalytic structures has been achieved using DIW for the production of Ni-Al<sub>2</sub>O<sub>3</sub>-based monolithic multi-channel systems for CO<sub>2</sub> methanation [68], Cu/Al<sub>2</sub>O<sub>3</sub> woodpile porous structures for different Ullmann reactions [73], barium hexaaluminate washcoated on Al<sub>2</sub>O<sub>3</sub> for catalytic combustion of CH<sub>4</sub> [71], Cu and Pd on supported on SiO<sub>2</sub> for multicatalytic multicomponent reactions [79], Ni/CeO<sub>2</sub>-ZrO<sub>2</sub> washcoated on printed stainless-steel honeycomb monoliths for CH<sub>4</sub> dry reforming [58] or Pt on printed Al<sub>2</sub>O<sub>3</sub> monoliths tested for the oxidation of CO.

Powder-based techniques for direct catalyst printing have been explored as well, but in comparison to the numerous aforementioned examples using DIW, there are no scientific studies on catalytic structures dealing with binder jetting (BJ). There are comprehensive reviews on the topic of 3D printing in catalysis by Hurt et al. [40], Parra-Cabrera et al. [41], Bogdan and Michorczyk [42] and most recently, Laguna et al. [44]. If BJ is mentioned as a manufacturing option at all, no specific examples are listed. Only two industrial catalyst manufacturers are known to have attempted a powder-based printing approach. Johnson Matthey patented a manufacturing strategy for shaped alumina-silica catalysts which were calcined at 1000 °C, offering a greater geometric surface area than conventional catalysts [173]. BASF patented a  $\alpha$ -Al<sub>2</sub>O<sub>3</sub> structure which was fired at 1600 °C. The monolithic structures with a cross-channel geometry were similar to Montz or Sulzer structured packings for distillation columns [174]. Both patents either do not accomplish pure alumina bodies or sinter at very high temperatures to achieve a mechanically stable final part. Huo et al. [175] fabricated  $\gamma$ -Al<sub>2</sub>O<sub>3</sub> catalyst carriers with hierarchical porosity and a relatively high specific surface area by using the powder bed fusion technology. Very similar to BJ, this powder bed-based technology generates inherently porous parts with weak mechanical properties. Adjusting the printing parameters and impregnating the green part with colloidal silica enabled the fabrication of highly porous (72.9 %) and mechanically stable catalyst carriers while reducing the sintering temperature to 1100 °C to maintain a relatively high specific surface area of 56 m<sup>2</sup>/g.

Summarizing the existing knowledge on Binder Jet-printed alumina-based catalysts or catalyst supports, there is a lack of information which can be extracted from studies so far. The multidisciplinary BJ technology requires knowledge about powder deposition, ink rheology, powder-liquid interaction and post-processing methods [176] so that a multitude of variables have to be considered simultaneously. Since the printed outcome relies heavily on the utilized starting materials, the thorough selection and characterization thereof

is crucial [21]. These demands combined with the physico-chemical requirements of a catalyst complicate the development a generic process for catalyst or catalyst support printing via BJ, potentially explaining the limited knowledge in comparison to other printing techniques.

### 4.1.2 Motivation

Alumina supports manufactured in this study are intended for use in heterogeneous catalytic fixed bed reactors which are among the most commonly used and most important types of chemical reactors utilized for the large-scale production of basic chemicals [1]. The tubular reactor is either filled with small catalyst pellets (random packing) or monolithic structures (structured packing).

Catalytic steps solely occur on the surface of a catalyst and include diffusion of the reactants from the bulk fluid phase through the macro- and micropores to the catalyst surface, chemisorption on active centers, the reaction and back-diffusion into the outer fluid phase. It is important to mention that not only the interparticle voids between single particles play an important role in catalysis but also the surface area that correlates with micro- and mesoporous pores within a particle. As an example, binder jet printed orthopedic scaffolds are highly porous ceramic structures, but only on a macroscopic scale. The recommended minimum pore diameter is 100  $\mu\text{m}$  for successful bone tissue regeneration and even 250  $\mu\text{m}$  for bone formation [177, 178]. Solid catalysts require pores in the micropore ( $d_p < 2\text{ nm}$ ) and mesopore ( $2\text{ nm} < d_p < 50\text{ nm}$ ) region to offer a sufficient surface area for the catalytic surface processes, so that additive catalyst manufacturing requires a fabrication strategy different from already existing ones to obtain desired material properties.

Optimum geometric design of the reactor packing is crucial in order to assure good external mass and heat transfer (especially for exothermal reactions), low pressure loss, short diffusion paths inside the catalyst particle in and out of accurately sized pores and the availability of active sites for sufficient reactant conversion. Furthermore, these parameters directly correlate with the size of a pellet, specific surface area, pore size distribution, voidage and abrasion resistance of the ceramic material [1, 2]. Therefore, multitudinous studies, particularly fluid dynamic simulations, have covered the influence of catalyst shape in packed beds. Scientific studies have exemplarily covered the effect of catalyst shape on systems for methane steam reforming [5–7], hydrolysis of COS and CS<sub>2</sub> in a Claus converter [8], natural gas reforming [9], partial oxidation of methanol [4] or Fischer-Tropsch synthesis for hydrocarbons production from synthesis gas [10]. Analyzed

shapes included simple cylinders, spheres, hollow cylinders, trilobes, quadrilobes, daisy shaped bodies, multi-channel cylinders, multi-channel cubes and monoliths with varying channel geometry. There is agreement across all mentioned studies that a more or less complex geometry significantly affects the overall performance of a reactor.

The conventional catalyst shaping techniques are pelleting, granulation and extrusion [11, 12]. Although these methods are well-developed, they produce relatively simple shapes that are mostly modified versions of the standard cylinder or spherical shapes. Therefore, additive manufacturing of ceramic supports could enable new possibilities for the shaping of packings in fixed bed reactors for improved catalytic performance.

Apart from the geometric aspects, selecting suitable feedstock material and adjusting the processing steps poses a substantial challenge for the development of a new BJ procedure. In the case of  $\text{Al}_2\text{O}_3$  carriers, requirements such as high porosity and specific surface area prohibit the application of temperatures well above  $1200\text{ }^\circ\text{C}$  which are usually applied to sinter transition aluminas to the thermodynamically stable but catalytically undesirable  $\alpha\text{-Al}_2\text{O}_3$  phase due to its low surface area. Transition aluminas are broadly employed in heterogeneous catalysis [68, 179–181] due to their favorable combination of surface area, pore volume, pore size distribution, acid/base characteristics as well as chemical and hydrothermal stability [182, 183]. The contradictory properties of high porosity and mechanical robustness were already addressed for 3D printed monolithic catalysts by Quintanilla et al. [81] where increasing sintering temperature increases the robustness but progressively decreases the porosity.

Another important aspect is chemical suitability of the used materials which implies that potential catalyst poisons such as alkaline and alkaline earth metals, sulfuric compounds etc. would impede the catalytic activity if present in the final product. Consequently, an additional motivation for this study is to source chemically suitable raw materials.

The aim of this paper is to establish a route for the 3D printing of sufficiently porous and high surface area alumina carriers for use in heterogeneous catalysis via the binder jetting technology as so far, little effort was done to produce high surface area catalysts supports out of pure transition phase alumina coupled with sufficient mechanical strength [21].

## 4.2 Materials and methods

### 4.2.1 General Process Chain

Fig. 4.1 gives an overview of the process steps in a flow chart, leading to the finished printed  $\text{Al}_2\text{O}_3$  catalyst support structure. The first step, namely the layer-by-layer printing

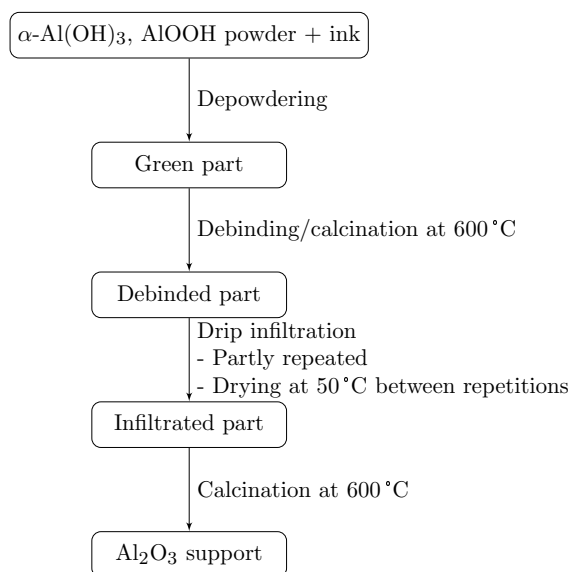


**Figure 4.1:** Flowchart of the process chain for generating a catalyst support via binder jetting.

process itself, is described in section 3.2 and generates a green part. The test bodies for this study were cylinders with a diameter of  $d = 8\text{ mm}$  and a height of  $h = 8\text{ mm}$ . The entire



**Figure 4.2:** Debinded alumina cylinders placed on a stainless steel grid before post-processing.

powder volume of the build platform was then removed from the printer and transferred into a drying oven for at least 3 h at  $75\text{ }^\circ\text{C}$  to further solidify the cylinders which were still surrounded by unbound, loose powder. After curing the freshly printed part in the oven, unbound powder was removed by gently blowing it off with compressed air. The

depowdered green parts (Fig. 4.2) were transferred to a calcination oven for debinding in stagnant air. Fig. 4.3 provides the exact temperature program which includes three isothermal stages at 60 °C, 120 °C and 600 °C. The first two were held for 30 min and the last one for 1 h. The heating rates were kept slow at 1 K/min for the first two stages. Between 120 °C and 600 °C the rate was increased to 5 K/min. After the calcination procedure, all in-bed binder is supposed to be burnt off, leaving a relatively unstable and porous part, not stable enough for further handling. Therefore, additional particle introduction by infiltration followed the debinding process, in which an aqueous boehmite slurry was slowly dripped onto the debinded part with a pipette until pore saturation. This infiltration step might be repeated one or two more times. If the infiltration step

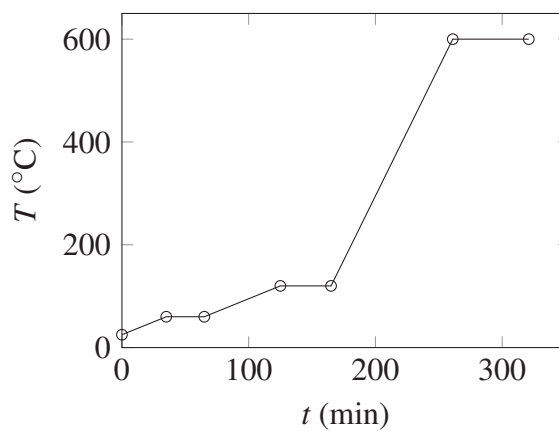


**Figure 4.3:** Temperature program for debinding as well as calcination.

is repeated, the dripped parts were dried in an oven at 50 °C between two dripping procedures until most of the liquid had evaporated and the infiltration was reiterated. The infiltration step cannot be performed before the binder burnout as the in-bed binder PVP is water soluble and consequently dissolves after contact with the water-based infiltration slurry, resulting in disintegration of the green part. After the drip infiltration, the last step included the calcination to consolidate the subsequently introduced particles with the already existing body and transform boehmite to  $\gamma\text{-Al}_2\text{O}_3$ . The temperature program for the final calcination step was identical to the one used for debinding (Fig. 4.3).

## 4.2.2 Raw Materials

### 4.2.2.1 Printing Liquid

The particle-loaded ink was water-based and contained dispersed boehmite particles for additional particle introduction during printing and part densification [184]. The aqueous printing liquid was prepared by mixing distilled water with 10 wt.% isopropyl alcohol

and 10 wt.% 1,4-butanediol (Merck KGaA, Germany) for surface tension and viscosity adjustment, respectively. Water-dispersible boehmite Dispal 14N4-80 (Sasol Chemicals, USA) was added to the solution and stirred thoroughly with a magnetic stirrer for 30 min to ensure sufficient dispersion of the particles. At the end, a stable colloidal dispersion was attained, where the particles were dispersed homogeneously in the liquid. Table 4.1 shows relevant measured parameters for the used ink. Particle loading was kept at 7 wt.%

**Table 4.1:** Physical parameters for used printing liquid.

Printing liquid property	Value
Particle loading $w$ (wt.%)	7.0
Surface tension $\sigma$ (mN/m)	35.4
Dynamic viscosity $\eta$ (mPa s)	1.99
Density $\rho$ (g/cm <sup>3</sup> )	1.03

to maintain the weight percentage of particles in a range that permits continuous ejection of droplets from the printhead without clogging during nozzle plate cleaning cycles.

Surface tension and dynamic viscosity were mainly adjusted by adding isopropyl alcohol and 1,4-butanediol (Merck KGaA, Germany), respectively. Measured values were  $\sigma = 35.4$  mN/m for the surface tension and  $\eta = 1.99$  mPa s for the dynamic viscosity. The value for  $\eta$  significantly deviates from the printhead manufacturer's recommendation of  $9 \text{ mPa s} < \eta < 11 \text{ mPa s}$  and the viscosity  $\eta$  partly deviated from the recommended range of  $\sigma = 23$  to  $30$  mN/m. However, the ink was ejectable and generated a subjectively defect-free print image on the powder bed, so that no in-depth analysis, such as optical droplet observation of the printing liquid was conducted.

#### 4.2.2.2 Powder Bed

The powder mixture used for all print jobs consisted of three powders, two of them being Al<sub>2</sub>O<sub>3</sub> transition phases and one being the solid in-bed binder (Table 4.2). Pural BT (Sasol GmbH, Germany) is a bayerite and Actilox S40 (Nabaltec AG, Germany) an amorphous transition aluminum oxide. Solid polyvinylpyrrolidone (PVP) Sokalan K17P (BASF SE, Germany) was used as in-bed binder. Having positive effects on the drop penetration behavior and green part stability due to its hygroscopic properties, PVP was a suitable binder for this application. The powder blend was prepared by weighing each component (see Table 4.2) and mixing the blend in a SpeedMixer (Hauschild GmbH & Co KG, Germany). The blend was mixed in 4 cycles with 1000 rpm for 1 min each, manually shaking the container in between cycles to loosen up the powder.

**Table 4.2:** Composition of used powder blend.

Component	Compound	Amount (wt.%)
Pural BT	$\alpha\text{-Al(OH)}_3$	73
Actilox S40	AlOOH	7
PVP	$(\text{C}_6\text{H}_9\text{NO})_n$	20

#### 4.2.2.3 Post-processing

The infiltration substance for additional particle introduction into the porous debinded parts consisted of an aqueous slurry. Stirring together distilled water and 15 wt.% water-dispersible boehmite particles (Dispal 14N4-80, Sasol Chemicals, USA), a stable colloidal dispersion formed and was slowly dripped onto the debinded parts with a pipette under atmospheric pressure conditions. The dripping process was performed as long as the part absorbed the infiltration slurry. Placing the parts on a stainless steel grid beforehand made sure that excess slurry which was not held inside the body due to over-saturation could drip down onto a collection pan (cf. Fig. 4.2).

### 4.2.3 Characterization and Analysis

Table 4.3 gives an overview of the characterization methods used to obtain all relevant measuring data to analyze the raw materials (powder bed and ink) as well as the product after the printing process.

**Table 4.3:** Overview of methods used for material characterization and analysis.

Parameter	Method	
Particle size distribution (PSD)	Laser diffraction	Raw materials
Binder burnout	Thermogravimetric analysis (TGA)	
	Elemental analysis	
Surface tension $\sigma$	X-ray diffraction (XRD)	
Dynamic viscosity $\eta$	Stalagmometric method	
	Rheometer	Printed part
Phase determination	XRD	
Size accuracy	Size & hardness tester	
	X-ray microtomography ( $\mu\text{CT}$ )	
	Caliper (for debinded parts)	
Side crushing strength $\sigma_{\text{comp}}$	Uniaxial compression test	
Powder bed density $\rho_{\text{bed}}$	Measurement with density cups	
Part densities $\rho$	Archimedes buoyancy method	
Porosity and void fraction $\epsilon$	$\text{N}_2$ physisorption (BJH)	
	Archimedes buoyancy method	
	$\mu\text{CT}$	
Specific surface area $S_{\text{BET}}$	$\text{N}_2$ physisorption (BET)	

#### 4.2.3.1 Characterization of Raw Materials

The PSD of the powder mixture for the powder bed (fresh and used powder after printing) as well as the particles in the printing liquid were measured with a laser diffraction particle size analyzer (LS 13 320 Particle Size Analyzer, Beckman Coulter, USA). Hereby, the powder bed material was measured as dry powder with the Tornado Dry Powder System module. The PSD of the dispersed particles in the ink were measured with the Universal Liquid module of the same device, using suspended particles as the sample feed.

The extent of binder burnout after calcination was determined with TGA (TGA Q5000, TA Instruments, USA). Approximately 10 mg were placed in an open Pt pan and measured under a synthetic air flow of 25 mL/min. The heating ranged from ambient temperature to 1000 °C (1 K/min to 60 °C, 5 K/min to 1000 °C). The temperature program was chosen accordingly to represent the actual conditions during calcination and debinding. TGA measurements were conducted for pure PVP powder as well as a thermally cured green body.

Additionally, elemental analysis (CHNS) was accomplished by combustion analysis (Euro EA, HEKAtech GmbH, Germany) to determine the percentage carbon residue after debinding, indicating possible incomplete PVP removal. The sample was analyzed by dynamic spontaneous combustion at 1800 °C and chromatographic separation. The result was determined by means of a thermal conductivity detector.

For the rheological characterization of the ink, the surface tension  $\sigma$  was measured using a Traube stalagmometer (Neubert-Glas GbR, Germany) with 2.5 mL capacity and a mountable needle valve for drip rate adjustment. The dynamic viscosity  $\eta$  was determined using a rotational rheometer (Kinexus Lab+, Netzsch, Germany) with a 40 mm plate-plate geometry and a sample gap of 0.1 mm. As the ink was already known to show Newtonian behavior,  $\eta$  measurement was carried out for 5 min at a constant shear rate of 80 1/s, capturing one data point every 5 s. Surface tension and viscosity measurements were both conducted at ambient conditions.

#### 4.2.3.2 Characterization of Printed Parts

Aside from TGA, binder burnout was analyzed using powder XRD (Empyrean, Malvern Panalytical, UK), operating with Cu-K $\alpha$  radiation and a monochromator. The powders were scanned with a stepsize of 0.007° and 70 steps/min. XRD analysis was also used for alumina phase determination at different Al<sub>2</sub>O<sub>3</sub> support fabrication stages (green part, debinded, infiltrated).

Dimensional accuracy of the print job and associated linear shrinkage of the cylinders after debinding, calcination and infiltration,  $d$  and  $h$  were measured for parts at all process stages (green part, debinded, infiltrated). These geometrical values were obtained using a tablet hardness testing system with an integrated option for length measurement (Multi-Test 50, Dr. Schleuniger Pharmatron, Switzerland). The part to be tested is placed in the measuring area between two stainless steel brackets, one moving towards the other with a constant moving speed of 2 mm/s. Once a certain resistance from the inserted test body is recognized, the diameter or height, depending on the testing orientation, is recorded. All samples were tested with the tablet hardness tester, except for parts directly after debinding. Insufficient part stability due to binder burnout did not permit measurement with the hardness tester. Therefore, height and diameter were manually measured with a digital caliper for freshly debinded samples.

Side crushing strength was measured with the MultiTest 50, which was also used for above described size measurement. Uniaxial compression on the lateral surface of the samples between two opposite metal plates was performed, characterizing the cylinder's response to loading perpendicular to its length, until fracturing occurs. One of the plates moved towards the other with a constant velocity of 2 mm/s. The fracture load  $F$  was automatically collected and used in equation 3.19, yielding the side crushing strength  $\sigma_{\text{comp}}$ .

Powder bed density was determined by employing a methodology that uses density cup samples [185]. Hereby, a density cup is fabricated via BJ under regular printing conditions, where only the contour of the cup is printed, thus leaving a cavity containing unbound powder. After curing, the density cup was gently brushed to remove unbound powder outside of the cup. The mass and volume of the loose powder were correlated to determine the powder bed density. The cup was designed so that the cylindrical cavity has a diameter of 10 mm and height of 10 mm. For later density calculation, perfect cylinder volume according to the computer aided design (CAD) file was assumed. The mass of the loose powder inside of the cup was weighed with a balance by subtracting the mass of bound powder of the cup contour from the total mass comprising bound and unbound powder.

Densities and void fractions of the printed and post-processed samples were acquired using the Archimedes buoyancy method according to DIN EN 623-2 [186]. Because the printed specimens are highly porous, open voids, which are accessible from the sample surface, have to be considered when measuring the part density, requiring full impregnation with a fluid of known density [187]. In this case, distilled water was chosen as the fluid. The specimen was degassed at 25 mbar in a rotary evaporator before distilled water

was added, following repressurization to atmospheric pressure. For density calculations, the sample was weighed in its dry, water-impregnated and submerged state.

Further porosity analysis, especially regarding the catalytically relevant pore size distribution, was conducted with N<sub>2</sub> physisorption (Nova 4200e, Quantachrome Instruments, USA) using the method of Barrett, Joyner, Halenda (BJH) for calculations. Outgassing prior to adsorption at 120 °C for 120 min ensured removal of any physisorbed species. Adsorption and desorption isotherms were measured in the range  $0.001 \leq p/p_0 \leq 1$ .

Specific surface area  $S_{\text{BET}}$  and pore size analysis were performed simultaneously by N<sub>2</sub> physisorption, thus using the same experimental procedure.  $S_{\text{BET}}$  was determined according to the method of Brunauer, Emmett, and Teller (BET) and calculated between  $0.05 \leq p/p_0 \leq 0.3$ .

Structural analysis of the printed parts, namely qualitative porosity characterization and relative particle distribution for different process stages, was accomplished by  $\mu\text{CT}$  (versaXRM 500, Zeiss, Germany). The X-ray source is a transmission tube with a Tungsten target (NT100, Nordson Dage, UK). The peak voltage was set to 80 kVp and the power to 6 W for every scan. The detector is a CCD camera (iKon-L, Andor, UK) with 2048 x 2048 pixels and a detector pixel size of 13.5  $\mu\text{m}$ . The versaXRM has a two stage detection system. First, a geometrically magnified X-ray projection of a specimen is converted to visible light in a scintillator. Afterwards, the scintillator light is imaged with an objective onto the CCD detector. With a geometric magnification by a factor of 7.47 and a  $0.3971 \times$  demagnifying objective, the resulting effective voxel size was 4.55  $\mu\text{m}$ .

## 4.3 Results and Discussion

### 4.3.1 Raw Materials

#### 4.3.1.1 Powder Analysis

Generally, the maximum particle diameter predefines the minimum thickness of a powder layer [188], as one layer should be at least as thick as the biggest particle diameter or, preferably, three times the particle size [189]. Therefore, the main interest for the powder bed analysis lies in the PSD assessment as it also significantly influences the powder bed density, thus affecting the printed part density and stability in the end. Laser diffraction analysis resulted in the PSD seen in Fig. 4.4. The PSD of all single components as well

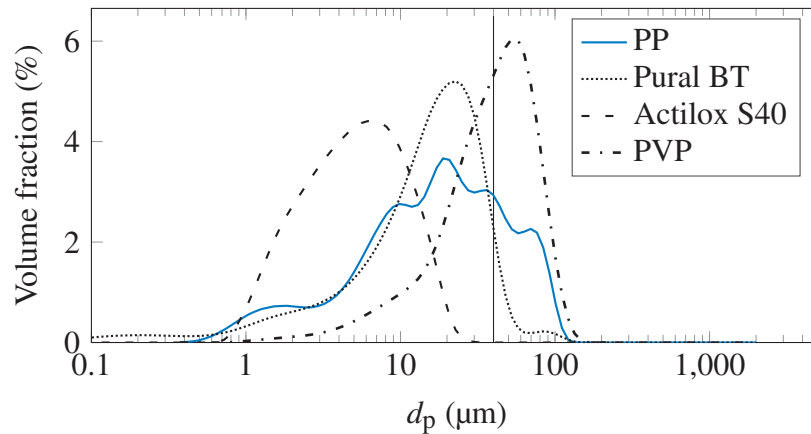


**Figure 4.4:** PSD of the printing powder (PP) and its single components, measured with laser diffraction. The vertical line marks the layer thickness of 40  $\mu\text{m}$ .

as the mixed powder "PP" (for "printing powder") which is ultimately used in the printer were measured. As for the single components, all three powders have a for the most part unimodal PSD. Pural BT has a median particle size of 16.78  $\mu\text{m}$  with small fractions of fine and coarse particles. Actilox S40 has a unimodal PSD with  $d_{50} = 5.32 \mu\text{m}$ . The in-bed binder PVP is relatively coarse in comparison to the two transition alumina powders. Actilox S40 with its finer PSD is added, as bimodal powders are observed to show a higher packing density and thus lower shrinkage during post-processing in comparison to monodisperse powders. The fine powder particles would fill interstitial voids between the larger particles, creating more particle-particle contact points and yielding a greater powder bed density and part integrity overall [190]. Thus, a high percentage of Actilox S40 is desirable. However, depositability and spreading become more difficult due to increasing cohesive forces between very small particles. Moreover, the liquid penetration behavior was affected negatively with increasing amounts of Actilox S40. This behavior is either caused by the hydrophobic surface property of Actilox S40 or the fact that finer powders generally aggravate fluid migration in  $z$ -direction through the powder bed due to smaller pores and higher saturation capillary pressures [23, 191]. Therefore, the amount of Actilox S40 was limited to 7 wt.% in this study (see Table 4.2).

The powder blend PP shows a broad multimodal PSD with several local maxima, caused by the different PSDs of the individual components of the blend (blue solid line in Fig. 4.4). Larger particles, mainly stemming from PVP, facilitate spreading with the rotating roller, whereas the smaller particles offer the aforementioned benefits.

The layer thickness for all print jobs was 40  $\mu\text{m}$ , as described in section 3.2. As Fig. 4.4 indicates, the particles of PP exceed 40  $\mu\text{m}$ . A too small layer thickness could result in rough layers, as the spreading roller pushes bigger particles across the build platform, not incorporating them into to the build bed. This could also lead to a filter effect, as

increasing amounts of particles with a diameter above the layer thickness would remain in the leftover loose powder, reducing the recyclability of the utilized powder blend.

In order to validate if this filter effect occurs, Fig. 4.5 compares the PSD of fresh powder with used PP after reuse in three print jobs. Under optimum conditions, fresh and recycled

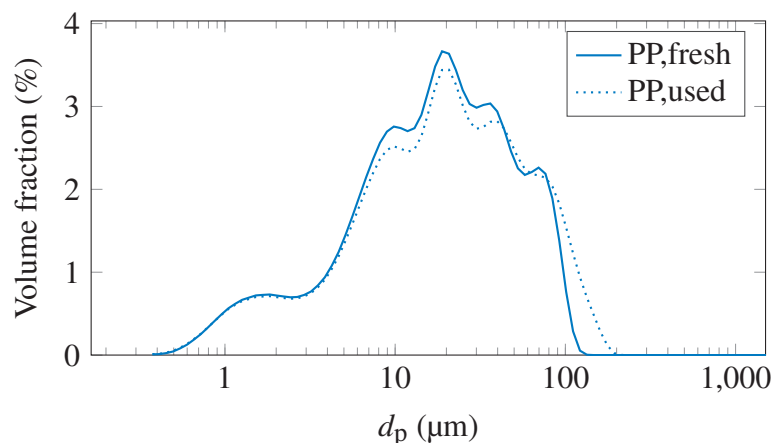


**Figure 4.5:** PSD of fresh PP powder blend (blue, solid) and recycled powder after 3 print cycles (blue, dotted).

PSD plots should exhibit congruence. In this case, the PSD of recycled printing powder shifts slightly to larger diameters. Furthermore, volume percentage of particles in the range between  $7\mu\text{m} < d_p < 50\mu\text{m}$  exhibit a decline. The fine fraction up to  $d_p = 7\mu\text{m}$  remains unaffected, suggesting uniform incorporation of fines into the print bed. The findings hint an overall coarsening of the recycled powder. Incomplete integration of particles above  $40\mu\text{m}$  into the print bed and additional agglomeration affects could explain this outcome.

The described combination of the layer thickness and PP powder composition was maintained during the experiments despite the identified deficiencies as parameter variation was partially limited. Increasing the layer thickness led to insufficient vertical binder permeation into the powder bed, resulting in collapsing green bodies. A more detailed analysis of the PSD of PP and its components is listed in Table 4.4. Most of the particles in the mixture are sized smaller than  $40\mu\text{m}$ , so that the small percentage of oversized particles is tolerated in this case. Moreover, the main contribution to the oversized particles stems from the PVP powder, as fresh Pural BT and Actilox S40 marginally cross the size threshold. Subsequent burnout of the in-bed binder regardless of its particle size, visually smooth spreading with the leveling roller after repeated print cycles and satisfying ink penetration caused to maintain the formulated powder composition and neglect the flaws.

**Table 4.4:** PSD ( $d_{50}$  and  $d_{90}$ ) of the starting materials and the fresh powder blend PP.

Powder material	$d_{50}$ ( $\mu\text{m}$ )	$d_{90}$ ( $\mu\text{m}$ )
Pural BT	16.78	36.36
Actilox S40	5.32	13.30
PVP	42.23	82.61
PP	18.66	66.32

#### 4.3.1.2 Ink Characterization

Key variables for the ink formulation are the surface tension, viscosity and the PSD of the dispersed boehmite particles. Table 4.1 lists all measured printing liquid properties. In order to prevent nozzle clogging during printing, especially to be considered for particle-loaded ink, the permitted maximum particle diameter for this printhead was  $1\ \mu\text{m}$ . This condition is fulfilled, as the largest particle with a size of  $d_p = 0.21\ \mu\text{m}$ , remains well below the allowed threshold (Fig. 4.6). The PSD also suggests a well dispersed and colloidal system, as the PSD is very narrow around the median value of  $d_{50} = 0.13\ \mu\text{m}$ . Useful

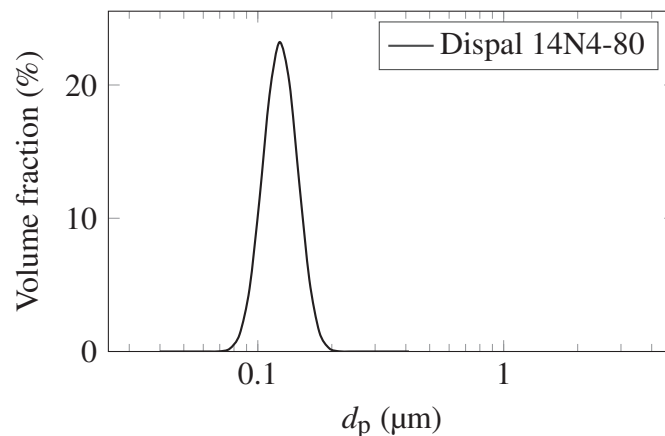


**Figure 4.6:** PSD of the dispersed boehmite particles Dispal 14N4-80 in the water-based ink, measured by laser diffraction.

observations of drops and jets emerging from a nozzle using a camera and stroboscopic techniques can give evidence for the actual drop size and jetting velocity [192]. This analysis method was not available for this study, so that the quantitative printability of the developed ink could only be vaguely estimated.

The drop forming behavior is complex and the physics behind it has been thoroughly investigated, but not unequivocally clarified yet [192, 193]. The printability of a liquid can be characterized by a set of dimensionless numbers consisting of the Ohnesorge number  $Oh$  [24], the Weber number  $We$  and the Reynolds number  $Re$  [26] (Eq. 2.1, 2.2 and 2.3).

The mean jetting velocity was assumed to be 5 m/s and the drop diameter  $l$ , was calculated for a mean drop volume of 14 pL, assuming a spherical droplet. The values for  $u$  and  $l$  are determined by the printhead vendor under inspection conditions. Calculations give  $Re = 77.4$ ,  $Oh = 0.060$ ,  $We = 21.7$ , and  $Z = 16.6$ . In the context of the  $We-Re$  plot [26], the operating point is located slightly outside of the zone for printable liquids. According to the diagram, the used ink would be prone to satellite drop formation. This effect could be mainly caused by high viscosity, corroborating the hypothesis that viscosity adjustment could improve jetting performance for this ink. Aforementioned estimations give a vague orientation for the drop forming behavior. However, for this printing process, mostly visual assessment was applied. The ink was deemed suitable due to constant streak-free and homogeneous images during prints without frequent nozzle clogging.

#### 4.3.1.3 Binder Burnout

The in-bed binder PVP must fulfill the prerequisite of complete burnout after debinding of the green part. For usage as a catalyst or catalyst support, the sample must not contain impurities or traces of elements that could lead to catalyst poisoning. Depending on the intended technical application, alkaline or alkaline earth metals could potentially impede the catalytic activity by decreasing the number of active sites and acidity on the alumina surface [194]. The extent of binder burnout was analyzed with three methods, i.e. TGA, XRD and elemental trace analysis.

The weight loss curves in Fig. 4.7 demonstrate complete evaporation of PVP after 600 °C. 100 % weight loss was obtained by TGA for pure PVP powder. Liquid ink additives, water and PVP are the only compounds that are expected to evaporate during debinding, so that, according to the weight loss curve, debinding the green body leaves pure Al<sub>2</sub>O<sub>3</sub> behind. The TGA curve of the green part corroborates this assumption as the weight loss curve for the printed part also stagnates at 600 °C. Combining the TGA curve of pure PVP with the one for the green part indicates that the residue after debinding, which constitutes about 50 % of the original mass, is presumably entirely composed of Al<sub>2</sub>O<sub>3</sub>. Fig. 4.8 compares the XRD patterns of two debinded parts. Both samples were debinded at a temperature of 600 °C, the difference being the holding time in the calcination oven (1 h and 2 h). Normal debinding follow the routine depicted in Fig. 4.3 with a 1 h holding time. The time variation clarifies whether 1 h suffices to remove all PVP or if phase changes still occur after that. The vertical dashed lines denote the diffraction peaks of pure PVP, located at about 11° and 21° (2θ) [195, 196]. Neither one of the measured XRD patterns display peaks matching the reference pattern for pure PVP, indicating that no binder was left after debinding. Moreover, the patterns for dwell times of 1 h and 2 h resemble each other to a

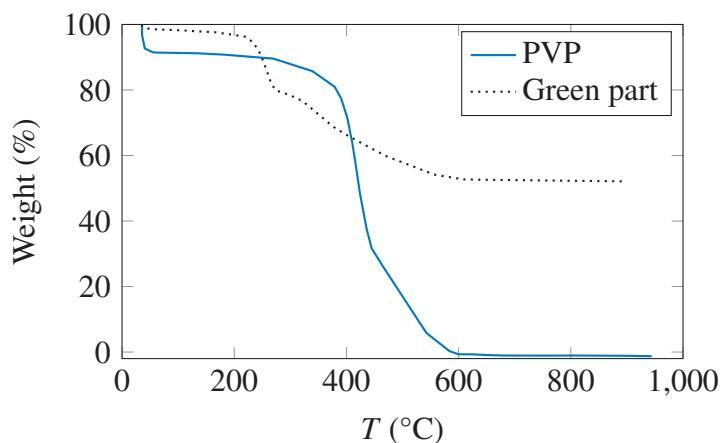


**Figure 4.7:** TGA curves for pure PVP powder (blue) and a green body (dotted) under synthetic air.

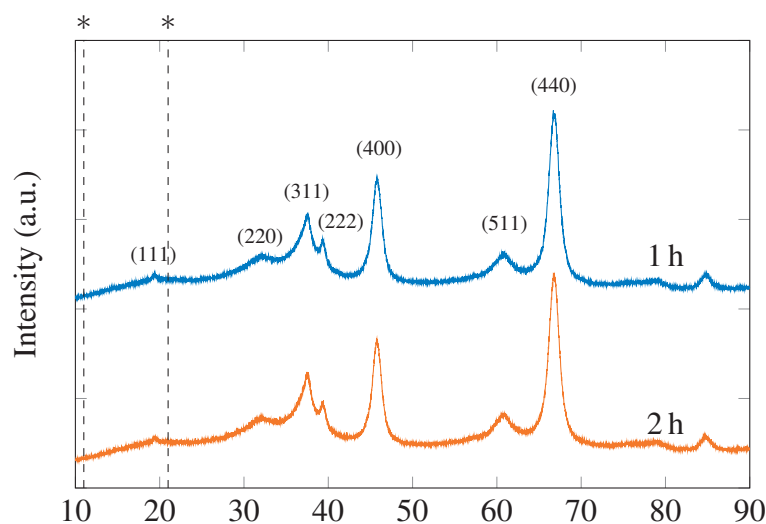


**Figure 4.8:** XRD patterns of a debinded part, heated until 600 °C, held for 1 h (blue) and 2 h (orange). The vertical dashed lines correspond to the reference pattern of pure PVP.

great extent. This leads to the conclusion that holding the debinding temperature of 600 °C for 1 h is sufficient for complete binder removal.

CHNS analysis revealed that 0.11 wt.% of C was left after debinding at 600 °C for 1 h. This value is sufficient to assume complete binder removal and affirms the suitability of the temperature program used for debinding (Fig. 4.3). The debinding duration of 1 h was adequate for complete evaporation of PVP in the relatively small test cylinders. Debinding time should be adapted to the size of the sample so that bigger parts will require an extended holding time in the oven. Nitrogen and sulfur were not present in the sample, suggesting no introduction of impurities or catalyst poisons through PVP.

## 4.3.2 Printed Part Analysis

### 4.3.2.1 Alumina Phase Identification

Phase identification of debinded samples via powder XRD (Fig. 4.9) confirmed that the remains after debinding consist of pure alumina. Fig. 4.9 includes a matching reference pattern from the International Center for Diffraction Data database (ICDD 04-0875). Every reference reflection data can be matched with the measured XRD pattern of the debinded part regarding location and intensity, so that the presence of alumina without unwanted impurities is guaranteed with the current manufacturing procedure. The XRD

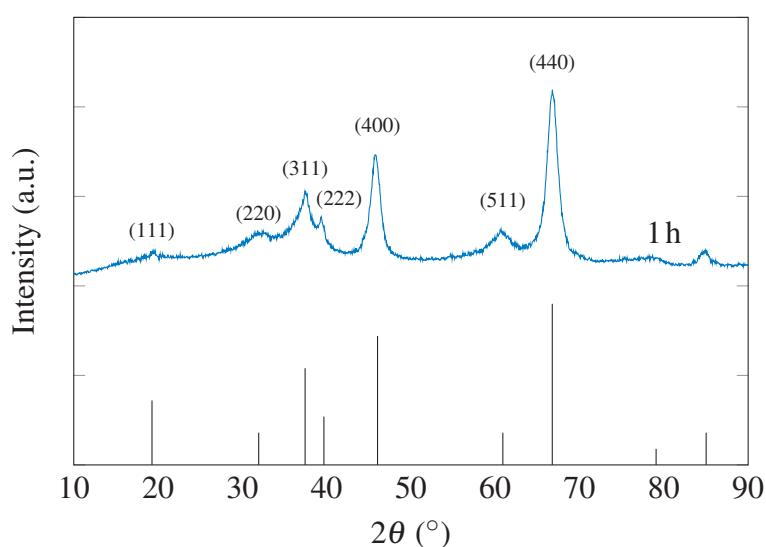


**Figure 4.9:** Comparison of the XRD pattern of a debinded part, heated until 600 °C and held for 1 h with a reference pattern for Al<sub>2</sub>O<sub>3</sub> (ICDD 04-0875).

pattern in Fig. 4.9 distinctly displays the diffraction pattern of meta-stable transition alumina phases [197, 198]. Although unequivocal differentiation between transition alumina phases via XRD is generally challenging [199], it is reasonable to presume that the diffraction patterns can be assigned to a mixture of  $\eta$ -Al<sub>2</sub>O<sub>3</sub> and  $\gamma$ -Al<sub>2</sub>O<sub>3</sub>. These are the widely suggested thermal decomposition products at 600 °C of the starting materials bayerite and (pseudo)boehmite, respectively [200–202]. Unless the sample is highly crystalline,  $\eta$ -Al<sub>2</sub>O<sub>3</sub> and  $\gamma$ -Al<sub>2</sub>O<sub>3</sub> are hardly distinguishable because both are spinel type and due to their only difference being the defect sites on the tetrahedral and hexagonal sites, respectively [199, 203]. At some point, the extent of similarity even justified the assumption that  $\eta$ - and  $\gamma$ -Al<sub>2</sub>O<sub>3</sub> were identical [204]. For a more elaborate alumina transition phase differentiation, solid state <sup>27</sup>Al NMR has been proposed to observe the coordination of Al cations in more detail [199, 205] and elucidate the structural differences. Considering the applied powder bed composition, the calcined samples should mainly consist of  $\eta$ -Al<sub>2</sub>O<sub>3</sub>

and to a minor extent of  $\gamma\text{-Al}_2\text{O}_3$  which evolves from  $\text{AlOOH}$  in the powder mix and from Dispal 14N4-80 in the ink.

#### 4.3.2.2 Dimensional Accuracy

The target value for the cylindrical test specimens was 8 mm for both the height and diameter. Table 4.5 presents the dimensional deviation of the test samples from the value initially specified by CAD. Green part dimensions barely differ from the target value. Especially axial measurements, with an average deviation of zero, conform to the set value. Green part dimensions smaller than expected could arise from abrasion by powder removal after curing or handling. This oftentimes signals poor ink penetration into the powder, thus insufficient liquid saturation to adequately bond the particles. Depowdering then tends to blow off weakly bound powder, leading to a reduced part size.

Increased size could stem from incomplete depowdering, when pressurized air flow is too little to blow off a particularly cohesive powder blend. More likely, powder-ink interaction shows radial oversaturation, causing binder bleeding (not required binding of surrounding support powder). However, the green part radial dimension exceeds the set value by only 0.2 %, a satisfactory and reasonable value, also considering the standard deviation of the values.

**Table 4.5:** Deviation of cylinder height and radius from the target value of 8 mm. For the infiltrated parts (i1c, i2c and i3c) the deviation as compared to the debinded part is shown additionally. Sample number for each measurement  $n \geq 7$ .

	Axial (%)	Radial (%)	Shrinkage (%)	
Green part	$0.0 \pm 0.5$	$0.2 \pm 0.7$		
	Axial total	Radial total	Axial from debinded part	Radial from debinded part
Debinded	$4.2 \pm 1.1$	$2.9 \pm 1.0$	0.0	0.0
i1c	$5.3 \pm 0.4$	$4.4 \pm 0.8$	$1.2 \pm 0.5$	$1.6 \pm 0.8$
i2c	$4.4 \pm 0.9$	$5.2 \pm 0.7$	$0.0 \pm 0.1$	$2.4 \pm 0.9$
i3c	$4.4 \pm 0.7$	$4.7 \pm 1.6$	$0.2 \pm 0.7$	$1.9 \pm 1.6$

Debinding reduced the cylinder height by 4.2 % and the diameter by 2.9 %. PVP makes up 20 wt.% of the total powder blend (see Table 4.2), so that debinding creates a considerable mass loss after burnout, as discussed in section 4.3.1.3. The main powder components boehmite and bayerite transform to the thermodynamically most stable form  $\alpha\text{-Al}_2\text{O}_3$  at ca. 1050 °C [202, 206]. The debinding temperature of 600 °C lies well below the

common sintering temperature for Al<sub>2</sub>O<sub>3</sub> between 1400 °C and 1650 °C (50-80% of the melting temperature) [207]. Consequently, intermediate or final stage sintering in terms of substantial densification is not induced under these conditions. Binder burnout even reduces part density hereby. Initial stage sintering which includes particle neck growth by diffusion along and to grain boundaries causes slight part shrinkage. Additionally, calculations by Zheng et al. [208] suggest that sintering shrinkage is inversely proportional to the green density for highly porous materials. The low-density test specimens could correspond to these findings, reinforcing a proportionality between the amount of pores and shrinkage.

Table 4.5 shows unequal reduction of axial and radial dimensions for the debinded samples, although the shrinkage could be considered very similar for both directions, regarding the small magnitude. The layer-wise fabrication inevitably generates more voids between layers than within a layer because particle consolidation in  $z$ -direction is less enhanced than it is in  $x$ - and  $y$ -direction due to limited mass transport of the ink into the powder [209]. Therefore, the hereby observed anisotropic shrinkage of the debinded samples with more pronounced decrease in  $z$ -direction could be inherent to the powder-based layering process.

The influence of gravity on sintering has been studied before, where height decrease due to gravity has been reported [210–212]. Gravity imposes an axial load gradient which increases from top to bottom, causing height reduction during calcination. Higher linear shrinkage in  $z$ -direction of Binder Jet printed parts has been observed in previous studies [213, 214]. This effect probably affects bigger specimens to a greater extent and can be neglected in this case. For the small test objects in this study, the anisotropy of shrinkage plays a minor role but should be considered in general during part creation via CAD.

The names i1c, i2c and i3c in Table 4.5 denote post-processed specimens which were infiltrated one, two and three times, respectively. Axial and radial shrinkage of the infiltrated parts appear to be of similar magnitude in comparison to the green body shrinkage, but more isotropic. Infiltration increases the particle packing density of the debinded part which notably affects the shrinking behavior [215, 216]. Drip infiltration introduces particles where voids have been generated by binder burnout, stabilizing the weakened alumina structure. The added grain boundaries consolidate after the second calcination step, ultimately forming a more durable part. Higher particle density is possibly the main reason for more uniform shrinking as a reduced number of voids and cavities mitigates the vertical collapse of the alumina scaffold during calcination. Similar total shrinkage values for debinded and infiltrated specimens lead to the conclusion that, in this case, infiltration does not fulfill the function of shrinkage prevention but structural stabilization.

Size reduction of the infiltrated parts after the second calcination step was max. 2.4 %, thus significantly reduced as compared to shrinkage after the first calcination. Previously calcined parts undergo less shrinkage after repeated heat treatment due to an already consolidated structure which is less prone to deformation.

#### 4.3.2.3 Part Density and Void Fraction

Density and associated void fraction within a printed specimen are closely related to the side crushing strength as well as catalytic properties. The hereby used term "void" refers to the macroscopically scaled interparticle free space caused by particle arrangement within the examined sample. Voids can again be differentiated into open and closed voids. Closed voids denote isolated cavities inside the sample, whereas open voids are channels or air pockets with an exit to the outside at the sample surface.

Table 4.6 presents the density of the powder bed and of the parts after all infiltration stages. Part stability of the debinded green parts was insufficient for density measurement with the Archimedes buoyancy method, thus corresponding density values in Table 4.6 are denoted with "n.d." (not determined). Bulk density  $\rho_{\text{bulk}}$  is the mass divided by the external volume, i.e. the volume of the solid including open and closed voids. The apparent solid density  $\rho_{\text{app,s}}$  is the mass divided by the volume of the solid including closed voids. The fraction of open voids  $\epsilon_{\text{open}}$  describes the ratio between the volume of open voids and the bulk volume. The powder bed density is the lowest out of all bulk

**Table 4.6:** Measured bulk density  $\rho_{\text{bulk}}$ , apparent solid density  $\rho_{\text{app,s}}$  and open void fraction  $\epsilon_{\text{open}}$  for the powder bed and post-processed specimens.

	Powder bed	Debinded	i1c	i2c	i3c
$\rho_{\text{bulk}}(\text{g}/\text{cm}^3)$	0.57	n.d.	0.61	0.72	0.82
$\rho_{\text{app,s}}(\text{g}/\text{cm}^3)$	n.d.	n.d.	3.01	2.88	2.75
$\epsilon_{\text{open}}$	0.80	n.d.	0.80	0.75	0.70

densities, as it consists of loose powder, compacted only by the powder roller during printing. After debinding, bulk density is expected to decrease even more due to binder removal. However, the value could not be measured. Infiltrated part densities expectedly increase in bulk density because particle content increases while part volume remains constant (Table 4.5). A steady improvement of bulk density from the powder bed stage to i3c proves the positive impact of infiltration.

The parameters  $\rho_{\text{app,s}}$  and  $\epsilon_{\text{open}}$  help to assess how infiltration affects the general void distribution. From i1c to i3c, apparent solid density declines from 3.01 g/cm<sup>3</sup> to 2.75 g/cm<sup>3</sup>.

A downward trend for  $\rho_{app,s}$  can only be induced by decrease of sample mass or increase of the apparent solid volume which includes closed voids and the solid material. Table 4.7 presents the percentage mass increase for each infiltration stage, which implies that a decrease in apparent solid density must be a direct consequence of infiltration. Particles penetrate from the outside to the center during infiltration, causing open surface voids to be sealed. Open voids with previous access to the outside are closed by infiltration and become closed voids inside the sample. As a result, solid volume and fraction of closed voids increase with the number of infiltration steps.

**Table 4.7:** Mass increase of all stages between part debinding and third infiltration step.  $\Delta m_{debind-i3c}$  denotes the total mass increase achieved by slurry infiltration.

Step	Mass increase (%)
$\Delta m_{debind-i1c}$	14
$\Delta m_{i1c-i2c}$	16
$\Delta m_{i2c-i3c}$	6
$\Delta m_{debind-i3c}$	40

Complementary to the hypothesis that the number of closed voids increases due to inward motion of the infiltration slurry, the volume fraction of open voids decreases from 80 % for i1c to 70 % for i3c. Mass increase is generally a measure for the effectiveness of the infiltration process as more particle introduction into the specimen leads to a higher bulk density and final part strength. The results in Table 4.7 suggest that the last infiltration step between i2c and i3c is less effective than the first two starting from the debinded part to i2c. The fraction of open voids declines by 5 % after every step, whereas the mass increase between the second and third infiltration is only 6 % in comparison to 16 % between i1c and i2c. During the first infiltrations, voids already become saturated to such an extent that less particles are incorporated into the body afterwards. The mass difference  $\Delta m_{debind-i1c} = 14\%$  is similarly high as  $\Delta m_{i1c-i2c}$  (Table 4.7), indicating that infiltration after debinding adds a significant amount of boehmite particles into the printed cylinder structure.

#### 4.3.2.4 Side Crushing Strength

Fig. 4.10 displays the crushing strength development of Binder Jet printed parts along the process chain from the green body up to three times infiltrated parts. A debinded part is approximately one third as robust as a green part, as binder burnout removes the majority

of particle coherence. Infiltration restores and even increases the crushing strength massively, so that  $\sigma_{\text{crush},i1c}$  is 20 times greater than  $\sigma_{\text{crush},\text{debinded}}$ , proving the indispensability of an infiltration procedure after debinding. The trend of calculated crushing strengths

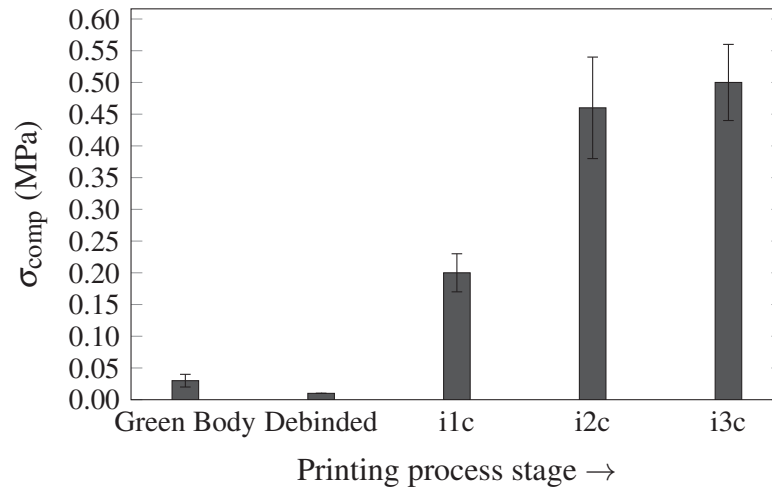


**Figure 4.10:** Side crushing strengths of printed parts at different process stages.

accords with the results for the mass increase in Table 4.7. The significant increase in  $\sigma_{\text{comp}}$  by 130 % between i1c and i2c agrees with a relatively steep mass increase of 16 %. In contrast,  $\sigma_{\text{comp}}$  merely improves by 9 % from i2c to i3c and corresponds to the small mass growth of only 6 %. Combining the findings from density and crush strength measurements, the effectiveness of infiltration declines with additional infiltration steps, so that the necessity of the third infiltration stage is debatable. Little improvement in  $\sigma_{\text{comp}}$  is traded for a decrease in open voids. High  $\epsilon_{\text{open}}$  provides utilizable surface area and access to active sites on the catalyst. Ultimately, depending on the technical application, side crush strength and sufficient void fraction have to be balanced out.

#### 4.3.2.5 Structural Analysis With $\mu$ CT

Nondestructive structural analysis of the Binder Jet printed parts were conducted by  $\mu$ CT analysis. The scan results for the green part, i1c and i2c are depicted in Fig. 4.12 and Fig. 4.14. For each sample, cross-sectional views perpendicular to each coordinate axis were recorded. For ease of visualization, Fig. 4.11 shows the analyzed planes in different colors which can be correlated to the images in Fig. 4.12 and 4.14. No  $\mu$ CT scan of the debinded part was performed due to lack of part stability, similar to the bulk density measurement. Analysis of the sample i3c was omitted due to the intention to only test the feasibility of  $\mu$ CT for the printed samples which can already be deduced from the green part to the sample i2c.

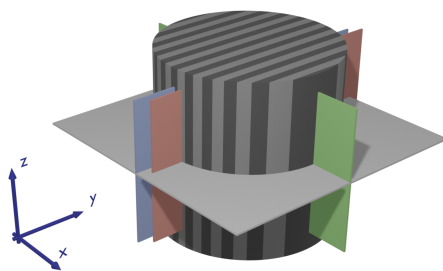


**Figure 4.11:** Coordinate system used for  $\mu\text{CT}$  analysis with colors for easier visualization.  $y$  is the printing direction. Gray cross-sections in Fig. 4.12 are perpendicular to the cylinder axis. Blue and red cross-sections in Fig. 4.14 go through loose and dense planes, respectively, parallel to the cylinder axis. Green cross-sections run through the cylindrical center of rotation and perpendicular to the red and blue slices.

The overall structure of the green part (Fig. 4.12a) shows a fine and even void structure. Fig. 4.12b and 4.12c display samples i1c and i2c, respectively, which seem to develop a coarser and more porous structure due to post-processing measurements. The bottom row of Fig. 4.12 displays the averaged pixel values of the top row figures over 1000 vertical slices, elucidating an overall structural pattern. For all three samples, the Binder Jet printed character becomes clear as a periodical stripe pattern is visible, stemming from the printhead movement in  $y$ -direction and the nozzle spacing. The print density variation attributed to the printhead nozzle distance has also been observed by others for Binder Jet printed parts [214, 217] but is in this case clearly visible via CT analysis.

Binder burnout leaves voids where the PVP powder was located, generating a fragile part. Overall mass and bulk density increase (Table 4.6 and 4.7) prove the effective introduction of boehmite particles via the infiltration slurry. However, in section 4.3.2.3 it has been discussed that the main purpose of the infiltration process in this study is more the structural stabilization of the porous scaffold due to debinding than actual density maximization. This assumption is confirmed by the  $\mu\text{CT}$  scan of the sample i1c (Fig. 4.12b). It shows larger voids compared to the green part but is evidently stronger (Fig. 4.10) than the green part. Fig. 4.12b and 4.12c demonstrate how repeated infiltration affects the particle arrangement. The averaged images in Fig. 4.12 reveal a visual effect of infiltration inside the samples of i1c and i2c. Both samples show a light circle, caused by infiltration from outside to the center whereas the green part does not show such an effect. Appearing in the averaged images implicates that the circle is featured in every slice in vertical direction. These observations lead to the assumption that atmospheric pressure infiltration does not fill the voids of the entire sample with the particle suspension but slurry uptake is somehow limited, e.g. by capillary forces. With progressing repetitions of infiltration, sealed voids hinder penetration from the outside and therefore make the light ring more visible due to increased particle accumulation up to this region. It is assumed that the size of the circle in sample i1c and i2c does not correlate to the number

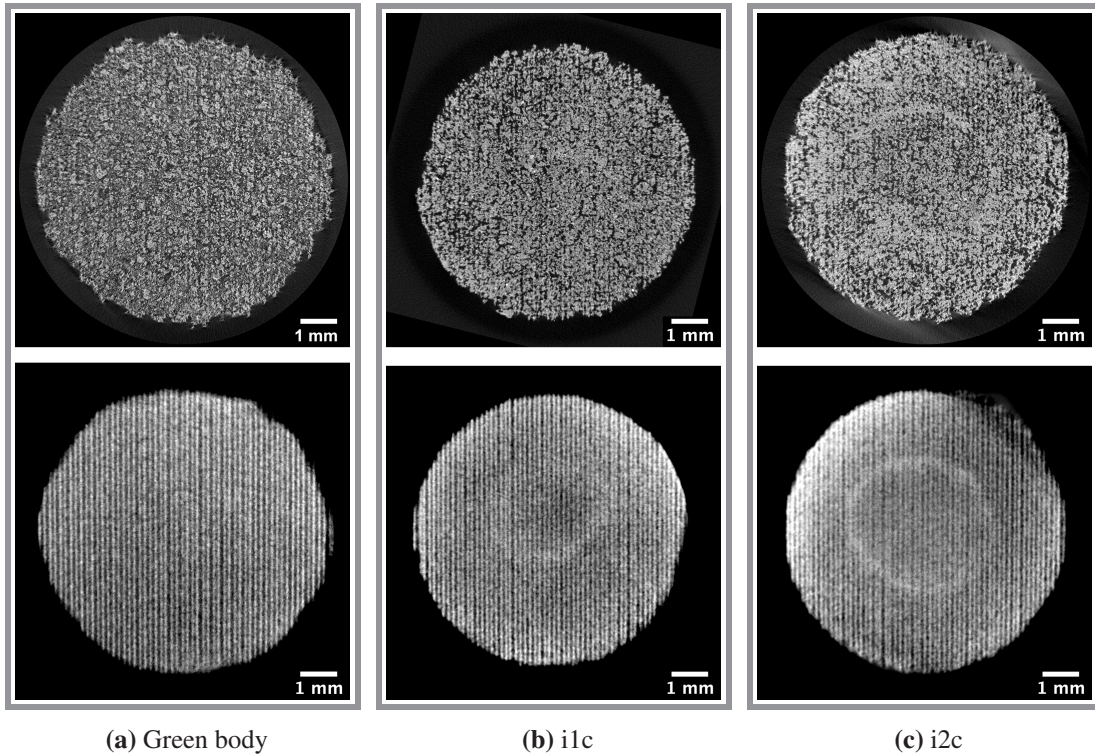


**Figure 4.12:** Cross-sectional views of  $\mu$ CT scans of printed cylinders perpendicular to the  $z$ -axis of the green body, i1c and i2c samples (top row). The bottom row shows the respective averaged pixels over 1000 slices. The orientation corresponds to the gray cross-section in Fig. 4.11. The horizontal direction is along the  $x$ , the vertical direction is along the  $y$  axis depicted in Fig. 4.11.

of infiltration repetitions. Due to slightly different liquid uptake behaviors and the nature of manual infiltration slurry addition with a pipette, the ring formation can differ between the samples to a certain extent. Nevertheless, the  $\mu$ CT scans clearly show the migration of particles of the infiltration slurry to the center of the bodies. In this case,  $\mu$ CT can provide a method to assess the effectivity or completeness of infiltration for Binder Jet printed parts.

Discrete Fourier Transform (DFT) of the cross-sectional views in Fig. 4.12 allows an independent assessment of the part shrinkage next to the one performed in section 4.3.2.2. Due to the periodically repeating pattern originating from nozzle spacing, particle shrinkage should be observable by CT through decreasing line distances in  $x$ -direction. The periods per inch by Fourier analysis of the cross-sectional views in Fig. 4.12 are calculated considering the pixel distance  $D$  from the center and the detector pixel distance  $p$ , which is  $4.55 \mu\text{m}$  in this case. Alternatively, analyzing the gray values of the same profiles within a distance of 7 mm (Fig. 4.13) and averaging the pixel distances over the number of density maxima observable from the gray value profiles yields results congruent with DFT analysis (Table 4.8). As the printhead resolution is 180 dpi, greater values for periods per inch after post-processing indicate part shrinkage. Radial shrinkage from Table 4.5 and

results yielded from  $\mu$ CT are compared in Table 4.8 and match partly. Taking into account the standard deviations and that  $\mu$ CT analysis was conducted for one sample of each infiltration step only, the shrinkage results are relatively similar, so that CT interestingly poses a method for shrinkage analysis.

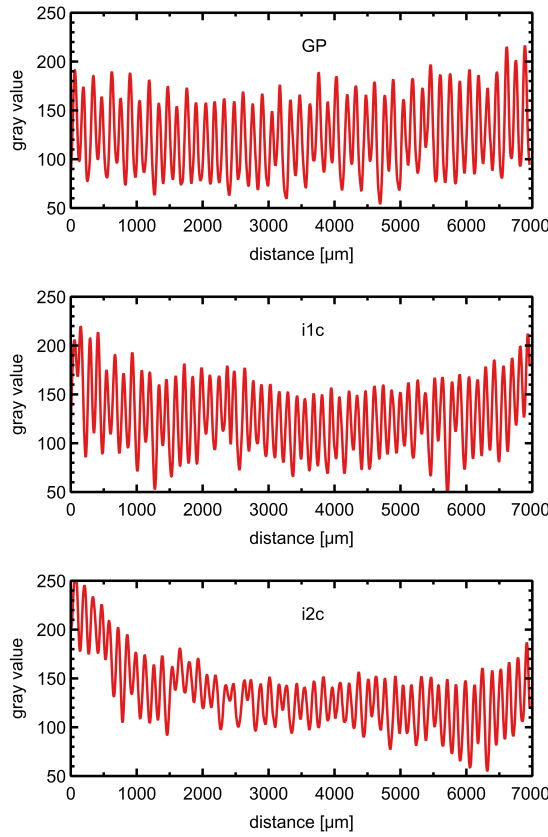


**Figure 4.13:** Gray value profiles along  $x$ -direction through the averaged cross-sectional views of Fig. 4.12, bottom row. The number of density maxima within a distance of 7 mm are 49, 54 and 52 for GP, i1c and i2c, respectively.

**Table 4.8:** Calculated values for periods per inch according to the DFT and gray value methods and resulting shrinkage, compared to measured radial shrinkage.

	Periods per inch (1/inch)		Radial shrinkage (%)	
	DFT	Gray value profile	CT	Size measurement
GP	178.8	178.6	-0.7	$0.2 \pm 0.7$
i1c	195.0	194.4	8.2	$4.4 \pm 0.8$
i2c	189.8	189.6	5.4	$5.2 \pm 0.7$

Fig. 4.14 shows three cross-sectional views of each of the three samples, one being perpendicular to the  $y$ - and two to the  $x$ -axis. It was observed that slices in the  $yz$ -plane

show alternating loose and dense layers, visible in Fig. 4.14 (middle and bottom row), therefore matching the pattern in Fig. 4.12 caused by the nozzle arrangement.

Oftentimes, 3D printed parts show distinctly visible layers in build direction as observed in other reconstructed CT scans of powder-based additively manufactured bodies [217, 218]. Vertical slices through the printed cylinders in Fig. 4.14 do not show these periodic density differences in  $z$ -direction. In conclusion, the layer thickness of  $40\ \mu\text{m}$  and a sufficient binder saturation generate a seamless linking of alumina particles in build direction.

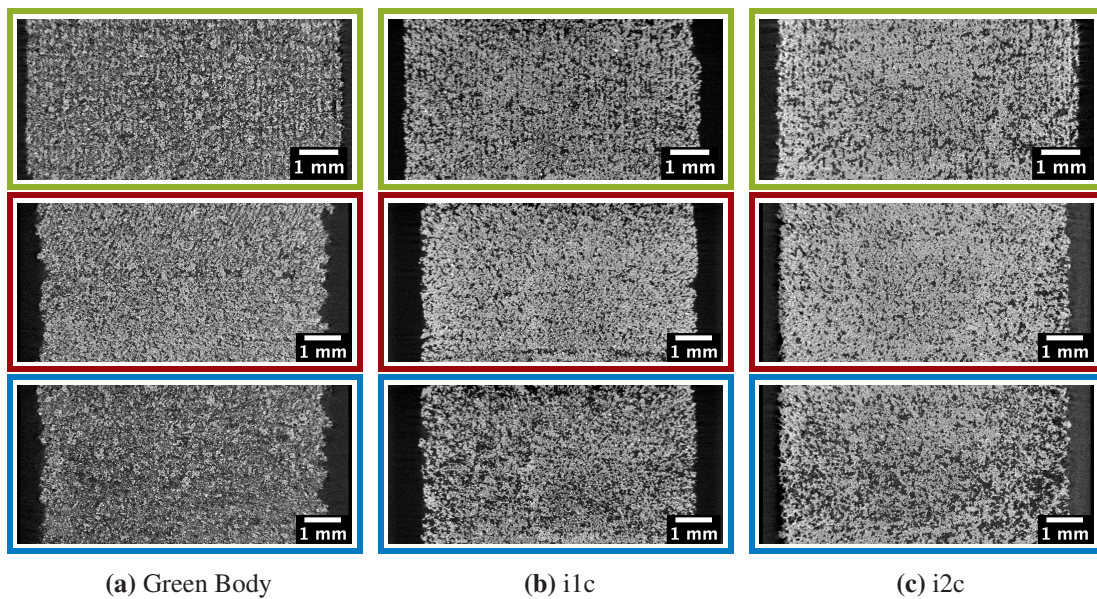


**Figure 4.14:** Cross-sectional views with identical grayscaleing of the green body, i1c and i2c. Green frame (top row) =  $xz$ -plane, red (middle row) = slice of dense  $yz$ -plane, blue (bottom row) = slice of loose  $yz$ -plane. The colors correspond to the cross-sections depicted in Fig. 4.11. The vertical direction of all 9 images is along the  $z$ -direction.

The physical limitations of capillary infiltration have been addressed before and become more visible with repeated infiltration. Pressure infiltration is in most cases preferred over pure capillary infiltration for BJ objects [219, 220] due to above discussed reasons. It was explored that water molecules even require a certain critical external pressure to overcome the energy barrier at the entrance of a small pore [221, 222]. However, pressure application tended to overly destabilize the fragile debinded parts in this case, leading to part deformation or even complete disintegration. Therefore, infiltration slurry adjustment regarding the surface tension, viscosity, particle loading could improve the infiltration effectiveness greatly. Increasing the infiltration slurry temperature from ambient temperature to more elevated temperatures could influence the surface tension or viscosity towards increased infiltration depths. Nevertheless, the currently applied procedure already substantially strengthens the debinded parts (Fig. 4.10) by consolidation of the established scaffold. For the hereby tested cylinder samples it was decided that two infiltration steps achieve

a sufficiently stable alumina support, so that i2c would be the final stage of the production process. Differently shaped and sized bodies may require more or less infiltration repetitions, depending on the wall thickness and powder volume to be penetrated by the infiltration slurry.

#### 4.3.2.6 Specific Surface Area

Besides the durability and mechanical strength, the surface area and pore size distribution also determine the practical suitability of a catalyst support. In contrast to the previously used term "void" in sections 4.3.2.3 and 4.3.2.4, the hereby used term "pore" corresponds to the nano- and mesopore sized intraparticle vacancies which play an important role for the catalytic application. Fig. 4.15 compares the bulk density  $\rho_{\text{bulk}}$  and the specific surface area  $S_{\text{BET}}$  of fabricated samples at various stages of the printing process. The thermally untreated mixture of bayerite and (pseudo)boehmite used in the powder bed has a relatively low  $S_{\text{BET}}$  of 61 m<sup>2</sup>/g. Upon debinding (calcination) at 600 °C the specific surface area increases considerably to a value of 223 m<sup>2</sup>/g. After debinding,  $S_{\text{BET}}$  seems to have reached a maximum. Infiltrated specimens, which were each calcined one more time, show a declining surface area with increasing infiltration steps. While  $S_{\text{BET}}$  of i1c drops marginally to 221 m<sup>2</sup>/g, i2c and i3c show a reduced surface area of 179 m<sup>2</sup>/g and 169 m<sup>2</sup>/g, respectively. The surface area and morphology of thermally

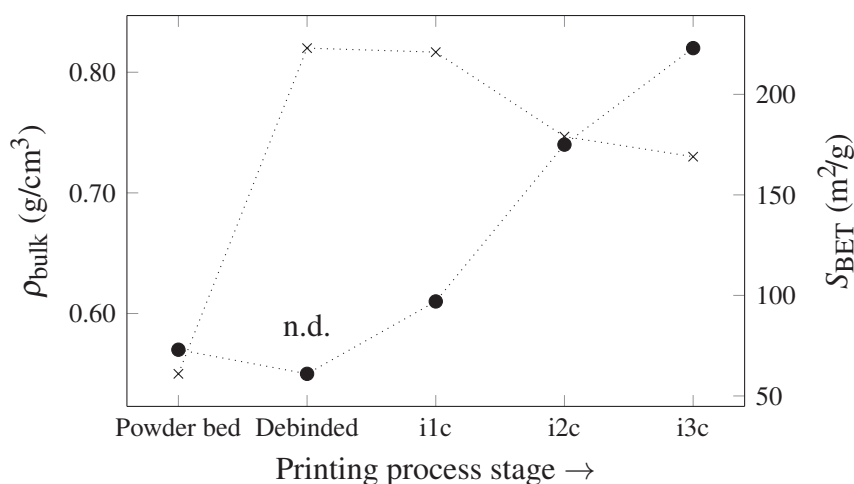


**Figure 4.15:** Bulk density  $\rho_{\text{bulk}}$  and specific surface area  $S_{\text{BET}}$  at various stages of catalyst support fabrication via binder jetting.  $\rho_{\text{bulk}}$  could not be determined for the debinding stage but is assumed to decrease due to burnout of the in-bed binder.

decomposed AlO(OH) and Al(OH)<sub>3</sub> have been thoroughly studied before, where a strong dependence of pore structure and surface area on the calcination temperature has been observed [223, 224]. Crystalline aluminum hydroxides usually have a small surface area [225] that increases up to a certain value upon heating. This is caused by the rapid

expulsion of adsorbed water. Dehydration generates an extended porous network inside the particle while the external dimensions of the aluminum hydroxide particles remain constant, leading to an increase in  $S_{\text{BET}}$  [200, 225]. Upon reaching the maximum surface area,  $S_{\text{BET}}$  decreases with further or additional heating due to internal reorientation of the metastable material system, causing progressive particle shrinkage and collapse of the crystalline network [225]. Generally, further increase of the calcination temperature would lead to a continuous decrease of the specific surface area due to formation of a more thermodynamically stable structure.

Concomitant with the surface area decrease because of aforementioned pseudomorphic transformations, the bulk density of i1c samples increases. This behavior is clearly observable in Fig. 4.15. Interestingly, the declining  $S_{\text{BET}}$  of i2c and i3c can only be attributed to the rising amount of alumina particles in the specimen by infiltration. If the reduction of surface area was influenced by the second calcination after infiltration,  $S_{\text{BET}}$  would have been expected to show a similar value compared to i1c. Apparently, infiltration occludes canals and pores which were accessible from the outside prior to particle introduction. Added boehmite particles are transformed to  $\gamma\text{-Al}_2\text{O}_3$  which contains newly generated surface area, but this process is likely outweighed by the blockage of previously accessible space.  $S_{\text{BET}}$  decrements between i1c, i2c and i3c agree with the findings from section 4.3.2.3 and 4.3.2.4 regarding the decreasing effectiveness of infiltration with each iteration. A relatively small specific surface area reduction between i2c and i3c concurs with an analogically minor increase in mass and crushing strength (Table 4.7 and Fig. 4.10, respectively).

#### 4.3.2.7 Pore Size Analysis With $\text{N}_2$ Physisorption

Surface area and porosity of a solid material are usually strongly related. The pore structure of the catalyst support determines whether reactants and products can sterically adsorb on and desorb from the surface. The analysis of the detailed pore geometry goes beyond the scope of this paper. However, Fig. 4.16 compares the pore size distribution of infiltrated samples in reference to different infiltration repetitions from  $\text{N}_2$  physisorption measurements. Fig. 4.17 represents the pore size distributions of a debinded sample and samples which were infiltrated one to three times. The pore size distribution of the one time calcined part (regular procedure) in Fig. 4.17 seems to follow a narrow unimodal distribution, peaking at a pore diameter of  $d_p = 3.6$  nm. This indicates a relatively regular and fine pore structure of the alumina support after debinding. After infiltration, the general pore size distribution shifts to a bimodal mode, seen in all samples regardless of the number of infiltrations (Fig. 4.16). The bimodality is attributed to the infiltration

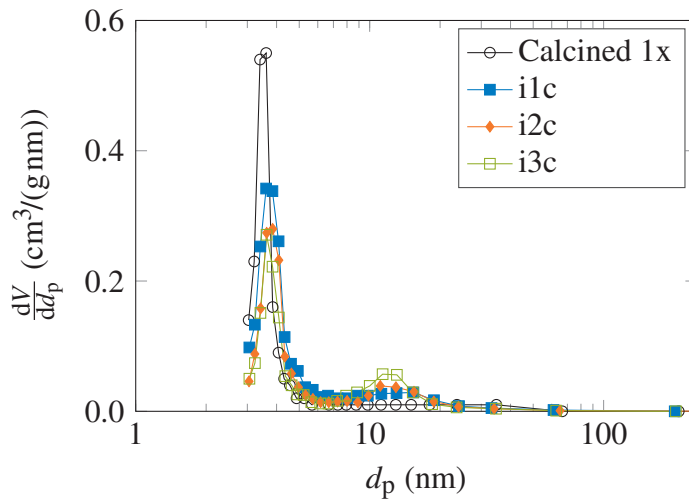


**Figure 4.16:** Pore size distribution of one to three times infiltrated samples compared to the debinded (calcined) part.

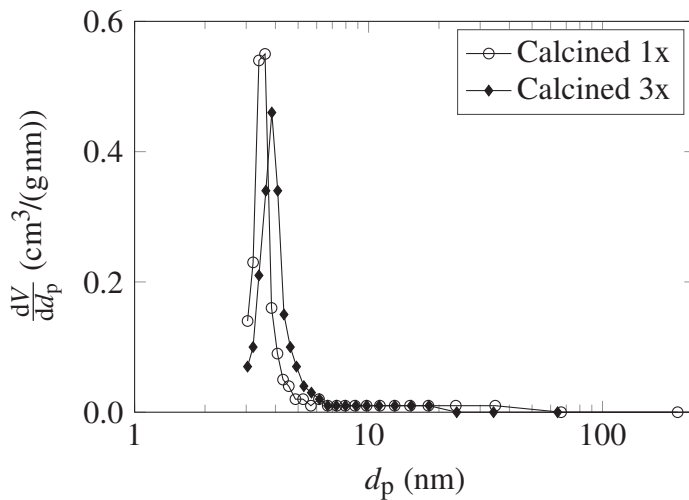


**Figure 4.17:** Pore size distribution of a one time calcined green part (according to normal preparation procedure) and a three times calcined specimen.

process and not to the second calcination step, as Fig. 4.17 shows that samples which were calcined three consecutive times without infiltration maintain the unimodal distribution type.

The major pore volume of infiltrated parts is associated with pores in the small mesopore region at around  $d_p = 3.6\text{ nm}$ , similar to the distribution of the debinded parts. Additionally, pores with  $d_p = 12\text{ nm}$  seem to form. A clear trend of declining small mesopores at  $3.6\text{ nm}$  and a simultaneous increase in pore volume at  $12\text{ nm}$  is observed from i1c to i3c, while the total pore volume stays approximately constant. This effect must be associated with repeated infiltration procedures and thus, increased particle introduction, as thermal treatment was equal for all infiltrated specimens.

Pressureless drip infiltration was chosen for its simplicity and the preservation of the dimensional accuracy of the samples. Infiltration at atmospheric pressure is governed by two forces, namely gravity and capillarity. Due to the small scale of the pores and channels, it is assumed that capillary action dominates the permeation process in this case. Moreover, it is understood that the relationship between capillary filling of pores and pore size is not trivial [226, 227]. Diminishing smaller pores and growing volume of larger mesopores as seen in Fig. 4.16 could be a result of incomplete propagation of the infiltration slurry through the capillary systems. Small air pockets are consequently trapped which transform to closed pores after calcination. This theory complies with the decreasing  $\rho_{app,s}$  values in Table 4.6 which indicate an increasing volume of closed porosity from i1c to i3c. The spontaneous infiltration of confined pores and resulting errors thereof are caused by an interplay of different parameters such as the particle size [227], pore dimensions, fluid properties and fluid-solid interaction. The hysteresis loop obtained by gas adsorption (Fig. 4.18) displays a H2 type hysteresis, typically indicative of disordered pores associated with pore blocking, percolation phenomena and ink bottle pore shapes [228]. The same hysteresis type was observed for the debinded sample and the other two infiltrated samples i1c and i3c. Thus, an irregular pore network is assumed, promoting an uneven permeation of the particle slurry through the narrow pores. The following paragraph discusses possible reasons for irregular imbibition of the printed samples. Ceratti et al. [226] investigated the effect of pore characteristics on capillary

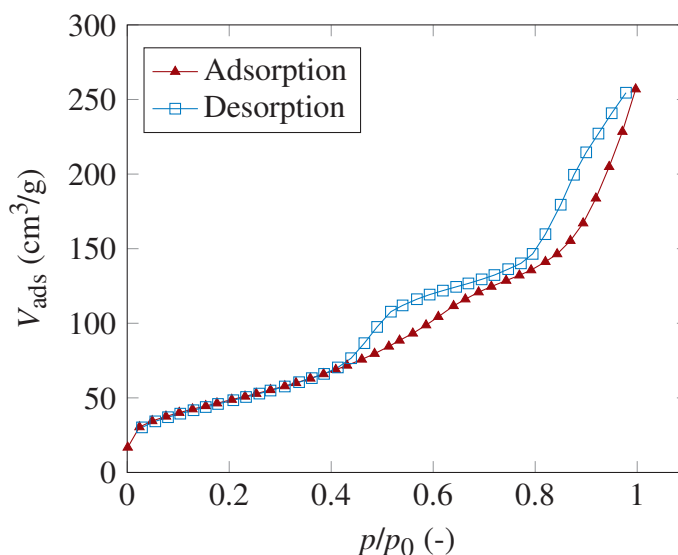


**Figure 4.18:** N<sub>2</sub> physisorption isotherms of the sample i2c.

infiltration and observed that in the case of pores < 50 nm, the presence of bottle neck pores impedes the infiltration rate and that larger pores are filled faster in general. The existence of bottle neck pores is suspected (Fig. 4.18) so that a gradient in the filling rate could cause trapped air. It has also been reported that gradients in fluid concentration could hinder complete saturation over a certain length. Produced locked air pockets

may block the permeation path of the infiltration slurry due to alteration of the flow pattern which again reduces the permeability [229]. Furthermore, assuming a random capillary model, small-diameter capillaries can experience a pinch-off mechanism where small air bubbles are trapped inside the pores while large diameter pores are bypassed [230]. The mechanism of aqueous liquid infiltration was investigated by Si et al. [221]. Chun et al. [231] investigated the relation between the pore size distribution and the infiltration efficiency in the context of BJ. The results suggest that the surface pore volume is proportional to the initial capillary pressure. As a result, small pore volumes relate to reduced capillary pressures and accordingly decreased liquid penetration into the pores. Other parameters on the infiltration efficiency have been discussed by Si et al. [221], who outlined that nanopores strongly interact with the solid phase. The smaller the pore dimension, the more is the fluid progression prevented by frictional forces by the solid. Moreover, for pore diameters smaller than 5 nm, which were detected for the tested specimens (Fig. 4.16), the pore length may play an important role insofar as inherent parameters such as the liquid-solid contact angle and the surface energy raise the energy barrier which has to be overcome.

## 4.4 Conclusions

In summary, a process for the powder-based additive manufacturing of porous but robust alumina supports applied in heterogeneous catalysis was developed and analyzed. The powder bed consisted of boehmite, bayerite and the in-bed binder PVP, indispensable for green part stability. The calcination temperature of 600 °C was sufficient to fully remove the PVP as well as to transform the transition alumina phases to presumably  $\eta$ - and  $\gamma$ -Al<sub>2</sub>O<sub>3</sub>. Drip infiltration with a boehmite slurry and subsequent calcination led to a significantly increased side crushing strength while the surface area remained in a catalytically relevant range.

Considering the absence of scientific studies on the powder-based 3D printing of catalyst supports consisting of pure transition phase alumina with a catalytically relevant specific surface area and porosity, this paper presents a viable procedure that generated ceramic parts stable enough for operation as a packing in a catalytic fixed bed reactor. Ceramic bodies 3D printed with a powder-based technology have not been reported to be fabricated under the hereby described thermal conditions so that the presented manufacturing routine poses a general and novel procedure for Binder Jet-printed alumina supports. As the first calcination step at 600 °C resulted in a fairly unstable part due to insufficient particle consolidation at such a low temperature, the key step is the drip infiltration which significantly reinforces the part due to particle introduction and binding properties of the

infiltration slurry, facilitating the production of porous and high surface area bodies in the first place. Besides the porosity and specific surface area, the final printed part consisted of pure  $\eta$ - and  $\gamma$ - $\text{Al}_2\text{O}_3$  without any potential catalyst poisons. The combination of the hereby presented low temperature thermal treatment and post-processing infiltration strategy could offer new manufacturing possibilities by decreasing the necessary calcination temperature for sufficient particle consolidation. Transferring the findings of this study to other applications, low porosity parts which still have a low bulk density after sintering could still be manufactured with the BJ technique.

The performance of the printed alumina supports could be optimized by further adjustments of the BJ process. A finer PSD of the powder materials would increase the green part stability and lessen shrinkage. Tweaking the ink composition regarding surface tension and viscosity and development towards a higher particle loading could enable stronger parts and finer structural details which could affect the catalytic activity and fluid dynamics inside a reactor positively. Adjusted surface tension and viscosity values of the boehmite slurry could greatly improve the liquid penetration behavior towards complete wetting.

The successful design of this BJ procedure for an alumina support paves the way for the preparation of impregnated printed supports applied in random packings or geometrically more challenging monolithic structures. Additionally, if a binder with a lower boiling point than PVP is used, an even lower debinding and overall calcination/sintering temperature is possible. This point could be important in the further development of 3D printing strategies for other catalyst types which do not permit high calcination temperatures due to catalyst deactivation induced by high temperatures. Moreover, the findings of this study can be used to develop a method for the direct printing of heterogeneous catalysts by already including active metal components into the printing powder, thus modifying and further developing the procedure presented in this work.



# 5 Comparison of Direct Ink Writing and Binder Jetting for Additive Manufacturing of Pt/Al<sub>2</sub>O<sub>3</sub> Catalysts for the Dehydrogenation of Perhydro-dibenzyltoluene

---

**This chapter was published in similar form in:**

H. M. Bui, P. F. Großmann, A. Berger, A. Seidel, M. Tonigold, N. Szesni, R. Fischer, B. Rieger, O. Hinrichsen, "Comparison of Direct Ink Writing and Binder Jetting for additive manufacturing of Pt/Al<sub>2</sub>O<sub>3</sub> catalysts for the dehydrogenation of perhydro-dibenzyltoluene", *Chemical Engineering Journal*, **2023**, 141361, DOI 10.1016/j.cej.2023.141361.

©2023 Elsevier B.V. All rights reserved.

---

## Abstract

Two additive manufacturing (AM) techniques, namely extrusion-based direct ink writing (DIW) and powder-based binder jetting (BJ) were thoroughly compared to assess their respective advantages and drawbacks for catalyst shaping. The 3D printed monolithic Al<sub>2</sub>O<sub>3</sub> supports were wet impregnated with H<sub>3</sub>Pt(SO<sub>3</sub>)<sub>2</sub>(OH) and tested for the dehydrogenation of perhydro-dibenzyltoluene (H18-DBT), a liquid organic hydrogen carrier (LOHC). The supports were analyzed regarding their specific surface area, compression strength, shrinkage behavior and pore size distribution with calcination temperatures ranging from 600 to 1200 °C as well as 3D print specific characteristics. Benefiting the liquid phase reaction, pore diameters below 26 nm were diminished above  $T_{\text{calc}} = 1050$  °C, revealing a BET surface area of 26 m<sup>2</sup>/g for BJ and 11 m<sup>2</sup>/g for DIW printed supports.

Furthermore, increasing the impregnation duration from 0.5 h to 12 h showed increased Pt loading, larger metal particles, and a deeper penetration into the support. Most notably, for BJ the Pt loading is generally higher due to higher meso- and macroporosity of the support. Catalytic H18-DBT dehydrogenation with powder and monolithic catalysts showed equal dehydrogenation rates with both 3D printing methods, respectively. The achieved Pt productivity was about  $4.3 \text{ g}_{\text{H}_2} \text{ g}_{\text{Pt}}^{-1} \text{ min}^{-1}$  for powder tests and  $2.7 \text{ g}_{\text{H}_2} \text{ g}_{\text{Pt}}^{-1} \text{ min}^{-1}$  for monolithic pellets.

## 5.1 Introduction

Since the first additive manufacturing (AM) concept was patented 1986 by Charles W. Hull [20], numerous AM technologies have been introduced using a wide range of materials [232, 233] for different applications ranging from the (bio)medical [234], dental [235], to automotive [37, 236] and aerospace [237, 238] industry. The chemical industry, including heterogeneous catalysis, has been hesitant due to its relatively low agility and adaptability of its oftentimes large scale productions [16, 40]. However, AM increasingly finds its way into the chemical engineering sciences to facilitate process intensification, e.g. for gas adsorption [15, 46, 239, 240].

From an advanced manufacturing viewpoint, 3D printing of structured catalysts becomes relevant since it facilitates the design of complex tailor-made shapes, optimizing pressure drop, heat and mass transfer properties, fluid and particle flow, as well as reaction thermodynamics. Therefore, the catalyst performance and overall reactor design and efficiency can be rapidly manipulated and customized to the need of each chemical reactor system by AM [16, 17].

Several review and research articles have already outlined the current state of the art of AM for catalytic applications [40, 42, 44, 45]. Not all AM methods are suitable for catalyst manufacturing since processing of ceramic material poses certain challenges due to the material's inherent brittleness and low toughness [74, 241]. Direct Ink writing (DIW) is the most commonly used printing method to generate catalysts such as Fe/ $\gamma$ -Al<sub>2</sub>O<sub>3</sub> monoliths for the hydroxylation of phenol [242], doped HZSM-5 zeolite for *n*-hexane cracking [48] or Ni/Al<sub>2</sub>O<sub>3</sub> for CO<sub>2</sub> methanation [68] as examples of studied catalytic systems. Furthermore, Stuecker et al. compared robocasted woodpile-structured monoliths to conventional honeycomb ceramic structures and discovered enhanced catalytic methane combustion activity of 3D printed structures [71]. Binder jetting (BJ) has only been used by Bui et al. for fabrication of precipitated NiAl catalysts for CO<sub>2</sub> methanation in a single pellet string reactor [243], necessitating further studies on the use of BJ in catalysis.

Ludwig et al. [21] investigated the suitability of different 3D printing methods for the generation of pure  $\text{Al}_2\text{O}_3$  parts for catalytic purposes. Among the evaluated printing techniques, BJ and DIW were chosen as suitable methods.

Direct ink writing, or so-called robocasting, is categorized as Material Extrusion by ISO [244] and can further be distinguished in discontinuous (droplet based) and continuous extrusion [245, 246]. The latter operating mode is used in this work. Hereby, high-viscosity slurries are used as printing material and extruded through a thin nozzle [246–248]. The process occurs at ambient temperature and no chemical reactions take place. Therefore, solely the rheological, shear thinning properties of the ink determine the solidification process after printing [247, 249, 250]. After successful printing, post-processing in form of binder removal or calcination can be necessary to obtain required material properties [251, 252].

Binder jetting is a powder-based 3D printing technology, which uses a roller to distribute and spread a thin powder layer over a print platform. An inkjet print head selectively jets a printing liquid over each powder layer in order to glue the powder particles together to form a three-dimensional part. After printing, the so-called green part is still embedded in unbound powder, which has to be removed. BJ creates inherently porous parts, making post-processing steps such as infiltration crucial for sufficient mechanical stability [253]. Moreover, BJ offers a relatively high build rate and easier scalability as the duration of a print is mainly determined by the height of the print job and the number of printable object is limited by the print bed area. Nevertheless, the powder-ink interaction regarding powder wetting [254], adequate powder flowability [255], and rheological properties of the ink needs to be considered when developing new material combinations [28, 29]. Different powdery materials such as metal, polymers, ceramics and biomaterials can be processed with BJ [176], making it a versatile alternative to conventional manufacturing methods.

The additively manufactured  $\text{Pt}/\text{Al}_2\text{O}_3$  catalysts in this study were tested for the dehydrogenation of perhydro-dibenzyltoluene, the hydrogen-rich form of the liquid organic hydrogen carrier pair perhydro-dibenzyltoluene/ dibenzyltoluene (H0-DBT). In contrast to the conventional hydrogen storage technologies, LOHC poses an attractive method for the decentralized storage of renewable excess energy. LOHCs can be handled, transported and stored using the existing fuel infrastructure [138, 256, 257]. H0-DBT, which has been commercially used as a heat transfer oil, is hydrogenated to H18-DBT at about  $140^\circ\text{C}$ . Subsequent dehydrogenation takes place at  $270$  to  $320^\circ\text{C}$ , mostly catalyzed by  $\text{Pt}/\text{Al}_2\text{O}_3$  egg-shell catalysts [145, 258], see Fig. 5.1. The reaction is endothermic with a reaction enthalpy for H18-DBT of  $65.4\text{ kJ/mol}_{\text{H}_2}$  [256, 259] and is a the key step for the release of hydrogen in this LOHC system.

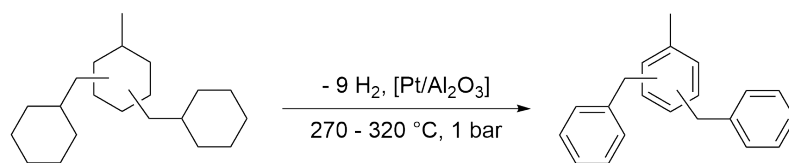


**Figure 5.1:** Schematic representation of the H18-DBT dehydrogenation.

This paper aims to directly compare the two 3D printing techniques BJ and DIW regarding the fabrication of a monolithic alumina support for Pt/Al<sub>2</sub>O<sub>3</sub> catalysts for the dehydrogenation of H18-DBT. To the best of our knowledge, this study is the first to comprehensively compare two AM methods with profoundly different functional principles in order to assess their potential for a specific catalytic application regarding e.g. shrinkage, and stability alongside physicochemical properties such as BET surface area and pore size. With respect to these properties, impregnation experiments were carried out which point out differences based on the printing method used. The more commonly used technique DIW is compared to BJ which lacks insights regarding catalytic application. Consequently, the findings from this study help to further the utilization of AM in catalysis and provide manufacturing guidelines for preparation of catalysts involving 3D printing. Generating more insights into the dehydrogenation step of a liquid organic hydrogen carrier (LOHC) additionally contributes to the application of 3D printing to improve the performance of chemical hydrogen storage and release and helps to face the future demand thereof.

## 5.2 Experimental

Fig. 5.2 gives an overview of the general experimental outline of this work. Two different shaped alumina supports were additively manufactured by BJ as well as DIW. First, alumina cylinders with a target height and diameter of 6 mm were fabricated with both printing methods and calcined at different temperatures  $T_{\text{calc}}$ . Cylinders were used for characterization regarding their specific surface area  $S_{\text{BET}}$ , pore size distribution (poreSD), part shrinkage and compression strength  $\sigma_{\text{comp}}$ . Based on the findings of the characterization experiments, the optimum  $T_{\text{calc}}$  of  $1100 \text{ }^\circ\text{C}$  was chosen for further support preparation. Subsequently, monolithic structures were printed by BJ and DIW and calcined at  $1100 \text{ }^\circ\text{C}$ . Monolithic structures were used for impregnation experiments and the catalytic tests. The monolith design is displayed in Fig. 5.3 and is a cylindrical base body with seven holes located in the corners of an equilateral triangle. This shape was chosen based on the fact that it is equally printable with DIW as well as BJ, neglecting the advantages of each printing technique. Based on the previously determined shrinkage of the calcined 3D printed parts, the CAD model of the monolithic structure was adjusted so that the

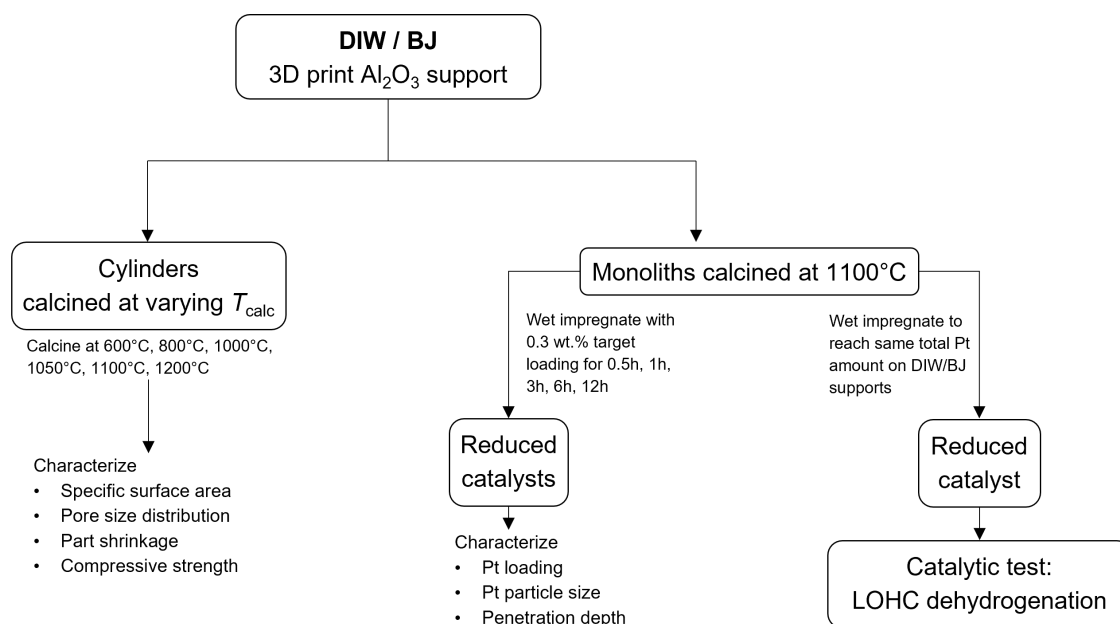


**Figure 5.2:** Overview of the experimental outline.

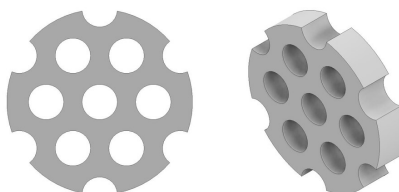


**Figure 5.3:** Front (left) and isometric view (right) of the monolith CAD file.

resulting parts after printing and calcination at 1100 °C had a diameter of 18 mm and a hole diameter of 3 mm. The distance between two holes was 2 mm. The surface-to-volume ratio of the supports after thermal treatment was  $S/V = 1.27 \text{ mm}^{-1}$ . The effect of impregnation time on the Pt loading, particle size and penetration depth was investigated using the alumina monoliths. Ultimately, catalytic tests were performed on monolithic Pt/Al<sub>2</sub>O<sub>3</sub> catalysts calcined at 1100 °C and wet impregnated for 3 h.

### 5.2.1 Catalyst Preparation

DIW and BJ vary significantly in feedstock preparation and post-processing steps. The studied alumina supports were calcined under identical thermal conditions. Moreover, the final outer part dimensions of the monolithic shapes were identical taking as different shrinkage behaviors of both printing methods were taken into account.

### 5.2.1.1 Alumina Support Fabrication by BJ

The additive manufacturing process for the Binder Jet printed alumina supports generally followed the procedure reported by Bui et al. [13] and only differed in the second thermal treatment step where different calcination temperatures were applied in this study. The powder feedstock consisted of 73 wt.% bayerite Pural BT (Sasol Chemicals, USA), 7 wt.% Actilox S40 (Nabaltec AG, Germany), and 20 wt.% of the solid binder polyvinyl pyrrolidone (PVP) Sokalan K17P (BASF SE, Germany). All powder components were homogeneously mixed in a SpeedMixer (Hauschild GmbH & Co KG, Germany). The powder bed was selectively wetted with an aqueous particle-loaded printing liquid consisting of 7 wt.% finely dispersed pseudo-boehmite Dispal 14N4-80 (Sasol Chemicals, USA), 10 wt.% isopropyl alcohol and 10 wt.% 1,4-butanediol (Merck KGaA, Germany). A general scheme of a BJ printer setup is depicted in Fig. 5.4a.

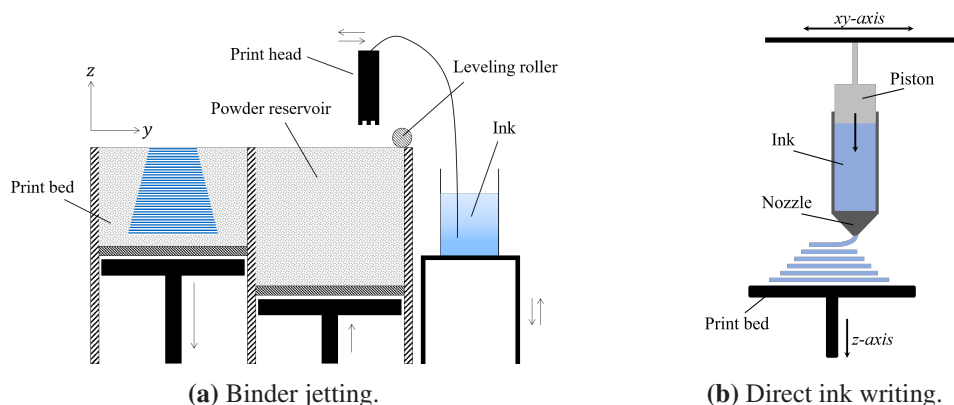


**Figure 5.4:** General schemes of the printing techniques used in this study.

The green parts were cured at 75 °C for at least 2 h after printing and debinded at 600 °C for 3 h in a muffle furnace (witeg Labortechnik GmbH, Germany) until PVP decomposed completely. The debinded parts were infiltrated with a boehmite slurry (see Ref. [13]) and calcined at varying temperatures (600, 800, 1000, 1050, 1100 and 1200 °C). The first step of the temperature program included heating to 120 °C with a ramp of 2 K/min held for 2 h followed by heating to the desired calcination temperature with a ramp of 3 K/min held for 3 h.

### 5.2.1.2 Alumina Support Fabrication by DIW

The paste composition for the alumina support obtained via DIW has already been published elsewhere [21]. 45.5 wt.% Disperal 60 and 19.5 wt.% Pural SB (both Sasol Germany GmbH) were mixed two times with 35 wt.% acetic acid (pH 3, Sigma Aldrich,

Germany) by means of a SpeedMixer at a maximum of 3500 rpm for 2 min with 3 min cooldown time in between. The paste was then filled into a syringe and installed in a self-constructed DIW printer that was equipped with a 0.41 mm nozzle. A general setup of a DIW printer is shown in Fig. 5.4b. To improve removal of the printed monolithic structures from the printbed, it was covered with a thin layer of Formentrennöl C (Clariant Produkte Deutschland GmbH). The printed parts were dried on the printbed for 24 h prior to calcination at different temperatures. Similar to the BJ procedure, a two step calcination in a muffle furnace (witeg Labortechnik GmbH, Germany) was performed with an isothermal step at 120 °C and final temperatures of 600, 800, 1000, 1050, 1100 and 1200 °C. The first step was held for 2 h, the second one for 3 h with heating rates of 2 K/min and 3 K/min, respectively.

### 5.2.1.3 Wet Impregnation with $\text{H}_3\text{Pt}(\text{SO}_3)_2(\text{OH})$

Monoliths used for impregnation time variation experiments were impregnated with a target Pt loading of 0.3 wt.% for both 3D printing methods. The monoliths were immersed while hanging in a constant volume of bidistilled water. Subsequently,  $\text{H}_3\text{Pt}(\text{SO}_3)_2(\text{OH})$  solution was weighed and added. The platinum sulfite acid solution was stirred at 500 rpm for 0.5, 1, 3, 6 and 12 h.

Monoliths used for the LOHC dehydrogenation test were wet impregnated ensuring that BJ and DIW printed monoliths contained the same total Pt loading per shape, as the weight per calcined shapes varied significantly between BJ and DIW. Thus, BJ printed monoliths were impregnated for 3 h with a target loading of 0.4 wt.% Pt and DIW printed parts with a target loading of 0.2 wt.%.

After wet impregnation, the monoliths were calcined in a muffle furnace (witeg Labortechnik GmbH, Germany). The temperature program comprised heating to 60 °C with a rate of 1 K/min held for 1 h, then a second drying step at 120 °C heated with a rate of 1 K/min and an isothermal phase of 3 h, followed by heating with 2 K/min to 400 °C which was held for 3 h.

The calcined monoliths were then reduced in a tube furnace (Nabertherm GmbH, Germany) under a constant flow of 10 %  $\text{H}_2/\text{N}_2$  (Westfalen GmbH, Germany) at 400 °C for 3 h using a heating rate of 1 K/min.

## 5.2.2 Catalyst Characterization

### 5.2.2.1 Variation of Calcination Temperature

Height and diameter of the printed test cylinder before and after calcination were obtained using a tablet hardness testing system with an integrated option for length measurement (MultiTest 50, Dr. Schleuniger Pharmatron, Switzerland). The part to be measured was placed in the measuring area between two stainless steel brackets, one moving towards the other with a constant moving speed of 2 mm/s. Once a certain resistance from the inserted test body is recognized, the diameter or height, depending on the testing orientation, is recorded.

The compression strength was measured with the MultiTest 50, which was also used for above described size measurement. Uniaxial compression on the lateral surface of the samples between two opposite metal plates was performed, characterizing the cylinder's response to loading perpendicular to its length, until fracturing occurs. One of the plates moved towards the other with a constant velocity of 2 mm/s. The fracture load  $F$  was automatically collected and used in Eq. 3.19 to yield the compression strength  $\sigma_{\text{comp}}$ .

The poreSD of the test cylinders calcined at 1100 °C was determined by mercury intrusion porosimetry (MIP) (AutoPore 9600, Micromeritics Instrument Corporation). Per measurement, two cylinders were added to the penetrometer comprised of a 5 mL bulb volume and 0.392 mL stem volume. To reduce the influence of the hydrostatic pressure of mercury in the low pressure region, the pressure range of 0.5 to 45 psi was measured in a horizontal penetrometer position, while the pressure range from 45 to 61 000 psi was obtained in vertical penetrometer position. The pressure steps were chosen to achieve an even spacing on the logarithmic scale with 25 points per decade in a pressure range between 0.5 and 4000 psi and with 40 points per decade in a pressure range between 4000 and 61 000 psi. The latter pressure range with higher resolution correlates to pore diameters of 3.5 to 53.3 nm, respectively. The pressure at each pressure step was held constant until the intrusion rate was below 0.01  $\mu\text{L}/(\text{g s})$ . To convert the pressure  $p$  to a pore diameter  $d_{\text{pore}}$ , Washburn's equation (Eq. 3.18) was applied.

N<sub>2</sub> physisorption at 77 K (Nova 4200e, Quantachrome Instruments) was used to determine the specific surface area  $S_{\text{BET}}$ . Sample pretreatment comprised degassing under vacuum at 120 °C for 3 h.  $S_{\text{BET}}$  was determined according to the method of Brunauer, Emmett, and Teller (BET) and calculated between  $0.05 \leq p/p_0 \leq 0.3$ . Moreover, the Barrett, Joyner, Halenda (BJH) method was applied to analyze the poreSD using the desorption branch of the isotherm. Data points were collected from  $p/p_0 = 0.01 - 0.999$ .

Phase determination of the alumina supports was obtained via XRD analysis (Empyrean, Malvern Panalytical, UK). Cu-K $\alpha$  radiation ( $\lambda = 1.54056 \text{ \AA}$ ) and a monochromator were employed to scan the samples applying a step size of  $0.007^\circ$  and 70 steps/min from  $2\theta = 5$  to  $90^\circ$ .

### 5.2.2.2 Variation of Impregnation Time

Inductively coupled plasma optical emission spectrometry (ICP-OES) measurements were performed on an Agilent 700 Series ICP Optical Emission Spectrometer to investigate the amount of platinum loaded on the different carriers. Ground catalyst powder of the respective catalysts was dissolved in aqua regia overnight consisting of hydrochloric acid and nitric acid (both Sigma Aldrich, Germany) at a ratio of 3:1 vol.%. The sample was then diluted with bidistilled water and filtered with a  $0.45 \mu\text{m}$  syringe filter (VWR, Germany). A platinum standard (AAS grade, Sigma Aldrich, Germany) was used for calibration. Furthermore, the wavelength of 214.42 nm was used to calculate the platinum loading.

Transmission electron microscopy (TEM) was carried out on a JEOL JEM 1400 plus instrument at an acceleration voltage of 120 kV to determine the metal particle diameter  $d_M$  and the resulting metal dispersion  $D_M$ . The samples were finely ground, suspended in absolute ethanol (Sigma-Aldrich) and finely dispersed by ultrasound. After sedimentation of larger particles, two drops of the suspension were deposited onto a Holey Multi A copper grid (Quantifoil Micro Tools GmbH) and left to dry. The metal particle diameter  $d_M$  was determined using the image processing software imageJ. For each sample, a minimum of 460 particles was counted on several micrographs taken on different zones of the TEM grid.  $D_M$  is indirectly proportional to  $d_M$  and is determined with Eq. 3.15.

The penetration depth of the Pt layer after wet impregnation for varying durations was measured with a light microscope MZ8 (Leica, Germany) equipped with a MicroCam II (Bresser, Germany). The monoliths were fragmented at different locations with a scalpel and microscopically examined. The penetration depth was manually determined with the corresponding software at at least 35 locations and averaged arithmetically.

### 5.2.3 LOHC Dehydrogenation

The catalytic performance of the BJ and DIW printed Pt/Al $_2$ O $_3$  catalysts was investigated using the dehydrogenation of perhydro-dibenzyltoluene. The experimental setup

was a semi-batch reactor, consisting of a heated three-neck round-bottom flask with flow breakers connected to a reflux condenser, an overpressure valve and a Type K thermocouple for temperature regulation of the endothermic reaction. The reaction was carried out under an inert Ar atmosphere at ambient pressure. H18-DBT (Hydrogenious LOHC Technologies GmbH, Germany) was preheated to 325 °C before the catalyst was added to the liquid and stirred at a constant speed of 500 rpm. After complete insertion of the catalyst into the H18-DBT, the temperature was immediately regulated down to the reaction temperature of 310 °C. Catalytic tests with monoliths were performed using two monoliths for each measurement. The 3D printed catalysts were stacked on top of each other on a mesh made of stainless steel and immersed into the liquid reactant. For catalyst powder tests, two monoliths were ground and added to the H18-DBT once the start temperature was reached. The catalyst powder was not pressed and sieved to ensure the usage of the complete egg-shell catalyst during reaction without sorting out Pt-rich or Pt-lean parts of the monolith. The average particle size of 89 μm was determined via laser diffraction (see Supporting Information, Fig. 5.15). The weight ratio of Pt/H18-DBT = 0.08 mg<sub>Pt</sub>/g<sub>H18-DBT</sub> was kept constant. Consequentially, the amount of used H18-DBT was adjusted for each reaction.

To determine the degree of dehydrogenation (DoD) during the reaction, 24 samples were withdrawn with a syringe at certain time points during the total reaction time of 9 h. The aliquots were analyzed using proton nuclear magnetic resonance spectroscopy (<sup>1</sup>H-NMR) on a Bruker Ascend spectrometer at 400 MHz. All spectra were referred to the residual proton signal of the solvent acetone-d<sub>6</sub>. The DoD was calculated using the ratio  $x$  of the integral of the aromatic to the integral of all protons based on the <sup>1</sup>H-NMR data according to Do et al. [257] and Preuster [260]:

$$\text{DoD} = 1.3945 \cdot x^6 - 4.9037 \cdot x^5 + 5.6287 \cdot x^4 - 5.207 \cdot x^3 + 4.00985 \cdot x^2 - 2.9217 \cdot x + 1 \quad (5.1)$$

The Pt productivity  $P$  is introduced for better comparison between measured dehydrogenation activities.  $P$  describes the ratio between the released amount of hydrogen per amount of Pt and time [147, 261]:

$$P = \frac{m_{\text{H}_2}}{m_{\text{Pt}} \cdot t} = \frac{\Delta \text{DoD} \cdot m_{\text{H}_{18\text{-DBT}}} \cdot \frac{M_{\text{H}_2}}{M_{\text{H}_{18\text{-DBT}}}} \cdot \frac{\nu_{\text{H}_2}}{\nu_{\text{H}_{18\text{-DBT}}}}}{m_{\text{cat}} \cdot w_{\text{Pt}} \cdot \Delta t} \quad (5.2)$$

$m_{\text{H}_2}$ ,  $m_{\text{H}_{18\text{-DBT}}}$  and  $m_{\text{cat}}$  represent the mass of evolved H<sub>2</sub>, mass of H18-DBT and catalyst mass, respectively.  $M_{\text{H}_2}$  and  $M_{\text{H}_{18\text{-DBT}}}$  are the respective molar masses of hydrogen and Pt while  $\nu_{\text{H}_2}$  and  $\nu_{\text{H}_{18\text{-DBT}}}$  are the stoichiometric coefficients.  $w_{\text{Pt}}$  is the platinum loading.  $P$  was determined in the range  $\Delta \text{DoD} = 10$  to 60 % while using the corresponding time difference  $\Delta t$ .

## 5.3 Results and Discussion

### 5.3.1 3D Printed Catalysts

Fig. 5.5 displays the printed alumina supports as well as the reduced  $\text{Pt}/\text{Al}_2\text{O}_3$  catalysts for BJ and DIW next to each other. For both parts, different surface structure characteristics can be observed that are closely related to the respective printing techniques. DIW

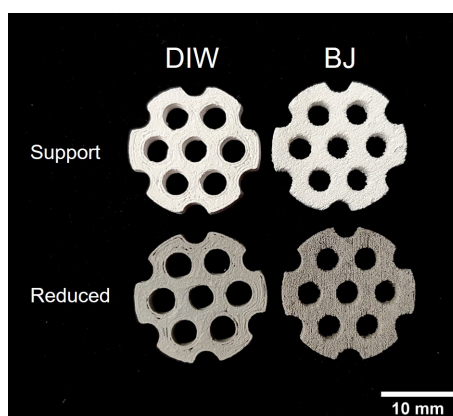


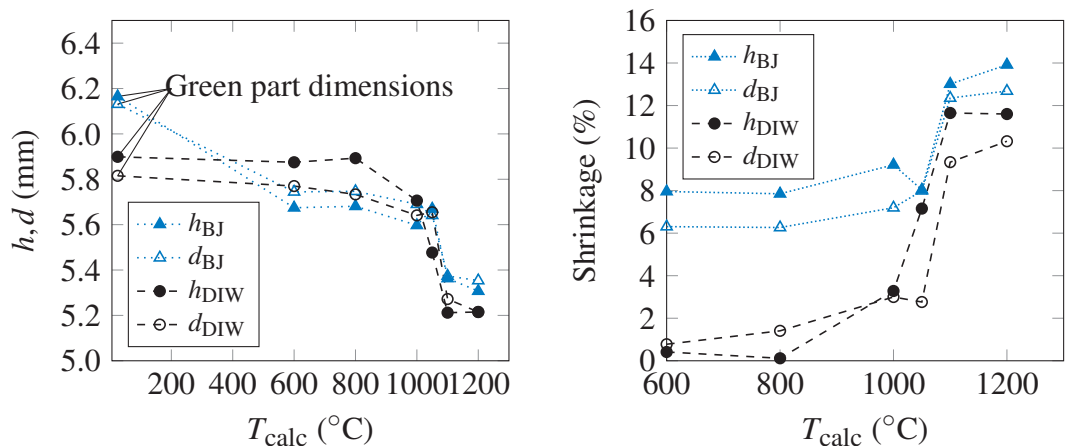
**Figure 5.5:** Photos of monolithic alumina supports (first row) and reduced  $\text{Pt}/\text{Al}_2\text{O}_3$  catalysts (second row) fabricated by DIW (first column) and BJ (second column).

creates smoother surfaces with a partially visible printing pathway due to the extrusion-based layering technique. The BJ printed parts are substantially more porous as can be seen by the rough surface texture. Furthermore, the printing and print head moving direction can be detected for the BJ printed based on the parallel line pattern caused by the print head moving back and forth in one direction during printing.

### 5.3.2 Calcination Temperature Variation

#### 5.3.2.1 Shrinkage

Due to differing printing methods, feedstock properties and post-processing procedures, shapes produced *via* binder jetting and direct ink writing differ in the dimensions of the final part. Fig. 5.6a and 5.6b compare the shrinkage behavior of the two printing methods with increasing calcination temperature  $T_{\text{calc}}$ . Hereby, Fig. 5.6a displays the absolute height and diameter of the printed test cylinders of the green bodies as well as after calcination.



(a) Height  $h$  and diameter  $d$  of calcined cylinders. Target size is  $d = h = 6$  mm.

(b) Vertical and horizontal shrinkage of height  $h$  and diameter  $d$  of calcined cylinders relative to the green part dimension.

**Figure 5.6:** Size change of BJ and DIW printed alumina test cylinders in dependence of calcination temperature.

Apart from the green part, both BJ and DIW show the same trend towards decreasing dimensions. For BJ, the green part dimensions exceed the target value of 6 mm for the height and diameter. This is caused by hardware related printing inaccuracies or bleeding, which is macroscopic flow of binder caused by slight oversaturation of the powder bed due to high ink saturation levels [176, 262]. Because DIW printed parts are left to dry at room temperature on the print bed immediately after the print job has finished, the green parts are smaller than the target dimensions due to shrinking (see Fig. 5.6a). Fig. 5.6b depicts the shrinkage of both printing methods relative to the green part dimension. While shrinkage for DIW amounts to about 3 % until 1100 °C, BJ printed parts exhibit larger relative shrinkage of up to 9 % due to a more porous particle framework and the generation from a loose powder bed. Within the ink used for DIW and due to the drying the solid components are more tightly packed, therefore generally inhibiting extensive shrinkage of the printed structure compared to BJ. Furthermore, it has to be taken into account that both green parts, on which the shrinkage is based, vary in height and diameter. Significant shrinkage occurs for BJ and DIW after 1100 °C, visible by a steep decline in cylinder height and diameter (Fig. 5.6a) and a relatively sharp increase in relative shrinkage (Fig. 5.6b). The transition to the thermodynamically most stable phase  $\alpha$ -Al<sub>2</sub>O<sub>3</sub> starts at this temperature range and induces pronounced sintering and particle shrinkage [263] followed by part densification and mechanical stabilization. Between 1100 °C and 1200 °C part dimensions do not change considerably as further heating does not alter the alumina morphology any more. These differences regarding the shrinkage behavior should be taken into account for accurately sized final parts.

### 5.3.2.2 Compression Strength

The effect of  $T_{\text{calc}}$  on the compression strength  $\sigma_{\text{comp}}$  is reflected in the uniaxial compression strength test results summarized in Fig. 5.7. The threshold of 1100 °C is also visible here, where especially DIW printed cylinders gained significant stability compared to shapes calcined below 1100 °C. While cylinders calcined at 1050 °C show a compression strength of 1.4 MPa,  $\sigma_{\text{comp}}$  increases less than four times to 5.2 MPa at 1100 °C and reaches 6.0 MPa at 1200 °C.

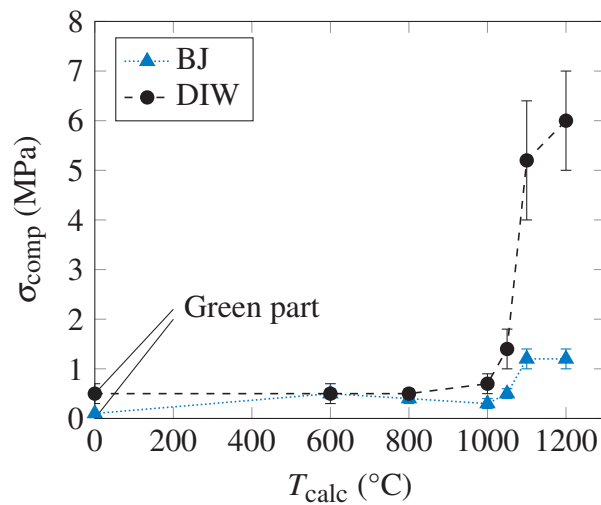


**Figure 5.7:** Comparison of DIW and BJ compression strengths of printed alumina supports calcined with varying calcination temperatures.

Except for the green part, BJ printed test cylinders show a similar robustness as DIW printed parts until 1000 °C. Green parts produced by DIW are more stable by default because of the already consolidated structure after drying at ambient conditions, whereas the particles of the green parts generated by BJ are relatively weakly connected.

The distinct stability increase at 1100 °C is observable for BJ as well, but the absolute  $\sigma_{\text{comp}}$  reaches slightly lower values. Calcined at 1050 °C,  $\sigma_{\text{comp}}$  is located at 0.5 MPa and stagnates at 1.2 MPa above 1100 °C. In accordance with constant part dimensions at high calcination temperatures in Fig. 5.6a and 5.6b, further increase of  $T_{\text{calc}}$  does not improve the part stability due to no more densification by sintering.

At 1100 °C, the compression strength of DIW exceeds the stability of BJ printed parts by a factor of 4.3 and even a factor of 5 at 1200 °C. Again, this effect originates from print technique related part properties, which were previously discussed for the shrinkage behavior and specific surface area. The similar compression strength values of BJ and DIW until 1000 °C stem from minor sintering activity in this temperature range so that densification

by thermal processing is equally low for both AM techniques. However, above 1100 °C the more densely packed alumina particles in the pasty printing feedstock come into effect by providing a larger number of contacting points, resulting in more effective densification by sintering leading to improved sintering and compression strength.

### 5.3.2.3 Specific Surface Area

The above discussed part shrinkage and increase in compression strength with increasing  $T_{\text{calc}}$  correlates directly with a decline in specific surface area  $S_{\text{BET}}$  (see Table 5.1). Calcined at 600 °C, BJ and DIW printed alumina cylinders have a specific surface area of 166 m<sup>2</sup>/g and 102 m<sup>2</sup>/g, respectively. In accordance with the observations in Fig. 5.6a and 5.6b  $S_{\text{BET}}$  decreases sharply above 1100 °C due to sintering processes, diminishing micro- and mesoporous structures.

**Table 5.1:** Specific surface area  $S_{\text{BET}}$  of 3D printed alumina supports calcined at varying calcination temperatures.

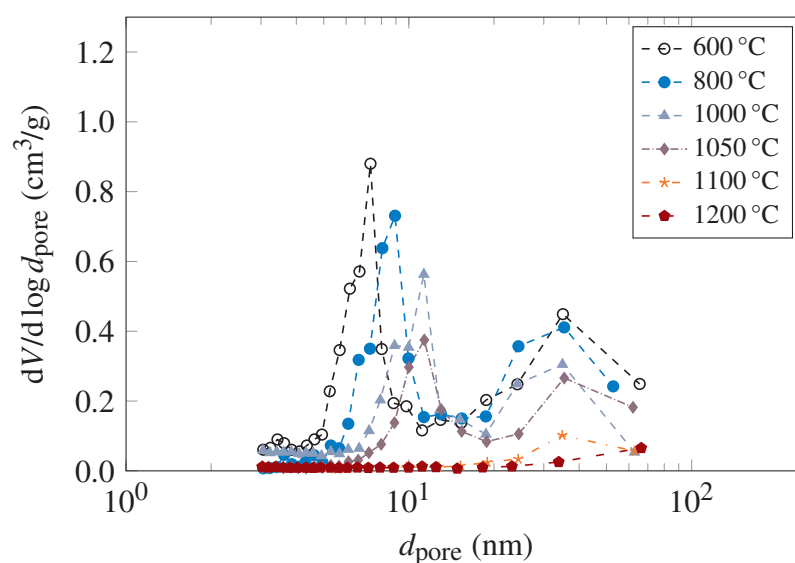
$T_{\text{calc}}$ (°C)	$S_{\text{BET}}$ (m <sup>2</sup> /g)	
	BJ	DIW
600	166	102
800	92	69
1000	65	57
1050	70	36
1100	26	11
1200	9	9

At low calcination temperatures below 1200 °C, BJ printed parts generally possess a larger  $S_{\text{BET}}$  than DIW. Again, the printing principle inherently causes BJ to generate more porous shapes which manifests itself in higher surface areas. Still with the declining trend, the values of  $S_{\text{BET}}$  converge more and more and above 1200 °C the final sintering state is reached where the majority of pores detectable by N<sub>2</sub> physisorption were eliminated, resulting in the same low final specific surface area of 9 m<sup>2</sup>/g for both printing methods.

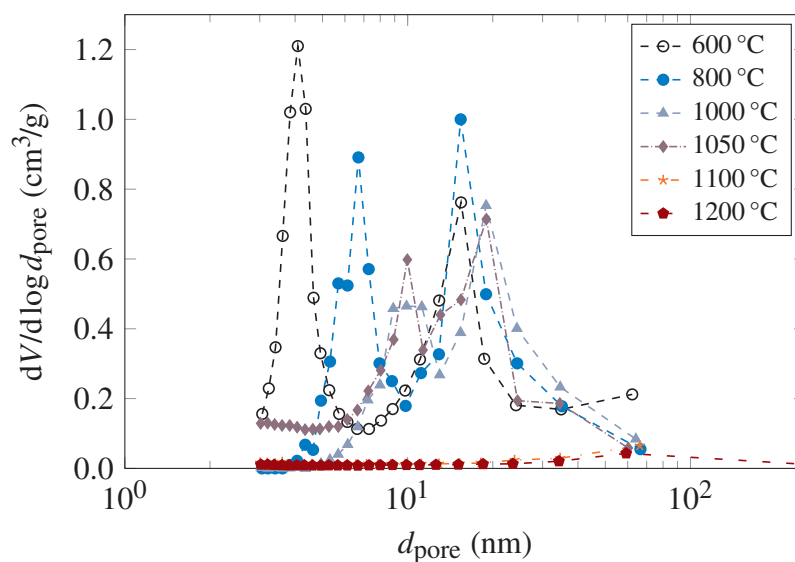
### 5.3.2.4 Pore Size Distribution

In order to assess the optimal calcination temperature for catalysts for application in the dehydrogenation of perhydro-dibenzyltoluene, the poreSD was analyzed via N<sub>2</sub> gas adsorption. Studies regarding diffusional phenomena during LOHC dehydrogenation on

Pt/Al<sub>2</sub>O<sub>3</sub> by Seidel [261] and Auer [147] revealed that a minimum mean pore diameter of 26 nm is necessary in order to avoid reduced activity due to restricted diffusion of the reactant during the dehydrogenation of H18-DBT. The poreSD of DIW and BJ printed test cylinders are summarized in Fig. 5.8 and agree with each other such that below  $T_{\text{calc}} = 1100^{\circ}\text{C}$  a bimodal poreSD is present in both cases. According to general consensus [264], pores enlarge and eventually disappear during the heating process. Moreover, the correlation between specific surface area and pore size is inversely proportional, noticeable in Fig. 5.8.



(a) Direct Ink Writing (DIW)



(b) Binder Jetting (BJ)

**Figure 5.8:** Pore size distribution of the 3D printed alumina supports from (a) DIW and (b) BJ calcined at varying calcination temperatures, determined by N<sub>2</sub> physisorption.

Below 1100 °C, DIW printed parts show two major pore sizes (Fig. 5.8a). The larger pores were located at about 33 nm, while the smaller pore sizes shift from 7 nm at 600 °C to larger pore sizes of about 11 nm at 1050 °C. Within this temperature range, BJ printed parts display a similar trend (Fig. 5.8b). Larger pores are found between 15 to 20 nm, while the smaller pores also shift to larger sizes ranging between 4 to 10 nm as the calcination temperature rises. Gas adsorption measurements revealed that upon exceeding  $T_{\text{calc}} = 1100\text{ °C}$  3D printed parts made by both printing techniques show almost no inherent porosity, visible by the flat curves for the poreSD for  $T_{\text{calc}} = 1100\text{ °C}$  and  $1200\text{ °C}$ . This finding is consistent with the previous observation of declining specific surface area (Table 5.1) and increasing compression strength with increasing calcination temperature (Fig. 5.7).

Based on the pore size analysis by nitrogen gas adsorption it was determined that the calcination temperature of 1100 °C was most suitable for the preparation of H18-DBT dehydrogenation catalyst supports in this study. This way, mean pore diameters below 26 nm could be diminished so that diffusional restrictions during the reaction were avoided.  $T_{\text{calc}} < 1100\text{ °C}$  were therefore excluded for further investigations. Furthermore, the mechanical stability already increased tremendously at 1100 °C (see Table 5.7) which also favors this choice.  $T_{\text{calc}} > 1100\text{ °C}$  would lead to slightly higher  $\sigma_{\text{comp}}$  values, but also correlates with a reduced specific surface area and consequently, reduced activity, making higher  $T_{\text{calc}}$  unideal.

Additionally, the poreSD was measured by mercury intrusion porosimetry for the printed samples. Fig. 5.9 compares BJ and DIW alumina supports calcined at 1100 °C regarding their poreSD. In contrast to N<sub>2</sub> physisorption, larger interparticle pores, hereafter referred to as "voids", are detected by MIP due to its large measurement range spanning from 3 to 500 000 nm in comparison to gas adsorption, which can theoretically detect pores between 0.3 to 300 nm. However, in this case, pores greater than 100 nm could not be recorded with gas adsorption. N<sub>2</sub> physisorption does not reveal any pores in the micro and mesopore region in Fig. 5.8, whereas MIP does show a small percentage of pores at 4 to 5 nm (less than 0.3 cm<sup>3</sup>/g), see Fig. 5.9. This difference might be caused by the different measuring methods.

Voids originate from the random powder particle arrangement of specific size and shape and their agglomeration within the paste (DIW) or powder bed (BJ) and the resulting particle framework after thermal treatment. The most prominent difference between BJ and DIW depicted in Fig. 5.9 is the percentage of very large voidages at about 30 000 nm for BJ alumina supports. These voids do not exist in DIW printed parts.

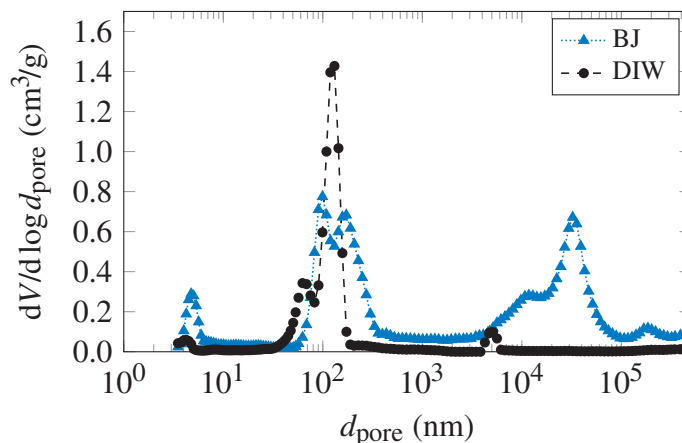


**Figure 5.9:** Pore size distribution of 3D printed alumina supports calcined at 1100 °C, determined by MIP.

In general, the data highlights structural differences due to the additive manufacturing method and underlines the coarser pore size structure generated from a powder-based printing method, also indicated by a porosity of 77 % for BJ and 56 % for DIW, determined directly by MIP.

### 5.3.3 Impregnation Time Variation

#### 5.3.3.1 Metal loading

The fabricated monoliths calcined at 1100 °C were impregnated with a target Pt loading of 0.3 wt.%. The duration of immersion in the impregnation solution was varied to investigate the reached loading, impregnation depth and Pt particle size. As expected, the platinum loading rises with increased impregnation time. However, Fig. 5.10a suggests that neither BJ nor DIW monoliths reach the calculated  $w_{Pt}$  but achieve a maximum Pt loading of 0.21 wt.% and 0.15 wt.%, respectively after 12 h.

The reason for incomplete impregnation of monoliths printed with both methods could be given by the comparably small external surface area due to the geometric design. Choosing another monolith shape with an extended outer surface area would facilitate a higher metal loading. Furthermore, the internal surface area  $S_{BET}$  (see Table 5.1), controllable by certain parameters including the calcination temperature, plays a role for the impregnation efficiency. At a calcination temperature of 1100 °C,  $S_{BET}$  of BJ and DIW alumina supports drops to 26 m<sup>2</sup>/g and 11 m<sup>2</sup>/g, respectively. Reducing  $T_{calc}$  would lead to a larger specific surface area available for Pt impregnation but in this case would interfere with the minimum requirement for the mean pore diameter of 26 nm.

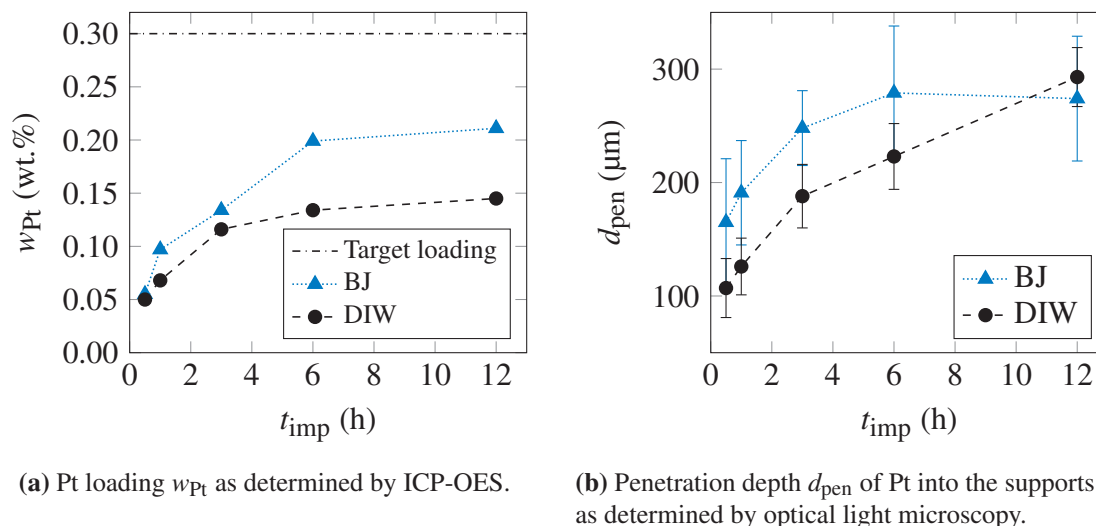


**Figure 5.10:** Pt loading and penetration depth in dependence of the wet impregnation duration  $t_{imp}$ . Supports were calcined at 1100 °C and impregnated with a target Pt loading of 0.30 wt.%. (a) Pt loading  $w_{Pt}$  as determined by ICP-OES. (b) Penetration depth  $d_{pen}$  of Pt into the supports as determined by optical light microscopy.

The difference in obtainable Pt loading between the two printing methods is caused by the pore size and surface area characteristics of each technique. As already discussed in the previous sections, BJ printed objects are significantly more porous (Fig. 5.9) and possess a larger specific surface area (Table 5.1). Therefore, a higher amount of Pt can adsorb on the surface in comparison to a DIW printed support with an identical external surface area.

After an impregnation time of 12 h,  $w_{Pt}$  does not increase substantially, so that the achieved loading after 12 h approximates the highest possible Pt loading. Fig. 5.10a corroborates this by asymptotically approaching a  $w_{Pt}$  maximum.

### 5.3.3.2 Metal Particle Size and Dispersion

TEM was used to determine the particle size distribution and the resulting metal dispersion of the Pt particles on the alumina support (Table 5.2). The detailed particle size distributions are displayed in the Supporting Information (see Figs. 5.16 and 5.17). The data shows that prolonged impregnation time leads to increasing metal particle size  $d_p$ . Moreover,  $d_p$  is similar for BJ and DIW, taken into account the relatively high standard deviation, which is in the same range for both printing methods. After 0.5 h, BJ catalysts have a particle size of  $1.10 \pm 0.27$  nm which grows to  $1.50 \pm 0.32$  nm after 12 h. Similarly, the Pt particle size increases from  $1.05 \pm 0.23$  nm to  $1.48 \pm 0.33$  nm for DIW printed catalysts. However, with diameters ranging from 1.05 to 1.50 nm overall, the metal

particle size is very small in general for all prepared catalysts, resulting in relatively high Pt dispersion (see Table 5.2).

As the dispersion is inverse proportional to the platinum particle diameter  $d_p$ , DIW and BJ catalysts show a similar dispersion for the same impregnation duration, suggesting that the crystalline structure of the alumina supports is comparable. Previous studies suggest that metal particle size and dispersion of Pt/Al<sub>2</sub>O<sub>3</sub> catalysts are more strongly affected by the crystalline phase of the support than the BET surface area [159, 265]. The available data corroborates this statement, as the specific surface area of BJ printed alumina supports is more than double the DIW printed ones (Table 5.1) but the dispersion of BJ supports is not superior to DIW. The DIW feedstock consists of boehmite ( $\gamma$ -AlOOH), whereas the BJ powder feedstock is mainly bayerite ( $\alpha$ -Al(OH)<sub>3</sub>). At 1100 °C, both bayerite and boehmite undergo a similar transformation to late transition alumina phases, which could be either  $\theta$ -Al<sub>2</sub>O<sub>3</sub> or possibly already  $\alpha$ -Al<sub>2</sub>O<sub>3</sub> [199, 201]. Nevertheless, the transition pattern is similar for boehmite and bayerite at this temperature range, so that the similar surface morphology of the printed alumina support explains the comparable Pt particle sizes and dispersion.

Increasing impregnation times decrease the metal dispersion, as after 12 h,  $D_{Pt}$  is below 70 % in comparison to over 90 % after 0.5 h of impregnation. Numerous studies confirm that at lower loadings ( $\leq 1$  wt.%) the amount of Pt per anchoring site on the alumina support is lower so that a high dispersion, even atomical dispersion, is possible [159, 266–268]. Increasing the amount of Pt in the dispersed phase favors the formation of Pt clusters as the Pt loading tends to exceed the number of anchoring sites. However, TEM images of the wet impregnated alumina monoliths (Fig. 5.12) still give evidence for highly dispersed Pt species on the support surface as no severe agglomerates are visible.  $d_p$  increases with increasing impregnation time. Still, the overall particle size is very small, so that the wet impregnation technique is suitable to immobilize Pt species finely dispersed on the printed alumina supports.

**Table 5.2:** Overview of characterization data for monoliths calcined at 1100 °C: Pt loading  $w_{Pt}$ , average particle size  $d_{Pt}$ , resulting Pt dispersion  $D_{Pt}$  and Pt penetration depth  $d_{pen}$  of BJ and DIW printed samples depending on the impregnation time  $t_{imp}$ .

$t_{imp}$ (h)	$w_{Pt}^a$ (wt.%)		$d_p^b$ (nm)		$D_{Pt}$ (%)		$d_{pen}^c$ (μm)	
	BJ	DIW	BJ	DIW	BJ	DIW	BJ	DIW
0.5	0.06	0.05	1.10 ± 0.27	1.05 ± 0.23	91.9	96.0	165 ± 56	107 ± 26
1.0	0.10	0.07	1.19 ± 0.30	1.10 ± 0.24	84.7	91.6	191 ± 46	126 ± 25
3.0	0.13	0.12	1.21 ± 0.28	1.32 ± 0.28	83.5	76.4	248 ± 33	188 ± 28
6.0	0.20	0.13	1.28 ± 0.33	1.39 ± 0.29	78.9	72.7	279 ± 59	223 ± 29
12.0	0.21	0.15	1.50 ± 0.32	1.48 ± 0.33	67.4	68.3	274 ± 55	293 ± 26

<sup>a</sup> Determined by ICP-OES. Target loading:  $w_{Pt} = 0.3$  wt.%

<sup>b</sup> Determined by TEM.

<sup>c</sup> Measured with incident light microscope.

### 5.3.3.3 Platinum Penetration Depth

Table 5.2 indicates that the penetration depth of Pt varies with impregnation time. Penetration depth for DIW printed samples with a target Pt loading of 0.3 wt.% increases from 107 μm to 293 μm when left in the impregnation solution for 0.5 h and 12 h, respectively. Analogous, the smallest penetration depth of 165 μm for BJ catalysts was achieved after 0.5 h whereas the layer thickness grew to 274 μm after 12 h.

By applying the wet impregnation method, the printed supports were prewetted with bidistilled water before the platinum sulfite salt solution was added, so that the only driving force moving the impregnation front inwards is diffusion [269, 270]. Fig. 5.11 shows light microscopic images of the impregnated catalysts where an egg-shell structure is discernible for all samples, meaning adsorption was faster than diffusion in general and/or relatively strong during wet impregnation. Fig. 5.11 shows the resulting sharp border visible in the prepared catalysts in this study. The impregnation front moves further inward with increasing impregnation duration (Table 5.2) because a longer equilibration time for diffusion of the solvated metal species towards the center is provided [87]. Thus, theoretically there is the possibility that the metal eventually approaches a uniform distribution. However, the large pellet size presumably prevents complete penetration into the center in this case.

The trends in Fig. 5.10b suggest that the impregnation front still has the potential to move further inward for DIW, implied by the continuously rising trend until 12 h in Fig. 5.10b. Contrary to this,  $d_{pen}$  for BJ reaches its maximum after 6 h at a thickness of about 280 nm. Factors leading to dissimilar penetration depths between BJ and DIW despite an identical impregnation routine are the surface morphology of the support and the porous

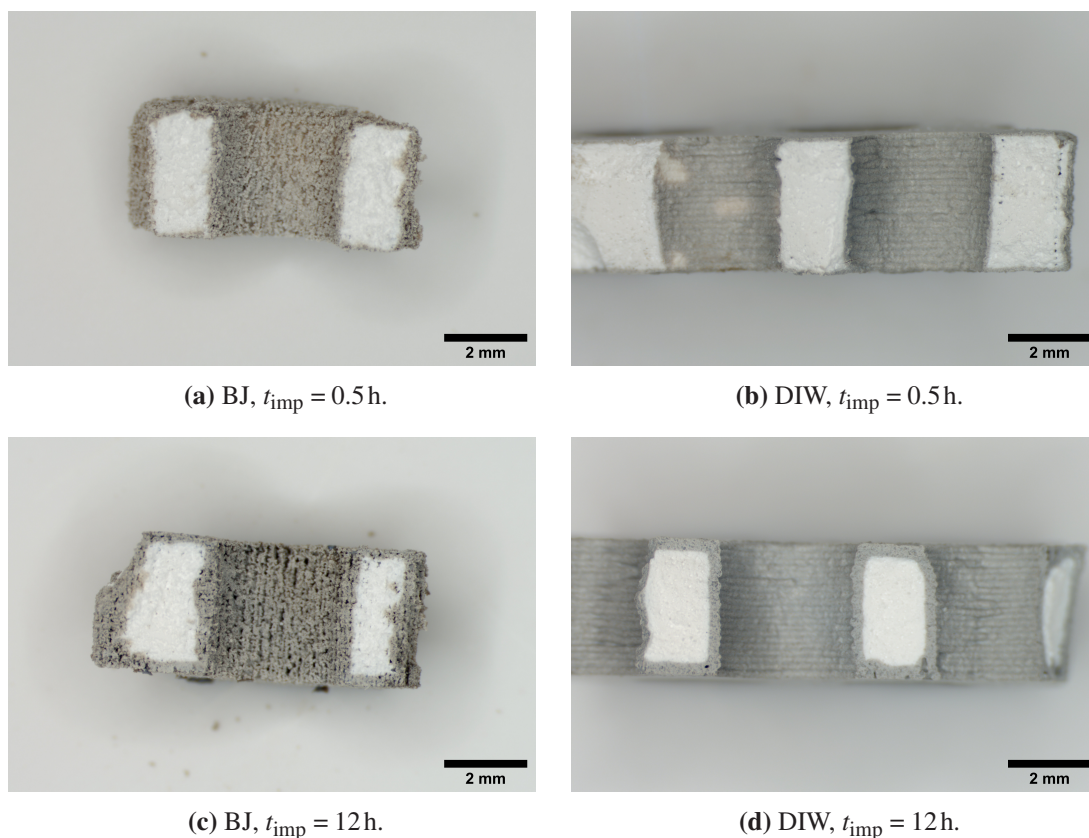


**Figure 5.11:** Light microscopic images of printed Pt/Al<sub>2</sub>O<sub>3</sub> catalysts used for Pt penetration depth analysis in dependence of the wet impregnation times  $t_{\text{imp}}$  for BJ and DIW printed supports calcined at 1100 °C. Target Pt loading  $w_{\text{Pt,target}} = 0.3$  wt.%.

structure of the printed supports. DIW shows a higher penetration depth at 12 h due to a lower BET surface area available for Pt deposition. Thus, Pt diffuses deeper into the catalyst center. Additionally, the catalyst loading is calculated mass based. As the DIW supports are double the mass of BJ parts, the amount of Pt per monolith is higher for DIW which is another reason for the deeper penetration at 12 h. These effects are ruled out at lower impregnation times, as the considerably higher macroporosity of BJ parts enables faster penetration. The impregnation front is much sharper for DIW catalysts, see Figs. 5.11b and 5.11d than for BJ. The higher voidage generated by BJ (Fig. 5.9) offers a less obstructed diffusion pathway for the dissolved Pt species, therefore resulting in a deeper impregnation with a frayed impregnation front (Figs. 5.11a and 5.11c). This effect is also visible in the higher standard deviations for  $d_{\text{pen}}$  of BJ samples, see Table 5.2.

### 5.3.4 Characterization of Catalysts Used for Testing

Pt/Al<sub>2</sub>O<sub>3</sub> catalysts which were eventually used for the catalytic tests were prepared by impregnation of printed monolithic supports which were calcined at 1100 °C. Phase determination of the alumina supports via XRD (see Supporting Information, Fig. 5.14) reveals that BJ printed supports consist of  $\alpha$ -Al<sub>2</sub>O<sub>3</sub> only, and DIW printed supports also contain mainly  $\alpha$ -Al<sub>2</sub>O<sub>3</sub> but include weak reflexes assigned to  $\vartheta$ -Al<sub>2</sub>O<sub>3</sub>. Due to slightly differing feedstock compositions, namely bayerite for BJ and boehmite for DIW, the final alumina phase composition after calcination at 1100 °C can slightly vary but is assessed to be very similar. Furthermore, the observed alumina phases correspond to reported transition temperatures found in literature [199]. Moreover, the alumina lattice structure is unaffected by 3D printing as no shifts in diffraction angle are visible.

For all dehydrogenation reactions, the total amount of platinum per monolith was held constant, independent of the printing technique. One calcined monolith fabricated via DIW has an average weight of 0.81 g whereas calcined BJ monoliths weigh 0.41 g. Based on the previous results regarding the specific surface area and weight, a target Pt loading of 0.2 wt.% for DIW and 0.4 wt.% for BJ was chosen. The Pt impregnation time of 3 h was selected such that the difference between the characterization data (see Table 5.3) was minimized or a compromise was found. Ultimately, a Pt dispersion  $D_{Pt} > 90\%$  and small metal particle sizes of about 1.1 nm were targeted for both catalysts.

**Table 5.3:** Characterization data for Pt catalysts fabricated with DIW and BJ which were used for the catalytic tests. Impregnation time  $t_{imp} = 3$  h.

AM Method	$w_{Pt}$ (wt.%)	$d_{Pt}$ (nm)	$D_{Pt}$ (%)	$d_{pen}$ ( $\mu$ m)	$S_{BET}$ (m <sup>2</sup> /g)	$\epsilon^a$ (%)
BJ	0.21 <sup>b</sup>	1.12 ± 0.26	90.4	361 ± 36	26	77
DIW	0.11 <sup>c</sup>	1.06 ± 0.26	95.0	200 ± 22	11	56

<sup>a</sup> Porosity determined by MIP

<sup>b</sup> Target loading  $w_{Pt,BJ} = 0.4$  wt.%

<sup>c</sup> Target loading  $w_{Pt,DIW} = 0.2$  wt.%

Similar to previous Pt loading determination by ICP-OES (see Section 5.3.3.1), the target values were again not met. Instead of 0.4 wt.% for BJ and 0.2 wt.% for DIW, only 0.21 wt.% and 0.11 wt.% were reached, respectively. However, for both printing methods, the loading is lower than intended by almost the same factor, so that the prerequisite of same total Pt amount of approximately 0.88 mg<sub>Pt</sub>/monolith was ensured.

The metal particles were equally well distributed on supports produced by both AM methods. The particle size is approximately 1.1 nm ( $d_{Pt,BJ} = 1.12$  nm and  $d_{Pt,DIW} = 1.06$  nm),

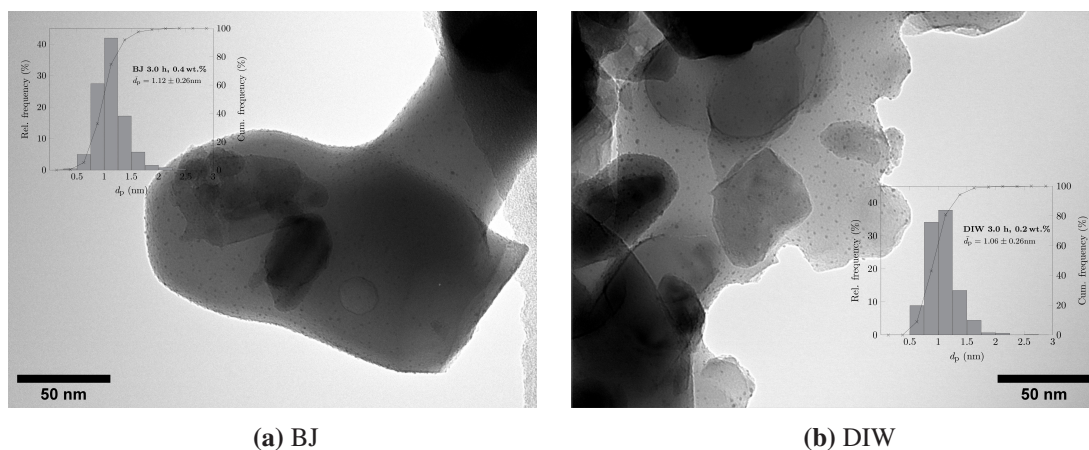


**Figure 5.12:** TEM images of the ground Pt/Al<sub>2</sub>O<sub>3</sub> monoliths used for catalytic testing, calcined at 1100 °C and wet impregnated for 3 h, including respective metal particle size distribution.

with a similar standard deviation of 0.26 nm (see Figs. 5.12a and 5.12b), indicating similar and fine Pt particle sizes achieved by wet impregnation. TEM image analysis resulted in a dispersion of 90 % and 95 % for BJ and DIW, respectively.

### 5.3.5 Catalytic test

Catalytic tests with Pt impregnated monoliths as well as ground monoliths were carried out for BJ and DIW. Fig. 5.13 compares the degree of dehydrogenation for each reaction while the productivity  $P$  for each catalyst between DoD = 10 to 60 % is displayed in Table 5.4.

#### 5.3.5.1 Test With Powder Catalysts

For the activity test with catalyst powder, the impregnated and reduced monoliths fabricated with both printing methods were ground. Powder tests were carried out as a reference to investigate the catalytic activity under exclusion of mass transfer limitations. Fig. 5.13 reveals that powder samples fabricated with both techniques show the same DoD trend and overall similar values for the DoD, suggesting that the powder catalysts perform equally well regardless of the 3D printing method used for support fabrication. Until about 2 h, a steep initial dehydrogenation rate is visible. At this point, a DoD of about 66 % is reached. After 2 h the DoD curve flattens and reaches a plateau at an apparent maximum DoD of 92 % after a reaction time of 9 h.

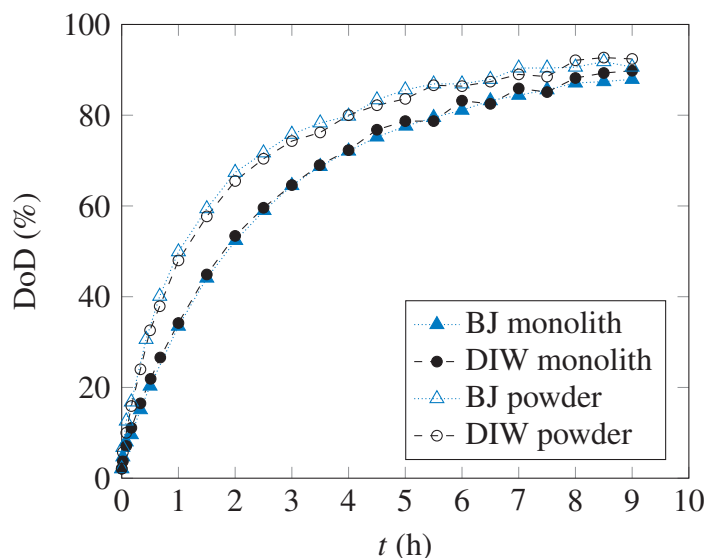


**Figure 5.13:** H18-DBT dehydrogenation over BJ and DIW printed Pt/Al<sub>2</sub>O<sub>3</sub> catalysts in a semi-batch reactor setup, tested with monolithic and powder catalysts, respectively. For each reaction, two monoliths were used.

The almost congruent dehydrogenation rates are confirmed by the results tabulated in Table 5.4 which show similar productivity values for both powder catalysts. The ground catalyst fabricated by BJ shows a productivity  $P_{\text{powder}}$  of  $4.4 \text{ g}_{\text{H}_2} \text{g}_{\text{Pt}}^{-1} \text{min}^{-1}$  and the DIW printed sample  $4.2 \text{ g}_{\text{H}_2} \text{g}_{\text{Pt}}^{-1} \text{min}^{-1}$ . Due to differences regarding the reactor setup (batch/continuous), catalyst particle size and molar ratio of Pt/H18-DBT, direct comparison of the precious metal productivity from this study with previously conducted dehydrogenation experiments involving Pt/Al<sub>2</sub>O<sub>3</sub> catalysts [94, 140, 144, 261] is hardly possible. Nevertheless, the hereby determined Pt productivity showcases the similar dehydrogenation activities of the catalyst powders stemming from differing AM processes.

### 5.3.5.2 Test with Monolithic Catalysts

Besides catalytic tests with powder, activity tests with monoliths were conducted (Fig. 5.13). After a reaction time of 2 h, DoD reaches 53 %, in contrast to 66 % which are achieved by the powder catalyst. However, after 9 h, powder and monolith samples reach a similar DoD of about 90 %. Nevertheless, the overall lower catalytic activity of the monolith samples is attributed to the mass transfer limitations affecting larger catalyst particles more significantly due to longer diffusion pathways within the catalyst particle. This explains the expected lower activity of the monolithic samples. The platinum productivity data in Table 5.4 corroborates this observation as the average productivity of the monolith samples  $P_{\text{monolith}} = 2.7 \text{ g}_{\text{H}_2} \text{g}_{\text{Pt}}^{-1} \text{min}^{-1}$  reaches 63 % of  $P_{\text{powder}}$ . Analogous to the powder tests, BJ and DIW printed monoliths show the same catalytic activity for

H18-DBT dehydrogenation. Consequently, differences resulting from the usage of two 3D printing methods such as varying penetration depths and specific surface areas (Table 5.3) do not affect the dehydrogenation rate significantly in this case.

**Table 5.4:** Platinum productivities of powder ( $P_{\text{powder}}$ ) and monolithic catalysts ( $P_{\text{monolith}}$ ), determined for the dehydrogenation reaction between DoD = 10 to 60%.

Catalyst		$P$ ( $\text{g}_{\text{H}_2} \text{g}_{\text{Pt}}^{-1} \text{min}^{-1}$ )
Powder	BJ	4.4
	DIW	4.2
Monolith	BJ	2.7
	DIW	2.7

The active layer thickness  $d_{\text{pen}} = 361 \mu\text{m}$  for BJ is larger than for DIW printed parts where the depth is  $200 \mu\text{m}$ . Auer [147] examined the influence of active layer thickness on the reactivity for H18-DBT dehydrogenation where the Pt containing layer was washcoated onto an  $\alpha\text{-Al}_2\text{O}_3$  core. Decreasing layer thicknesses from over  $200 \mu\text{m}$  to  $92 \mu\text{m}$  increased the Pt productivity, while layer thicknesses below  $92 \mu\text{m}$  lead to a productivity plateau due to the absence of mass transport limitations for very thin layers.  $90 \mu\text{m}$  was chosen to be the optimal layer depth, making a compromise between high activity and mechanical stability of the coating. Peters et al. [94] reported how different active layer thicknesses between  $24$  and  $88 \mu\text{m}$  affect pore diffusion on washcoated Pt/ $\text{Al}_2\text{O}_3$  catalysts. The kinetic regime of the dehydrogenation of perhydro-N-ethylcarbazole was limited even at very thin catalyst layers of  $24 \mu\text{m}$  so that it was concluded that pore diffusion affects the dehydrogenation in nearly all commercial catalyst pellets. Transferring those findings to the penetration depths measured in this study, the relatively deep advancement of the impregnation front for the 3D printed catalysts, especially the BJ printed parts (see Table 5.3), could negatively affect the catalytic activity of the monolith tests due to mass transfer limitations as the reactant has to travel far into the pore system or does not reach certain regions of the pellet at all. Since the catalytic performance of monolithic DIW and BJ catalysts are congruent, the deeper Pt penetration for BJ does not seem to be an influencing factor. The drawbacks caused by a larger  $d_{\text{pen}}$  are possibly compensated by a greater void fraction and macroporosity in comparison to DIW printed supports ( $\epsilon_{\text{BJ}} = 77\%$  vs.  $\epsilon_{\text{DIW}} = 56\%$ , see Fig. 5.9 and Table 5.3), leading to improved pore diffusion of the reactant. Nevertheless,  $d_{\text{pen}}$  was relatively deep for both 3D printed catalysts so that adjustment of the support properties regarding the poreSD, specific surface area as well as the impregnation duration and Pt loading could alleviate mass transfer limitations and therefore further increase catalytic activity.

## 5.4 Conclusions

Alumina supports were successfully fabricated with the extrusion-based AM technique DIW and the powder-based method BJ. Subsequently, the 3D printed supports were impregnated to obtain Pt/Al<sub>2</sub>O<sub>3</sub> catalysts, which were tested for the dehydrogenation of the liquid organic hydrogen carrier H18-DBT in a semi-batch reactor setup.

Until a calcination temperature of 1100 °C, the mechanical stability is similar for both printing methods. However, DIW parts are almost six times more robust than BJ parts when calcined at  $T_{\text{calc}} > 1100\text{ °C}$  which is attributed to the paste extrusion principle and the feedstock preparation from a ceramic paste, whereas BJ inherently generates larger intraparticle voids. Further catalyst characterization revealed finely dispersed Pt particles in all cases. Increasing impregnation duration led to deeper penetration of Pt into the monolith of up to 293 μm for DIW based carriers after 12 h. Despite the differences, catalytic tests revealed that both catalysts perform equally well, regardless of the chosen printing method and the resulting structural variations as the Pt productivities of  $2.7\text{ g}_{\text{H}_2}\text{g}_{\text{Pt}}^{-1}\text{min}^{-1}$  were almost equal for BJ and DIW.

This study demonstrates the importance of catalyst shape and showcases how the advantages of two different additive manufacturing techniques can be exploited to generate tailor-made monolith or pellet geometries, benefiting individual process requirements. Insights from lab-scale catalytic tests using 3D printed catalyst packings can be used to derive improvements for larger industrial-scale chemical reactors. As an outlook, the potential of AM for catalysis can be further exploited by combining it with CFD tools to investigate the influence of differing pellet geometries which can be rapidly realized by 3D printing, enabling quick process adaptations. DIW generally facilitates lattice- or woodpile-like structures with a high surface-to-volume-ratio for enhanced metal deposition, whereas BJ is more suitable to generate complex channel geometries for improved fluid flow. Since AM of catalysts is still in its early stages, the characterization results provide practical comparative AM guidelines for alumina-based catalysts in terms of surface area, porosity, stability, and impregnation behavior. Moreover, findings in this study generate additional insights into adequate additive processing steps and conditions to achieve active catalysts, which paves the way for smart chemical process development and reactor design by rapid prototyping.

## 5.5 Supporting Information

### 5.5.1 Alumina Phase Determination

Phase determination of the 3D printed alumina supports was obtained via XRD analysis (Empyrean, Malvern Panalytical, UK). Cu-K $\alpha$  radiation ( $\lambda = 1.54056 \text{ \AA}$ ) and a monochromator were employed to scan the samples applying a step size of  $0.007^\circ$  and 70 steps/min from  $2\theta = 5$  to  $90^\circ$ . Fig. 5.14 compares the diffraction pattern of DIW and BJ printed supports calcined at  $1100^\circ\text{C}$ , as used for the LOHC dehydrogenation test. The reflex patterns reveal that the BJ printed support contains only  $\alpha\text{-Al}_2\text{O}_3$  whereas the DIW support consist of mainly  $\alpha\text{-Al}_2\text{O}_3$  with weak reflexes of  $\vartheta\text{-Al}_2\text{O}_3$  phase. The two applied additive manufacturing techniques do not result in an alteration of the alumina structure, since the preparation of the raw materials only involve powder mixing. Moreover, thermal treatment in form of calcination and reduction was equal to conventional catalyst preparation, meaning that the alumina lattice structure is unaffected by processing by 3D printing which is also visible by no shifts in diffraction angle.

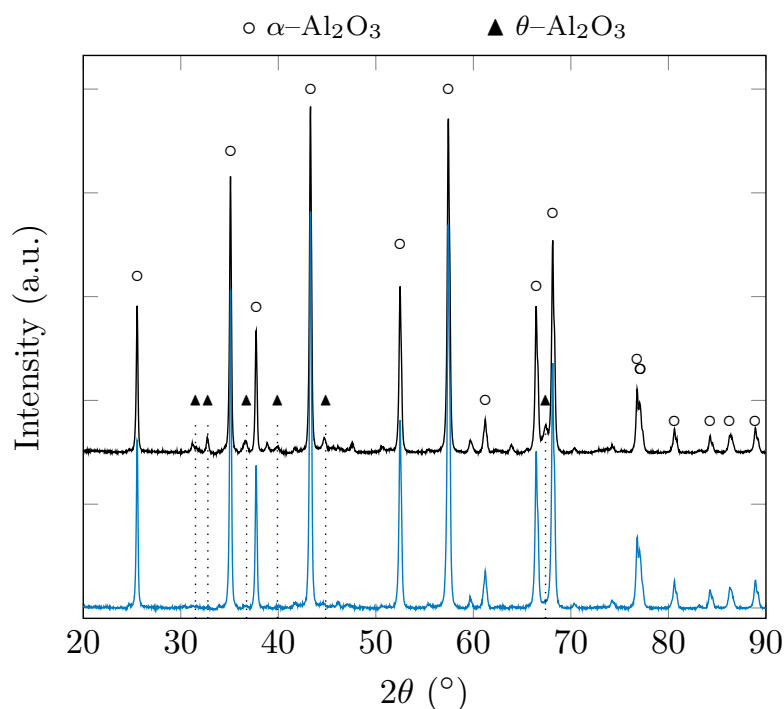


**Figure 5.14:** XRD diffraction pattern of alumina supports, printed by BJ (blue) and DIW (black). (Reference patterns:  $\alpha\text{-Al}_2\text{O}_3$ : ICSD 01-075-1862,  $\vartheta\text{-Al}_2\text{O}_3$ : PDF 00-023-1009).

## 5.5.2 Particle Size of Catalyst Powder for LOHC Dehydrogenation

Fig. 5.15 shows the particle size distribution of the used powder material. The particle

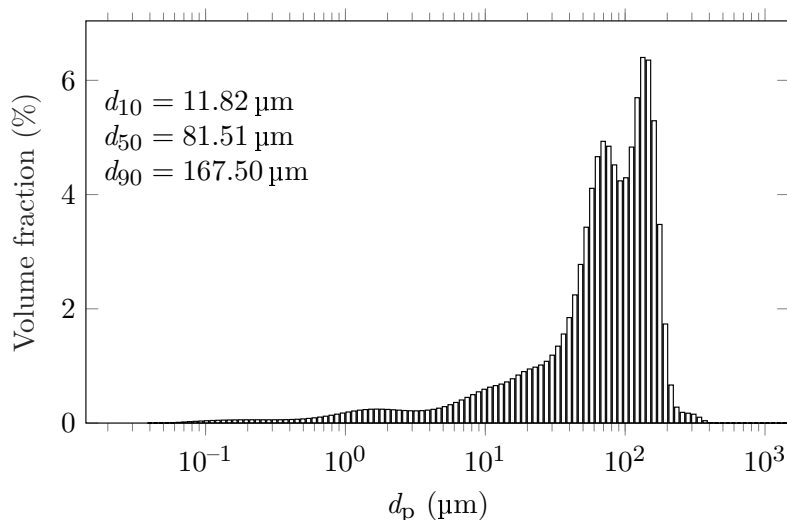


**Figure 5.15:** Particle size distribution of powder used for LOHC dehydrogenation, prepared by grinding of whole monoliths.

size distribution of the ground monoliths used for the LOHC dehydrogenation test was determined by a laser diffraction particle size analyzer (LS 13 320 Particle Size Analyzer, Beckman Coulter, USA). The sample was measured after dispersion in distilled water as this represents the reaction conditions best (solid catalyst particles in liquid reactant).  $d_{10}$ ,  $d_{50}$ ,  $d_{90}$  values of the powder are 11.82  $\mu\text{m}$ , 81.51  $\mu\text{m}$  and 167.50  $\mu\text{m}$ , respectively. The mean diameter is 89.20  $\mu\text{m}$ .

## 5.5.3 Pt Particle Size Distribution by TEM

### 5.5.3.1 Binder Jetting

Figs. 5.16 and 5.17 show the particle size distribution of the Pt nanoparticles on the 3D printed Pt/Al<sub>2</sub>O<sub>3</sub> catalysts. A minimum of 460 particles was counted on several micrographs taken on different zones of the TEM grid.

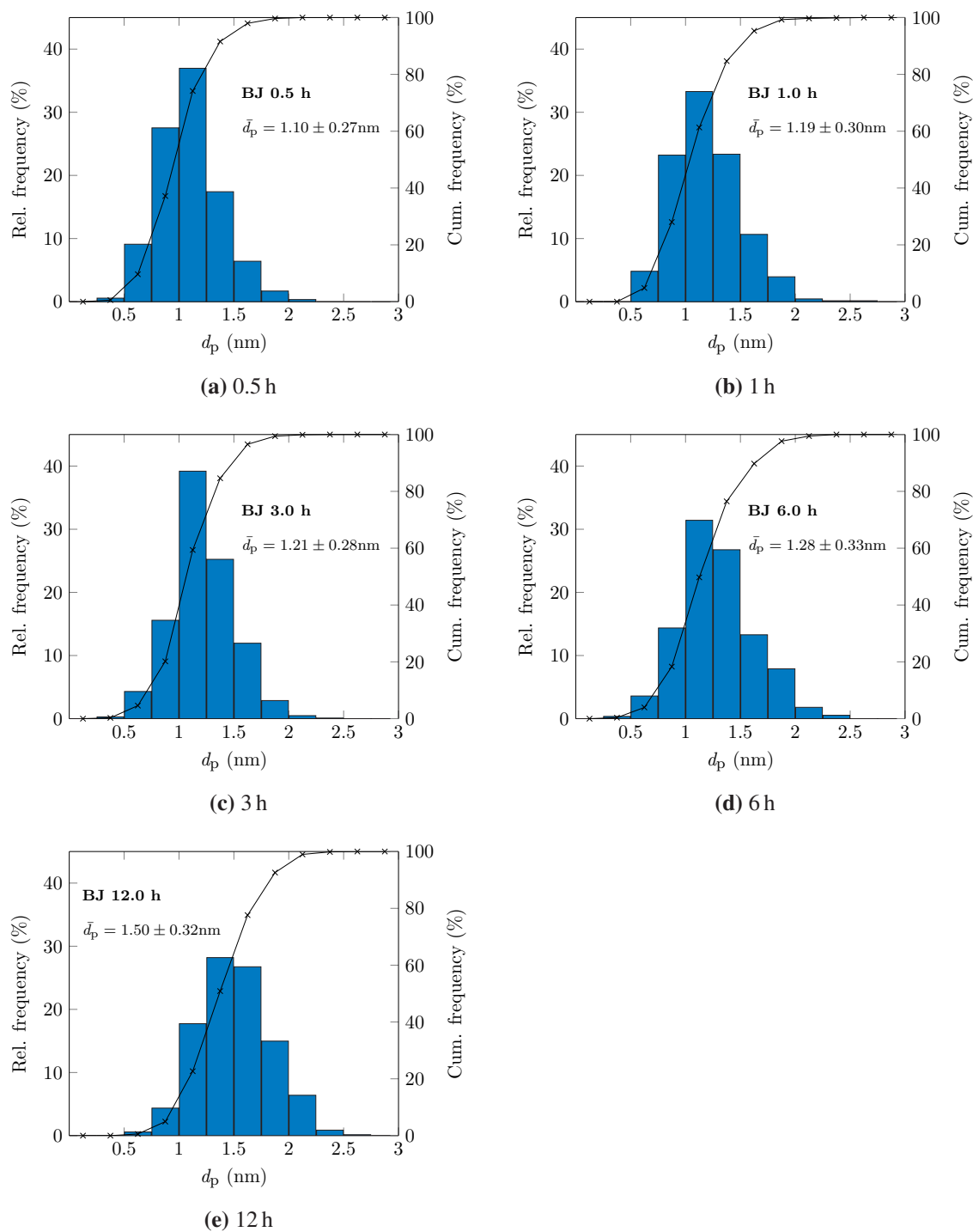


**Figure 5.16:** Pt particle size distribution by TEM of BJ printed Pt/Al<sub>2</sub>O<sub>3</sub> catalysts which were wet impregnated for varying durations.

### 5.5.3.2 Direct Ink Writing

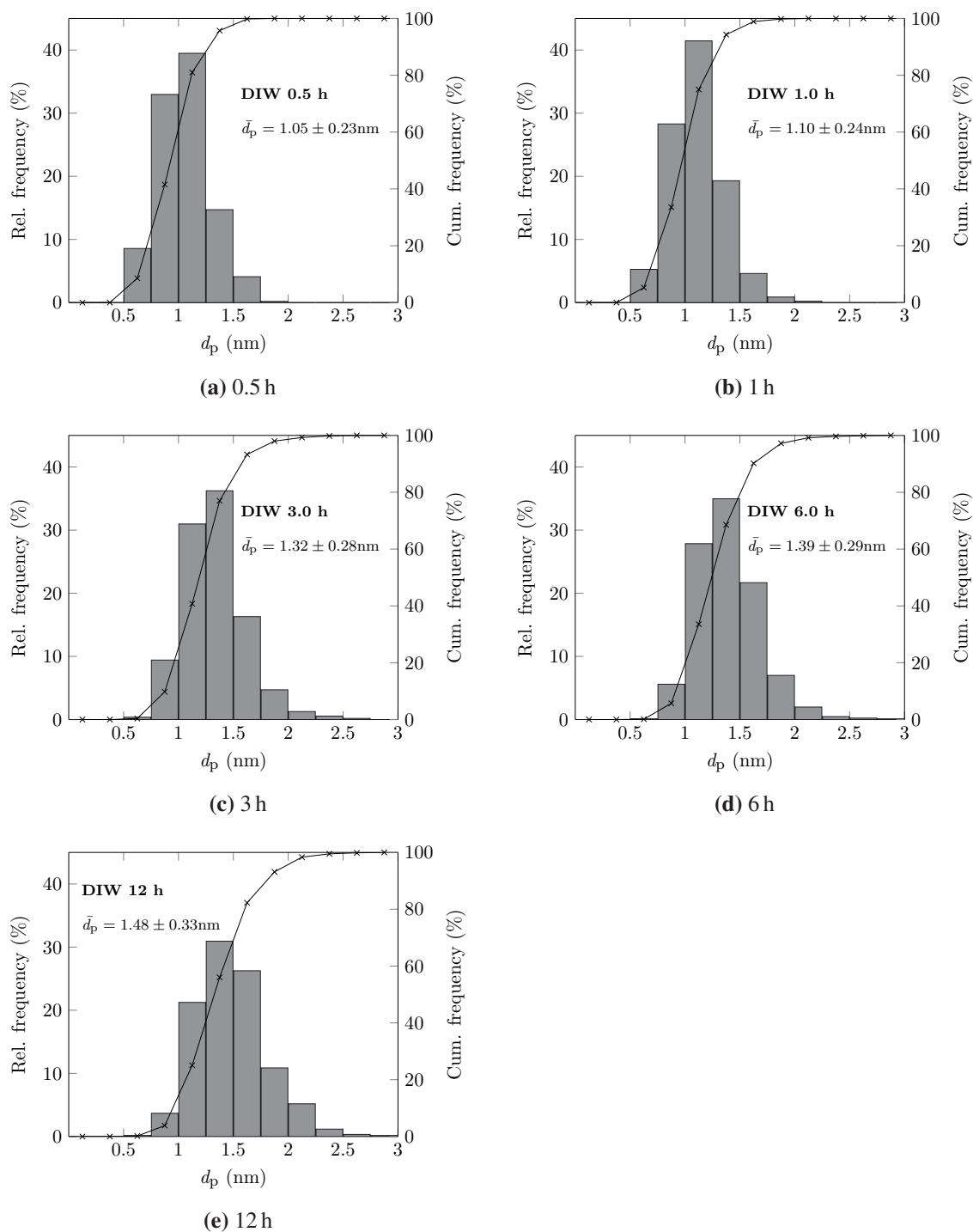


**Figure 5.17:** Pt particle size distribution by TEM of DIW printed Pt/Al<sub>2</sub>O<sub>3</sub> catalysts which were wet impregnated for varying durations.

# 6 3D Printed Co-Precipitated Ni-Al CO<sub>2</sub> Methanation Catalysts by Binder Jetting: Fabrication, Characterization and Test in a Single Pellet String Reactor

---

**This chapter was published in similar form in:**

H. M. Bui, P. F. Großmann, T. Gros, M. Blum, A. Berger, R. Fischer, N. Szesni, M. Tonigold, O. Hinrichsen, "3D Printed Co-Precipitated Ni-Al CO<sub>2</sub> Methanation Catalysts by Binder Jetting: Fabrication, Characterization and Test in a Single Pellet String Reactor", *Applied Catalysis A: General*, **2022**, 118760, DOI 10.1016/j.apcata.2022.118760.

©2022 Elsevier B.V. All rights reserved.

---

## Abstract

The binder jetting 3D printing technique was used to fabricate spherical Ni-Al CO<sub>2</sub> methanation catalysts from co-precipitated catalyst precursor powder. Catalysts with different nickel loadings were prepared by varying the molar Ni/Al ratio (1/1, 2/1, 3/1, 5/1) during precipitation or the amount of admixed precursor powder (10, 20, 30 wt.%) for printing. XRD and TG analysis revealed phase composition and reducibility characteristics analogous to conventionally prepared Ni-Al catalysts. TEM displayed nickel particle sizes as small as 3.9 nm with a Ni dispersion of up to 13.4 % determined by H<sub>2</sub> chemisorption. Moreover, meso- and macroporous catalyst pellets were generated with a specific surface area of up to 192 m<sup>2</sup>/g<sub>cat</sub>. The catalysts NiAl11-20, NiAl21-20 and NiAl51-20 were exemplarily tested in a single pellet string reactor where CO<sub>2</sub> conversions of up

to 99 % and a high selectivity towards CH<sub>4</sub> was observed at  $p_{\text{tot}} = 9$  bar upon reaching thermodynamic equilibrium.

## 6.1 Introduction

The intermittency of renewable energy sources and seasonal as well as regional changes in human energy demand brings the focus to the issue of finding reliable, flexible and large-scale storage systems for surplus electricity to balance out a mismatch between power supply and demand. While numerous mechanical, electrical, electrochemical and thermal storage technologies already exist, chemical storage of renewable energy is another viable alternative. Power-to-X (PtX) technologies, in this particular case Power-to-Methane, is a promising option which has gained increased attention due to the possibility to exploit an already existing gas grid and distribution network while simultaneously contributing to the reduction of CO<sub>2</sub> emissions [271–273]. Electricity generated from surplus renewable energy produces H<sub>2</sub> via water electrolysis. Hydrogen is subsequently converted to the value-added chemical CH<sub>4</sub> using CO<sub>2</sub> which can be ideally recovered from industrial process streams [274], power plants or biomass processes [275].

Key component for the efficiency of the PtX technology is the catalyst design for the methanation step. Sabatier and Senderens discovered the methanation reactions in 1902 [108] where CO (Reaction R1) and CO<sub>2</sub> (Reaction R2) were converted to methane over a nickel catalyst. The water-gas shift reaction (R3) connects the two aforementioned methanation reactions, converting CO to CO<sub>2</sub>. All three reactions are exothermic at standard conditions. The morphology and dispersion of the active species as well as the catalyst support selection along with the preparation route substantially affect the stability, selectivity and activity of the catalyst. Moreover, an adequate catalyst packing geometry assures advantageous mass and heat transfer for reaction systems on an industrial scale, a pivotal factor particularly for exothermic reactions.

This study uses binder jetting (BJ) as a novel technology to 3D print Ni-Al catalysts and characterizes the fabricated catalysts in order to assess their suitability for CO<sub>2</sub> methanation. Like all additive manufacturing techniques, BJ uses a layer-wise working principle. Layers of loose powder are distributed on top of each other, while an inkjet print head deposits a printing liquid in between the layering steps in order to selectively bind the particles together. This way, a three-dimensional body is generated [276]. The layer height has to be chosen such that a sufficient liquid saturation between the layers is achieved for layer adhesion. An inappropriate choice in layer thickness can lead to insufficient part stability when defined too large, or to dimensional inaccuracy due to

blinder bleeding into the surrounding powder when the layer height is defined too small [277].

### 6.1.1 Additive Manufacturing of Heterogeneous Catalysts

In a packed bed reactor, the catalyst shape significantly influences the overall performance. Short diffusion paths within the catalyst particle, low pressure loss and appropriate mass and heat transfer properties directly correlate with the size, surface area, and voidage of a catalyst packing. Conventional catalyst shaping techniques include pelleting, extrusion and granulation [11, 12] which are limited regarding shape complexity. Thus, additive manufacturing (AM) is an emerging fabrication technology which has gained increased attention in the field of catalyst development during the last decade [44].

In this study, catalysts were manufactured using a direct 3D printing approach. In contrast to indirect printing strategies where a polymeric mold is printed which is subsequently filled with catalytic material and burnt off [54–56], direct printing straightforwardly produces shapes without a mold. On top, the hereby applied approach does not fabricate a support for subsequent impregnation [58, 71, 79, 278] but includes the active species directly in the printing feedstock, therefore saving the post-printing deposition of catalytically active species. In so far published studies extrusion-based principles (Direct Ink Writing/Robocasting) have been the method of choice to fabricate solid catalyst structures due to the relatively straightforward development process [68, 73, 82, 279]. Until now, the powder-based printing technology has rarely been exploited to print metal oxide catalyst supports [13, 173–175] while no study has been published for directly printed active catalysts via Binder Jetting. This study expands the printing procedure developed by Bui et al. [13] where porous alumina supports were printed under low-temperature conditions by adding an active catalytic component into the printing powder.

### 6.1.2 Single Pellet String Reactor

On a laboratory scale, in most cases intrinsic catalytic testing for preliminary screening is done in an isothermal plug flow reactor (PFR) where very small catalyst particles are measured [280]. A critical factor in catalyst testing is collecting data while excluding transport phenomena due to the flow, the catalyst and the reactor type [281]. Oftentimes it is desirable to evaluate the catalytic performance in a commercial or large scale context at a small scale [282]. In this case, direct scale up from lab-scale testing of real-sized catalyst shapes without having to crush the pellet is the main objective. At the same time, identical

space velocity, temperature, pressure, feed composition should be maintained while the catalyst bed is significantly downscaled. In the 1970s, Scott et al. [283] proposed the concept of a single pellet string reactor (SPSR) in which uniform spherical pellets are stacked on top of each other in a tube with a inner diameter only slightly larger than the particle diameter. It was concluded that the SPSR closely approximates the behavior of a fixed bed reactor (FBR) due to similar axial dispersion and external mass transfer coefficients. In the past, the SPSR concept was employed for the determination of mass transfer coefficients [284–287]. SPSRs attracted moderate attention temporarily but seem to gain increased interest as a topic of research [288–290].

### 6.1.3 Motivation

This study applies a powder-based 3D printing technology to fabricate tailor-made solid catalysts where the active material is directly integrated in the printing feedstock in contrast to first printing a metal oxide support for subsequent impregnation with catalytically active material. The binder jetting technique was employed to manufacture Ni-Al CO<sub>2</sub> methanation catalysts on the basis of co-precipitated mixed metal oxides. Co-precipitation was exploited because high metal loadings and dispersion can be achieved [291, 292]. The emphasis of this study lies on the fabrication and characterization of the printed Ni-Al catalysts. A catalytic test with spherical Ni-Al catalysts was conducted in a single pellet string reactor as a proof-of-concept in order to assess the feasibility of the hereby developed direct 3D printing strategy for heterogeneous catalysts. The concept combines the freedom of catalyst shape design offered by additive manufacturing and the possibility to test the fabricated product in a reactor setup which enables destruction-free testing of whole catalyst pellets.

## 6.2 Experimental

### 6.2.1 Co-precipitation of Ni-Al Catalyst Precursor

Co-precipitated nickel-alumina precursors with varying Ni/Al molar ratios were prepared according to a synthesis route already described elsewhere [293–295]. 1 L of distilled water was placed in a 3 L double-walled glass vessel with flow breakers which was heated to 30 °C and stirred at 150 rpm. The precipitating agent consisting of an equimolar mixture of 1 M Na<sub>2</sub>CO<sub>3</sub> (Sigma-Aldrich) and 1 M NaOH (Merck KGaA) was continuously added by an autotitrator (716 DMS Titrino, Metrohm GmbH & Co. KG) to maintain pH 9 during

the entire precipitation process. 300 mL of an aqueous solution of 1 M  $\text{Ni}(\text{NO}_3)_2 \cdot 6\text{H}_2\text{O}$  (Merck KGaA) and 1 M  $\text{Al}(\text{NO}_3)_3 \cdot 9\text{H}_2\text{O}$  (Merck KGaA) was mixed according to the desired Ni/Al molar ratios and dosed dropwise into the vessel by a peristaltic pump (medorex TL, MDX Biotechnik GmbH). After complete dosing of the metal nitrate solution, the precipitate was aged in the mother liquor for 18 h at 30 °C under constant stirring. The slurry was subsequently filtered and washed repeatedly with distilled water until pH 7 was reached. The resulting filter cake was dried overnight at 80 °C. Precursors with the molar Ni/Al ratios of 1/1, 2/1, 3/1 and 5/1 were prepared, denoted as NiAl11\_p, NiAl21\_p, NiAl31\_p and NiAl51\_p, respectively.

## 6.2.2 Catalyst Preparation

The feedstock preparation and printing procedure followed the procedure presented in a previously published paper [13]. The bayerite component in the printing powder was hereby partly substituted by the priorly prepared Ni-Al precursor.

### 6.2.2.1 Printing Feedstock

The Ni-Al precursor was thoroughly ground with a pestle and mortar. The final print bed material consisted of 7 wt.% Actilox S40 boehmite (Nabaltec AG), 20 wt.% polyvinylpyrrolidone (PVP) binder Sokalan K17P (BASF SE, Germany) as well as varying amounts of Pural BT bayerite (Sasol GmbH) and Ni-Al precursor. The ground Ni-Al precursor powder could not be used on its own as printing feedstock due to its cohesiveness, so that Pural BT bayerite powder was used to dilute the catalyst material so that sufficient flowability for printing was given. Actilox S40 boehmite was used to increase the powder bed density due to its relatively fine particle size distribution (PSD). Fine particles are supposed to fill the interstitial voids between coarser particles to achieve a greater packing density in comparison to a unimodal PSD [190]. PVP acted as the solid in-bed binder which binds the powder bed components upon contact with the aqueous printing liquid. Due to its hygroscopic and binding properties PVP in combination with the printing liquid was suitable to generate an acceptable green part stability.

The total Ni loading was varied by changing the Ni/Al molar ratio during co-precipitation but also by adding different amounts of precursor powder. For example, a sample containing 20 wt.% NiAl21\_p is denoted as NiAl21-20. In total, six catalysts were fabricated. Four of the six samples differ in the molar Ni/Al ratio but all contain 20 wt.% precursor powder (NiAl11-20, NiAl21-20, NiAl31-20, NiAl51-20). Three samples differ in the

amount of added precursor powder (10, 20 and 30 wt.%) but contain the same precursor NiAl51\_p (NiAl51-10, NiAl51-20, NiAl51-30). The printing powder composition of each prepared catalyst is broken down in Table 6.1. All powdery materials were prepared by blending them to a homogeneous mixture in a SpeedMixer (Hauschild GmbH & Co KG) in four one-minute cycles with 1200 rpm.

**Table 6.1:** Prepared catalysts and their printing powder composition.  $w_{\text{Alumina}}$  is the total amount of bayerite and boehmite powder in the mixture.

Catalyst	$w_{\text{Precursor}}$ (wt.%)	$w_{\text{Alumina}}$ (wt.%)	$w_{\text{Binder}}$ (wt.%)
NiAl11-20	20	60	20
NiAl21-20	20	60	20
NiAl31-20	20	60	20
NiAl51-20	20	60	20
NiAl51-30	30	50	20
NiAl51-10	10	70	20

The printing liquid formulation was identical to the prepared particle-loaded ink in reference [13]. The aqueous ink consisted of 7 wt.% colloiddally dispersible boehmite particles and rheological additives, namely 10 wt.% isopropyl alcohol and 10 wt.% 1,4-butanediol (Merck KGaA). The main rheological parameters for a flawless and defect-free ejection of ink from the inkjet printhead are surface tension and viscosity. The former is adjusted by addition of isopropyl alcohol and the latter by 1,4-butanediol. The described ink composition generated a surface tension of 35.4 mN/m and a dynamic viscosity of 1.99 mPa s which works well with the used piezo printhead.

### 6.2.2.2 Printing Procedure

All parts were printed with a layer height of 40  $\mu\text{m}$ . Fig. 6.1 shows the general generative manufacturing process of the 3D printed Ni-Al catalysts. The steps in Fig. 6.1 are explained hereafter:

- 1.) A digital model of the catalyst pellet is generated with a CAD software and converted to an stl file which can be processed by the 3D printer.
- 2.) After printing, the printed body is still embedded in the print bed (Fig. 6.1, step 2). The complete print bed is extracted from the 3D printer and transferred to a drying oven to establish the solidifying effect of the PVP binder. The resulting green part

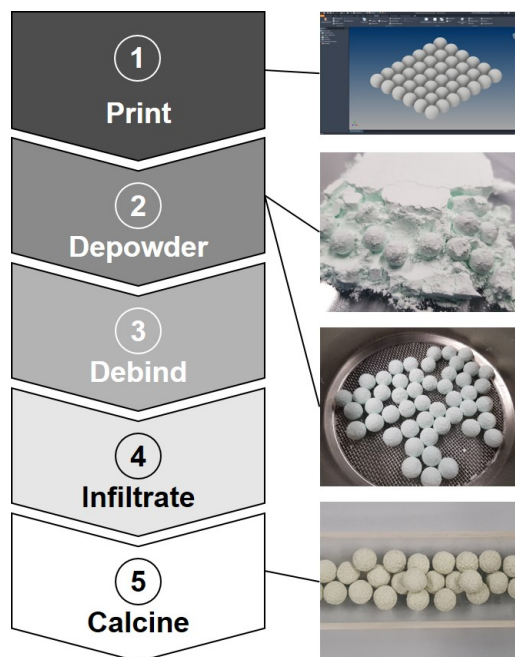


**Figure 6.1:** Catalyst manufacturing scheme for Ni-Al catalysts via Binder Jetting.

(pre-calcined state) is subsequently removed from the surrounding unbound powder by blowing with compressed air to expose the actual printed part.

- 3.) The depowdered green body still contains the PVP binder which has to be removed completely. The debinding process, which at the same time acts as a first calcination step, decomposes the PVP by thermal treatment at 600 °C for 2 h in a muffle furnace.
- 4.) Debinding significantly destabilizes the printed part by generating additional porosity. Infiltrating the debinded parts with an aqueous boehmite slurry is a crucial step to restore and increase part stability by introducing additional particles into the porous particle framework.
- 5.) A second calcination step is needed to transform the introduced boehmite in the infiltrated parts to  $\gamma\text{-Al}_2\text{O}_3$  at 600 °C for 4 h in a tube furnace.

Per Ni-Al sample, two print jobs were executed. The first one comprised 24 cylindrical pellets ( $d = h = 6$  mm) and the second one 42 spherical pellets with a green part diameter of 9.2 mm. All prints were done on a custom-built binder jetting printer (3d-figo GmbH, Germany) equipped with a drop-on-demand shear-mode piezo inkjet printhead (508GS, Seiko Instruments GmbH) moving with a speed of 44.2 mm/s.

### 6.2.3 Catalyst Characterization

The Ni loading of the precursor, printed green part, debinded and calcined samples were determined by atom absorption spectroscopy (AAS) (AA280FS, Varian) by dissolution in concentrated H<sub>2</sub>SO<sub>4</sub> and HNO<sub>3</sub>.

The particle size distribution (PSD) of the printing powder was analyzed via laser diffraction using the dry powder module (LS 13 320 Particle Size Analyzer, Beckman Coulter) where dry powder is dispersed in a vacuum-induced stream of air on the way to the analysis chamber in order to avoid particle agglomeration during analysis.

Mechanical stability of the cured green parts and the calcined samples were tested with a hardness tester with integrated size measurement (MultiTest 50, Dr. Schleuniger Pharmatron) by uniaxial compression tests. The tested geometries were cylinders measuring 6 mm in diameter and height because for crushing strength calculation a defined geometry was required. Testing direction was perpendicular to the cylinder axis, the bracket moving speed was set to 2 mm/s. The compressive strength  $\sigma_{\text{comp}}$  was calculated based on the fracture load  $F$  using equation 3.19.

Phase determination of the co-precipitated precursor material as well as the calcined and reduced samples were obtained via XRD analysis (Empyrean, Malvern Panalytical, UK). Cu-K $\alpha$  radiation ( $\lambda = 1.54056 \text{ \AA}$ ) and a monochromator were employed to scan the samples applying a step size of  $0.007^\circ$  and 70 steps/min from  $2\theta = 5$  to  $90^\circ$ . The printed cylindrical catalyst pellets were ground prior to the XRD measurement. XRD analysis of the previously in the H<sub>2</sub> chemisorption instrument reduced samples was executed under inert atmosphere by preparation in a glovebox using Kapton tape sample holders for air-sensitive samples and otherwise identical measuring parameters. Furthermore, the Ni crystallite size  $d_C$  was estimated from the full-width at half-maximum (FWHM) values using the Scherrer equation (see Eq. 3.3) for the (200) Ni reflex at  $2\theta = 51.8$  to  $51.9^\circ$  [296].

N<sub>2</sub> physisorption at 77 K (Nova 4200e, Quantachrome Instruments) was used to determine the specific surface area  $S_{\text{BET}}$  of the Ni-Al catalyst after every fabrication step. Sample pretreatment comprised degassing under vacuum at 120 °C for 3 h.  $S_{\text{BET}}$  was determined according to the method of Brunauer, Emmett, and Teller (BET) and calculated between  $0.05 \leq p/p_0 \leq 0.3$ . Moreover, the Barrett, Joyner, Halenda (BJH) method was applied to analyze the pore size distribution (poreSD) using the desorption branch of the isotherm. Data points were collected from  $p/p_0 = 0.01 - 0.999$ . No degassing was carried out prior to the measurement of reduced samples as they were handled in the glovebox and transferred under inert conditions.

H<sub>2</sub> chemisorption was carried out on an autosorb iQ (Quantachrome Instruments) at 35 °C after activation for 5 h in 5 % H<sub>2</sub> in Ar with a linear heating rate of 2 K/min to 480 °C. Both spherical and cylindrical Ni-Al pellets were used for this analysis. The active metal surface area  $S_{Ni}$  and the Ni dispersion were calculated by extrapolating the adsorption isotherm to zero pressure. A dissociative H<sub>2</sub> adsorption mechanism was assumed where one H atom adsorbs on one Ni atom. The metal dispersion  $D_M$  was calculated according to Eq. 3.13 with the adsorption stoichiometry  $S = 2$ .

In addition to the pore size measurement with N<sub>2</sub> physisorption, the poreSD of the printed spherical calcined samples was determined with mercury intrusion porosimetry (MIP) (AutoPore 9600, Micromeritics Instrument Corporation). Per measurement, one spherical catalyst pellet of 175 to 200 mg was added to the penetrometer comprised of a 5 mL bulb volume and 0.392 mL stem volume, resulting in a stem usage of 46 to 57 %. To reduce the influence of the hydrostatic pressure of mercury in the low pressure region, the pressure range of 0.5 to 45 psi was measured in a horizontal penetrometer position, while the pressure range from 45 to 61 000 psi was obtained in vertical penetrometer position. The pressure steps were chosen to achieve an even spacing on the logarithmic scale with 25 points per decade in a pressure range between 0.5 and 4000 psi and with 40 points per decade in a pressure range between 4000 and 61 000 psi. The latter pressure range with higher resolution correlates to pore diameters of 53.3 to 3.5 nm, respectively. The pressure at each pressure step was held constant until the intrusion rate was below 0.01 μL/(g s). To convert the pressure  $p$  to a pore diameter  $d_p$ , Washburn's equation was applied (Eq. 3.18).

Transmission electron microscopy (TEM) measurements were performed on a JEOL JEM 1400 plus instrument at an acceleration voltage of 120 kV to determine the mean metal particle diameter  $d_M$  and the resulting metal dispersion. Before analysis, the reduced Ni-Al samples were prepared in a glovebox. The sample material, which was recovered from the TGA reduction experiment using spherical pellets, was finely ground, suspended in absolute EtOH (Sigma-Aldrich) and finely dispersed. After sedimentation of larger particles, two drops of the suspension were deposited onto a Multi A copper grid (Quantifoil Micro Tools GmbH) and left to dry. The metal particle diameter  $d_M$  was manually measured using the image processing software imageJ. For each sample, a minimum of 100 particle size measurements were performed on several micrographs taken on different zones of the TEM grid. The metal dispersion  $D_M$  is indirectly proportional to  $d_M$  and is determined according to Eq. 3.15.

The degree of reduction  $d_{red}$  with varying Ni loading was calculated based on thermogravimetric analysis (TGA, SENSYS evo TG-DSC, SETARAM Instrumentation) [159]. The spherical calcined catalyst pellet was ground and about 50 mg placed in the TGA

crucible. In a first step, the sample was heated at 480 °C for 5 h in pure N<sub>2</sub> and then cooled down to room temperature. The second step comprised heating to 480 °C with a rate of 2 K/min and the subsequent in-situ reduction in 5 % H<sub>2</sub> in N<sub>2</sub>. The temperature was held for 5 h to replicate the conditions during catalytic testing in the SPSR. The degree of reduction  $d_{\text{red}}$  was subsequently calculated using Eq. 3.14. It was assumed that the entirety of  $\Delta m_{\text{O}}(t)$  and  $m_{\text{O,initial}}$  stemmed from NiO.

## 6.2.4 Catalytic Test

Three test reactions were conducted in a SPSR setup as a proof-of-concept to analyze the catalytic activity of Binder Jet 3D printed Ni-Al catalysts from co-precipitated powder feedstock. The samples NiAl11-20, NiAl21-20 and NiAl51-20 were exemplarily chosen and tested to investigate the CO<sub>2</sub> conversion and CH<sub>4</sub> yield with increasing Ni/Al ratio. Fig. 6.2 illustrates the general scheme of the SPSR used for the tests. The setup consisted

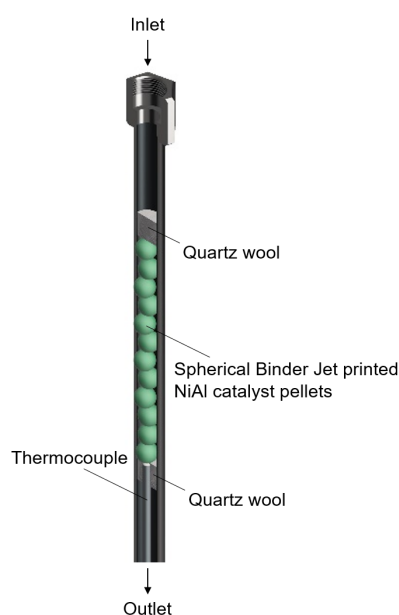


**Figure 6.2:** Scheme of the SPSR setup, packed with 12 printed spherical Ni-Al catalyst pellets.

of a glass-lined stainless steel tube reactor with an inner diameter of 9.5 mm. 12 spherical calcined catalyst pellets with an average diameter of 8.2 mm and weighing 2.4 g in total were stacked on top of each other to give a catalyst bed with a length of approx. 10 cm.

The pellet string was fixated at both ends with a plug of quartz wool. The stoichiometric feed gas mixture composition of CO<sub>2</sub>/H<sub>2</sub>/Ar/N<sub>2</sub> = 2/8/9/1 (purity of all gases 5.0) was supplied by a gas mixing unit, adjusted by calibrated mass flow controllers and enters

the reactor at the top. A K-type thermocouple contacts the pellets at the bottom closely monitoring the temperature in the reactor.  $N_2$  served as an internal standard for later quantitative analysis. The product gas stream was analyzed by a gas chromatograph (Agilent 7820A, Agilent Technologies) comprising two thermal conductivity detectors, a packed molecular sieve 5 Å column (Sigma-Aldrich) for  $H_2$ , Ar,  $N_2$ ,  $CH_4$  and CO quantification and a Porapak-N column (Sigma-Aldrich) for  $CO_2$  and  $H_2O$  quantification.

Prior to the activity test, reduction of the catalyst with 5%  $H_2$  in Ar was performed. With a heating rate of 2 K/min the reducing environment was held at 480 °C for 5 h. Subsequently, the reactor was cooled down to 250 °C and flushed with Ar until further testing was conducted. For catalytic testing, the reactor was flushed with feed gas ( $\dot{V} = 125$  sccm) and pressurized to 9 bar. The catalyst performance was then measured in the range from 175 to 480 °C with a repeating measurement at 250 °C to rule out catalyst deactivation.

## 6.3 Results and Discussion

### 6.3.1 Particle Size Distribution of Printing Powder

The PSD of the printing powder plays a crucial role for the feasibility of the 3D printing process as well as the final part integrity. The volumetric percentage of the PSD for the synthesized Ni-Al precursor, the printing powder composition without the precursor (bayerite + binder) and the resulting combination of both materials (printing powder = Ni-Al precursor + bayerite + binder) is shown in Fig. 6.3. Most of the catalyst precursor

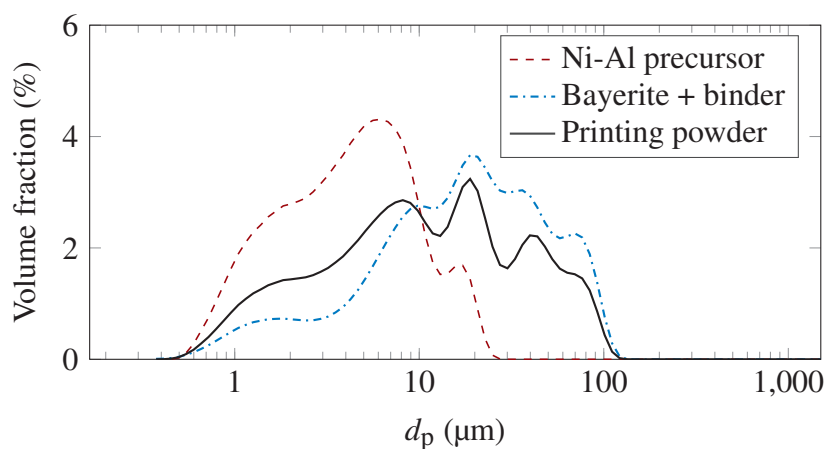


**Figure 6.3:** PSD of the co-precipitated Ni-Al precursor powder (red, dashed), alumina and binder powder (blue, dashdotted), and final printing powder material (black, solid line).

particles range at a diameter of about  $d_p = 6\ \mu\text{m}$ . The printing layer thickness of  $40\ \mu\text{m}$  should not be exceeded excessively as powder particles would not be incorporated into the print bed completely. Thus, the precursor material was ground fine enough for use in the printing process. Combined with the remaining solid components, the resulting PSD curve becomes multimodal with main peaks at about  $9\ \mu\text{m}$ ,  $11\ \mu\text{m}$  and  $40\ \mu\text{m}$ . The powder spreaded smoothly with the leveling roller, yielding a smooth printing surface. A single layer ink deposition gave adequate liquid saturation so that single layers adhere to each other sufficiently. Therefore, the powder composition fulfills the requirements for successful Binder Jetting.

The nickel loading of the printed catalyst could be maximized by omitting the admixing of alumina powder. This way, the binder PVP would be the only additional compound so that the final catalyst consists of pure co-precipitated Ni-Al catalyst material. However, poor flowability due to the agglomeration of the very fine precipitate particles prevented the application of this strategy. Therefore, adjustment of the precursor particle size distribution is necessary to facilitate printing without additional alumina powder.

### 6.3.2 Nickel Loading

The Ni and Al weight percentages of the as-synthesized Ni-Al precursors and the resulting Ni/Al molar ratios are presented in Table 6.2. The same table displays the Ni loading of the 3D printed samples in their debinded and calcined state. Expectedly, the Ni loading of the precursors as well as the subsequently fabricated catalysts increases from NiAl11 to NiAl51 so that in summary, the Ni loadings after the final fabrication stage of catalyst calcination range from 6.39 to 16.35 % (NiAl11-20 - NiAl51-30, respectively). Measured

**Table 6.2:** Elemental compositions ( $w_{\text{Al}}$ ,  $w_{\text{Ni}}$ ) and Ni/Al ratios  $n_{\text{Ni}}/n_{\text{Al}}$  of prepared Ni-Al precipitates as well as Ni loading  $w_{\text{Ni}}$  of the 3D printed catalysts in their debinded and calcined states, all values determined by AAS.

	$n_{\text{Ni}}/n_{\text{Al}}$ (-)	Precursor		Debinded	Calcined
		$w_{\text{Al}}$ (wt.%)	$w_{\text{Ni}}$ (wt.%)	$w_{\text{Ni}}$ (wt.%)	$w_{\text{Ni}}$ (wt.%)
NiAl11-20	1.0	12.7	27.7	9.82	6.39
NiAl21-20	2.0	8.4	36.3	12.17	7.77
NiAl31-20	3.0	6.2	40.7	13.79	9.24
NiAl51-20	5.0	3.8	41.3	15.11	9.79
NiAl51-30	5.0	3.8	41.3	18.15	16.35
NiAl51-10	5.0	3.8	41.3	5.83	5.10

molar ratios  $n_{\text{Ni}}/n_{\text{Al}}$  of all precursors agree very well with the calculated ratios, which

means that the ratios in the mixed metal salt solution and after precipitation are the same. Table 6.2 gives an overview of the Ni loading development with ongoing fabrication stages. During printing powder preparation the precursor is mixed with mainly transition alumina powder so that "dilution" of Ni results in notably decreased Ni loadings for the debinded samples. Ni loading again decreases transitioning from the debinded to the calcined state as the infiltration step introduces additional alumina particles into the catalyst, again reducing the overall Ni percentage but to a lesser extent than between the precursor and debinded state.

### 6.3.3 XRD Analysis

#### 6.3.3.1 Ni-Al Precursor

Overall, the XRD reflexes of the co-precipitated Ni-Al precursors in Fig. 6.4 agree with the reference pattern of the hydrotalcite takovite (JCPDS 015-0087). Beside the takovite reflexes, no other crystalline phases are observed. Sharp and symmetric reflections of the (003), (006), (110) and (113) planes at  $\theta = 11.3^\circ$ ,  $22.9^\circ$ ,  $61.2^\circ$  and  $62.6^\circ$ , respectively are characteristic for the hydrotalcite-like takovite phase [297, 298] whereas the remaining ones are more asymmetric and broad. This coincides with the XRD pattern in Fig 6.4. The crystal structure of the precipitate strongly depends on various synthesis parameters such as the pH, reactant concentration, time and temperature setting so that a difference in reflex sharpness within a sample could be attributed to layer disorder phenomena [299]. The reflex intensity is the highest for NiAl31\_p, indicating that NiAl31\_p shows the highest degree of crystallinity. NiAl31\_p resembles the stoichiometry of the natural takovite the most, potentially explaining why the sample is the best crystallized one. In comparison to the other samples, the main reflexes at  $2\theta = 11.3^\circ$  and  $22.9^\circ$  are flat and broad for sample NiAl11\_p. Furthermore, the (015) reflex at  $2\theta = 39.7^\circ$  is not clearly visible anymore. Where a doublet of reflections is observed at  $2\theta = 61.2^\circ$  and  $62.6^\circ$ , NiAl11\_p only displays a single reflex which is associated with low crystallinity and poorly ordered cations within the brucite layers [300].

Conforming with previous XRD studies of synthetic Ni-Al layered double hydroxides with varying Ni/Al ratios, reflexes shift towards smaller angles with increasing Ni loading [301–304]. Due to the larger ionic radius of  $\text{Ni}^{2+}$  compared to  $\text{Al}^{3+}$ , electrostatic interaction decreases, resulting in an expanded lattice. As a result, reflexes are shifted to lower  $2\theta$  values the more Ni is incorporated into the precursor.

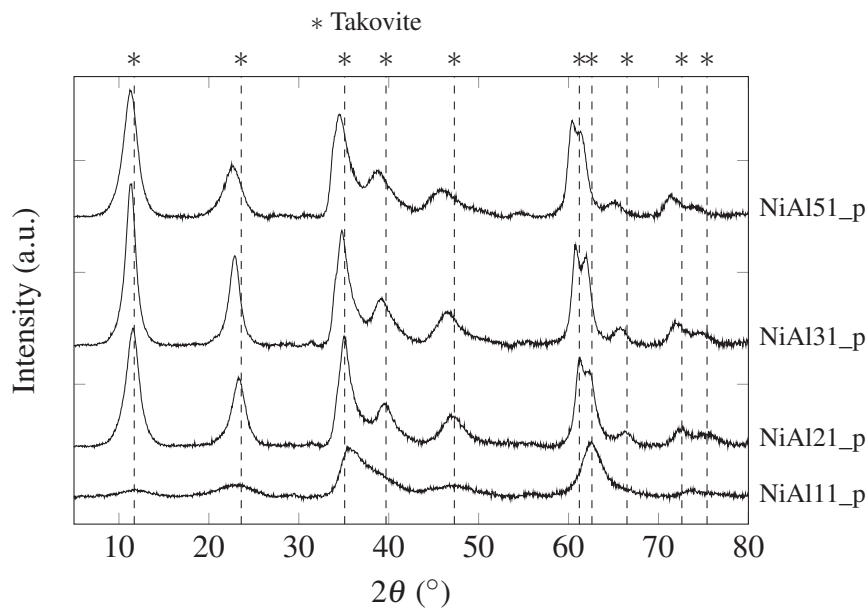


**Figure 6.4:** XRD pattern of the as-synthesized Ni-Al precursors with varying Ni/Al molar ratio. (Reference pattern: Takovite, JCPDS 015-0087.) Reflexes are shifted to smaller angles with increasing Ni loading due to lattice expansion.

### 6.3.3.2 Printed Calcined Catalysts

The XRD pattern of all printed and calcined Ni-Al spheres are compared in Fig. 6.5. The samples consist of the calcined Ni-Al precursor next to mainly  $\eta$ -Al<sub>2</sub>O<sub>3</sub> as the alumina component stems from bayerite which is converted to the  $\eta$  form at 600 °C [199, 305]. The XRD patterns verify the expectation that the calcined form should contain the phases NiO (bunsenite) and  $\eta$ -Al<sub>2</sub>O<sub>3</sub>. Generally, the reflex intensity of NiO decreases with decreasing Ni loading which is caused by reduced crystallinity. The sample NiAl51-30 and NiAl51-20 which were both synthesized with the catalyst precursor containing the highest amount of Ni, as well as NiAl31-20 do not indicate the presence of any other crystalline Ni containing phases but NiO, corroborating earlier findings that co-precipitated samples with higher Ni/Al ratios decompose more readily and show hardly any deviation from pure NiO [304, 306]. It is known that the structure strongly depends on the molar Ni/Al ratio of the co-precipitate [307, 308]. The XRD patterns of NiAl21-20 and NiAl11-20 show reflexes which cannot be assigned unambiguously to NiO or Al<sub>2</sub>O<sub>3</sub> anymore. It is assumed that in combination with the calcination temperature of 600 °C, metastable mixed oxides NiAl<sub>x</sub>O<sub>y</sub> develop. The reflections of the intermediate oxides are partly situated between the reflexes of  $\eta$ -Al<sub>2</sub>O<sub>3</sub>, NiO and NiAl<sub>2</sub>O<sub>4</sub>. For example, the XRD pattern of NiAl11-20 and NiAl21-20 show a reflection situated between the signal of the (220) plane of NiO at  $2\theta = 62.9^\circ$  and the (440) plane of nickel aluminate NiAl<sub>2</sub>O<sub>4</sub> at  $2\theta = 65.5^\circ$ . De Korte et al. [308] reported another intermediate oxide reflection between the (440) plane of NiAl<sub>2</sub>O<sub>4</sub> ( $2\theta = 65.5^\circ$ ) and the (440) plane of alumina ( $2\theta = 66.8^\circ$ ) for samples with a

Ni content below 50 %. This observation cannot be confirmed for the samples presented here. In general, the formed intermediate phases are declared as NiO rich and/or  $\text{Al}_2\text{O}_3$

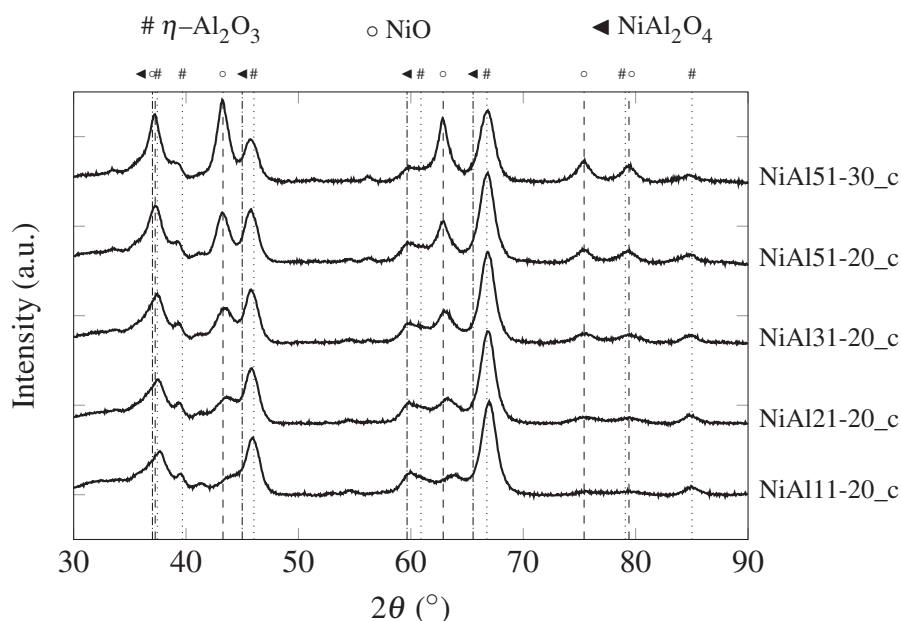


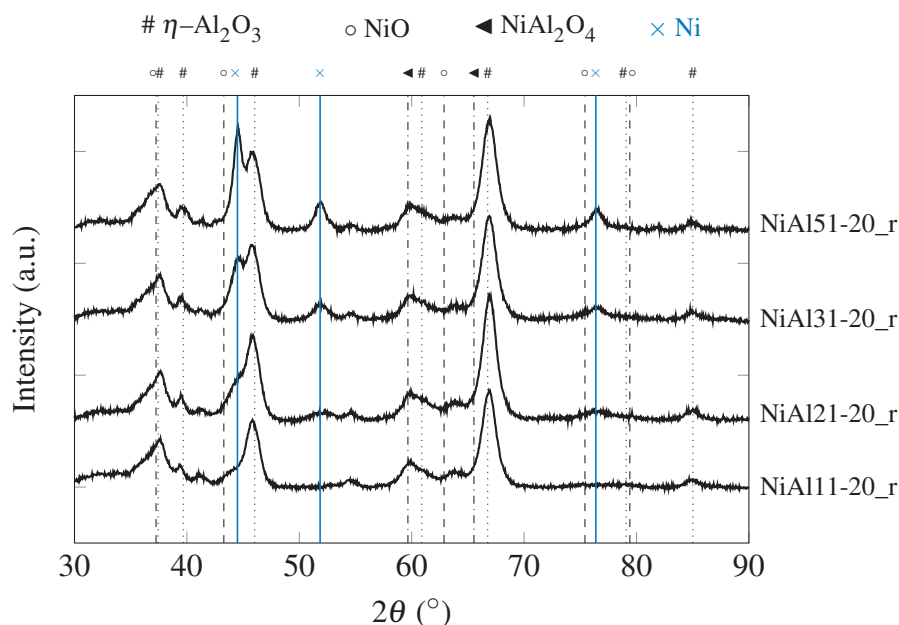
**Figure 6.5:** XRD pattern of the 3D printed and calcined Ni-Al catalysts with varying Ni/Al molar ratio. (Reference patterns:  $\eta\text{-Al}_2\text{O}_3$ : JCPDS 04-0875, NiO: 01-078-0429,  $\text{NiAl}_2\text{O}_4$ : 10-0339)

rich phases caused by diffusion of  $\text{Ni}^{2+}$  to alumina-rich regions [308] and diffusion of  $\text{Al}^{3+}$  to NiO-rich phases [306], respectively. It is reported by various studies that these intermediates could be a disordered spinel intermediate phase [307, 309, 310]. The XRD patterns in Fig 6.5 illustrate that the formation and composition of these mixed oxides depend on the molar Ni/Al ratio of the used co-precipitate.

Concerning the XRD patterns in Figs. 6.5 - 6.7, bulk characterization was executed where the whole pellet was ground and analyzed. In order to examine whether mass and heat transfer limitations would affect the Ni species within a catalyst pellet during drying or calcination, XRD measurements of the shell and core region of a spherical pellet were conducted. XRD results of three Ni-Al samples (see Supporting Information, Fig. 6.15) revealed that no significant effects on the generation of differing Ni species in radial direction were observed for the calcined 3D printed Ni-Al pellets. Therefore, it can be assumed that the chemical composition is mostly homogeneous throughout the calcined catalyst.

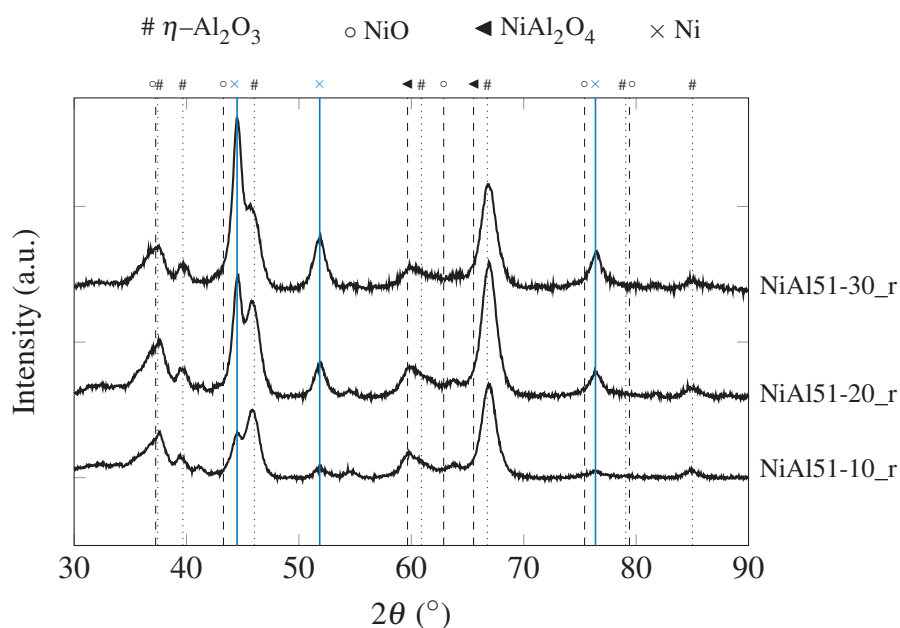
### 6.3.3.3 Printed Reduced Catalysts

Fig. 6.6 and 6.7 present the XRD patterns of reduced 3D printed samples prepared with different precursors (while the amount of precursor is 20 wt.%) and varying amount of precursor powder (while  $n_{\text{Ni}}/n_{\text{Al}} = \text{const.} = 5$ ), respectively.



**Figure 6.6:** XRD pattern of the 3D printed and reduced Ni-Al catalysts with varying Ni/Al molar ratio. (Reference patterns:  $\eta$ -Al<sub>2</sub>O<sub>3</sub>: JCPDS 04-0875, NiO: 01-078-0429, NiAl<sub>2</sub>O<sub>4</sub>: 10-0339, Ni: 01-087-0712.)

The patterns in Fig. 6.6 reveal that the molar Ni/Al ratio affects phase formation during the reduction process. Compared with the XRD pattern of the calcined catalysts in Fig. 6.5, the  $\eta$ -Al<sub>2</sub>O<sub>3</sub> reflexes are unchanged and appear equal in intensity for all Ni/Al ratios so that alumina does not perform any further phase transformation after calcination. NiO is clearly reduced to pure Ni, manifested in the vanishing NiO reflexes and the emerging Ni reflexes at  $2\theta = 65.5^\circ$  (111),  $2\theta = 51.9^\circ$  (200) and  $2\theta = 76.4^\circ$  (220) for all analyzed samples. Where the reflex intensity of the calcined samples at about  $2\theta = 37^\circ$  increases with increasing Ni content (Fig. 6.5) the crystalline phases were not clearly distinguishable due to NiAl<sub>2</sub>O<sub>4</sub>, NiO and Al<sub>2</sub>O<sub>3</sub> having reflexes at approximately the same position. Observing the same reflex position in Fig. 6.6 reveals that the NiO reflex at  $2\theta = 37.3^\circ$  flattens out due to being converted to pure Ni upon reduction so that the remaining reflex is attributed to alumina. Increasing the Ni loading by greater Ni/Al ratios correlated directly with increasing Ni reflex intensity. The basal Ni (111) reflex at  $2\theta = 44.5^\circ$  is partly superpositioned with the (400) reflex of Al<sub>2</sub>O<sub>3</sub> at  $2\theta = 46.0^\circ$ . While



**Figure 6.7:** XRD pattern of the 3D printed and reduced Ni-Al catalysts with varying amounts of admixed Ni-Al precursor. (Reference patterns:  $\eta$ - $\text{Al}_2\text{O}_3$ : JCPDS 04-0875, NiO: 01-078-0429,  $\text{NiAl}_2\text{O}_4$ : 10-0339, Ni: 01-087-0712.)

the Ni reflex appears as a shoulder of the alumina reflex in sample NiAl11-20 and NiAl21-20, the remaining samples NiAl31-20 and NiAl51-20 show an evident Ni reflex, although still paired up as a doublet reflex with alumina. The NiO reflex at  $2\theta = 62.9^\circ$  completely vanished in all catalyst samples and discloses a small reflex for all samples between  $2\theta = 62.9^\circ$  (NiO) and  $2\theta = 65.5^\circ$  ( $\text{NiAl}_2\text{O}_4$ ), respectively. The observed reflex has already been detected for the calcined samples (Fig. 6.5) and was declared as an intermediate  $\text{NiAlO}_x$  species which is now present in the reduced sample, potentially generated during the reduction process by ionic migration processes between NiO,  $\text{NiAl}_2\text{O}_4$  and  $\text{Al}_2\text{O}_3$ . The (511) nickel aluminate reflex is distinctly visible at  $2\theta = 59.7^\circ$  which is also the case for the calcined state in Fig. 6.5. This  $\text{NiAl}_2\text{O}_4$  type phase as well as mixed NiO/ $\text{Al}_2\text{O}_3$  phases are generally more difficult to reduce to metallic Ni. Therefore, fractions could remain unreduced.

Fig. 6.7 shows the three XRD patterns for printed Ni-Al catalysts with varying amounts of added precursor powder, ranging from 10 to 30 wt.%. The integral intensity of a XRD reflex correlates proportional to the amount of a phase in the powder mixture. The reflexes show an increasing intensity for Ni from NiAl51-10 to NiAl51-30 so that the increasing amount of Ni is represented with powder XRD. Zieliński [311] assumed that the increasing presence of nickel aluminate-like species induces coverage of Ni crystallites with nonreduced residues.

### 6.3.4 Degree of Reduction

Prior research generally agrees that decreasing Ni content in co-precipitated catalysts aggravates catalyst reducibility [304, 307, 310, 312, 313].  $d_{\text{red}}$  calculated from TG measurements also confirms this behavior for printed Ni-Al catalysts with varying molar Ni/Al ratios (Fig. 6.8). The final degree of reduction achieved at 480 °C in 5 % H<sub>2</sub> in N<sub>2</sub>

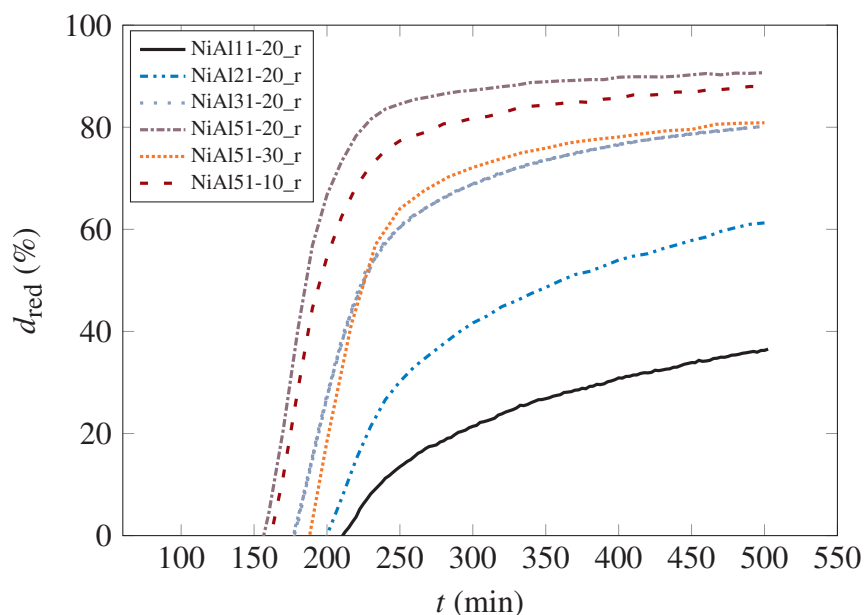


**Figure 6.8:** Calculated degrees of reduction  $d_{\text{red}}$  from TG analysis for 3D printed Ni-Al catalysts.

rises steadily from 37 % (NiAl11-20) to 91 % (NiAl51-20). In conformity with the XRD analysis of the calcined specimens (Fig. 6.5), increasing occurrence of nonstoichiometric nickel aluminate phases with increasing Al content inhibits the reduction process [311]. Bulk NiAl<sub>2</sub>O<sub>4</sub> (Fig. 6.5, 6.6, and 6.7) could contribute to incomplete reduction which was found in the calcined as well as reduced samples, agreeing with Li and Chen [314] who found three different NiO species and NiAl<sub>2</sub>O<sub>4</sub> in all precipitated Ni/Al<sub>2</sub>O<sub>3</sub> catalysts. NiAl51-20 achieved the highest degree of reduction among all examined samples with 91 %. Fig. 6.8 shows that the molar Ni/Al ratio significantly affects the reducibility whereas variation of admixed precursor powder amount does not influence the degree of reduction as considerably. The values for NiAl51-10, NiAl51-20 and NiAl51-30 do not follow an upward order according to their Ni loading but range similarly between 91 % and 81 %. Therefore, Ni loading adjustment by admixed amount of precursor is not as decisive for the reduction behavior as the Ni/Al ratio of the precursor. The molar Ni/Al ratio impacts the phase composition of the reducible species (as observed by XRD analysis, see Figs. 6.4 and 6.5) and the resulting morphology of the reduced species (as

observed by TEM analysis, see Fig. 6.9) more significantly than the amount of admixed precursor.

The ease of reduction clearly increases with higher Ni/Al ratios, so that the samples containing the precursor NiAl51\_p nearly reach their sample-specific maximum degree of reduction. The other samples have not yet reached a stagnant  $d_{\text{red}}$  after completion of the holding time of 5 h. Various TPR studies revealed that precipitated Ni-Al catalysts show a first reduction peak at 400 - 500 °C, attributed to the more easily reducible NiO. The presence of difficult to reduce  $\text{NiAl}_x\text{O}_y$  species causes another reduction peak at 600 - 720 °C [292, 301, 314]. Li et al. found that the maximum degree of reduction was reached at 870 °C [301]. Consequently, at a reduction temperature of 480 °C the 3D printed catalysts have most likely not reached their maximum degree of reduction due to remaining unreduced  $\text{NiAl}_x\text{O}_y$ . Fig. 6.8 provides evidence for the increased presence of  $\text{NiAl}_x\text{O}_y$  in samples with a lower Ni/Al ratio due to lower degrees of reduction. For ease of calculation, the Ni loading of the samples analyzed with TGA was assumed to stem from NiO. Considering the amount of unreduced  $\text{NiAl}_x\text{O}_y$  would improve the accuracy of reducibility determination. Nevertheless, the values presented in Fig. 6.8 demonstrate the general tendency to a sufficiently relevant extent.

The results from TGA show that for complete reduction, a higher reduction temperature should be applied if a catalyst with a low molar Ni/Al ratio is chosen. Adjusting the chemical nature of the Ni species by careful tweaking of the co-precipitation conditions could offer another option to improve the reducibility of the Ni-Al catalyst.

### 6.3.5 Sorption Properties

#### 6.3.5.1 Metal Particle Size

The morphology and structure of the reduced Binder Jet printed Ni-Al catalysts were observed by TEM analysis. Fig. 6.9 presents the TEM images of all Ni-Al catalysts where the distribution of Ni particles is mapped for each molar Ni/Al ratio. All samples show a mostly nodular nanoparticle structure. Moreover, the TEM images suggest growing Ni particle sizes with increasing Ni loading.

TEM measurements were used to determine the metal particle size distribution and the resulting average metal particle diameter  $d_{\text{Ni,TEM}}$ . The results for the mean Ni particle sizes are presented in Table 6.3. Confirming the visual impression when observing the TEM images in Fig. 6.9a to 6.9f, the Ni particle size steadily grows with increasing

**Table 6.3:** Nickel particle size  $d_{Ni}$  determined by TEM, XRD line broadening analysis and H<sub>2</sub> chemisorption.

Catalyst	$d_{Ni,TEM}^a$ (nm)	$d_{Ni,XRD}^b$ (nm)	$d_{Ni,c}^c$ (nm)
NiAl11-20_r	$3.9 \pm 0.6$	n.d.	7.9
NiAl21-20_r	$5.3 \pm 0.5$	6.4	7.5
NiAl31-20_r	$7.2 \pm 0.5$	8.0	9.9
NiAl51-20_r	$10.4 \pm 1.2$	11.0	17.0
NiAl51-30_r	$10.1 \pm 0.9$	10.5	15.1
NiAl51-10_r	$9.9 \pm 1.0$	10.1	17.7

<sup>a</sup> Measurement of at least 100 particles per sample.

<sup>b</sup> Determined using the Scherrer equation with FWHM of the Ni (200) reflex.

<sup>c</sup> Determined by H<sub>2</sub> chemisorption.

Ni/Al molar ratio. NiAl11-20\_r displays small Ni nanoparticles with  $d_{Ni,TEM} = 3.9 \pm 0.6$  nm while particles of NiAl51-20\_r increased by a factor of almost three to a size of  $10.4 \pm 1.2$  nm. However, the amount of admixed precursor powder does not affect the

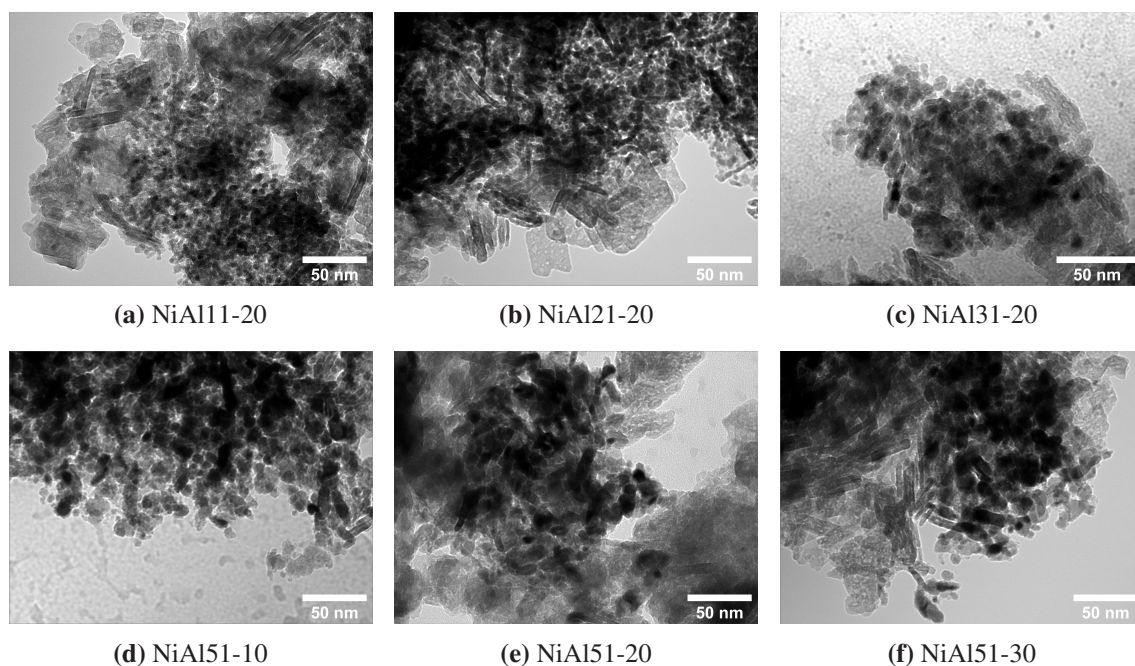


**Figure 6.9:** TEM images of 3D printed and reduced Ni-Al catalysts.

particle size, as all reduced NiAl51 samples show a similar particle size of about 10.1 nm, with respect to the consistent standard deviation values. This observation corroborates the findings from TGA regarding the degree of reduction where all three samples based on the NiAl51 precursor showed a similar  $d_{red}$  (Fig. 6.8). The standard deviations for  $d_{Ni,TEM}$  in Table 6.3 imply decreasing metal dispersion with increasing molar Ni/Al ratio as the particle size distributions for the samples NiAl11 - NiAl31 are more narrow than

for NiAl51, suggesting a more homogeneous Ni distribution over the catalyst support. NiAl51 reduces readily (see section 6.3.4) and exhibits more pronounced sintering, thus generating bigger metal particles and clusters. Therefore, more diversely sized Ni particles double the standard deviation value of all NiAl51 samples in comparison to samples with a lower Ni loading (Table 6.3).

Additionally, the crystallite size was calculated by line broadening analysis of the XRD patterns in Fig. 6.6 and Fig. 6.7 using the Scherrer equation 3.3. The crystallite size could not be determined for the sample NiAl11-20\_r due to insufficient reflex intensity of the Ni reflex of the (200) plane at  $2\theta = 51.9^\circ$ , see Fig. 6.6. A reason is the very small nanocrystallite size of  $d_{\text{Ni,TEM}} = 3.9 \pm 0.6$  nm, leading to large specimen broadening in contrast to the instrumental broadening, producing a weak diffraction signal below the detection limit for XRD of 2 to 5 nm [315, 316]. Nevertheless, the remaining values for  $d_{\text{Ni,XRD}}$  are consistent with the ones determined by TEM, following the same trend. Moreover, line broadening analysis is subject to errors since it applies simplifications including the assumption of spherical crystallite shape, a narrow unimodal size distribution and neglects lattice defects such as microstrain or stacking faults [317]. Hence, it is safe to conclude that the metal particle sizes determined by TEM agree well with the crystallite size determined by line broadening analysis and therefore low crystallite agglomeration occurred in the samples.

Table 6.3 also shows the average Ni crystallite size determined by  $\text{H}_2$  chemisorption so that the crystallite size was analyzed by three different analysis methods. The general trend towards bigger crystallite size with increasing molar Ni/Al ratios is confirmed with  $\text{H}_2$  chemisorption as well, but crystallite sizes analyzed on the basis of  $\text{H}_2$  chemisorption are shifted to slightly larger particles than calculated by TEM and line broadening analysis, ranging from  $d_{\text{Ni,c}} = 7.9$  nm to 17.7 nm.  $d_{\text{Ni,TEM}}$  and  $d_{\text{Ni,c}}$  were calculated from reduced spherical pellets.  $d_{\text{Ni,XRD}}$  was determined from cylindrical samples which were reduced during  $\text{H}_2$  chemisorption measurement. Table 6.3 shows that the particle sizes determined by all three methods are similar so that a certain degree of reproducibility is deducible from the BJ 3D printing process. Especially the similarity of  $d_{\text{Ni,TEM}}$  (from spheres) and  $d_{\text{Ni,XRD}}$  values (from cylinders) indicate that the printing process produces consistent results.

### 6.3.5.2 $\text{H}_2$ Chemisorption

Table 6.4 includes the Ni surface area  $S_{\text{Ni}}$  and dispersion  $D_{\text{Ni,c}}$  determined by  $\text{H}_2$  chemisorption.  $S_{\text{Ni}}$  is overall declining with increasing molar Ni/Al ratio due to the

increasing Ni particle size (see Table 6.3). The Ni surface area of the samples NiAl51-10, -20 and -30 increases in this order from 1.9 up to 7.4 m<sup>2</sup>/g<sub>cat</sub> due to the increasing available Ni amount per gram catalyst.

$D_{Ni,c}$  decreases with increasing molar Ni/Al ratio which agrees with the results for particle size determination in section 6.3.5.1. Over all samples, the Ni dispersion ranges from 5.7 to 13.4 %. The dispersion drops due to the formation of larger Ni particles at higher Ni/Al ratios. Furthermore, TEM images suggest that metal cluster formation or agglomeration is more prominent in highly loaded Ni catalyst samples (Fig. 6.9), lowering the ratio of exposed number of metal atoms to the total number of metal atoms. Sintering of Ni nanoparticles could be limited for low Ni/Al ratios because of the strong and Ni stabilizing interaction between nickel and alumina, hindering the migration and diffusion of Ni to form clusters, thus explaining the increasing dispersion from NiAl51-20 to NiAl11-20. In conformity with the unchanged Ni particle size of the samples NiAl51-10, -20 and -30, the dispersions of 5.7 %, 6.0 % and 6.7 %, respectively are very similar and consequently do not correlate with the amount of added alumina surrounding the catalyst material.

To verify  $D_{Ni,c}$  determined by H<sub>2</sub> chemisorption, the dispersion  $D_{Ni,TEM}$  was additionally calculated using the Ni particle size  $d_{Ni,TEM}$  obtained from TEM (see Table 6.3). The results are also displayed in Table 6.4. The numbers show the same trend as  $D_{Ni,c}$  with slightly differing values. Considering the parameters in Eq. 3.15 used for dispersion calculation, the assumption of particle sphericity, the standard deviation of  $d_{Ni,TEM}$  and uncertainty regarding the determination of the degree of reduction via TGA,  $D_{Ni,TEM}$  agrees with the dispersion values obtained by chemisorption.

**Table 6.4:** Active metal surface area  $S_{Ni}$ , metal dispersion  $D_{Ni}$  of reduced samples and specific surface area  $S_{BET}$  of printed Ni-Al catalysts at varying process stages.

Catalyst	$S_{Ni}^a$ (m <sup>2</sup> /g <sub>cat</sub> )	$D_{Ni,c}^a$ (%)	$D_{Ni,TEM}$ (%)	$S_{BET}$ (m <sup>2</sup> /g <sub>cat</sub> )			
				Precursor	Debinded	Calcined	Reduced
NiAl11-20	5.4	12.7	9.3	117	240	192	131
NiAl21-20	7.0	13.4	11.6	74	209	131	140
NiAl31-20	6.3	10.2	11.2	85	166	133	149
NiAl51-20	3.9	6.0	8.8	74	182	161	147
NiAl51-30	7.3	6.7	8.9	74	176	136	140
NiAl51-10	1.9	5.7	8.1	74	199	154	171

<sup>a</sup> Determined by H<sub>2</sub> chemisorption.

### 6.3.5.3 N<sub>2</sub> Physisorption

The specific surface area of the 3D printed samples were determined by nitrogen physisorption. Table 6.4 summarizes the measured  $S_{\text{BET}}$  of the pure as-synthesized takovite-like precipitate as well as the printed samples in their debinded, calcined and reduced state. The precursors show a declining specific surface area with increasing Ni content which agrees with other studies [310].

The debinded sample is a mixture of alumina and a calcined Ni-Al catalyst. This means that the  $S_{\text{BET}}$  of the admixed alumina compound influences the result as it makes up to 80 wt.% of the total powder mixture. According to a prior study [13], the surface area of the pure debinded alumina in the used mixture is  $223 \text{ m}^2/\text{g}_{\text{cat}}$ . The surface area of the debinded Ni-Al catalysts should therefore be an intermediate value of the pure calcined Ni-Al precursor and the alumina component. The results in Table 6.4 confirm that decreasing the Ni content increases the surface area, both by varying the molar Ni/Al ratio and the amount of admixed precursor after debinding.

The  $S_{\text{BET}}$  of the calcined specimens follow a similar trend as the debinded samples but with overall decreased values. Calcination is executed under the same conditions as debinding, namely at  $600 \text{ }^\circ\text{C}$  for 3 h. The lowering in surface area is caused by sintering of the Ni species upon calcination and particle shrinkage of the admixed alumina.

Pure reduced Ni-Al catalysts prepared by co-precipitation normally exhibit a decrease in  $S_{\text{BET}}$  upon reduction [293, 301, 307, 310]. Printed Ni-Al catalysts also show decreased surface areas (Table 6.4) but the results partially do not deviate much from the samples in their calcined state. The weight percentage of admixed alumina powder is relatively high so that the development of surface area predominantly follows that of alumina.  $S_{\text{BET}}$  of the utilized alumina after two rounds of infiltration and calcination was reported to be  $179 \text{ m}^2/\text{g}_{\text{cat}}$  [13]. Due to the reduction temperature of  $480 \text{ }^\circ\text{C}$  being lower than the calcination temperature of  $600 \text{ }^\circ\text{C}$ , the alumina part presumably does not undergo any phase transformation and therefore change in surface area. Nevertheless, Table 6.4 shows a change in  $S_{\text{BET}}$  which means that the reduction in surface area of the precipitated nickel catalyst does influence the total surface area. Overall, the surface areas of the reduced and calcined Ni-Al catalysts do not differ significantly. Consequently, it is assumed that a greater variance in surface area would only be noticeable with an even greater difference in admixed precursor in the printing powder mixture.

### 6.3.6 Mechanical Stability

The results for the compressive strength  $\sigma_{\text{comp}}$  of the spherical Ni-Al 3D printed catalyst pellets obtained by uniaxial compression tests are displayed in Fig. 6.10. The plot compares the compressive strength of the green part directly after printing and the calcined part to emphasize the significance of the infiltration step to achieve sufficient mechanical strength for application of the pellets in a fixed bed reactor. The compressive strength of a finished calcined part is 0.21 MPa on average, which is about 20 times more robust than a green part with only 0.01 MPa. The infiltration with alumina slurry significantly stabilizes the ceramic scaffold and enables the powder-based AM of highly porous bodies and a simultaneously low calcination temperature which retains catalytically relevant physico-chemical properties. It is believed that the variation in chemical and quantitative

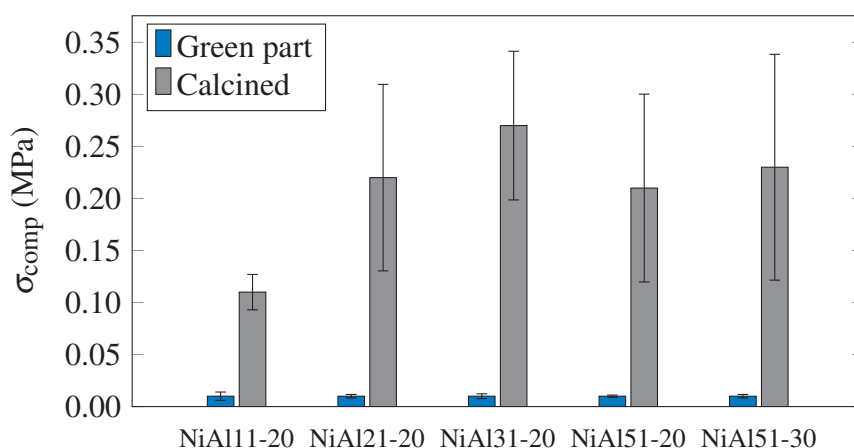


**Figure 6.10:** Compressive strength  $\sigma_{\text{comp}}$  of green and calcined printed Ni-Al catalysts.

composition in this study is not influential on the final compressive strength of the printed part. Although the texture of the Ni-Al precursor becomes softer with increasing molar Ni/Al ratio, an effect on the final  $\sigma_{\text{comp}}$  thereby is minimal. Moreover, comparing  $\sigma_{\text{comp}}$  for NiAl51-20 and NiAl51-30, a significant difference in compressive strength by varying the amount of admixed precursor powder is not observed. In this study, the variance of the compressive strengths for the calcined samples is more likely caused by user or printer induced inconsistencies during the printing process than by powder material properties. Consequently,  $\sigma_{\text{comp}}$  is similar for all investigated samples so that all 3D printed pellets show suitability for the use in a fixed bed reactor without experiencing detrimental effects concerning attrition or mechanical disintegration.

### 6.3.7 Pore Size Analysis

In contrast to lab scale experiments where small particles are used and the reaction conditions are chosen in order to avoid diffusion limitations, the application of larger catalyst geometries induces mass and heat transfer restrictions. Internal diffusion restriction of the reactant significantly affects catalyst performance and is determined by the pore size distribution and particle size so that porosity characterization is crucial.

#### 6.3.7.1 Pore Size Analysis by N<sub>2</sub> Physisorption

The poreSD of debinded and calcined samples are presented in Fig. 6.11. The individual poreSDs in Fig. 6.11a all follow a slightly bimodal distribution with a relatively sharp peak at about 3.6 nm and a broad peak at about 12 nm. Due to the printing powder preparation, the mixture is a homogeneous mixture but ultimately consists of alumina particles located next to catalyst precursor material. The pure alumina compound without Ni-Al precursor (NiAlO1) displays a unimodal poreSD after debinding peaking at 3.6 nm, see Fig. 6.11a. The poreSD of pure Ni-Al precursor powder is also unimodal but features a broader distribution between 9 - 10 nm. The separate poreSDs combined result in the plots observed in Fig. 6.11a in so far as the most distinct peak is located at the same position as NiAlO1 and the pore sizes attributed to the Ni-Al compound show up at the respective size range. However, the magnitudes of the volumetric fractions do not seem to correlate closely with either the molar Ni/Al ratio or the powder composition. Nevertheless, the general pore size characteristic is similar for all examined samples. After infiltration and calcination, the poreSD transforms from the one in Fig. 6.11a to the one depicted in Fig. 6.11b. The bimodal poreSD is significantly more distinct after calcination. The two peaks are located again in the small mesopore region at ca. 3.6 nm and 12 nm with the former peak now being lower than before but the latter becoming more pronounced. The sample NiAlO1 also shows this behavior which was reported to stem from the infiltration procedure which occludes small and open pores with alumina particles, resulting in a greater fraction of larger sized pores [13]. It is assumed that the reason for the bimodal poreSD of the calcined Ni-Al catalysts arises from a combination of the pore-occlusive effect by slurry infiltration and the fact that the pores of the Ni-Al component are situated in a similar pore region. The fusion of both pore size distributions generate a relatively broad peak with pore sizes ranging from 8 - 20 nm, see Fig. 6.11b.

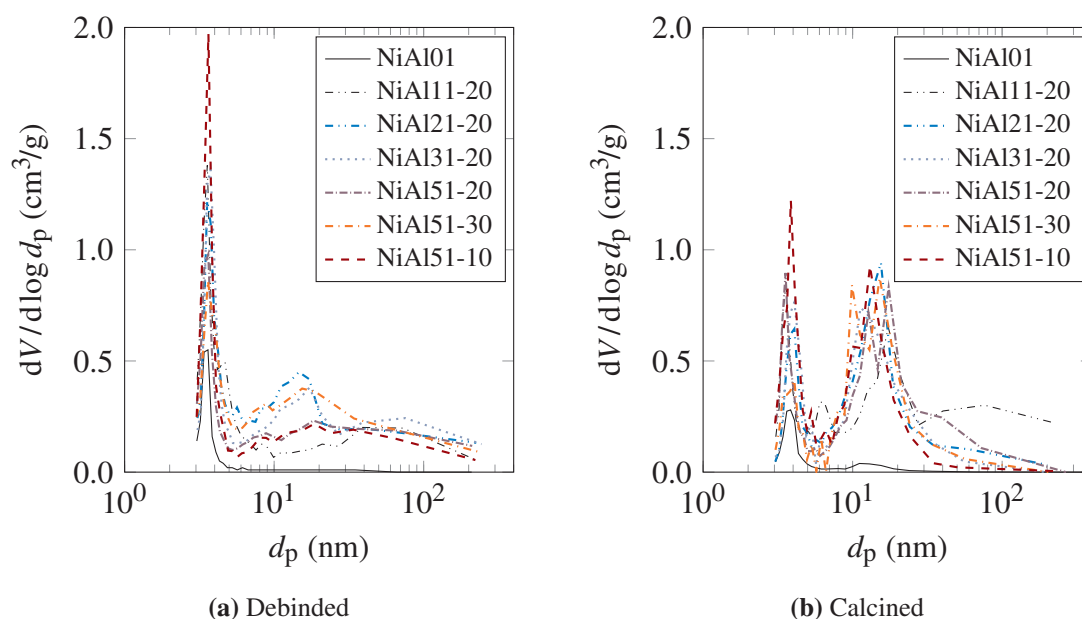


**Figure 6.11:** Pore size distribution of 3D printed Ni-Al catalysts, determined by N<sub>2</sub> physisorption using the BJH method on the desorption branch.

### 6.3.7.2 Pore Size Analysis by Mercury Intrusion Porosimetry

The pore size distribution obtained by gas adsorption (Fig. 6.11) presents the intraparticle porosity as the N<sub>2</sub> physisorption technique measures pores from approximately 0.3 to 300 nm. However, for a complete characterization of the porous sample structure including the interstitial voids between the catalyst particles within a pellet, the poreSD of the spherical printed catalysts were analyzed by mercury intrusion porosimetry (MIP) to obtain pore sizes neglected by gas adsorption. MIP covers a wide range of measurement from 500 000 nm down to 3 nm while gas adsorption offers analysis of an additional decade of very small pores down to 0.3 nm [318]. Fig. 6.12 presents the poreSD of all 3D printed and calcined Ni-Al catalysts determined by MIP.

Comparison of gas adsorption and MIP results are only valid for the overlapping region of measurement from 3 to 300 nm. Comparing the pore size distributions in this range in Fig. 6.11b with Fig. 6.12, the bimodal character is also clearly visible by MIP measurement. Fig. 6.13 illustrates the high level of concurrence between N<sub>2</sub> physisorption and MIP for the example of the calcined sample of NiAl21-20, especially for the peak at 12 nm. The small mesopores at 3.6 nm are recognized by MIP and gas adsorption equally. In general, both methods determine principal occurrences of pores at the same size range where the measuring range of gas adsorption and MIP coincide. Furthermore, the Washburn equation (Eq. 3.18) used for MIP as well as the BJH method assume cylindrical pore geometry, reinforcing the comparability of the two methods of measurement.

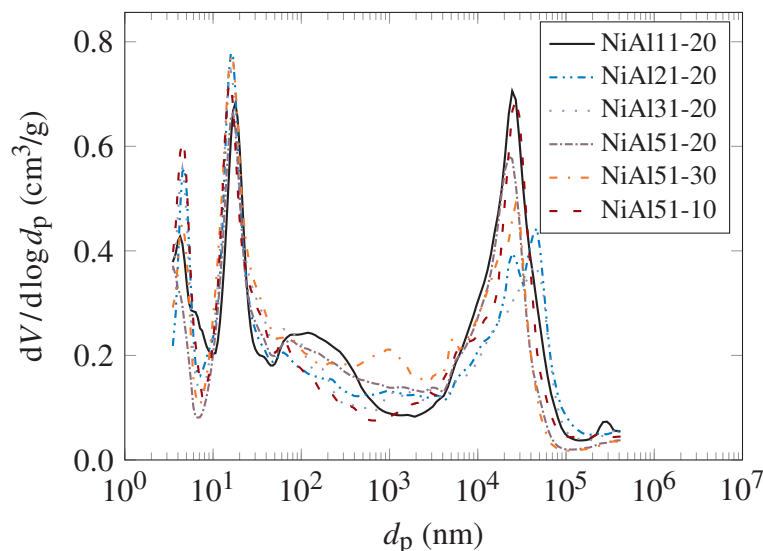


**Figure 6.12:** Pore size distribution of calcined Ni-Al catalysts, determined by MIP.

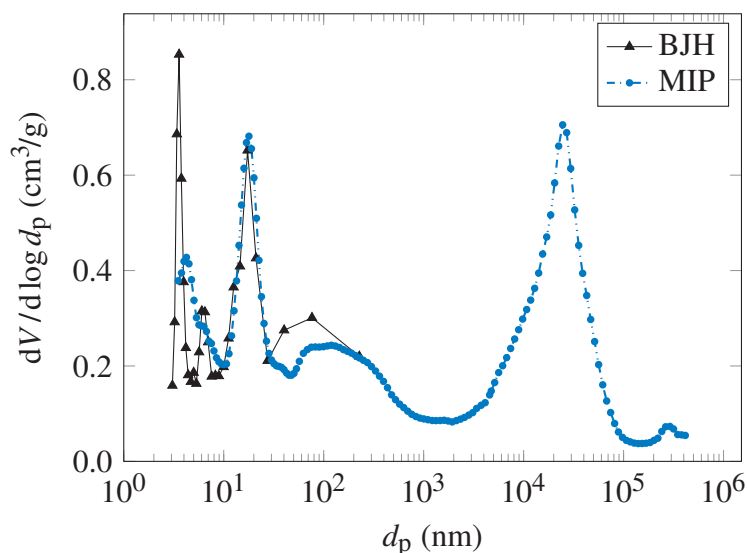


**Figure 6.13:** Comparison of pore size distributions obtained by gas adsorption (black) and mercury porosimetry (blue) for the calcined sample NiAl11-20.

However, MIP additionally reveals large voidages of about  $2 \cdot 10^4$  nm found in all examined samples (Fig. 6.12) induced by the powder-based AM process. These voids are not included in the range of measurement of gas adsorption. The binder jetting process inherently generates macroporous parts due to its building principle of selectively joining loose powder layers with a liquid binder. Therefore, the presence of large interparticle voids revealed by MIP aids characterizing the Binder Jet 3D printed character of the catalysts. The fabrication of highly porous meso- as well as macroporous shapes with an average porosity of  $77.7 \pm 2.0$  % could offer advantageous catalytic properties regarding fluid permeability, pressure drop behavior, and mass transfer limitations which are not feasible with other 3D printing techniques. A similar size range of the large interstitial

voids for all Ni-Al samples (see Fig. 6.12) implies that the pore size structure is reproducible for printed Ni-Al catalysts with the described material composition and printing parameters.

As a consequence, variation of the powder feedstock or binder material which acts as a pore-forming agent, depending on its particle size, allows control of the catalyst porosity during the printing process.

### 6.3.8 Catalytic Test in a SPSR

A proof-of-concept experiment was conducted to check the successful fabrication of active Ni-Al CO<sub>2</sub> methanation catalysts via Binder Jetting. The Ni-Al catalysts NiAl11-20, NiAl21-20 and NiAl51-20 were exemplarily chosen to be tested in a single pellet string reactor in order to investigate the influence of different Ni/Al ratios on the catalytic performance. Fig. 6.14 illustrates the results of the catalytic tests and indicates a clear increase in CO<sub>2</sub> conversion and CH<sub>4</sub> yield with increasing Ni loading. Therefore, the tested samples adequately represent the activity trend for the 3D printed Ni-Al catalysts with increasing molar Ni/Al ratio. Fig. 6.14a compares the CO<sub>2</sub> conversion for the three catalysts. Thermodynamic equilibrium is reached with all three tested catalysts. NiAl11-20, NiAl21-20 and NiAl51-20 achieved maximum conversions of 96 %, 97 % and 99 %, respectively at the corresponding reaction temperatures of 367 °C, 318 °C and 303 °C. Correspondingly, the temperature necessary to obtain about 50 % CO<sub>2</sub> conversion decreases with rising Ni/Al ratio so that the activity rises in the order NiAl11-20 (280 °C) < NiAl21-20 (240 °C) < NiAl51-20 (220 °C). Until approx. 200 °C the CO<sub>2</sub> conversion rate of NiAl21-20 and NiAl51-20 improves slowly with rising reaction temperature. Starting at 200 °C, rising the reaction temperature leads to a steep increase until conversion approaches the equilibrium value. The same conversion development is shifted to higher temperatures for NiAl11-20 due to its lower Ni loading and resulting lower catalytic activity. Differences between the measured data compared to the calculated thermodynamic equilibrium curve could stem from slight deviations of the feed gas composition from the stoichiometric CO<sub>2</sub>/H<sub>2</sub> (1/4) ratio, catalyst poisoning effects or hot spot formation within the catalyst pellet string.

The CH<sub>4</sub> and CO yields are compared in Fig. 6.14b. No CO is produced until 420 °C when the CO formation increases, following the trend of the equilibrium curve. Nevertheless, the CO yield remains below 1 % for all tested catalysts. Carbon monoxide is presumably formed due to the reverse water-gas shift reaction taking place, the backward reaction of Reaction (R3).

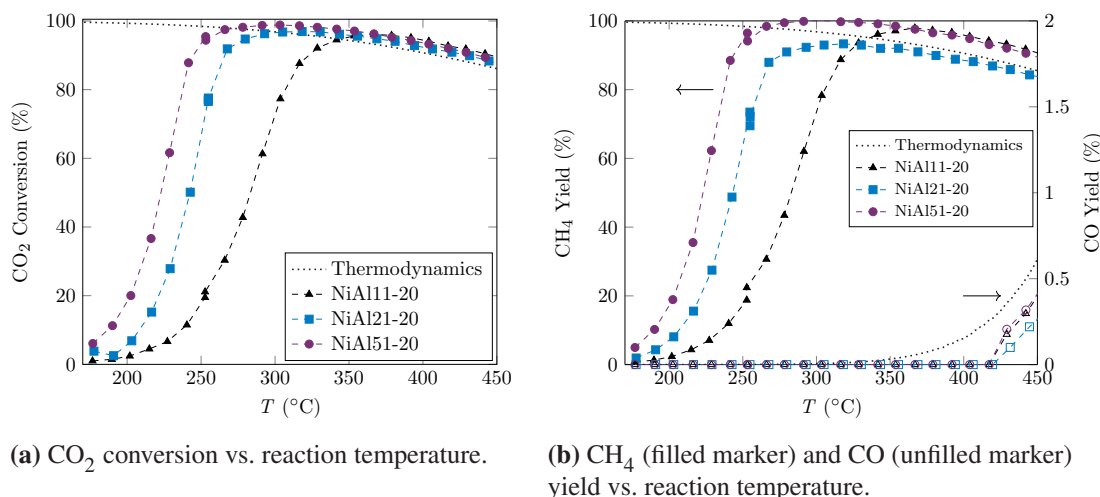


**Figure 6.14:** Results of the catalytic tests of the Binder Jet 3D printed Ni-Al catalyst NiAl11-20, NiAl21-20 and NiAl51-20. Reaction conditions:  $\text{CO}_2/\text{H}_2/\text{Ar}/\text{N}_2 = 2/8/9/1$ , total pressure  $p_{\text{tot}} = 9$  bar.

The 3D printed Ni-Al catalysts are highly selective towards  $\text{CH}_4$  for reaction temperatures below 420 °C. The methane yield increases significantly with higher Ni/Al ratio, see Fig. 6.14b. In general, Fig. 6.14 shows a clear relation between the Ni loading adjusted by the Ni/Al ratio during precipitation and  $\text{CO}_2$  conversion as well as methane yield.

Direct performance comparison of the Binder Jet printed catalysts with data from other existing studies of Ni-Al catalysts for  $\text{CO}_2$  methanation is difficult due to the special arrangement and the fact that whole spherical pellets were tested. Although the single pellet string reactor configuration is vastly different compared to the usually conducted intrinsic test reactions with powdery catalyst material, the general trend regarding conversion and yield (Fig. 6.14) agrees with those of other methanation studies [303, 319–321]. Moreover, the activation energy of all three tested catalysts, which ranges between 86 to 96 kJ/mol and was determined by linearization of the Arrhenius equation, is in good agreement with other literature values reporting activation energies between 71 to 109 kJ/mol [180, 294, 322–324]. Catalytic performance measurement was repeated two times at 250 °C. Fig. 6.14a and 6.14b show that  $\text{CO}_2$  conversion and  $\text{CH}_4$  yield, respectively, coincide after repeated measurement at 250 °C, so that catalyst deactivation can be ruled out for the duration of this experiment. Considering that co-precipitated hydrotalcite-like Ni-Al catalysts can reach Ni loadings over 70 % [319, 320], Ni loadings of NiAl11-20, NiAl21-20 and NiAl51-20 range between 6.4 to 9.8 wt.% due to dilution with admixed alumina powder (see Table 6.2). Nevertheless, the total catalyst mass of 2.4 g inside the reactor should be taken into account. Hence, the feasibility of a novel direct 3D printing strategy combining co-precipitated Ni-Al catalyst material and Binder Jetting is demonstrated hereby.

## 6.4 Conclusions

The binder jetting AM technology was successfully employed to establish a fabrication routine for mixed oxide Ni-Al CO<sub>2</sub> methanation catalysts with varying nickel loadings. So far, the strategy for Binder Jet printed catalysts included printing of the metal oxide support followed by subsequent immobilization of the active species by impregnation. In contrast, the hereby presented method produces catalysts where the catalyst precursor material is directly incorporated into the printing feedstock, therefore facilitating the omission of an additional impregnation step. In general, 3D printing enables the design of more complex catalyst shapes in contrast to the presently industrially used shaping techniques. Furthermore, using co-precipitation for catalyst synthesis presents the advantage to generate precursors with well-dispersed metal species and to achieve a high metal loading, providing more opportunities for parameter variation during printing.

XRD and TGA analysis revealed that the prepared catalysts display characteristics analogous to conventionally prepared Ni-Al catalysts regarding the phase composition and reducibility with varying molar Ni/Al ratios despite the modified post-processing including slurry infiltration and several thermal treatments. For the catalyst NiAl11-20, a Ni particle size as small as 3.9 nm was achieved so that a sufficient metal dispersion can be accomplished with a powder-based 3D printed method and the concomitant processing parameters. Total surface area evaluation with N<sub>2</sub> physisorption revealed specific surface areas up to 192 m<sup>2</sup>/g<sub>cat</sub> and pore size analysis disclosed a highly porous catalyst structure comprising meso- and macropores so that the examined physico-chemical qualities cover a catalytically relevant area.

The catalysts NiAl11-20, NiAl21-20 and NiAl51-20 were successfully tested for their CO<sub>2</sub> methanation activity in a SPSR as a proof-of-principle. Increasing Ni/Al ratio positively affected the CO<sub>2</sub> conversion and methane yield. All three catalysts reached conversions between 96 to 99 % without significant CO formation. Furthermore, thermodynamic equilibrium was reached during this experiment.

To elucidate the detailed correlations between the additive manufacturing method, the physicochemical properties of the catalyst and the SPSR configuration, further investigations should be conducted. Due to a limited number of experimental studies on methanation reactions in a SPSR, the influence of pellet size, amount of pellets, catalyst shape, as well as heat and mass transfer on the catalytic performance is not entirely clarified. Computational approaches such as computational fluid dynamic (CFD) simulations could provide further insights into this matter. Furthermore, future experiments could address

drawbacks induced by the use of AM for catalyst manufacturing. A comparison of additively and conventionally manufactured nickel catalysts, e.g., by incipient wetness or wet impregnation could reveal differences in the metal distribution between various preparation techniques. More detailed activity tests and kinetic studies which can further clarify the influence of the processing steps related to 3D printing on the catalyst properties need to be conducted in order to investigate whether catalyst effectiveness is negatively affected by AM due to mass transfer limitations to the core of the pellet.

The binder jetting method offers a high freedom in design as no support structures are needed, and co-precipitation enables highly loaded and finely dispersed catalytic material for use as printing feedstock. In addition, the combination of additive manufacturing and SPSR experiments offers a holistic way to generate custom three-dimensional catalyst shapes which can be assessed as a whole in a lab-scale reactor setup. Furthermore, Binder Jetting introduces flexibility for catalytic parameter studies regarding the development and modification of physicochemical qualities combined with varying catalyst geometry, enabling fast assessment and optimization of catalytic performance measurements.

## 6.5 Supporting Information

### 6.5.1 Ni Species in Relation to the Distance from the Pellet Core

In order to analyze whether Ni exists in different species within the spherical 3D printed pellet as a function of the distance from the pellet core, XRD measurements were performed on a Rigaku MiniFlex of the pellet shell (outer) and the pellet core (inner) of the calcined Ni-Al catalysts (see Fig. 6.15). The outer shell material was scraped off with a scalpel whereas the inner core material was obtained by cutting a sphere in half and removing the core material for analysis. The powder samples were placed on a Si waver for XRD measurement.

Different Ni species could arise from temperature gradients within the pellet during the drying or calcination process or from mass transfer limitations during the burnout of the PVP binder material. Fig. 6.15 exemplarily compares the XRD patterns of the inner and outer pellet material of the calcined samples NiAl11-20\_c, NiAl31-20\_c and NiAl51-20\_c in order to reveal possible differences in phase composition.

Overall, the XRD patterns of the inner and outer Ni-Al pellet material are mostly congruent for each sample. Differences would be expected for the occurrence of NiO after

calcination. NiAl51-20\_c reflexes of the inner and outer pellet material are almost identical, whereas marginal differences in reflex intensity are observed for NiAl11-20\_c and NiAl31-20\_c. The (200) plane at  $2\theta = 43.3^\circ$  shows slightly more intensive reflexes for the inner core material than the outer shell material, but the remaining NiO reflexes are mostly similar for the two samples. The slight differences could stem from different PVP burnout behavior and resulting temperature maldistribution (hot spots) in the pellet core as the (200) reflex seems more intensive in the pellet core. However, no other Ni species

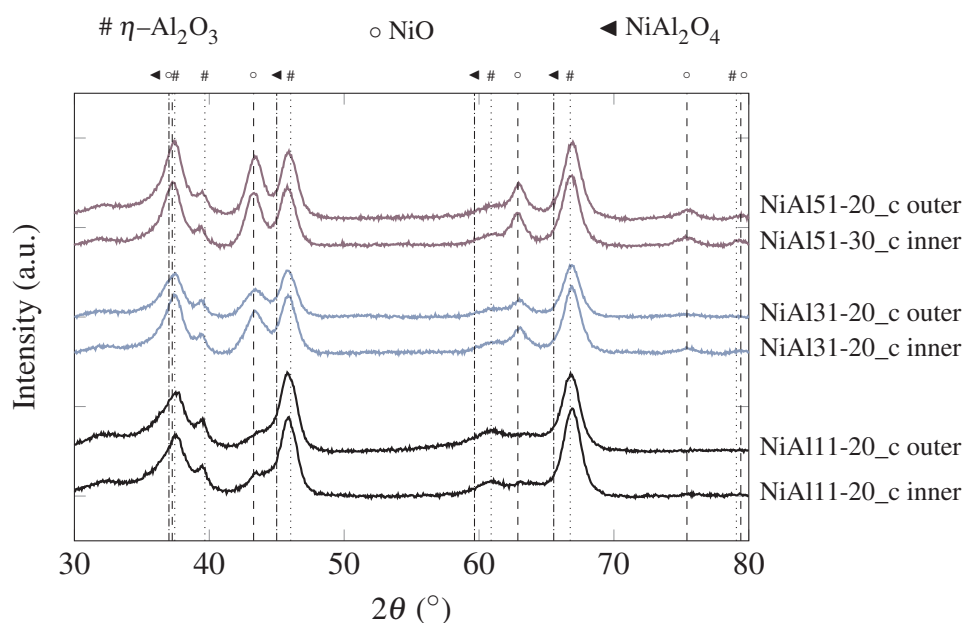


**Figure 6.15:** Exemplary XRD patterns of NiAl11-20\_c, NiAl31-20\_c and NiAl51-20\_c. The spherical 3D printed catalysts were used where the outer shell layer material (manually removed with a scalpel) was measured. The inner core material was measured separately.

which were not already existent in the bulk XRD measurements (see Fig. 6.5) are detected in Fig. 6.15. Conclusively, due to the absence of major differences, no significant effects on the generation of differing Ni species within pellets were observed in radial direction for the calcined spherical 3D printed Ni-Al pellets so that it can be assumed that the chemical composition is mostly homogeneous throughout the calcined catalyst.

## 6.5.2 Particle Size Distribution by TEM

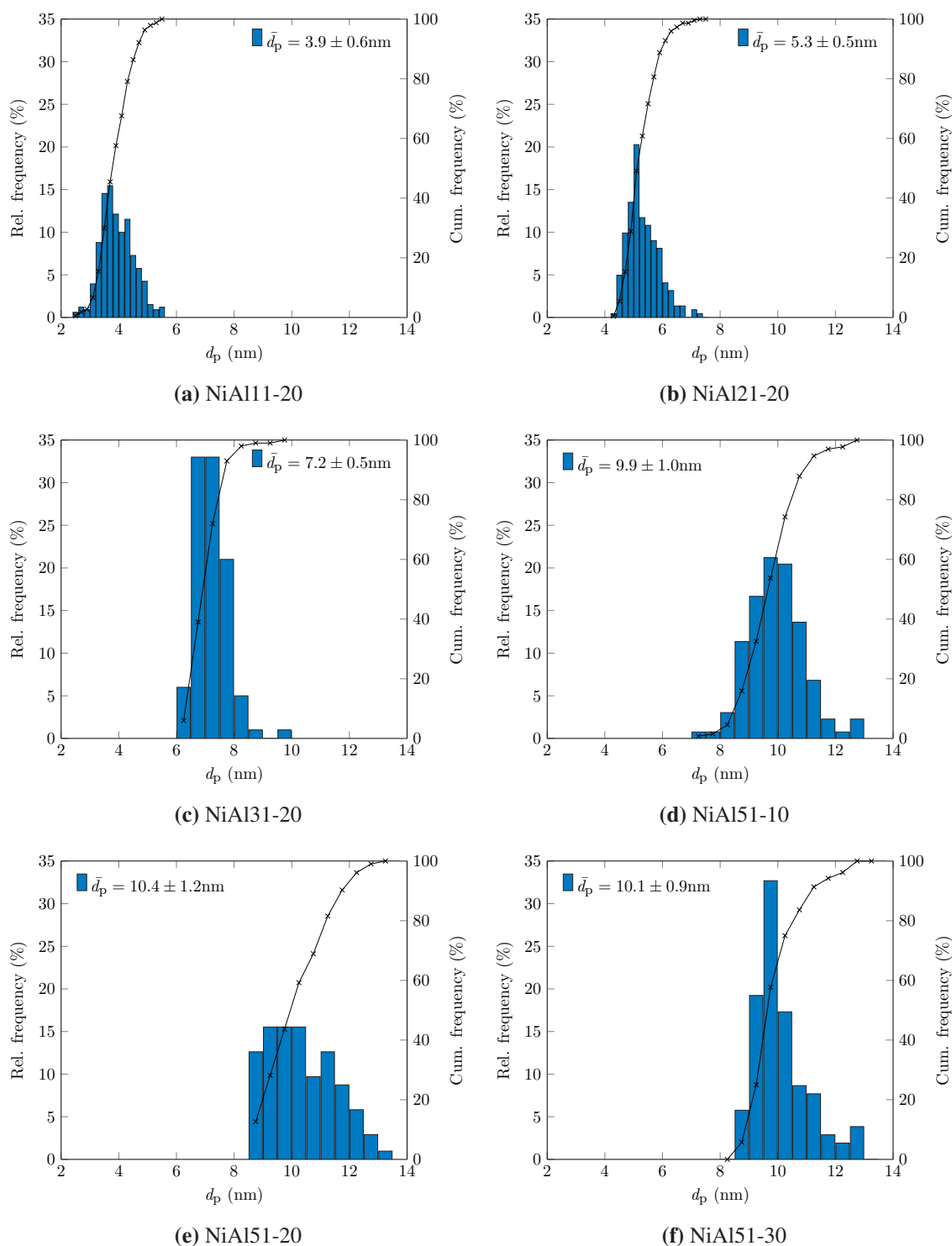


**Figure 6.16:** Particle size distributions of all Ni-Al catalysts determined by TEM analysis. Measurement of at least 100 particles per sample.

### 6.5.3 Pore Size Distribution Analysis by Mercury Intrusion Porosimetry

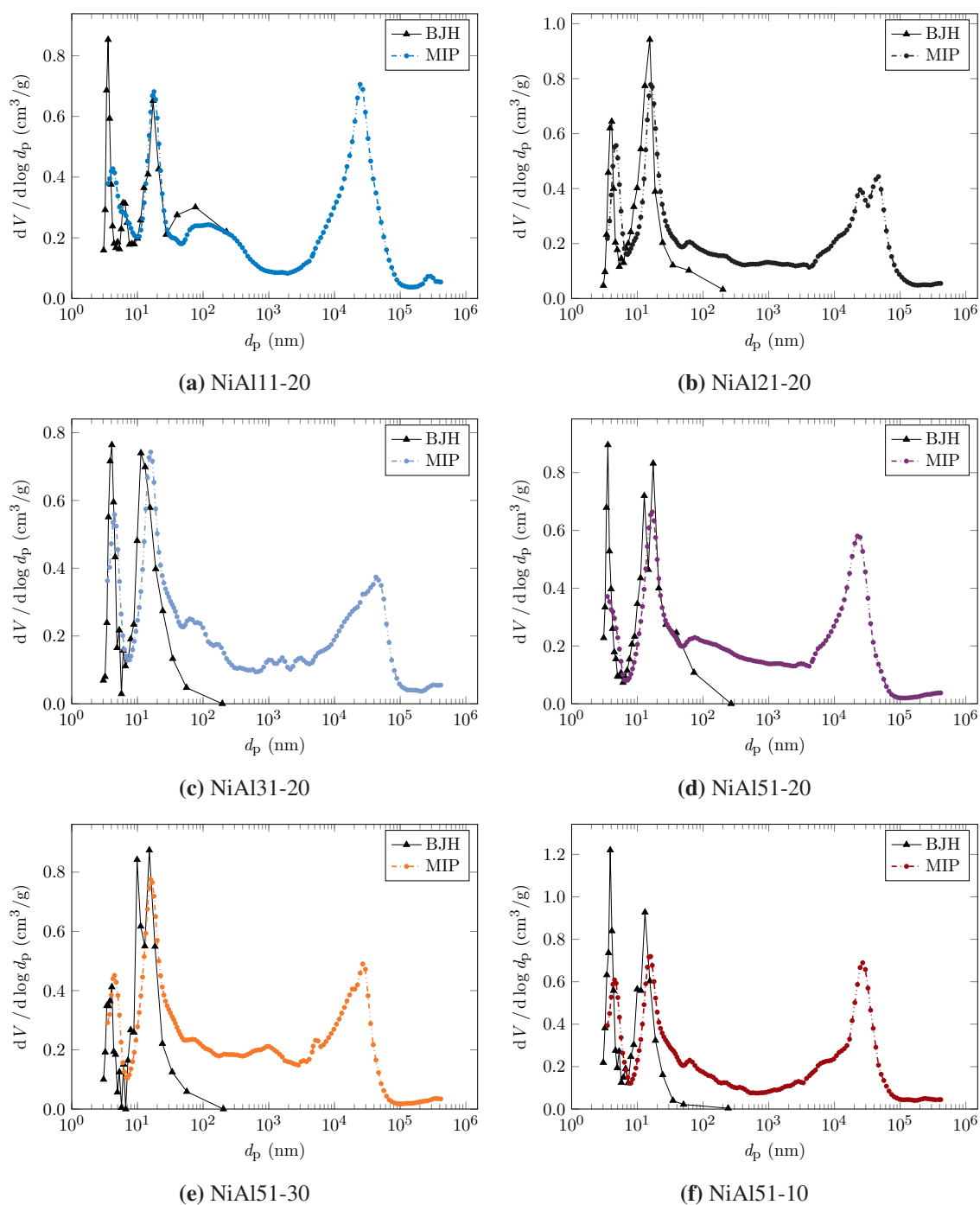


**Figure 6.17:** Comparison of pore size distributions obtained by gas adsorption and MIP for all 3D printed Ni-Al catalysts.

# 7 In Situ Impregnated Ni/Al<sub>2</sub>O<sub>3</sub> Catalysts Prepared by Binder Jet 3D Printing Using Nickel Nitrate-containing Ink

---

**This chapter was published in similar form in:**

H. M. Bui, T. Kratky, I. Lee, R. Khare, M. Hiller, S. Wedig, S. Günther, O. Hinrichsen, "In situ impregnated Ni/Al<sub>2</sub>O<sub>3</sub> catalysts prepared by binder jet 3D printing using nickel nitrate-containing ink", *Catalysis Communications*, **2023**, 106738, DOI 10.1016/j.catcom.2023.106738.

©2023 Elsevier B.V. All rights reserved.

---

## Abstract

The binder jetting printing technique enables in situ impregnation of alumina using a Ni(NO<sub>3</sub>)<sub>2</sub>-containing ink (NI), facilitating omission of impregnation. NI was compared to wet impregnation (WI). Full characterization by quasi-in situ XPS, XAS and TPR revealed the presence of Ni as NiAl<sub>2</sub>O<sub>4</sub> spinel. TPR analysis identified surface NiO and NiAl<sub>2</sub>O<sub>4</sub> species with facilitated reduction by NI, in addition to the respective species in bulk form. Post-processing affects active site accessibility by coverage. 3D printing limited the Ni loading, but XPS revealed higher metal dispersion by NI. CO<sub>2</sub> hydrogenation confirmed active Ni/Al<sub>2</sub>O<sub>3</sub> catalysts with enhanced activity by NI.

## 7.1 Introduction

Supported catalysts are the most common form of heterogeneous catalysts prepared by depositing small crystallites of an catalytically active component on a porous support [325]. The method of catalyst immobilization influences the catalyst performance since the resulting metal-support interaction controls crucial properties such as active phase dispersion and long-term stability. Apart from co-precipitation and the sol-gel method [326], wet or incipient wetness impregnation are the most relevant and frequently used preparation methods. In this process, the support is immersed in the impregnation solution, dried and subsequently reduced by calcination and/or reduction [325]. Numerous studies have extensively explored and compared the influence of mentioned catalyst immobilization methods on metal speciation, particle size, dispersion, reducibility and associated catalyst activity and deactivation behavior [180, 266, 301, 327–329] and they have proven correlations between the preparation technique and catalyst performance.

The usage of powdered catalysts is a standard approach for most academic questions. However, catalyst shaping is essential for the application of heterogeneous catalysts on a technical scale, especially in fixed bed reactors. Good abrasion resistance, mechanical durability, ease of separation from the reactants, and decreased pressure drop inside the reactor necessitate forming techniques such as agglomeration, spray granulation, tableting or extrusion to enlarge the size of the catalyst [330]. The latter two methods are well-established and represent the most commonly used catalyst shaping techniques on an industrial scale [331]. Related thereto, the active phase distribution in a formed catalyst (e.g. uniform, egg-shell, egg-white, egg-yolk) influences the performance of a catalytic reactor by varying accessibility of the active sites [87, 332, 333].

Based on the growing number of publications, additive manufacturing (AM) or 3D printing has been increasingly exploited for catalyst shaping to meet the growing interest in intensification of industrial and environmental heterogeneous catalysis [15, 42, 45, 46, 50, 334].

In general, catalysts can be 3D printed *indirectly* by manufacturing a template with a polymeric 3D printer. This mold is filled with a paste of ceramics or catalytic material and thermally treated to burn off the polymer to expose the monolithic catalyst structure [54–56]. *Direct* printing involves 3D printing without removable templates, namely printing of catalyst support for further impregnation or incorporation of the active phase into the printing feedstock.

Several printing techniques from the plethora of AM technologies available nowadays have been applied for printing of predominantly monolithic catalyst geometries. Direct Ink writing (DIW/robocasting) or fused deposition modeling (FDM) are extrusion-based principles and most commonly used due to their relatively intuitive material design, especially regarding processing of metal oxide feedstock [335–340]. Powder-based techniques oftentimes require more detailed material and process development. Selective laser melting (SLM) has been used to generate monolithic metal frameworks which are subsequently washcoated with catalytically active material [134, 341, 342]. The printing technique used in this paper is binder jetting (BJ), a powder-based AM technique. BJ allows for fabrication of highly porous ceramic bodies for catalysis [13, 21] while enabling relatively complex structures without support structures.

Previous studies on catalyst manufacturing strategies utilizing binder jetting exist. One of them includes printing of the metal oxide support which has to be followed by impregnation with the active phase [13]. The second strategy integrates powdery co-precipitated catalyst precursor into the printing powder [243]. This paper explores the preparation of binder jet 3D printed Ni/Al<sub>2</sub>O<sub>3</sub> catalysts by deposition of nickel containing ink onto Al<sub>2</sub>O<sub>3</sub> powder, therefore resembling impregnated Ni/Al<sub>2</sub>O<sub>3</sub> catalysts regarding their physicochemical properties. The nickel precursor is dissolved in the printing liquid which is deposited selectively and layer-by-layer onto the alumina print bed by the inkjet print head. This method constitutes an in situ impregnation of the support during 3D printing, thus omitting the successive impregnation step. Due to the ejection of fine liquid droplets, this method could influence the morphology of the active phase applied onto the support surface. Combined with the extensive freedom for catalyst forming provided by AM, the new manufacturing strategy could add improvements to conventional catalyst preparation procedures by offering tailor-made catalyst shapes coupled with effective active phase distribution.

## 7.2 Experimental

### 7.2.1 Catalyst Preparation by Binder Jetting with Ni-Containing Ink

The general manufacturing strategy is based on a previously presented method for alumina supports printed by binder jetting [13]. Fig. 7.1 depicts the setup of the printer used for catalyst printing. The powder reservoir and the print platform were filled with the printing

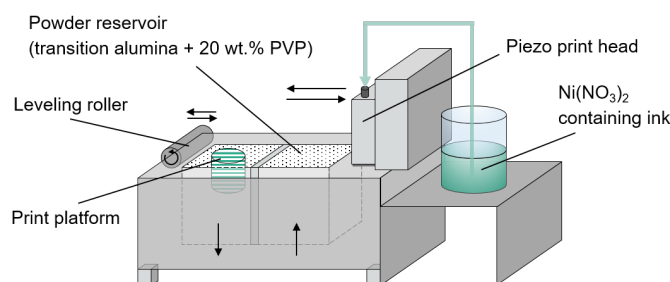
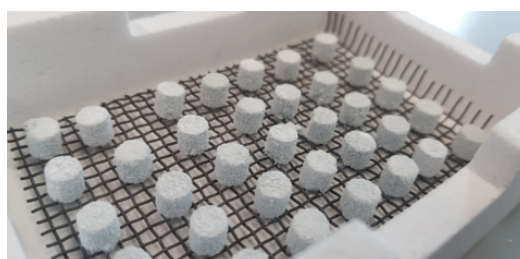


**Figure 7.1:** Schematic of the binder jetting printer used in this study.

powder consisting of 73 wt.% bayerite Pural BT (Sasol Chemicals, USA), 7 wt.% Actilox S40 (Nabaltec AG, Germany), and 20 wt.% of the solid binder polyvinyl pyrrolidone (PVP) Sokalan K17P (BASF SE, Germany). The aqueous printing liquid consisted of distilled water, 10 wt.% isopropyl alcohol, 10 wt.% 1,4-butanediol and varying amounts of nickel nitrate Ni(NO<sub>3</sub>)<sub>2</sub> · 6H<sub>2</sub>O (all purchased from Merck KGaA, Germany), depending on the desired Ni loading. The powder was selectively bound layer-by-layer with the Ni containing printing liquid which is conveyed from an ink reservoir by a drop-on-demand (DOD) shear-mode piezo inkjet printhead (508GS, Seiko Instruments GmbH, Japan) via hydrostatic pressure. After printing, the light green Ni nitrate impregnated alumina supports (diameter  $d$  = height  $h$  = 6 mm) were transferred to a drying oven to cure the PVP binder for at least 2 h (Fig. 7.2a) at 75 °C. Subsequently, the green parts



**(a)** Green part after curing at 70 °C. Light green color indicates deposition of nickel nitrate ink on alumina powder.



**(b)** Calcined at 600 °C. Light blue coloration due to predominant conversion of Ni precursor to nickel aluminate spinel.

**Figure 7.2:** Test cylinders at different processing stages printed by Ni ink deposition.

were debinded in a muffle furnace for 3 h at 600 °C in order to fully remove the binder, resulting in highly porous debinded samples. Subsequently, an aqueous boehmite slurry was slowly dripped onto the debinded parts until pore saturation for additional particle introduction by infiltration. Another calcination step (600 °C, 3 h) followed, resulting in a mechanically stable 3D printed nickel catalyst (Fig. 7.2b).

## 7.2.2 Catalyst Preparation by Wet Impregnation

Wet impregnated Ni catalysts were prepared using binder jet printed cylindrical alumina supports which were subsequently impregnated in an excess of nickel nitrate solution of adequate concentration. The  $\text{Al}_2\text{O}_3$  carriers were printed using the same powder mix as described in section 7.2.1 but using ink without any nickel nitrate. The detailed manufacturing procedure for porous alumina supports is described in a previous study [13]. Printed supports were immersed in an aqueous solution of  $\text{Ni}(\text{NO}_3)_2 \cdot 6\text{H}_2\text{O}$  with varying Ni concentration for 2 h under constant stirring. The liquid was then fully removed using a rotary evaporator. After drying, the precursors were calcined in a muffle furnace ( $450\text{ }^\circ\text{C}/600\text{ }^\circ\text{C}$ , 6 h).

## 7.2.3 Sample Nomenclature

Table 7.1 summarizes all samples characterized in this study. The novel nickel ink depo-

**Table 7.1:** Sample nomenclature of catalysts prepared by Ni ink deoposition (NI) and wet impregnation (WI) with respective nickel loading  $w_{\text{Ni}}$ , calcination  $T_{\text{calc}}$  and reduction Temperature  $T_{\text{red}}$ .

Sample	$w_{\text{Ni}}$ (wt.%) <sup>a</sup>	$T_{\text{calc}}$ (°C)	$T_{\text{red}}$ (°C)	Preparation method
<b>Calcined samples</b>				
NI_d_c600	3.4	600	-	Ni ink deposition, debindered
NI_i_c600	2.5	600	-	Ni ink deposition, infiltrated
<b>Reduced samples</b>				
NI_d_c600_r480	3.4	600	480	Ni ink deposition, debindered
NI_d_c600_r600	3.4	600	600	Ni ink deposition, debindered
NI_i_c600_r480	2.5	600	480	Ni ink deposition, infiltrated
WI_c600_r480	1.6	600	480	Wet impregnation
WI_c450_r480	1.8	450	480	Wet impregnation

sition 3D printing method (NI) was compared to the well-established wet impregnation (WI) method. The letters "d" and "i" denote debindered or infiltrated samples, respectively. The precursors were either calcined at  $450\text{ }^\circ\text{C}$  (c450) or  $600\text{ }^\circ\text{C}$  (c600) and reduced with  $\text{H}_2$  at  $480\text{ }^\circ\text{C}$  (r480) or  $600\text{ }^\circ\text{C}$  (r600).

## 7.2.4 Catalyst Characterization

### 7.2.4.1 Elemental Analysis

Ni loading was determined by graphite furnace atomic absorption spectroscopy (GFAAS), using an ICE 3500 AAS by Thermo Fisher Scientific. Ground samples were dissolved in boiling, fuming sulfuric acid and diluted with distilled water. Subsequently, 5 to 20  $\mu\text{L}$  of the diluted sample was inserted into the GFAAS and analyzed.

### 7.2.4.2 Compressive Test

Mechanical stability of the 3D printed catalysts were tested with a hardness tester with integrated size measurement (MultiTest 50, Dr. Schleuniger Pharmatron) by uniaxial compression test. Sample size for each measurement was 10. The tested geometries were cylinders measuring 6 mm in diameter and height. Testing direction was perpendicular to the cylinder axis, the bracket moving speed was set to 2 mm/s. The compressive strength  $\sigma_{\text{comp}}$  was calculated with Eq. 3.19 based on the fracture load  $F$  using the equation given by Timoshenko and Goodier [165].

### 7.2.4.3 Archimedes Buoyancy Method

Densities and void fractions of the printed and post-processed samples were acquired using the Archimedes buoyancy method according to DIN EN 623-2 [186, 187]. Distilled water was chosen as the fluid. The sample was degassed at 25 mbar in a rotary evaporator at ambient temperature before distilled water was added, following repressurization to atmospheric pressure. For density calculations, the sample was weighed in its dry, water-impregnated and submerged state.

### 7.2.4.4 X-ray Photoelectron Spectroscopy and CO<sub>2</sub> Hydrogenation Activity

X-ray photoelectron spectra (XPS) were recorded on a Leybold-Heraeus LHS 10 spectrometer using a non-monochromatized Al K $\alpha$  source (1486.7 eV). 3D printed cylindrical catalysts were ground prior to measurement. The obtained powders were pressed into cavities and measured as pellets ( $\sim 50$  mg). All spectra were recorded in an ultra-high vacuum chamber at a pressure below  $5 \cdot 10^{-8}$  mbar. The analyzer was operated at a constant

pass energy of 100 eV leading to an energy resolution with a full width at half-maximum (FWHM) of ca. 1.1 eV. The energy scale of the spectra was corrected for sample charging by using the Al 2s signal at 120.0 eV.

Reduction of the catalyst samples (50 mbar H<sub>2</sub>, 400 °C, 5 sccm, > 2h) and in situ CO<sub>2</sub> hydrogenation (2 mbar CO<sub>2</sub>, 8 mbar H<sub>2</sub>, 1 mbar Ar, 300 °C) were carried out in a preparation chamber directly attached to the XPS analysis chamber enabling sample transfers without exposing the catalyst to air. The composition of the gas phase was analyzed by a differentially pumped Pfeiffer Vacuum PrismaPro QMG 250 M3 quadrupole mass spectrometer which was operated at pressures below 10<sup>-6</sup> mbar. The intensity of all traces were scaled to the intensity of Ar ( $m/z = 40$ ) to account for volume contraction upon CO<sub>2</sub> hydrogenation.  $m/z = 15$  was used as characteristic fragment for the partial pressure of CH<sub>4</sub>. The intensity of  $m/z = 28$  indicating the partial pressure of CO was corrected for the fraction resulting from CO<sub>2</sub> fragmentation by subtracting the intensity of  $m/z = 44$  multiplied by the fragmentation ratio. The fragmentation ratio was determined by the intensity ratio of  $m/z = 28$  to  $m/z = 44$  in the initial feed gas as the entire  $m/z = 28$  intensity is caused by CO<sub>2</sub> fragmentation only. Details of the experimental setup and the activity measurements are given in the Supporting Information.

#### 7.2.4.5 Ni K-edge X-ray Absorption Spectroscopy

Ni K-edge X-ray absorption spectroscopy (XAS) measurements were carried out on beamline P65 at PETRA III of DESY in Hamburg, Germany. Reduced samples were reduced ex situ at 480 °C or 600 °C. Furthermore, samples were kept under inert conditions after reduction and transferred to a glovebox, where the samples were ground and filled into a quartz capillary with a diameter of 2 mm. A double-crystal Si(111) monochromator was used to adjust the incident photon energy, and the spectra were recorded with ionization chambers in transmission and in total fluorescence yield using a passivated implanted planar silicon (PIPS) detector. ATHENA software was used for the background processing. XAS normalization followed standard protocol used within the Athena software [343].

#### 7.2.4.6 Temperature Programmed Reduction

Temperature programmed reduction (TPR) was measured on a Micromeritics Autochem II analyzer equipped with a thermal conductivity detector (TCD). Pre-treatment by degassing at 300 °C for 2 h under inert gas flow had no influence on the TPR signals so that

no outgassing was necessary. About 300 mg of sample was heated at a rate of 5 K/min until 1100 °C. 5% H<sub>2</sub>/Ar was used as reducing gas with a flow of 30 mL/min [160]. Evolving H<sub>2</sub>O was frozen out in a cold trap using an isopropyl alcohol/liquid N<sub>2</sub> frigorific mixture.

## 7.3 Results

### 7.3.1 Proof of Concept by Preliminary Printing Tests

The feasibility of the Ni ink deposition method was verified by preliminary tests. Ni containing inks with varying molar concentrations of nickel nitrate were used as printing liquid and deposited on the alumina print bed (see Table 7.2). The final Ni loading can be adjusted by the concentration of nickel nitrate in the ink or the amount of deposited nickel ink during the printing process. Naturally, a higher concentration of Ni(NO<sub>3</sub>)<sub>2</sub> in the printing liquid increases the final Ni loading  $w_{\text{Ni}}$  of the catalyst. However, the permitted ink pH range declared by the hardware manufacturer needs to be considered. The ink pH decreases with increasing nickel nitrate concentration so that the print head compatibility poses an upwards limitation regarding nickel salt concentration in the ink. Moreover, the liquid drop size generated by the print head as well as the required amount of ink for adequate powder bed saturation determines the final metal loading of the 3D printed catalyst.

**Table 7.2:** Molar nickel nitrate concentration  $c_{\text{Ni(NO}_3)_2}$  of used ink, its pH, resulting Ni loading of the catalyst  $w_{\text{Ni}}$  and sample densities  $\rho$  after final post-processing.

$c_{\text{Ni(NO}_3)_2}$ (mol/L)	pH of ink	$w_{\text{Ni}}$ (wt.%)	$\rho_{\text{app,s}}$ (g/cm <sup>3</sup> )	$\epsilon_{\text{open}}$
3.0	1.5	3.4	3.2	0.74
2.0	2.5	1.8	3.1	0.74
1.0	3.2	1.0	3.0	0.74
0.5	3.9	0.5	3.1	0.76

Fig. 7.3 presents the results of compression tests for samples conducted after the de-binding step and in their final state after second calcination. The compressive strength of debindered samples is low in general with values below 0.08 MPa since the evaporation of PVP leads to high porosity and voidage, decreasing the number and strength of contacting points between the alumina particles. However, their  $\sigma_{\text{comp}}$  indicates a trend towards increased mechanical stability with increasing pH of the ink. Therefore, we can infer that

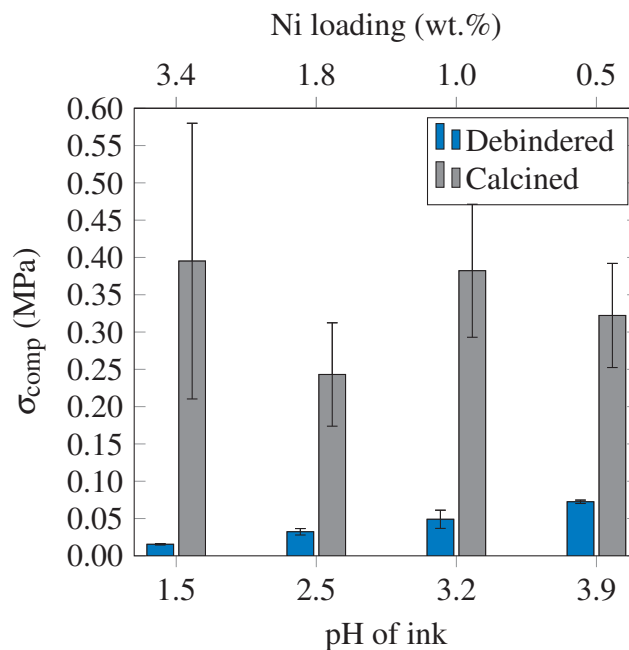


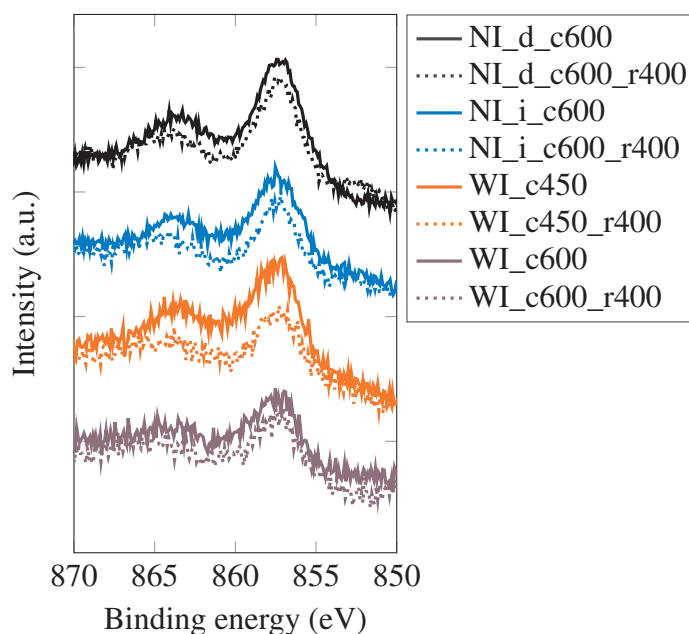
**Figure 7.3:** Compressive strength  $\sigma_{\text{comp}}$  of debinded (blue) and calcined (gray) test cylinders for varying pH values of the Ni ink (see Table 7.2).

decreased ink pH impairs the binding ability of PVP to consolidate the green part, the unprocessed geometry formed immediately after 3D printing. After drip infiltration with boehmite slurry and subsequent calcination, compression strength increases significantly for all samples. Considering the relatively large standard deviation of  $\sigma_{\text{comp}}$  for calcined parts, the final mechanical stability is similar for all investigated samples, ranging between  $0.24 \pm 0.07$  MPa and  $0.40 \pm 0.18$  MPa. Therefore, the infiltration step is crucial for the binder jetting procedure and decisive for mechanical robustness and practical applicability of the catalyst inside a chemical reactor.

The catalytically relevant open porosity  $\epsilon_{\text{open}}$  and the apparent solid density  $\rho_{\text{app,s}}$  in dependence of the nickel nitrate concentration and the ink pH are tabulated in Table 7.2.  $\rho_{\text{app,s}}$  is defined by the sample mass divided by the total volume of the solid including closed voids.  $\rho_{\text{app,s}}$  and  $\epsilon_{\text{open}}$  remain nearly constant throughout all four studied samples (Table 7.2), meaning that the catalytically accessible surface area is similar regardless of the pH of the ink. Thus, the NI method allows fabrication of catalysts with a consistent pore structure. Moreover, the porosity and specific surface area values agree with results determined in a previous study which introduced the basic catalyst support printing process this paper is based on [13] so that the reproducibility of the printing process is given. Results for the specific surface area can be taken from Table 7.4 in the Supporting Information.

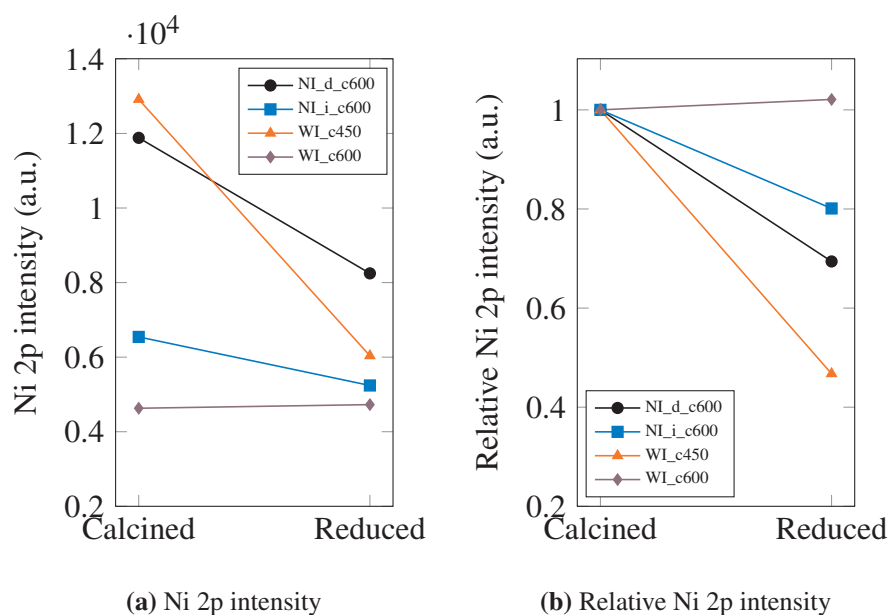
### 7.3.2 XPS Analysis

Fig. 7.4 displays the Ni 2p core level spectra of the catalysts synthesized by Ni ink deposition before (NI\_d\_c600) and after post-processing (NI\_i\_c600) as well as the samples obtained by conventional impregnation after calcination at 450 °C and 600 °C (WI\_c450 and WI\_c600, respectively). The intensity of the spectra is scaled to the Al 2s peak



**Figure 7.4:** XPS Ni 2p spectra of NI\_d (debindered), NI\_i (infiltrated), and WI samples, calcined at 450 °C (c450) and 600 °C (c600, solid line) and reduced at 400 °C (r400, dotted line).

intensity as well as the Ni loading so that the intensity reflects the amount of Ni present on the sample surface. The binding energy of the Ni 2p main peak and its satellite is centered around 857.3 eV and 863.4 eV, respectively, regardless of the synthesis method and calcination temperature. Both binding energy and peak shape are characteristic for Ni<sup>2+</sup> and expected for Ni/Al<sub>2</sub>O<sub>3</sub> catalysts after calcination [180]. Drip infiltration of the printed catalysts with a boehmite slurry physically covers the Ni surface species, leading to an attenuation of the Ni 2p signal as observed by the surface sensitivity of XPS. Thus, the intensity of the Ni 2p core level of NI\_d\_c600 exceeds the one of NI\_i\_c600 by a factor of almost 2, indicating an influence of the AM post-processing on the calcined samples (see Fig. 7.5a). The Ni ink deposition method reveals an up to three times higher Ni 2p intensity compared to conventional Ni wet impregnation after calcination at the same conditions (see Fig. 7.5a). The increased signal intensity proves a higher Ni coverage on the oxidic support structure. As intensity correction for slightly differing metal loadings was executed, a higher coverage of Ni can be derived from smaller Ni oxide particles and, thus, a higher metal oxide dispersion on the catalyst surface. The



**Figure 7.5:** Ni 2p intensities of calcined and reduced samples.

increased Ni dispersion might be introduced by the binder jetting 3D printing process as small ink droplets are generated when Ni nitrate solution is jetted through the fine nozzles of the printhead.

Surprisingly, Fig. 7.5a also shows that lowering the calcination temperature from 600 °C to 450 °C results in a three times higher Ni 2p intensity for the WI catalysts. Note that a calcination temperature of 600 °C is required for entire removal of the binder materials in NI samples and cannot be decreased [13]. As the preparation by wet impregnation creates Ni(NO<sub>3</sub>)<sub>2</sub> particles on the alumina support, calcination converts the nitrate to an oxide. Although sintering of NiO particles upon calcination at a higher temperature cannot be ruled out entirely, the lower Ni coverage on the surface at elevated temperatures is likely explained by Ni bulk diffusion. The formation of NiAl<sub>2</sub>O<sub>4</sub> spinel structures instead of NiO/Al<sub>2</sub>O<sub>3</sub> is thermodynamically favored [344]. This could occur by diffusion of nickel and oxygen ions through the aluminate [345], counterdiffusion of NiO and Al<sub>2</sub>O<sub>3</sub> through the spinel layer or counterdiffusion of Ni<sup>2+</sup> and Al<sup>3+</sup> [346]. Huang et al. reported on the formation of different nickel species as a function of the Ni loading in wet impregnated Ni/Al<sub>2</sub>O<sub>3</sub> systems and found the exclusive formation of NiAl<sub>2</sub>O<sub>4</sub> at weight loadings below 1 % while both NiO and NiAl<sub>2</sub>O<sub>4</sub> are formed at higher Ni loadings [327]. This goes in line with our spectroscopic results; the fairly low Ni loading of 1.7 wt.% on average favors predominant formation of NiAl<sub>2</sub>O<sub>4</sub>. The preceding diffusion of Ni into the alumina structure reduces the amount of Ni surface species leading to a strongly diminished Ni 2p signal. At lower calcination temperatures, Ni bulk diffusion is kinetically hindered so that the metal oxide remains on the catalyst surface as observed by a significantly higher Ni 2p intensity after calcination at 450 °C. Those findings are supported by quasi-in situ XPS

analysis after reduction of all samples in 50 mbar of hydrogen at 400 °C (see dotted lines in Fig. 7.4).

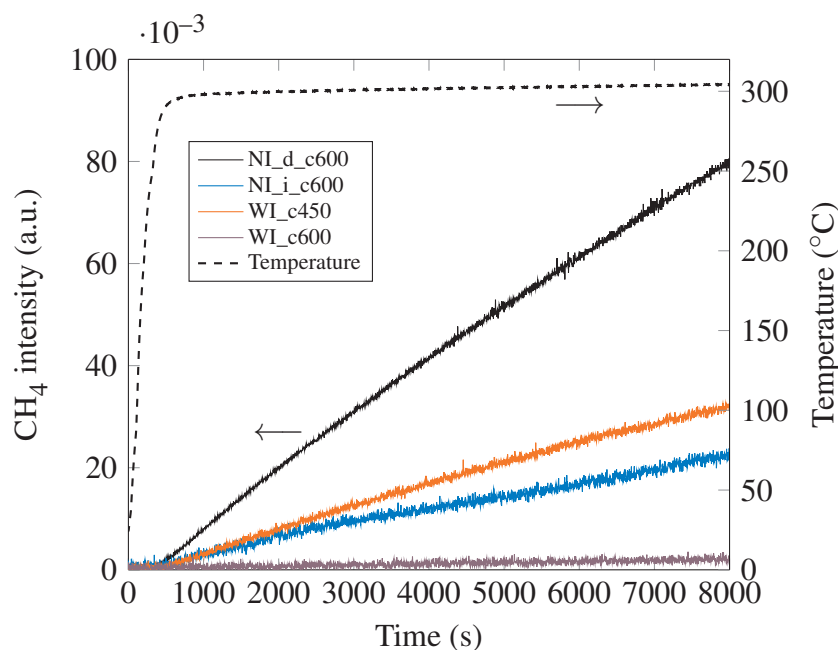
While Ni 2p peak shape and intensity remain constant for the WI\_c600 catalyst, the intensity of WI\_c450 is decreased by ~55 % compared to the calcined state (see Fig. 7.5b). The low amount of Ni species on the WI\_c600 surface is presumably incorporated in a nickel aluminate spinel structure and, hence, hard to reduce. In contrast, Ni<sup>2+</sup> species on the WI\_c450 surface are strongly affected by the reductive treatment as can be deduced from the change in signal intensity. However, no metallic Ni 2p component is found in XPS. This might originate from the formation of metallic particles which do not contribute to the Ni 2p peak intensity if they cover a negligible surface fraction of the support. It is well known that reduction of co-precipitated nickel aluminum mixed oxides reveals metallic nanoparticles on a Ni-poor mixed oxide surface [306, 347]. As the Ni<sup>0</sup> particles contribute less to the overall surface area than homogeneously distributed Ni<sup>2+</sup> in the mixed oxide, a lower Ni 2p intensity is observed. Considering the loss in Ni 2p intensity during reduction of WI\_c450, the expected intensity of the metallic component might be below the detection limit due to the low Ni loading.

Reduction of NI\_d\_c600 and NI\_i\_c600 leads to a decrease of the Ni 2p signal of 30 % and 20 %, respectively (see Fig. 7.5b), which corresponds to the portion of Ni<sup>0</sup> particles in coexistence with Ni<sup>2+</sup> species. Since the Ni<sup>2+</sup> species exclusively cause the Ni 2p photoemission yield, the XPS data show that in both cases, the Ni<sup>2+</sup> present at the catalyst surface cannot be reduced completely under typical activation conditions used for Ni/Al<sub>2</sub>O<sub>3</sub> catalysts. This confirms the formation of nickel aluminate spinel structures upon calcination at 600 °C, which are barely reducible (see TPR studies discussed in section 7.3.4 further below). The higher reducibility of the samples before AM post-processing (NI\_d\_c600) corroborates blocking of the Ni species by infiltration with boehmite slurry. Covering the surface Ni by alumina inhibits the accessibility by the reductive gas atmosphere and, thus, formation of metallic Ni particles significantly. Nonetheless, 20 % of the Ni is still reduced under mild conditions, proving the successful fabrication of Ni/Al<sub>2</sub>O<sub>3</sub> catalysts by the novel Ni ink deposition method.

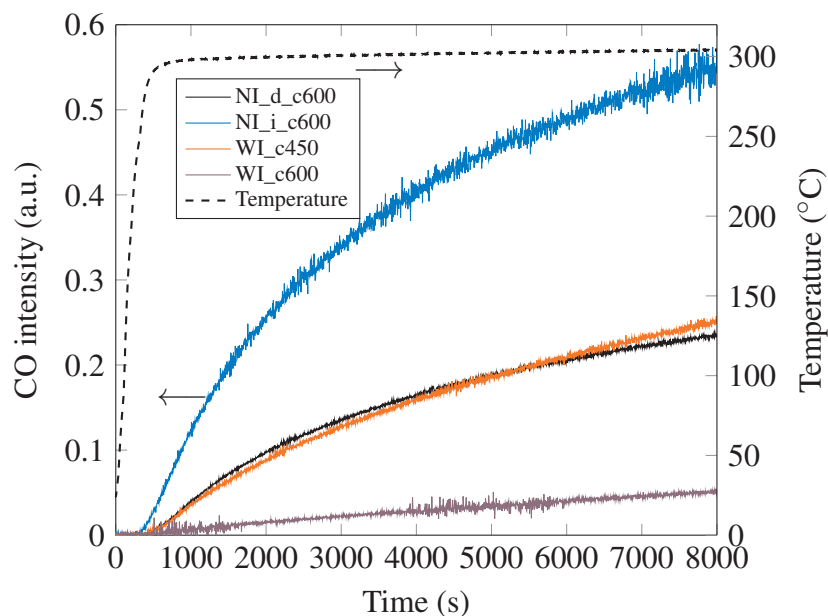
### 7.3.2.1 CO<sub>2</sub> Hydrogenation Activity

After reducing the NI and WI samples, their catalytic activity for the hydrogenation of CO<sub>2</sub> was studied by converting a gas mixture of CO<sub>2</sub> and H<sub>2</sub> ( $p = 10$  mbar, CO<sub>2</sub>/H<sub>2</sub> = 1/4) at 300 °C in a batch-type reaction cell (for experimental details, see Supporting Information). The mass traces of the reaction products CH<sub>4</sub> and CO are depicted in Fig. 7.6. The

methanation rate is slow for all analyzed samples while CO is the main product. Comparison with a co-precipitated Ni-Al benchmark catalyst reveals that the most active 3D printed catalyst exhibits a CO<sub>2</sub> methanation rate that is more than two orders of magnitude slower (see Fig. 7.13 in the supplementary materials). Wet impregnated WI\_c600 shows



(a) CH<sub>4</sub> signal intensity.



(b) CO signal intensity.

**Figure 7.6:** Quadrupole mass spectrometry signal intensities of the CO<sub>2</sub> hydrogenation reaction products methane and carbon monoxide. Feed gas composition: CO<sub>2</sub>/H<sub>2</sub>/Ar = 2/8/1.

negligible activity in general, producing almost no CH<sub>4</sub> (Fig. 7.6a) and only a minor

amount of CO (Fig. 7.6b). The activity of the corresponding WI\_c450 is significantly higher, which conforms with the XPS findings. The higher amount of surface Ni and enhanced reducibility improve the catalytic activity of the wet impregnated sample calcined at lower temperatures. Catalysts fabricated with Ni ink deposition yield the highest activities. While the debindered sample NI\_d\_c600 favors CH<sub>4</sub>, the selectivity is driven towards CO after infiltration with boehmite slurry and subsequent calcination. Based on the XPS surface analysis, this might originate from a lower Ni coverage combined with an inferior reducibility after AM post-processing. The CO/CH<sub>4</sub> selectivity and reaction pathway have been proven to be highly sensitive to the Ni particle size or dispersion [348]. Wu et al. [349] studied the CO<sub>2</sub> hydrogenation on Ni/SiO<sub>2</sub> catalysts with a Ni loading of 0.5 wt.% and 10 wt.% and revealed that the selectivity towards methane is significantly enhanced on large Ni particles (high Ni loading), whereas CO formation was preferred at low Ni loadings. Co-adsorbed CO<sub>2</sub> and H<sub>2</sub> on Ni<sup>0</sup> particles form the key intermediate *m*-HCOO which is subsequently decomposed to CO and may follow a consecutive reaction pathway to CH<sub>4</sub>. However, due to the low coverage of the active centers by H<sub>2</sub> at low metal loadings, CO formation is favored [349, 350].

### 7.3.3 Ni K-edge XAS Analysis

Samples reduced at two different temperatures (480 °C and 600 °C) were analyzed regarding the chemical form and oxidation state of Ni to investigate the presence of nickel aluminate by 3D printing. Furthermore, the preparation methods NI and WI were compared as well as the influence of post-processing.

#### 7.3.3.1 Calcined State

Ni K-edge XANES spectra of the calcined samples show a pre-edge peak at around 8335 eV (see exemplary spectrum Fig. 7.7a, all other spectra see Fig. 7.10), which is attributed to dipole forbidden 1s to 3d transitions, thus confirming the Ni<sup>2+</sup> character of the sample [351, 352]. Furthermore, the white line area strongly resembles that of the reference samples, indicating the dominant presence of nickel as Ni<sup>2+</sup> [353]. The pre-edge feature as well as the edge energy of all calcined samples notably match with NiAl<sub>2</sub>O<sub>4</sub>, substantiating the surface analysis by XPS that not only the catalyst surface but also the bulk material mainly contains Ni aluminate species. Fig. 7.7a presents the Ni K-edge XANES of NI\_i\_c600. The spectra of the remaining calcined samples NI\_d\_c600, WI\_c600 and WI\_c450 can be accessed through the Supporting Information (Fig. 7.10). The strong nickel aluminate character of all samples indicates that calcination

at 450 °C as well as 600 °C is sufficient to induce growth of nickel aluminate spinel due to incorporation of nickel particles into the alumina lattice. Despite the overall similar-

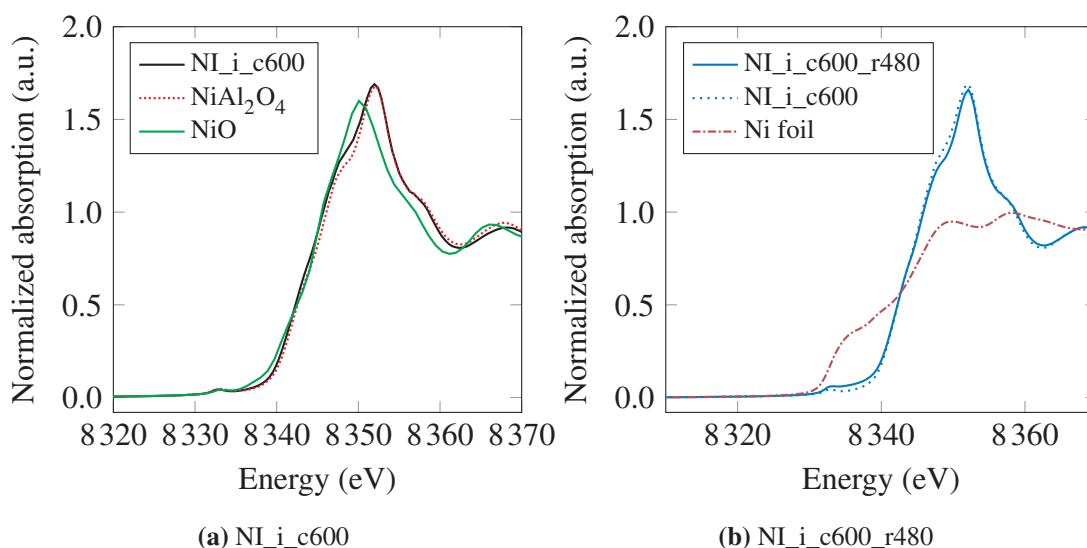


**Figure 7.7:** Ni K-edge XANES spectrum of (a) NI\_i\_c600 (infiltrated, calcined at 600 °C) and references NiAl<sub>2</sub>O<sub>4</sub> and NiO and (b) NI\_i\_c600\_r480 (reduced at 480 °C) and corresponding references NI\_i\_c600 and Ni foil.

ity to NiAl<sub>2</sub>O<sub>4</sub>, the effect of calcination temperature is visible comparing the samples WI\_c450 and WI\_c600 (see Fig. 7.10c and 7.10d, respectively). WI\_c450 shows a more pronounced NiO character at about 8348 eV, distinguishing it from the wet impregnated sample calcined at 600 °C (WI\_c600) which matches with Ni aluminate across the entire energy range. This observation suggests that at a calcination temperature of 450 °C NiO is preferably formed than at 600 °C and  $T_{\text{calc}}$  affects the Ni speciation on the catalyst support surface. Fig. 7.8 shows the  $k^2$ -weighted Fourier-transformed EXAFS at the Ni K-edge of calcined NI\_i\_c600 and its reduced form NI\_i\_c600\_r480. Both samples show a prominent peak at ca. 1.5 Å, which corresponds well to backscattering from oxygen, directly bonded to Ni. This feature is in good agreement for first shell M-O metal oxide bonds, which are expected to be located between 1 to 2 Å. Furthermore, the prominent peak at ca 2.5 Å is associated to Ni-Ni scattering paths of metal oxides. The mentioned features of calcined NI\_i\_c600 show approximately the same positions compared to the NiO reference, reconfirming a Ni<sup>2+</sup> character of the calcined samples.

### 7.3.3.2 Reduced State

All calcined samples were reduced ex situ at 480 °C and kept under inert conditions afterwards. NI\_d\_c600 was additionally reduced at 600 °C to examine the effect of reduction temperature. Ni foil was the metallic Ni standard and the corresponding calcined sample

acted as the fully oxidized reference sample. Fig. 7.7b presents an exemplary Ni K-edge XANES spectrum of a reduced sample. Remaining plots are displayed in the Supporting Information (Fig. 7.11). The extent of reduction to metallic nickel is low in general since the character of the calcined sample is mostly maintained, as seen in Fig. 7.10. The existence of the pre-edge feature at 8333 eV for all samples confirms an incomplete reduction of Ni<sup>2+</sup> to metallic nickel which does not display this pre-edge peak.

Although XANES shows small signs of reduced Ni, the k<sup>2</sup>-weighted Fourier-transformed EXAFS at the Ni K-edge of different NI prepared samples exhibits different features. After reduction, NI\_i\_c600\_r480 shows a decrease and broadening of the Ni-Ni scattering paths, see Fig. 7.8. The broadening is interpreted as partial reduction of Ni(II) species to

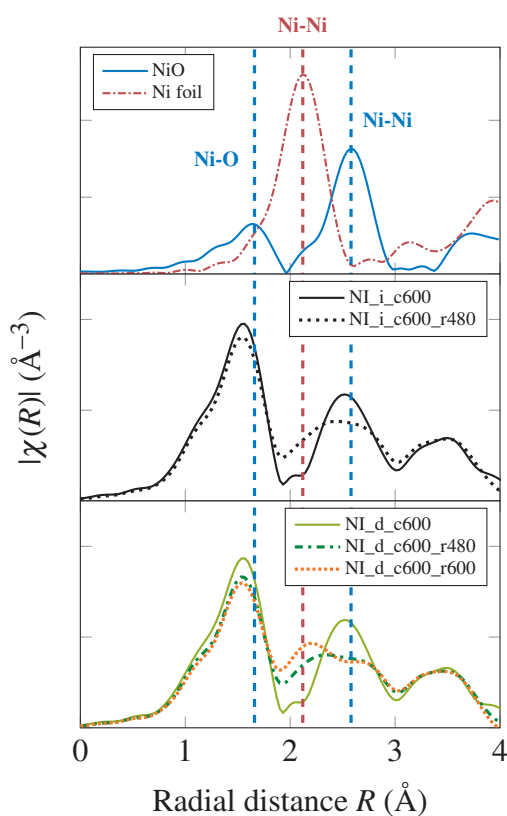


**Figure 7.8:** Comparison of k<sup>2</sup>-weighted Fourier-transformed EXAFS of different NI prepared samples at the Ni K-edge. Bottom: Debindered samples reduced at 480 °C and 600 °C. Middle: Infiltrated samples, calcined and reduced. Top: References.

metallic Ni. As seen in Fig. 7.8, Ni metal foil shows the first shell Ni-Ni at ca. 2.1 Å. In fact, NI\_i\_c600\_r480 exhibits a broadening towards 2.1 Å, indicating a certain extent of reduction to metallic nickel. This phenomenon is even more distinct for the sample NI\_d\_c600 which is also illustrated in Fig. 7.8. Upon increase of reduction temperature from 480 to 600 °C, the broadened Ni-Ni peak of the metal oxide shifts about 0.7 Å towards a distinct Ni-Ni feature at ca. 2.1 Å, corroborating that reduction takes place.

### 7.3.4 TPR Analysis

Fig. 7.9a compares the normalized  $H_2$  consumption by TPR of two Ni catalysts prepared by Ni ink deposition, one being debindered and the other infiltrated (d/i). Degrees of reduction ranging from 95 to 100 % indicate that TPR conducted until 1100 °C fully reduces all present Ni species to metallic  $Ni^0$  (see  $d_{red,TPR}$  in Table 7.3).

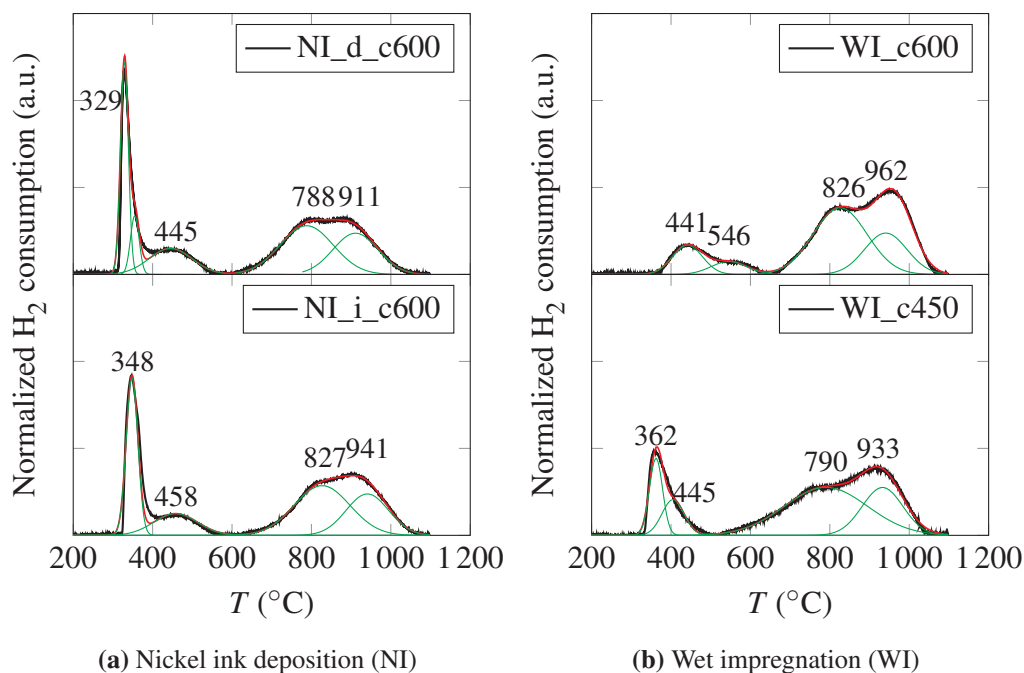


**Figure 7.9:** TPR profiles with normalized  $H_2$  consumption of (a) catalysts printed by nickel ink deposition (NI) after infiltration/debinder (i/d) and calcination at different temperatures (c450/c600), and (b) wet impregnation (WI), calcined at different temperatures (c450/c600).

Both NI samples reveal four reduction peaks with the first and the last two ones overlapping, thus representing two regions. NiO contributes to the first two peaks and Ni aluminate species are associated with the last two peaks, corroborating previous findings that multiple Ni species can coexist, depending on the preparation conditions (calcination temperature, duration of calcination, Ni loading) [311, 314, 354, 355]. It is generally known that NiO can already start interacting with  $Al_2O_3$  at about 400 °C and that the amount and crystallinity of  $NiAl_2O_4$  grows with increasing  $T_{calc}$  and  $t_{calc}$  [354].

The two NiO signals can be divided into a relatively sharp low temperature peak at 330 to 350 °C and a broad higher temperature peak at 420 to 460 °C. The low temperature NiO peak is assumed to stem from 3D printing with nickel ink which finely disperses small Ni particles onto the alumina support. This "surface NiO" (sNiO) is weakly bound and therefore easily reducible at temperatures below 350 °C. The second broad peak is

matched to bulk nickel oxide (bNiO). Comparison of the TPR signals in Figs. 7.9a and 7.9b confirms the prevalence of sNiO by nickel ink deposition via binder jetting in contrast to conventionally wet impregnated samples. Table 7.3 lists the fraction of present Ni species determined by peak fitting of the TPR signal and reveals that sNiO represents 26 to 30 % of NI samples whereas WI samples contain half of the amount of sNiO (WI\_c450) or even none (WI\_c600). The set of two broad reduction peaks above 780 °C match the

**Table 7.3:** Ni loading  $w_{\text{Ni}}$ , degree of reduction  $d_{\text{red,TPR}}$  of NI and WI samples determined by TPR analysis weight percentage of nickel oxide (surface NiO: sNiO, bulk NiO: bNiO) and Ni aluminate determined by peak fitting of H<sub>2</sub> consumption determined by TPR.

Sample	$w_{\text{Ni}}$ (wt.%)	$d_{\text{red,TPR}}$ (wt.%)	NiO (wt.%)	sNiO (wt.%)	bNiO (wt.%)	NiAl <sub>2</sub> O <sub>4</sub> (wt.%)
NI_i_c600	3.0	108	43	28	15	65
NI_d_c600	3.5	100	43	28	14	57
WI_c600	2.5	99	17	0	17	82
WI_c450	2.4	95	22	12	10	73

reduction temperature of nickel aluminate species since sufficient energy is provided for integration of Ni ions into the alumina lattice. Analogous to NiO, the signal at 780 to 830 °C could stem from weakly bound NiAl<sub>2</sub>O<sub>4</sub> and the high temperature peak at 910 to 940 °C results from bulk crystalline NiAl<sub>2</sub>O<sub>4</sub>. TPR profiles of NiAl<sub>2</sub>O<sub>4</sub> featuring two high-temperature peaks were reported before [356–359]. Furthermore, pure bulk NiO and NiAl<sub>2</sub>O<sub>4</sub> were additionally analyzed by TPR as reference (see Supporting Information, Fig. 7.12) and confirm the presented regions of reduction temperature in Figs. 7.9a and 7.9b. The bulk reference samples only feature the reduction peaks for bNiO and bulk NiAl<sub>2</sub>O<sub>4</sub> at about 550 °C and 900 °C, respectively and therefore confirm the presence of surface Ni species with facilitated reduction behavior when catalysts are prepared by NI. Nevertheless, with a fraction of about 60 %, nickel aluminate is overall predominantly formed in contrast to nickel oxide.

Although the NI samples differ in post-processing stage (d/i), the ratio of NiO to NiAl<sub>2</sub>O<sub>4</sub> unchangingly approximates 40:60 (see Table 7.3), indicating that under the studied conditions, NI binder jetting generates Ni/Al<sub>2</sub>O<sub>3</sub> catalysts with a consistent Ni species composition. The different post-processing conditions shift the TPR signals of the NI catalysts as shown in Fig. 7.9a. Comparing NI\_i\_c600 and NI\_d\_c600, infiltration shifts the reduction temperature to higher temperatures. Since the in situ impregnation with Ni nitrate containing ink facilitates fine dispersion of nickel (as shown with XPS), and a low Ni loading, nickel aluminate is formed easily, even at relatively low  $T_{\text{calc}}$  which would normally yield less spinel phase [360].

## 7.4 Conclusion

This work advances heterogeneous catalyst preparation by introduction of a fabrication method for supported nickel catalysts utilizing the powder-based AM technique binder jetting. Preliminary tests provided a proof of concept for the feasibility of printing mechanically stable  $\text{Al}_2\text{O}_3$ -supported Ni catalysts via BJ where the nickel precursor is directly integrated into the printing process, therefore omitting a subsequent impregnation step.

The 3D printed catalysts were characterized thoroughly using XPS, XAS and TPR. All three methods complemented each other by providing insights into the simultaneous formation of NiO and  $\text{NiAl}_2\text{O}_4$  with varying ratios considering the underlying preparation conditions such as the preparation method (NI/WI) and thermal preparation conditions. NI generated Ni catalysts with similar characteristics as conventionally wet impregnated samples prepared under comparable conditions. Due to Ni loadings of max. 3.5 wt.%, facilitated incorporation of nickel into the alumina support resulted in the formation of about 60 wt.% nickel aluminate spinel for in situ impregnated catalysts printed by BJ. XPS analysis evidenced a finer nickel dispersion using the NI method than wet impregnation due to the deposition of nickel nitrate through fine printhead nozzles onto the alumina powder. Moreover, a superior  $\text{CO}_2$  hydrogenation activity using NI catalysts was observed in comparison to WI catalysts treated under the same thermal conditions. The post-processing infiltration step, which distinguishes the preparation from conventional ones, covers active centers after nickel immobilization by introduction of alumina particles and aggravates reduction, observable by XPS, XAS and TPR.

This proof of concept enables further developments regarding the usage of AM in catalyst preparation, especially by incorporating catalyst precursor into the printing liquid in the context of BJ. A potential advancement is the usage of more than one metal salt solution to yield multi-metal catalysts by multi-component in situ impregnation. In addition, the nickel loading could be improved by repeated deposition of Ni ink onto a single powder layer or increasing the amount of metal per layer by process parameter optimization. Investigating the point of zero charge (PZC) may offer valuable insights into the interaction between the ink and (transition) alumina surface, leading to enhanced metal dispersion. Moreover, this knowledge could aid in optimizing the selection of material feedstock for 3D printing. At a later development stage, it becomes pertinent to conduct long-term stability tests to enhance catalyst performance and gain insights into its deactivation behavior.

## 7.5 Supporting Information

### 7.5.1 Specific Surface Area

N<sub>2</sub> physisorption at 77 K (Nova 4200e, Quantachrome Instruments) was used to determine the specific surface area  $S_{\text{BET}}$  of the catalysts. Sample pretreatment comprised degassing under vacuum at 120 °C for 3 h.  $S_{\text{BET}}$  was determined according to the method of Brunauer, Emmett, and Teller (BET) and calculated between  $0.05 \leq p/p_0 \leq 0.3$ . Tab. 7.4 presents the physisorption results.

**Table 7.4:** Specific surface area  $S_{\text{BET}}$  determined by N<sub>2</sub> physisorption.

Catalyst	$S_{\text{BET}}$ (m <sup>2</sup> /g <sub>cat</sub> )
NI_d_c600	190
NI_i_c600	161
WI_c450	142
WI_c600	131

### 7.5.2 Ni K-edge XAS

#### 7.5.2.1 Preparation of XAS References

The NiAl<sub>2</sub>O<sub>4</sub> reference for XAS measurements was prepared by calcination of co-precipitated stoichiometric Ni-Al precursor at 1100 °C for 6 h to ensure complete formation of nickel aluminate spinel. The NiO reference was prepared by diluting NiO (Sigma-Aldrich) with cellulose at a ratio of 1:15. All references samples were filled into capillary glass tubes for beamline measurements.

#### 7.5.2.2 Calcined Samples

Fig. 7.10 depicts the Ni K-edge XANES spectra of all prepared NI and WI samples including the reference samples NiO and NiAl<sub>2</sub>O<sub>4</sub> which were plotted simultaneously to provide a qualitative comparison to the measured sample.

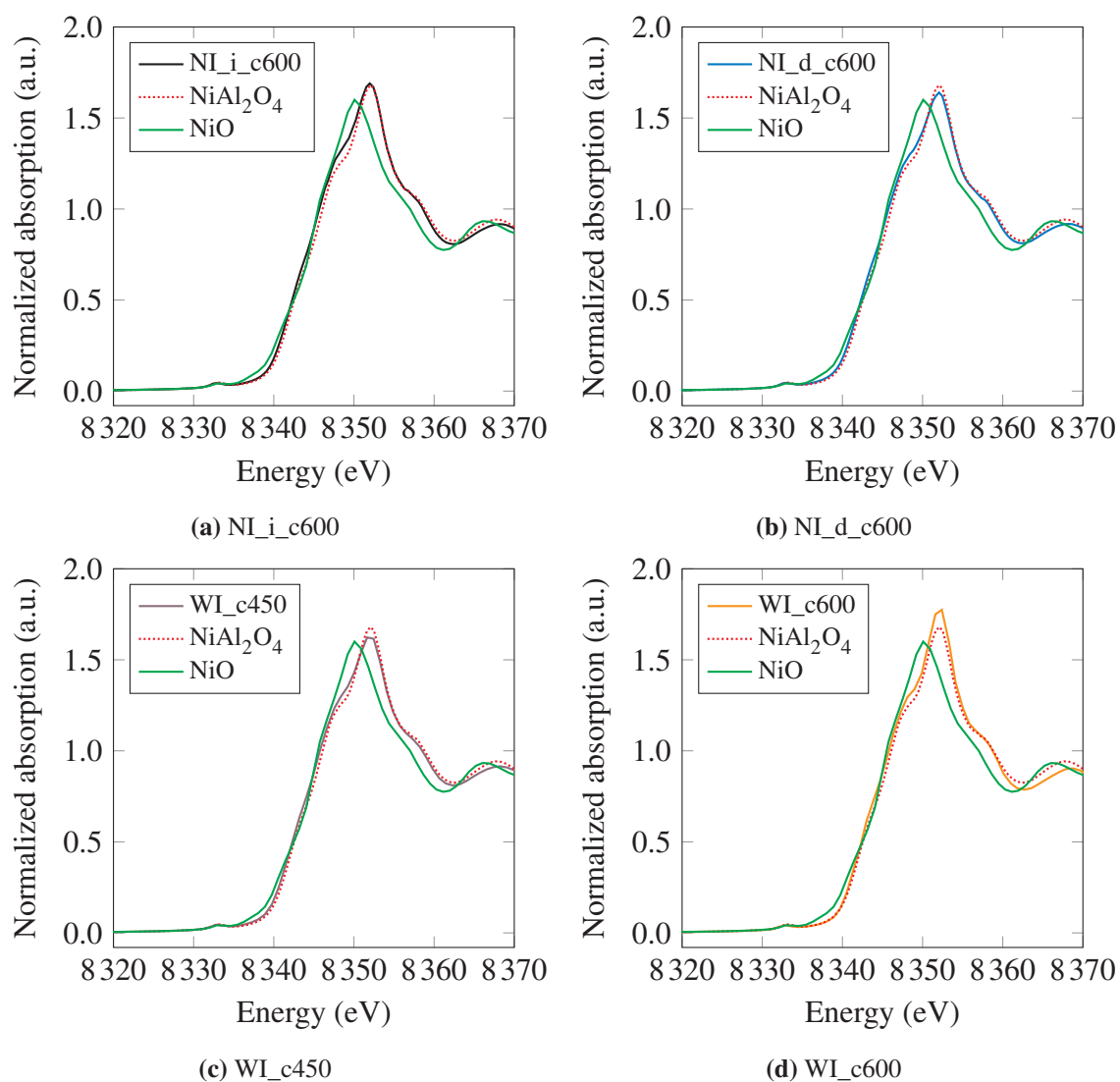


**Figure 7.10:** Ni K-edge XANES of calcined samples, including reference samples NiAl<sub>2</sub>O<sub>4</sub> and NiO.

### 7.5.2.3 Reduced Samples

Fig. 7.11 depicts the Ni K-edge XANES spectra of NI and WI samples including Ni foil and the respective calcined sample as reference.

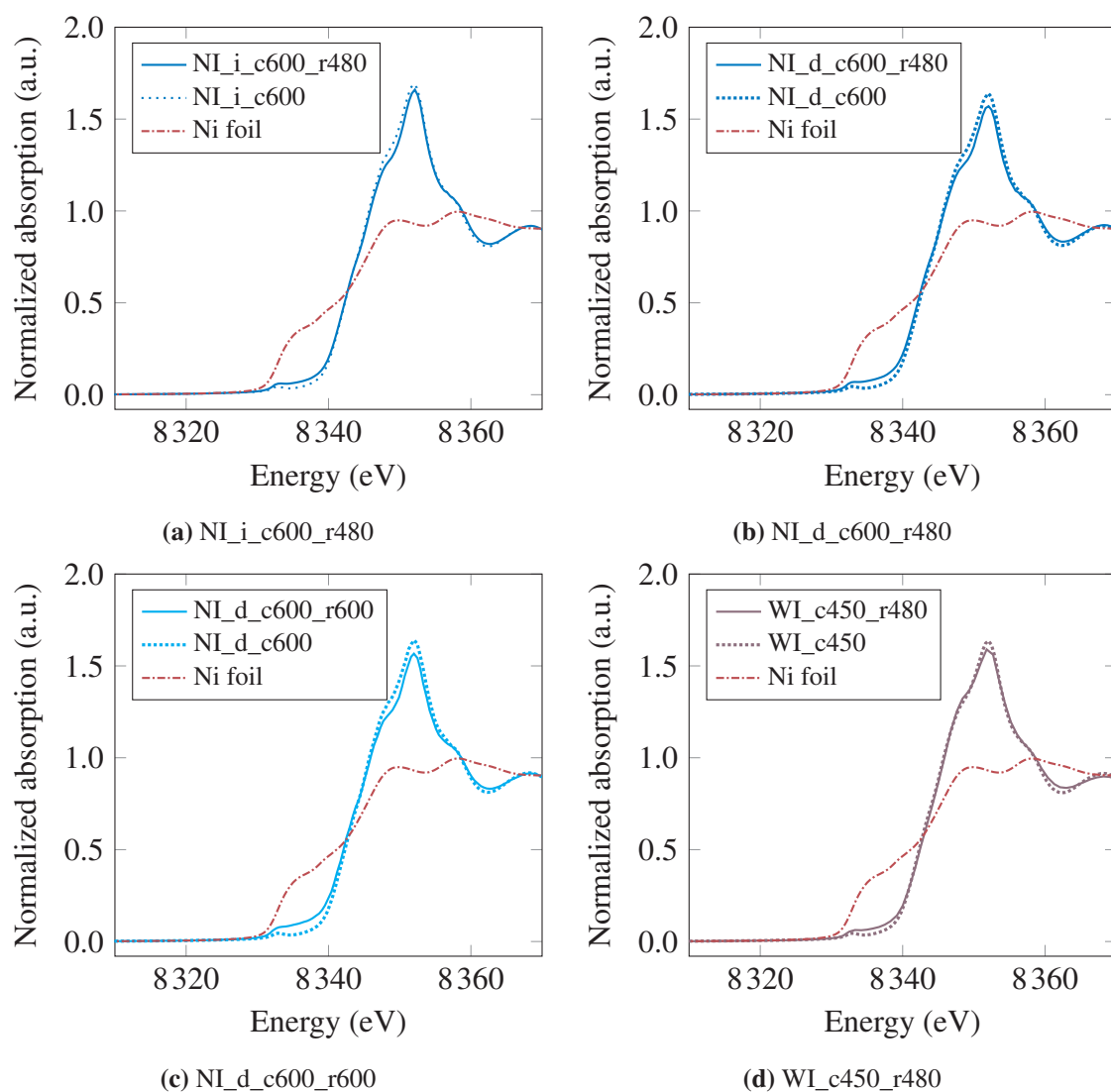


**Figure 7.11:** Ni K-edge XANES of reduced samples, including Ni foil and the respective calcined sample as reference.

### 7.5.3 TPR Reference Samples

Reference samples were prepared in order to compare the  $H_2$  reduction profile of the analyzed samples to pure bulk material. The  $NiAl_2O_4$  reference was prepared by calcination of co-precipitated Ni-Al precursor at  $1100\text{ }^\circ\text{C}$  for 6 h to ensure complete formation of nickel aluminate spinel. The  $NiO/Al_2O_3$  sample was prepared by calcination of co-precipitated Ni-Al precursor with a molar Ni/Al ratio of 1.0 at  $450\text{ }^\circ\text{C}$  for 6 h which should yield predominantly  $NiO/Al_2O_3$ . Fig. 7.12 clearly demonstrates the differing temperature regions where the reduction of  $NiAl_2O_4$  and  $NiO$  takes place. Furthermore, these results agree with the reduction profiles of NI and WI samples.

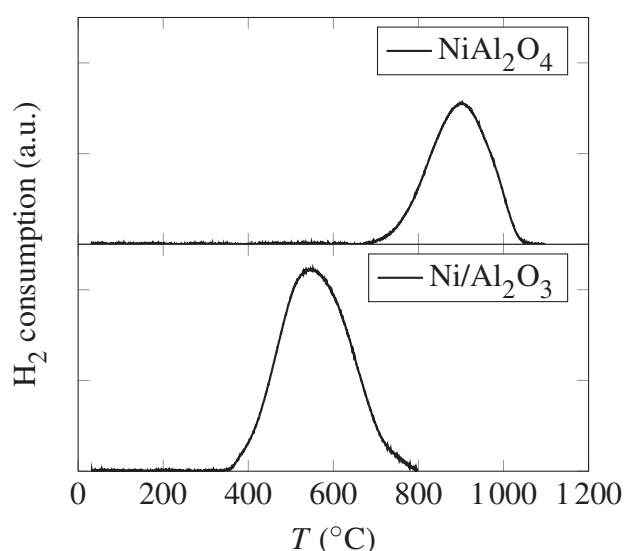


**Figure 7.12:**  $H_2$  consumption of  $NiAl_2O_4$  and co-precipitated Ni-Al catalyst (calcined at  $450\text{ }^\circ\text{C}$ ).

### 7.5.4 Activity Measurements

Measurements of the  $CO_2$  hydrogenation activity were conducted in a preparation chamber which is directly attached to the XPS analysis setup. Printed cylindrical catalysts in crushed form ( $m \approx 50\text{ mg}$ ) can be exposed to reaction mixtures up to 1 bar at temperatures of up to  $450\text{ }^\circ\text{C}$ . After removal of the gas phase, the catalyst is transferred to the XPS setup without exposure to moisture or air. It is reasonable that the surface present under reaction conditions is preserved in UHV.

The preparation chamber operates as a batch-type reaction cell, enabling static investigation of the  $CO_2$  hydrogenation activity. Gases are introduced by leak valves (2 mbar  $CO_2$ , 8 mbar  $H_2$  and 1 mbar Ar). The pressures are monitored by capacitive gauges.

The gas phase composition is analyzed by a differentially pumped quadrupole mass spectrometer attached to the XPS analysis chamber. A fraction of the gas phase in the preparation chamber is introduced into the analysis chamber using a leak valve, adjusting the pressure in the analysis chamber to  $p_{\text{analysis}} = 10^{-6}$  mbar. Assuming a pumping speed of  $S \approx 100$  L/s for the turbomolecular pump in the analysis chamber, the  $pV$  flux removed from the preparation chamber can be calculated:

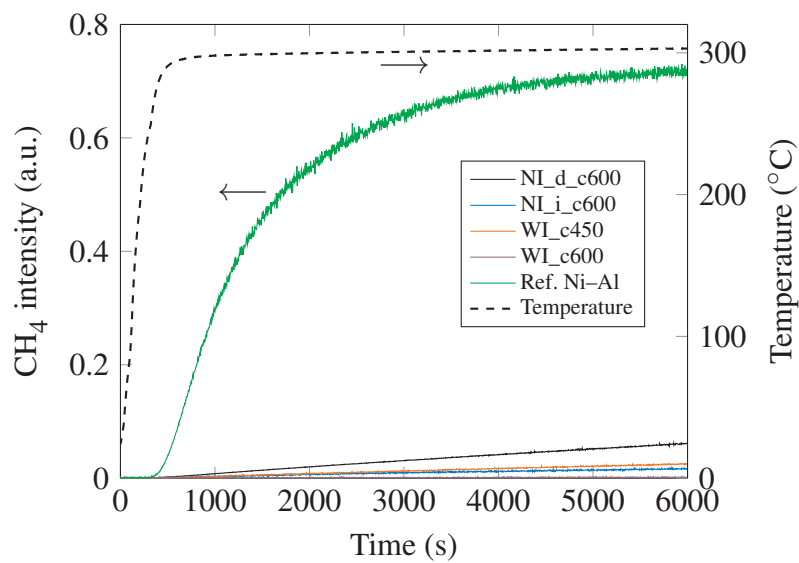
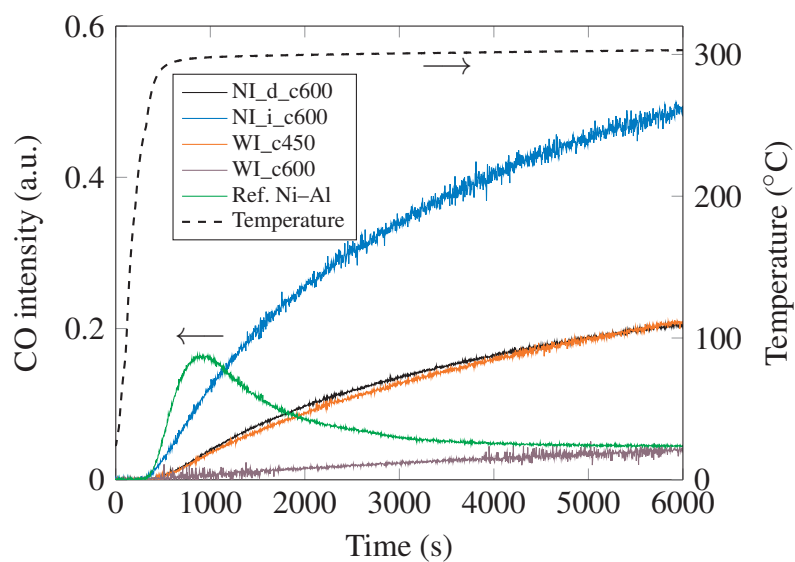
$$q_{pV} = p_{\text{analysis}} \cdot S = 10^{-6} \text{ mbar} \cdot 100 \frac{\text{L}}{\text{s}} = 10^{-4} \frac{\text{mbarL}}{\text{s}} \quad (7.1)$$

Considering the volume of the preparation chamber ( $V = 5.5$  L), the pressure change in the preparation chamber per time  $\frac{dp_{\text{prep}}}{dt}$  is given by:

$$\frac{dp_{\text{prep}}}{dt} = -\frac{q_{pV}}{V} = -\frac{10^{-4} \text{ mbarL/s}}{5.5 \text{ L}} = -1.8 \cdot 10^{-5} \frac{\text{mbar}}{\text{s}} \quad (7.2)$$

Thus, the gas phase analysis induces a pressure decrease of 0.15 mbar over the reaction time of 8000 s. Compared to the initial total pressure of 11 mbar, the pressure loss falls within the range of 1% and does not affect the thermodynamics of the reaction network.

Fig. 7.13 presents quadrupole mass spectrometry signal intensities of CO and CH<sub>4</sub>, the reaction products of CO<sub>2</sub> methanation. The plots additionally include results obtained from a co-precipitated Ni-Al catalyst with a nickel loading of approximately 40 %.

(a) CH<sub>4</sub> signal intensity.

(b) CO signal intensity.

**Figure 7.13:** Quadrupole mass spectrometry signal intensities of the CO<sub>2</sub> hydrogenation reaction products methane and carbon monoxide. Feed gas composition: CO<sub>2</sub>/H<sub>2</sub>/Ar = 2/8/1.



# 8 Summary and Outlook

## 8.1 Summary

This thesis delved into the exploration of binder jetting, a powder-based 3D printing technique, as an innovative approach to integrate additive manufacturing into heterogeneous catalysis. While other oftentimes extrusion-based printing strategies for catalysts exist, binder jetting has been used rarely since the material and process development is relatively elaborate, especially regarding the trade-off between part stability and surface area needed for catalysis. Because the powder bed material and the printing ink are adaptable components, there exist multiple opportunities to devise a catalyst printing approach using binder jetting. In contrast, in extrusion-based methods, the ultimate catalyst composition must be exclusively present within the paste. Starting from an initial process development which included a selection of material feedstock and exploring appropriate printing and post-processing conditions, generation of alumina catalyst supports marked the first milestone of this study. To provide a comprehensive understanding of catalyst 3D printing, this study compared  $\text{Al}_2\text{O}_3$  supports manufactured using both binder jetting and direct ink writing techniques. These supports were further evaluated as  $\text{Pt}/\text{Al}_2\text{O}_3$  catalysts in the dehydrogenation of LOHC, yielding valuable insights into their respective physicochemical properties and performance. In order to expand the potential of the additive manufacturing approach, transitioning from using pure alumina as powder feedstock to co-precipitated Ni-Al precursor opened the possibility to fabricate bulk-like nickel catalysts where the metal precursor is integrated into the printing powder. Lastly, the in situ impregnation of transition alumina powder was achieved through the ejection of nickel nitrate-containing ink onto an alumina powder bed during the 3D printing process, presenting an additional approach for catalyst printing. Through the strategic inclusion of the metal precursor at different stages of the printing process, precise engineering of active phase distributions can be achieved, enhancing the overall catalyst performance.

The development of a manufacturing strategy for porous  $\eta/\gamma\text{-Al}_2\text{O}_3$  supports revealed that the powder-ink interaction as well as the suitability for application in catalysis regarding specific surface area, porosity and catalyst poisons limits the choice of raw materials

so that the basic procedure contains a bayerite powder bed combined with water-based ink. PVP as an in-bed binder must be burnt off completely at 600 °C for at least 3 h. Infiltration with alumina slurry is an indispensable step to restabilize the porous, but fragile debinded part structure for further handling, improving the side crushing strength by a factor of 20. Bulk porosities of approximately 75 % and a specific surface area of up to 223 m<sup>2</sup>/g provide a suitable support for further impregnation.

Extrusion-based direct ink writing and binder jetting were thoroughly compared regarding their respective benefits and drawbacks for monolithic alumina support printing and subsequent wet impregnation to obtain egg-shell Pt/Al<sub>2</sub>O<sub>3</sub> catalysts for 18H-DBT dehydrogenation. At a calcination temperature of 1100 °C binder jetting provides significantly more surface area (26 m<sup>2</sup>/g vs. 11 m<sup>2</sup>/g) and mercury intrusion porosimetry detected large intraparticle pores at about 0.03 mm, caused by the powder layering technique. Other observed differences include greater Pt penetration depths for BJ due to increased porosity but similar Pt dispersion. 18H-DBT dehydrogenation tests in a semi-batch reactor setup revealed equal catalytic performance of DIW and BJ Pt monoliths, reaching Pt productivities of 2.7 g<sub>H<sub>2</sub></sub> g<sub>Pt</sub><sup>-1</sup> min<sup>-1</sup>. The results indicate the suitability of both printing techniques for alumina catalyst support manufacturing, while also highlighting that substantial enhancement of catalyst properties can be achieved through geometry alterations. The extent and nature of improvement may vary between the two tested AM techniques since they significantly differ in their printing principle and the resulting output, e.g. printing speed, print resolution, scalability of print jobs.

Unlike printing the support and subsequently performing wet impregnation, the integration of co-precipitated Ni-Al precursor powder into the powder bed enables the direct printing of Ni-Al catalysts with a uniform Ni distribution throughout the pellet. The examined catalysts exhibited a Ni loading ranging from 6.4 wt.% to 16.4 wt.%. XRD phase composition analysis of the as-prepared, calcined, and reduced 3D printed catalyst samples with varying molar Ni/Al ratios unveiled takovite-like, oxidic, and metallic Ni species, respectively, akin to conventionally prepared Ni-Al samples. Likewise, metal particle size distribution analysis by TEM, XRD, and H<sub>2</sub> chemisorption, demonstrates consistent findings, showing average particle sizes ranging from 4 to 18 nm. These sizes increase with a higher Ni/Al ratio. Selected 3D printed spherical Ni-Al catalyst pellets were tested for their CO<sub>2</sub> methanation activity in a single pellet string reactor. CH<sub>4</sub> conversions of up to 99 % are reached with nearly no CO formation.

An additional aspect of exploring the binder jetting printing technique involves incorporating the nickel precursor in the form of a nickel nitrate solution within the printing liquid. The metal salt solution is finely distributed on selective areas of the powder bed. In this process, the powder is impregnated in situ while printing. XPS examination of

alumina cylinders treated with in situ impregnation and traditionally wet impregnation techniques indicates that the former approach results in a greater dispersion of nickel. XPS, XAS and TPR analysis confirm the prevalent presence of nickel aluminate spinel after calcination at 600 °C due to the low Ni loading and concomitant high dispersion. Moreover, subsequent treatment involving alumina drip infiltration limits the accessibility of active sites, as evidenced by observations from XPS, TPR, and XAS analyses. Verification of catalyst effectiveness was obtained through CO<sub>2</sub> methanation tests. Nevertheless, the hydrogenation rate is comparatively slow, with CO being the primary product.

## 8.2 Outlook

The results presented in this thesis showcase the potential of binder jetting as a way to manufacture tailor-made catalysts with customized catalyst geometries, metal distributions within the monolith/pellet and the suitability of the 3D printed catalysts for various reactions. Apart from (transition) alumina powder, different commonly used metal oxide powders and mixtures thereof such as SiO<sub>2</sub>, TiO<sub>2</sub>, CeO<sub>2</sub>, MgO or zeolites could be used as powder bed feedstock to facilitate manufacturing of catalyst supports. Accordingly, various metal salts dissolved in the printing liquid offer diverse possibilities for catalysts other than nickel catalysts or mixed metal catalysts featuring highly dispersed metal particles and homogeneous active phase distribution combined with complex geometries. (Co-)precipitated catalysts offer a high degree of customization regarding the catalyst composition, mixed-metal synergy and tailored morphology. These advantages can be used to prepare further precipitates in powder form for binder jetting to expand the range of 3D printed catalysts. Furthermore, catalyst support material could be impregnated (e.g. via incipient wetness or wet impregnation) prior to loading the powder into the BJ printer's reservoir. This offers a new possibility for processing powder that incorporates the catalyst precursor. Depending on the used raw material combinations, (post-)processing parameters must be adapted to suit the new feedstock and requirements of the chemical reaction.

Improvements regarding the printing process lie in the debinding process since the temperature at which the binder is burnt off determines the subsequent catalyst calcination or reduction conditions. Further investigations on the decomposition pattern of PVP could bring benefits for catalyst preparation. For example, reducing the debinding temperature offers the possibility to prevent catalyst deactivation by particle sintering during thermal treatment. Moreover, widening the portfolio of usable in-bed binders, or even binders soluble in the printing liquid, increases the flexibility towards usage of other alternative raw materials.

Additive manufacturing harbors the inherent potential to create intricate geometrical structures. Since this thesis addresses basic printing process development and proof of principles regarding the general printability of investigated catalyst materials, possible upcoming steps could involve exploring geometric variations beyond the simple cylinders or spheres that have been examined thus far. Like this, it becomes possible to derive new insights into how the shape of the catalyst affects heat and mass transfer, consequently impacting the catalyst performance. Especially further utilizing the potential of the single pellet string reactor, geometrical parameter studies such as variation of outer shape, internal canal structures, size of the pellets etc. and their effect on hot spot formation and gas flow dynamics through the catalyst bed can be investigated for the CO<sub>2</sub> methanation (or other chemical reactions) in detail. A useful tool is CFD simulation for the screening of possible catalyst geometries modeled by CAD. Flow simulations combined with heat transport validated through experiments with printed catalysts aid in developing new design guidelines for catalyst shaping.

## A Bibliography

- [1] G. Eigenberger, W. Ruppel in *Ullmann's Encyclopedia of Industrial Chemistry*, Wiley-VCH, **2003**, DOI 10.1002/14356007.b04\_199.pub2.
- [2] S. Afandizadeh, E. Foumeny, "Design of packed bed reactors: guides to catalyst shape, size, and loading selection", *Applied Thermal Engineering* **2001**, *21*, 669–682, DOI 10.1016/S1359-4311(00)00072-7.
- [3] K. G. Manoharan, V. V. Buwa, "Structure-Resolved CFD Simulations of Different Catalytic Structures in a Packed Bed", *Industrial & Engineering Chemistry Research* **2019**, *58*, 22363–22375, DOI 10.1021/acs.iecr.9b03537.
- [4] B. Partopour, A. G. Dixon, "Effect of particle shape on methanol partial oxidation in a fixed bed using CFD reactor modeling", *AIChE Journal* **2020**, *66*, e16904, DOI 10.1002/aic.16904.
- [5] D. Pashchenko, "Flow dynamic in a packed bed filled with Ni-Al<sub>2</sub>O<sub>3</sub> porous catalyst: Experimental and numerical approach", *AIChE Journal* **2019**, *65*, e16558, DOI 10.1002/aic.16558.
- [6] G. M. Karthik, V. B. Vivek, "A computational approach for the selection of optimal catalyst shape for solid-catalysed gas-phase reactions", *Reaction Chemistry & Engineering* **2020**, *5*, 163–182, DOI 10.1039/C9RE00240E.
- [7] J. S. S. Mohammadzadeh, A. Zamaniyan, "Catalyst Shape as a Design Parameter - Optimum Shape for Methane-Steam Reforming Catalyst", *Chemical Engineering Research and Design* **2002**, *80*, 383–391, DOI 10.1205/026387602317446425.
- [8] S. Tong, I. G. Dalla Lana, K. T. Chuang, "Effect of Catalyst Shape on the Hydrolysis of COS and CS<sub>2</sub> in a Simulated Claus Converter", *Industrial & Engineering Chemistry Research* **1997**, *36*, 4087–4093, DOI 10.1021/ie970277g.
- [9] V. L. Hartmann, A. V. Obysov, A. V. Dulnev, S. V. Afanas'ev, "New basic shape of catalysts for natural gas reforming reactors", *Chemical Engineering Journal* **2011**.

- [10] K. M. Brunner, H. D. Perez, R. P. S. Peguin, J. C. Duncan, L. D. Harrison, C. H. Bartholomew, W. C. Hecker, “Effects of Particle Size and Shape on the Performance of a Trickle Fixed-Bed Recycle Reactor for Fischer-Tropsch Synthesis”, *Industrial & Engineering Chemistry Research* **2015**, *54*, 2902–2909, DOI 10.1021/ie503174v.
- [11] *Synthesis of Solid Catalysts*, (Ed.: K. P. de Jong), Wiley-VCH, Weinheim, DE, **2009**, DOI 10.1002/9783527626854.
- [12] J. Hagen, *Industrial Catalysis: A Practical Approach*, Third completely revised and enlarged edition, Wiley-VCH, Weinheim, DE, **2015**.
- [13] H. M. Bui, R. Fischer, N. Szesni, M. Tonigold, K. Achterhold, F. Pfeiffer, O. Hinrichsen, “Development of a manufacturing process for Binder Jet 3D printed porous Al<sub>2</sub>O<sub>3</sub> supports used in heterogeneous catalysis”, *Additive Manufacturing* **2022**, *50*, 102498, DOI 10.1016/j.addma.2021.102498.
- [14] U. M. Dilberoglu, B. Gharehpapagh, U. Yaman, M. Dolen, “The Role of Additive Manufacturing in the Era of Industry 4.0”, *Procedia Manufacturing* **2017**, *11*, 545–554, DOI 10.1016/j.promfg.2017.07.148.
- [15] M. Bracconi, “Intensification of catalytic reactors: A synergic effort of Multiscale Modeling, Machine Learning and Additive Manufacturing”, *Chemical Engineering and Processing - Process Intensification* **2022**, *181*, 109148, DOI 10.1016/j.cep.2022.109148.
- [16] S. Mehla, R. D. Gudi, D. D. Mandaliya, T. Hisatomi, K. Domen, S. K. Bhargava in *Additive Manufacturing for Chemical Sciences and Engineering*, Springer, Singapore, **2022**, pp. 239–307, DOI 10.1007/978-981-19-2293-0\_8.
- [17] Y. Li, S. Chen, X. Cai, J. Hong, X. Wu, Y. Xu, J. Zou, B. H. Chen, “Rational design and preparation of hierarchical monoliths through 3D printing for syngas methanation”, *Journal of Materials Chemistry A* **2018**, *6*, 5695–5702, DOI 10.1039/C8TA01597J.
- [18] A. Gebhardt, J.-S. Hötter, *Additive manufacturing: 3D printing for prototyping and manufacturing*, Hanser Publications, Munich, DE, **2016**, DOI 10.3139/9781569905838.
- [19] Todd Grimm, *User’s Guide To Rapid Prototyping*, Society of Manufacturing Engineers, Dearborn, MI, **2004**.
- [20] Charles W. Hull, “Apparatus for production of three-dimensional objects by stereolithography”, *US4575330A* **1986**.

- [21] T. Ludwig, J. Seckendorff, C. Troll, R. Fischer, M. Tonigold, B. Rieger, O. Hinrichsen, “Additive Manufacturing of Al<sub>2</sub>O<sub>3</sub>-Based Carriers for Heterogeneous Catalysis”, *Chemie Ingenieur Technik* **2018**, *90*, 703–707, DOI 10.1002/cite.201700151.
- [22] R. K. Holman, M. J. Cima, S. A. Uhlund, E. M. Sachs, “Spreading and infiltration of inkjet-printed polymer solution droplets on a porous substrate”, *Journal of Colloid and Interface Science* **2002**, *249*, 432–440, DOI 10.1006/jcis.2002.8225.
- [23] H. Miyajima, N. Momenzadeh, L. Yang, “Effect of powder characteristics on parts fabricated via binder jetting process”, *Rapid Prototyping Journal* **2019**, *25*, 332–342, DOI 10.1108/RPJ-03-2018-0069.
- [24] J. E. Fromm, “Numerical Calculation of the Fluid Dynamics of Drop-on-Demand Jets”, *IBM Journal of Research and Development* **1984**, *28*, 322–333, DOI 10.1147/rd.283.0322.
- [25] N. Reis, B. Derby, “Ink Jet Deposition of Ceramic Suspensions: Modeling and Experiments of Droplet Formation”, *MRS Proceedings* **2000**, *624*, DOI 10.1557/PROC-624-65.
- [26] B. Derby, “Inkjet Printing of Functional and Structural Materials: Fluid Property Requirements, Feature Stability, and Resolution”, *Annual Review of Materials Research* **2010**, *40*, 395–414, DOI 10.1146/annurev-matsci-070909-104502.
- [27] M. Lehmann, H. Panzer, C. G. Kolb, M. F. Zaeh, “Influence of the Pore Radius on the Penetration Depth of Inks in Binder Jetting - A Modification of the Washburn Equation”, *Journal of Manufacturing and Materials Processing* **2022**, *6*, 101, DOI 10.3390/jmmp6050101.
- [28] Y. Bai, C. Wall, H. Pham, A. Esker, C. B. Williams, “Characterizing Binder-Powder Interaction in Binder Jetting Additive Manufacturing Via Sessile Drop Goniometry”, *Journal of Manufacturing Science and Engineering* **2019**, *141*, DOI 10.1115/1.4041624.
- [29] S. Barui, H. Ding, Z. Wang, H. Zhao, S. Marathe, W. Mirihanage, B. Basu, B. Derby, “Probing Ink-Powder Interactions during 3D Binder Jet Printing Using Time-Resolved X-ray Imaging”, *ACS Applied Materials & Interfaces* **2020**, *12*, 34254–34264, DOI 10.1021/acsami.0c03572.
- [30] H. Deng, Y. Huang, S. Wu, Y. Yang, “Binder jetting additive manufacturing: Three-dimensional simulation of micro-meter droplet impact and penetration into powder bed”, *Journal of Manufacturing Processes* **2022**, *74*, 365–373, DOI 10.1016/j.jmapro.2021.12.019.

- [31] C. H. Hu, C. Chizallet, C. Mager-Maury, M. Corral-Valero, P. Sautet, H. Toulhoat, P. Raybaud, “Modulation of catalyst particle structure upon support hydroxylation: Ab initio insights into Pd<sub>13</sub> and Pt<sub>13</sub>/gamma-Al<sub>2</sub>O<sub>3</sub>”, *Journal of Catalysis* **2010**, 274, 99–110, DOI 10.1016/j.jcat.2010.06.009.
- [32] B. Lindström, L. J. Pettersson, “A Brief History of Catalysis”, *CATTECH* **2003**, 7, 130–138, DOI 10.1023/A:1025001809516.
- [33] J. N. Armor, “A history of industrial catalysis”, *Catalysis Today* **2011**, 163, 3–9, DOI 10.1016/j.cattod.2009.11.019.
- [34] I. Fechete, Y. Wang, J. C. Védrine, “The past, present and future of heterogeneous catalysis”, *Catalysis Today* **2012**, 189, 2–27, DOI 10.1016/j.cattod.2012.04.003.
- [35] A. Haleem, M. Javaid, “Additive Manufacturing Applications in Industry 4.0: A Review”, *Journal of Industrial Integration and Management* **2019**, 04, 1930001, DOI 10.1142/S2424862219300011.
- [36] A. Uriondo, M. Esperon-Miguez, S. Perinpanayagam, “The present and future of additive manufacturing in the aerospace sector: A review of important aspects”, *Proceedings of the Institution of Mechanical Engineers, Part G: Journal of Aerospace Engineering* **2015**, 229, 2132–2147, DOI 10.1177/0954410014568797.
- [37] J. C. Vasco in *Additive Manufacturing*, (Ed.: J. Pou), Handbooks in Advanced Manufacturing, Elsevier, San Diego, CA, **2021**, pp. 505–530, DOI 10.1016/B978-0-12-818411-0.00010-0.
- [38] S. Singh, S. Ramakrishna, “Biomedical applications of additive manufacturing: Present and future”, *Current Opinion in Biomedical Engineering* **2017**, 2, 105–115, DOI 10.1016/j.cobme.2017.05.006.
- [39] Web of Science, Results for the search words "additive manufacturing" and "catalysis", accessed April 4th 2023.
- [40] C. Hurt, M. Brandt, S. S. Priya, T. Bhatelia, J. Patel, P. Selvakannan, S. Bhargava, “Combining additive manufacturing and catalysis: a review”, *Catalysis Science & Technology* **2017**, 7, 3421–3439, DOI 10.1039/C7CY00615B.
- [41] C. Parra-Cabrera, C. Achille, S. Kuhn, R. Ameloot, “3D printing in chemical engineering and catalytic technology: structured catalysts, mixers and reactors”, *Chemical Society Reviews* **2018**, 47, 209–230, DOI 10.1039/C7CS00631D.
- [42] E. Bogdan, P. Michorczyk, “3D Printing in Heterogeneous Catalysis - The State of the Art”, *Materials* **2020**, 13, 4534, DOI 10.3390/ma13204534.
- [43] X. Zhou, C.-J. Liu, “Three-dimensional Printing for Catalytic Applications: Current Status and Perspectives”, *Advanced Functional Materials* **2017**, 27, 1701134, DOI 10.1002/adfm.201701134.

- [44] O. H. Laguna, P. F. Lieter, F. I. Godino, F. A. Corpas-Iglesias, “A review on additive manufacturing and materials for catalytic applications: Milestones, key concepts, advances and perspectives”, *Materials & Design* **2021**, 208, 109927, DOI 10.1016/j.matdes.2021.109927.
- [45] J. Zhu, P. Wu, Y. Chao, J. Yu, W. Zhu, Z. Liu, C. Xu, “Recent advances in 3D printing for catalytic applications”, *Chemical Engineering Journal* **2022**, 433, 134341, DOI 10.1016/j.cej.2021.134341.
- [46] L. R. Rosseau, V. Middelkoop, H. A. Willemsen, I. Roghair, M. van Sint Annaland, “Review on Additive Manufacturing of Catalysts and Sorbents and the Potential for Process Intensification”, *Frontiers in Chemical Engineering* **2022**, 4, DOI 10.3389/fceng.2022.834547.
- [47] J. R. McDonough, “A perspective on the current and future roles of additive manufacturing in process engineering, with an emphasis on heat transfer”, *Thermal Science and Engineering Progress* **2020**, 19, 100594, DOI 10.1016/j.tsep.2020.100594.
- [48] S. Lawson, A. Farsad, F. Rezaei, D. Ludlow, A. A. Rownaghi, “Direct Ink Writing of Metal Oxide/H-ZSM-5 Catalysts for n-Hexane Cracking: A New Method of Additive Manufacturing with High Metal Oxide Loading”, *ACS Applied Materials & Interfaces* **2021**, 13, 781–794, DOI 10.1021/acsami.0c20752.
- [49] N. Li, K. Tong, L. Yang, X. Du, “Review of 3D printing in photocatalytic substrates and catalysts”, *Materials Today Energy* **2022**, 29, 101100, DOI 10.1016/j.mtener.2022.101100.
- [50] O. A. Alimi, R. Meijboom, “Current and future trends of additive manufacturing for chemistry applications: a review”, *Journal of Materials Science* **2021**, 56, 16824–16850, DOI 10.1007/s10853-021-06362-7.
- [51] H. Maleki, V. Bertola, “Recent advances and prospects of inkjet printing in heterogeneous catalysis”, *Catalysis Science & Technology* **2020**, 10, 3140–3159, DOI 10.1039/D0CY00040J.
- [52] A. I. Lysikov, E. E. Vorobyeva, A. V. Polukhin, N. S. Lazarenko, V. A. Vdovichenko, E. V. Parkhomchuk, “Novel 3D-Printed Alumina Monolith Catalysts for Hydroconversion of Tar”, *Petroleum Chemistry* **2022**, 62, 1154–1161, DOI 10.1134/S096554412210005X.
- [53] E. Bogdan, B. Michorczyk, A. Rokicińska, M. Basta, M. Myradova, P. Kuśtrowski, P. Michorczyk, “Monolithic composites with geometry controlled by polymeric 3D printed templates: Characterization and catalytic performance in OCM”, *Applied Surface Science* **2021**, 553, 149554, DOI 10.1016/j.apsusc.2021.149554.

- [54] A. Davó-Quiñonero, D. Sorolla-Rosario, E. Bailón-García, D. Lozano-Castelló, A. Bueno-López, “Improved asymmetrical honeycomb monolith catalyst prepared using a 3D printed template”, *Journal of Hazardous Materials* **2019**, 368, 638–643, DOI 10.1016/j.jhazmat.2019.01.092.
- [55] P. Michorczyk, E. Hedrzak, A. Wegrzyniak, “Preparation of monolithic catalysts using 3D printed templates for oxidative coupling of methane”, *Journal of Materials Chemistry A* **2016**, 4, 18753–18756, DOI 10.1039/C6TA08629B.
- [56] O. A. Alimi, C. A. Akinnawo, R. Meijboom, “Monolith catalyst design via 3D printing: a reusable support for modern palladium-catalyzed cross-coupling reactions”, *New Journal of Chemistry* **2020**, 44, 18867–18878, DOI 10.1039/D0NJ03651J.
- [57] O. A. Alimi, T. B. Ncongwane, R. Meijboom, “Design and fabrication of a monolith catalyst for continuous flow epoxidation of styrene in polypropylene printed flow reactor”, *Chemical Engineering Research and Design* **2020**, 159, 395–409, DOI 10.1016/j.cherd.2020.04.025.
- [58] F. Agueniou, H. Vidal, J. de Dios López, J. C. Hernández-Garrido, M. A. Cauqui, F. J. Botana, J. J. Calvino, V. V. Galvita, J. M. Gatica, “3D-printing of metallic honeycomb monoliths as a doorway to a new generation of catalytic devices: the Ni-based catalysts in methane dry reforming showcase”, *Catalysis Communications* **2021**, 148, 106181, DOI 10.1016/j.catcom.2020.106181.
- [59] A. Lind, Ø. Vistad, M. F. Sunding, K. A. Andreassen, J. H. Cavka, C. A. Grande, “Multi-purpose structured catalysts designed and manufactured by 3D printing”, *Materials & Design* **2020**, 187, 108377, DOI 10.1016/j.matdes.2019.108377.
- [60] T. Zheng, W. Zhou, Da Geng, Y. Li, Y. Liu, C. Zhang, “Methanol steam reforming microreactor with novel 3D-Printed porous stainless steel support as catalyst support”, *International Journal of Hydrogen Energy* **2020**, 45, 14006–14016, DOI 10.1016/j.ijhydene.2020.03.103.
- [61] S. Danaci, L. Protasova, F. Snijkers, W. Bouwen, A. Bengaouer, P. Marty, “Innovative 3D-manufacture of structured copper supports post-coated with catalytic material for CO<sub>2</sub> methanation”, *Chemical Engineering and Processing - Process Intensification* **2018**, 127, 168–177, DOI 10.1016/j.cep.2018.03.023.
- [62] J. Noyen, A. Wilde, M. Schroeven, S. Mullens, J. Luyten, “Ceramic Processing Techniques for Catalyst Design: Formation, Properties, and Catalytic Example of ZSM-5 on 3-Dimensional Fiber Deposition Support Structures”, *International Journal of Applied Ceramic Technology* **2012**, 9, 902–910, DOI 10.1111/j.1744-7402.2012.02781.x.

- [63] J. Lefevere, S. Mullens, V. Meynen, “The impact of formulation and 3D-printing on the catalytic properties of ZSM-5 zeolite”, *Chemical Engineering Journal* **2018**, 349, 260–268, DOI 10.1016/j.cej.2018.05.058.
- [64] X. Li, F. Rezaei, A. A. Rownaghi, “Methanol-to-olefin conversion on 3D-printed ZSM-5 monolith catalysts: Effects of metal doping, mesoporosity and acid strength”, *Microporous and Mesoporous Materials* **2019**, 276, 1–12, DOI 10.1016/j.micromeso.2018.09.016.
- [65] F. Magzoub, X. Li, J. Al-Darwish, F. Rezaei, A. A. Rownaghi, “3D-printed ZSM-5 monoliths with metal dopants for methanol conversion in the presence and absence of carbon dioxide”, *Applied Catalysis B: Environmental* **2019**, 245, 486–495, DOI 10.1016/j.apcatb.2019.01.008.
- [66] M. Konarova, W. Aslam, L. Ge, Q. Ma, F. Tang, V. Rudolph, J. N. Beltramini, “Enabling Process Intensification by 3D Printing of Catalytic Structures”, *Chem-CatChem* **2017**, 9, 4132–4138, DOI 10.1002/cctc.201700829.
- [67] C. Y. Chaparro-Garnica, A. Davó-Quiñonero, E. Bailón-García, D. Lozano-Castelló, A. Bueno-López, “Design of Monolithic Supports by 3D Printing for Its Application in the Preferential Oxidation of CO (CO-PrOx)”, *ACS Applied Materials & Interfaces* **2019**, 11, 36763–36773, DOI 10.1021/acsami.9b12731.
- [68] V. Middelkoop, A. Vamvakeros, D. de Wit, S. Jacques, S. Danaci, C. Jacquot, Y. de Vos, D. Matras, S. Price, A. Beale, “3D printed Ni/Al<sub>2</sub>O<sub>3</sub> based catalysts for CO<sub>2</sub> methanation : a comparative and operando XRD-CT study”, *Journal of CO<sub>2</sub> Utilization* **2019**, 33, 478–487, DOI 10.1016/j.jcou.2019.07.013.
- [69] S. Hajimirzaee, A. M. Doyle, “3D printed catalytic converters with enhanced activity for low-temperature methane oxidation in dual-fuel engines”, *Fuel* **2020**, 274, 117848, DOI 10.1016/j.fuel.2020.117848.
- [70] C. A. Leclerc, R. Gudgila, “Short Contact Time Catalytic Partial Oxidation of Methane over Rhodium Supported on Ceria Based 3-D Printed Supports”, *Industrial & Engineering Chemistry Research* **2019**, 58, 14632–14637, DOI 10.1021/acs.iecr.9b01169.
- [71] J. N. Stuecker, J. E. Miller, R. E. Ferrizz, J. E. Mudd, J. Cesarano, “Advanced Support Structures for Enhanced Catalytic Activity”, *Industrial & Engineering Chemistry Research* **2004**, 43, 51–55, DOI 10.1021/ie030291v.
- [72] R. M. Ferrizz, J. N. Stuecker, J. Cesarano, J. E. Miller, “Monolithic Supports with Unique Geometries and Enhanced Mass Transfer”, *Industrial & Engineering Chemistry Research* **2005**, 44, 302–308, DOI 10.1021/ie049468r.

- [73] C. R. Tubío, J. Azuaje, L. Escalante, A. Coelho, F. Guitián, E. Sotelo, A. Gil, “3D printing of a heterogeneous copper-based catalyst”, *Journal of Catalysis* **2016**, 334, 110–115, DOI 10.1016/j.jcat.2015.11.019.
- [74] M. A. S. R. Saadi, A. Maguire, N. T. Pottackal, M. S. H. Thakur, M. M. Ikram, A. J. Hart, P. M. Ajayan, M. M. Rahman, “Direct Ink Writing: A 3D Printing Technology for Diverse Materials”, *Advanced Materials* **2022**, 34, e2108855, DOI 10.1002/adma.202108855.
- [75] J. Cesarano, P. D. Calvert, “Freeforming objects with low-binder slurry”, *US6027-326A* **1997**.
- [76] J. Cesarano, S. Grieco, “Robocasting: A New Technique for the Freeform Fabrication of Near-Net-Shape Ceramics”, *Materials Technology* **1997**, 12, 98–100, DOI 10.1080/10667857.1997.11752736.
- [77] Q. Chen, E. Tian, Y. Wang, J. Mo, G. Xu, M. Zhu, “Recent Progress and Perspectives of Direct Ink Writing Applications for Mass Transfer Enhancement in Gas-Phase Adsorption and Catalysis”, *Small Methods* **2023**, e2201302, DOI 10.1002/smt.202201302.
- [78] P. F. Großmann, M. Tonigold, N. Szesni, R. Fischer, A. Seidel, K. Achterhold, F. Pfeiffer, B. Rieger, “Influence of internal and external surface area on impregnation and activity of 3D printed catalyst carriers”, *Catalysis Communications* **2023**, 175, 106610, DOI 10.1016/j.catcom.2023.106610.
- [79] A. S. Díaz-Marta, C. R. Tubío, C. Carbajales, C. Fernández, L. Escalante, E. Sotelo, F. Guitián, V. L. Barrio, A. Gil, A. Coelho, “Three-Dimensional Printing in Catalysis: Combining 3D Heterogeneous Copper and Palladium Catalysts for Multicatalytic Multicomponent Reactions”, *ACS Catalysis* **2018**, 8, 392–404, DOI 10.1021/acscatal.7b02592.
- [80] A. Elgoro, L. Soler, J. Llorca, I. Casanova, “3D printed microstructured Au/TiO<sub>2</sub> catalyst for hydrogen photoproduction”, *Applied Materials Today* **2019**, 16, 265–272, DOI 10.1016/j.apmt.2019.06.007.
- [81] A. Quintanilla, J. A. Casas, P. Miranzo, M. I. Osendi, M. Belmonte, “3D-Printed Fe-doped silicon carbide monolithic catalysts for wet peroxide oxidation processes”, *Applied Catalysis B: Environmental* **2018**, 235, 246–255, DOI 10.1016/j.apcatb.2018.04.066.
- [82] J. Azuaje, C. R. Tubío, L. Escalante, M. Gómez, F. Guitián, A. Coelho, O. Caaño, A. Gil, E. Sotelo, “An efficient and recyclable 3D printed  $\alpha$ -Al<sub>2</sub>O<sub>3</sub> catalyst for the multicomponent assembly of bioactive heterocycles”, *Applied Catalysis A: General* **2017**, 530, 203–210, DOI 10.1016/j.apcata.2016.11.031.

- [83] M. V. Twigg, J. T. Richardson, “Effects of alumina incorporation in coprecipitated NiO–Al<sub>2</sub>O<sub>3</sub> catalysts”, *Applied Catalysis A: General* **2000**, *190*, 61–72, DOI 10.1016/S0926-860X(99)00269-0.
- [84] C. N. Satterfield, *Heterogeneous catalysis in industrial practice*. 2nd edition, McGraw Hill, New York, NY, **1991**.
- [85] *Contemporary catalysis: Science, technology, and applications*, (Eds.: P. C. J. Kamer, D. Vogt, J. W. Thybaut), Royal Society of Chemistry, Cambridge, **2017**.
- [86] E. M. Holt, “The properties and forming of catalysts and absorbents by granulation”, *Powder Technology* **2004**, *140*, 194–202, DOI 10.1016/j.powtec.2004.01.010.
- [87] P. Munnik, P. E. de Jongh, K. P. de Jong, “Recent developments in the synthesis of supported catalysts”, *Chemical Reviews* **2015**, *115*, 6687–6718, DOI 10.1021/cr500486u.
- [88] V. Russo, L. Mastroianni, R. Tesser, T. Salmi, M. Di Serio, “Intraparticle Modeling of Non-Uniform Active Phase Distribution Catalyst”, *ChemEngineering* **2020**, *4*, 24, DOI 10.3390/chemengineering4020024.
- [89] J. F. Roth, T. E. Reichard, “Determination and effect of platinum concentration profiles in supported catalysts”, *Journal of the Research Institute for Catalysis Hokkaido University* **1972**, 85–94.
- [90] E. R. Becker, J. Wei, “Nonuniform distribution of catalysts on supports - I. Bimolecular Langmuir reactions”, *Journal of Catalysis* **1977**, *46*, 365–371, DOI 10.1016/0021-9517(77)90220-2.
- [91] A. Gavriilidis, A. Varma, “Optimal catalyst activity profiles in pellets: 9. Study of ethylene epoxidation”, *AIChE Journal* **1992**, *38*, 291–296, DOI 10.1002/aic.690380215.
- [92] B. Liu, Y. Chai, Y. Liu, Y. Wang, Y. Liu, C. Liu, “A simple method for preparation of presulfided eggshell CoMoS/gamma-Al<sub>2</sub>O<sub>3</sub> catalysts for hydrodesulfurization of dibenzothiophene”, *Fuel* **2012**, *95*, 457–463, DOI 10.1016/j.fuel.2011.12.019.
- [93] Z. Zhou, T. Zeng, Z. Cheng, W. Yuan, “Kinetics of selective hydrogenation of pyrolysis gasoline over an egg-shell catalyst”, *Chemical Engineering Science* **2010**, *65*, 1832–1839, DOI 10.1016/j.ces.2009.11.028.
- [94] W. Peters, A. Seidel, S. Herzog, A. Bösmann, W. Schwieger, P. Wasserscheid, “Macrokinetic effects in perhydro-N-ethylcarbazole dehydrogenation and H<sub>2</sub> productivity optimization by using egg-shell catalysts”, *Energy & Environmental Science* **2015**, *8*, 3013–3021, DOI 10.1039/C5EE02024G.

- [95] H. Silva, M. G. Nielsen, E. M. Fiordaliso, C. D. Damsgaard, C. Gundlach, T. Kasama, I. Chorkendorff, D. Chakraborty, “Synthesis and characterization of Fe-Ni/ $\gamma$ - $\text{Al}_2\text{O}_3$  egg-shell catalyst for  $\text{H}_2$  generation by ammonia decomposition”, *Applied Catalysis A: General* **2015**, 505, 548–556, DOI 10.1016/j.apcata.2015.07.016.
- [96] K. Kunimori, I. Nakajima, T. Uchijima, “Catalytic performance of egg white type Pt/ $\text{Al}_2\text{O}_3$  catalyst in the oxidation of  $\text{C}_3\text{H}_8$  and CO”, *Chemistry Letters* **1982**, 11, 1165–1168, DOI 10.1246/cl.1982.1165.
- [97] K. Kunimori, E. Kawasaki, I. Nakajima, T. Uchijima, “Catalytic performance of egg-white type Pt/ $\text{Al}_2\text{O}_3$  catalyst: Multiple steady states in the oxidation of CO”, *Applied Catalysis* **1986**, 22, 115–122, DOI 10.1016/S0166-9834(00)82598-1.
- [98] M. Heise, J. A. Schwarz, “Preparation of metal distributions within catalyst supports. I. Effect of pH on catalytic metal profiles”, *Journal of Colloid and Interface Science* **1985**, 107, 237–243, DOI 10.1016/0021-9797(85)90167-5.
- [99] G. de La Puente, “On the distribution of oxygen-containing surface groups in carbons and their influence on the preparation of carbon-supported molybdenum catalysts”, *Solid State Ionics* **1998**, 112, 103–111, DOI 10.1016/S0167-2738(98)00200-8.
- [100] M. Kotter, L. Riekert in *Preparation of Catalysts II, Proceedings of the Second International Symposium*, Studies in Surface Science and Catalysis, Elsevier, **1979**, pp. 51–63, DOI 10.1016/S0167-2991(09)60204-4.
- [101] X. Liu, J. G. Khinast, B. J. Glasser, “Drying of Ni/Alumina Catalysts: Control of the Metal Distribution Using Surfactants and the Melt Infiltration Method”, *Industrial & Engineering Chemistry Research* **2014**, 53, 5792–5800, DOI 10.1021/ie500099c.
- [102] E. Iglesia, S. L. Soled, J. E. Baumgartner, S. C. Reyes, “Synthesis and Catalytic Properties of Eggshell Cobalt Catalysts for the Fischer-Tropsch Synthesis”, *Journal of Catalysis* **1995**, 153, 108–122, DOI 10.1006/jcat.1995.1113.
- [103] S.-Y. Lee, R. Aris, “The Distribution of Active ingredients in Supported Catalysts Prepared by Impregnation”, *Catalysis Reviews* **1985**, 27, 207–340, DOI 10.1080/01614948508064737.
- [104] A. V. Neimark, L. I. Kheifets, V. B. Felonov, “Theory of preparation of supported catalysts”, *Industrial & Engineering Chemistry Product Research and Development* **1981**, 20, 439–450, DOI 10.1021/i300003a006.
- [105] S. T. Sie, “Intraparticle diffusion and reaction kinetics as factors in catalyst particle design”, *The Chemical Engineering Journal and the Biochemical Engineering Journal* **1993**, 53, 1–11, DOI 10.1016/0923-0467(93)80002-E.

- [106] S. T. Sie, R. Krishna, “Process Development and Scale Up: II. Catalyst Design Strategy”, *Reviews in Chemical Engineering* **1998**, *14*, DOI 10.1515/REVCE.1998.14.3.159.
- [107] A. Lekhal, B. J. Glasser, J. G. Khinast, “Impact of drying on the catalyst profile in supported impregnation catalysts”, *Chemical Engineering Science* **2001**, *56*, 4473–4487, DOI 10.1016/S0009-2509(01)00120-8.
- [108] P. Sabatier, J. B. Senderens, “Direct hydrogenation of oxides of carbon in presence of various finely divided metals”, *Comptes rendus de l'Académie des Sciences* **1902**, *134*, 689–691.
- [109] L. Jürgensen, E. A. Ehimen, J. Born, J. B. Holm-Nielsen, “Dynamic biogas upgrading based on the Sabatier process: thermodynamic and dynamic process simulation”, *Bioresource Technology* **2015**, *178*, 323–329, DOI 10.1016/j.biortech.2014.10.069.
- [110] J. Gao, Y. Wang, Y. Ping, D. Hu, G. Xu, F. Gu, F. Su, “A thermodynamic analysis of methanation reactions of carbon oxides for the production of synthetic natural gas”, *RSC Advances* **2012**, *2*, 2358, DOI 10.1039/c2ra00632d.
- [111] S. Abate, C. Mebrahtu, E. Giglio, F. Deorsola, S. Bensaid, S. Perathoner, R. Pirone, G. Centi, “Catalytic Performance of gamma-Al<sub>2</sub>O<sub>3</sub>-ZrO<sub>2</sub>-TiO<sub>2</sub>-CeO<sub>2</sub> Composite Oxide Supported Ni-Based Catalysts for CO<sub>2</sub> Methanation”, *Industrial & Engineering Chemistry Research* **2016**, *55*, 4451–4460, DOI 10.1021/acs.iecr.6b00134.
- [112] P. Frontera, A. Macario, M. Ferraro, P. Antonucci, “Supported Catalysts for CO<sub>2</sub> Methanation: A Review”, *Catalysts* **2017**, *7*, 59, DOI 10.3390/catal7020059.
- [113] J. Ashok, S. Pati, P. Hongmanorom, Z. Tianxi, C. Junmei, S. Kawi, “A review of recent catalyst advances in CO<sub>2</sub> methanation processes”, *Catalysis Today* **2020**, *356*, 471–489, DOI 10.1016/j.cattod.2020.07.023.
- [114] J. R. Rostrup-Nielsen, K. Pedersen, J. Sehested, “High temperature methanation Sintering and structure sensitivity”, *Applied Catalysis A: General* **2007**, *330*, 134–138, DOI 10.1016/j.apcata.2007.07.015.
- [115] X. Bai, S. Wang, T. Sun, S. Wang, “The sintering of Ni/Al<sub>2</sub>O<sub>3</sub> methanation catalyst for substitute natural gas production”, *Reaction Kinetics, Mechanisms and Catalysis* **2014**, *112*, 437–451, DOI 10.1007/s11144-014-0700-8.
- [116] T. H. Nguyen, H. B. Kim, E. D. Park, “CO and CO<sub>2</sub> Methanation over CeO<sub>2</sub>-Supported Cobalt Catalysts”, *Catalysts* **2022**, *12*, 212, DOI 10.3390/catal12020212.

- [117] T. an Le, M. S. Kim, S. H. Lee, E. D. Park, “CO and CO<sub>2</sub> Methanation Over Supported Cobalt Catalysts”, *Topics in Catalysis* **2017**, *60*, 714–720, DOI 10.1007/s11244-017-0788-y.
- [118] J. Tu, H. Wu, Q. Qian, S. Han, M. Chu, S. Jia, R. Feng, J. Zhai, M. He, B. Han, “Low temperature methanation of CO<sub>2</sub> over an amorphous cobalt-based catalyst”, *Chemical Science* **2021**, *12*, 3937–3943, DOI 10.1039/d0sc06414a.
- [119] J. Kirchner, J. K. Anolleck, H. Lösch, S. Kureti, “Methanation of CO<sub>2</sub> on iron based catalysts”, *Applied Catalysis B: Environmental* **2018**, *223*, 47–59, DOI 10.1016/j.apcatb.2017.06.025.
- [120] W. Li, X. Nie, X. Jiang, A. Zhang, F. Ding, M. Liu, Z. Liu, X. Guo, C. Song, “ZrO<sub>2</sub> support imparts superior activity and stability of Co catalysts for CO<sub>2</sub> methanation”, *Applied Catalysis B: Environmental* **2018**, *220*, 397–408, DOI 10.1016/j.apcatb.2017.08.048.
- [121] J. Martínez, E. Hernández, S. Alfaro, R. López Medina, G. Valverde Aguilar, E. Albitar, M. Valenzuela, “High Selectivity and Stability of Nickel Catalysts for CO<sub>2</sub> Methanation: Support Effects”, *Catalysts* **2019**, *9*, 24, DOI 10.3390/catal9010024.
- [122] L. Shen, J. Xu, M. Zhu, Y.-F. Han, “Essential Role of the Support for Nickel-Based CO<sub>2</sub> Methanation Catalysts”, *ACS Catalysis* **2020**, *10*, 14581–14591, DOI 10.1021/acscatal.0c03471.
- [123] W. Gac, W. Zawadzki, M. Rotko, M. Greluk, G. Słowik, G. Kolb, “Effects of support composition on the performance of nickel catalysts in CO<sub>2</sub> methanation reaction”, *Catalysis Today* **2020**, *357*, 468–482, DOI 10.1016/j.cattod.2019.07.026.
- [124] Z. Liu, X. Gao, B. Liu, Q. Ma, T.-s. Zhao, J. Zhang, “Recent advances in thermal catalytic CO<sub>2</sub> methanation on hydrotalcite-derived catalysts”, *Fuel* **2022**, *321*, 124115, DOI 10.1016/j.fuel.2022.124115.
- [125] K. H. Eisenlohr, F. W. Moeller, M. Dry, “Influence of certain reaction parameters on the methanation of coal gas to SNG”, *American Chemical Society, Division of Fuel Chemistry* **1974**, *19*, 1–9.
- [126] H. Harms, B. Höhle, A. Skov, “Methanisierung kohlenmonoxidreicher Gase beim Energie-Transport”, *Chemie Ingenieur Technik* **1980**, *52*, 504–515, DOI 10.1002/cite.330520605.
- [127] Haldor Topsøe, From solid fuels to substitute natural gas (SNG) using TREMP, Lyngby, **2009**.
- [128] R. Lohmueller, “Synthesis of methane with combined isotherms and adiabatic reactors”, *Berichte aus Technik und Wissenschaft* **1977**, 3–11.

- [129] M. S. Graboski, E. K. Diehl in Proceedings of fifth synthetic pipeline gas symposium, Chicago, Bituminous Coal Research, Inc, **1973**.
- [130] Friedrichs G., Proplesch P., Wismann G., Lommerzheim W., *Methanisierung von Kohlevergasungsgasen im Wirbelbett: Pilot-Entwicklungsstufe*, Fachinformationzentrum Energie, Physik, Mathematik Karlsruhe, **1985**.
- [131] Frank M. E., Sherwin M. B., Blum D. B., Mednick R. L., “Liquid phase methanation – shift PDU results and pilot plant status”, *Proceeding of Eighth Synthetic Pipeline Gas Symposium* **1976**, 159–179.
- [132] Z. Liu, X. Gao, B. Liu, Q. Ma, T.-s. Zhao, J. Zhang, “Recent advances in thermal catalytic CO<sub>2</sub> methanation on hydrotalcite-derived catalysts”, *Fuel* **2022**, 321, 124115, DOI 10.1016/j.fuel.2022.124115.
- [133] T. Stiegler, K. Meltzer, A. Tremel, M. Baldauf, P. Wasserscheid, J. Albert, “Development of a Structured Reactor System for CO<sub>2</sub> Methanation under Dynamic Operating Conditions”, *Energy Technology* **2019**, 7, 1900047, DOI 10.1002/ente.201900047.
- [134] M. González-Castaño, F. Baena-Moreno, J. Carlos Navarro de Miguel, K. U. Miah, F. Arroyo-Torralvo, R. Ossenbrink, J. A. Odriozola, W. Benzinger, A. Hensel, A. Wenka, H. Arellano-García, “3D-printed structured catalysts for CO<sub>2</sub> methanation reaction: Advancing of gyroid-based geometries”, *Energy Conversion and Management* **2022**, 258, 115464, DOI 10.1016/j.enconman.2022.115464.
- [135] F. M. Baena-Moreno, M. González-Castaño, J. C. Navarro de Miguel, K. U. M. Miah, R. Ossenbrink, J. A. Odriozola, H. Arellano-García, “Stepping toward Efficient Microreactors for CO<sub>2</sub> Methanation: 3D-Printed Gyroid Geometry”, *ACS Sustainable Chemistry & Engineering* **2021**, 9, 8198–8206, DOI 10.1021/acssuschemeng.1c01980.
- [136] M. Felderhoff, C. Weidenthaler, R. von Helmolt, U. Eberle, “Hydrogen storage: the remaining scientific and technological challenges”, *Physical Chemistry Chemical Physics : PCCP* **2007**, 9, 2643–2653, DOI 10.1039/b701563c.
- [137] M. Niermann, S. Drünert, M. Kaltschmitt, K. Bonhoff, “Liquid organic hydrogen carriers (LOHCs) - techno-economic analysis of LOHCs in a defined process chain”, *Energy & Environmental Science* **2019**, 12, 290–307, DOI 10.1039/C8EE02700E.
- [138] P. Preuster, C. Papp, P. Wasserscheid, “Liquid Organic Hydrogen Carriers (LOHCs): Toward a Hydrogen-free Hydrogen Economy”, *Accounts of Chemical Research* **2017**, 50, 74–85, DOI 10.1021/acs.accounts.6b00474.

- [139] P. Modisha, R. Garidzirai, H. Güneş, S. E. Bozbag, S. Rommel, E. Uzunlar, M. Aindow, C. Erkey, D. Bessarabov, “A Promising Catalyst for the Dehydrogenation of Perhydro-Dibenzyltoluene: Pt/Al<sub>2</sub>O<sub>3</sub> Prepared by Supercritical CO<sub>2</sub> Deposition”, *Catalysts* **2022**, *12*, 489, DOI 10.3390/catal12050489.
- [140] L. Shi, Y. Zhou, S. Qi, K. J. Smith, X. Tan, J. Yan, C. Yi, “Pt Catalysts Supported on H<sub>2</sub> and O<sub>2</sub> Plasma-Treated Al<sub>2</sub>O<sub>3</sub> for Hydrogenation and Dehydrogenation of the Liquid Organic Hydrogen Carrier Pair Dibenzyltoluene and Perhydrodibenzyltoluene”, *ACS Catalysis* **2020**, *10*, 10661–10671, DOI 10.1021/acscatal.0c03091.
- [141] T. in Park, S. H. Lee, K.-Y. Lee, “Characteristics of La-doped Pt/Al<sub>2</sub>O<sub>3</sub> catalyst prepared by solvent-deficient method and effect on enhancement of dehydrogenation of perhydrodibenzyltoluene”, *Korean Journal of Chemical Engineering* **2023**, *40*, 97–103, DOI 10.1007/s11814-022-1319-5.
- [142] A. Ali, A. K. Rohini, Y. S. Noh, D. J. Moon, H. J. Lee, “Hydrogenation of dibenzyltoluene and the catalytic performance of Pt/Al<sub>2</sub>O<sub>3</sub> with various Pt loadings for hydrogen production from perhydro-dibenzyltoluene”, *International Journal of Energy Research* **2022**, *46*, 6672–6688, DOI 10.1002/er.7604.
- [143] L. Shi, Y. Zhou, X. Tan, S. Qi, K. J. Smith, C. Yi, B. Yang, “The effects of alumina morphology and Pt electron property on reversible hydrogenation and dehydrogenation of dibenzyltoluene as a liquid organic hydrogen carrier”, *International Journal of Hydrogen Energy* **2022**, *47*, 4704–4715, DOI 10.1016/j.ijhydene.2021.11.076.
- [144] F. Auer, A. Hupfer, A. Bösmann, N. Szesni, P. Wasserscheid, “Influence of the nanoparticle size on hydrogen release and side product formation in liquid organic hydrogen carrier systems with supported platinum catalysts”, *Catalysis Science & Technology* **2020**, *10*, 6669–6678, DOI 10.1039/D0CY01173H.
- [145] F. Auer, D. Blaumeiser, T. Bauer, A. Bösmann, N. Szesni, J. Libuda, P. Wasserscheid, “Boosting the activity of hydrogen release from liquid organic hydrogen carrier systems by sulfur-additives to Pt on alumina catalysts”, *Catalysis Science & Technology* **2019**, *9*, 3537–3547, DOI 10.1039/c9cy00817a.
- [146] S. Lee, J. Lee, T. Kim, G. Han, J. Lee, K. Lee, J. Bae, “Pt/CeO<sub>2</sub> catalyst synthesized by combustion method for dehydrogenation of perhydro-dibenzyltoluene as liquid organic hydrogen carrier: Effect of pore size and metal dispersion”, *International Journal of Hydrogen Energy* **2021**, *46*, 5520–5529, DOI 10.1016/j.ijhydene.2020.11.038.
- [147] F. Auer, PhD thesis, Friedrich-Alexander-Universität Erlangen-Nürnberg, **2020**.

- [148] P. T. Aakko-Saksa, M. Vehkamäki, M. Kemell, L. Keski­väli, P. Simell, M. Reinikainen, U. Tapper, T. Repo, “Hydrogen release from liquid organic hydrogen carriers catalysed by platinum on rutile-anatase structured titania”, *Chemical Communications* **2020**, 56, 1657–1660, DOI 10.1039/c9cc09715e.
- [149] L. Shi, S. Qi, J. Qu, T. Che, C. Yi, B. Yang, “Integration of hydrogenation and dehydrogenation based on dibenzyltoluene as liquid organic hydrogen energy carrier”, *International Journal of Hydrogen Energy* **2019**, 44, 5345–5354, DOI 10.1016/j.ijhydene.2018.09.083.
- [150] G. J. Hutchings, J. C. Védrine in *Basic Principles in Applied Catalysis*, (Eds.: A. W. Castleman, F. P. Schäfer, J. P. Toennies, W. Zinth, M. Baerns), Springer Series in Chemical Physics, Springer Berlin Heidelberg, **2004**, pp. 215–258, DOI 10.1007/978-3-662-05981-4\_6.
- [151] U. Holzwarth, N. Gibson, “The Scherrer equation versus the ‘Debye-Scherrer equation’”, *Nature Nanotechnology* **2011**, 6, 534, DOI 10.1038/nnano.2011.145.
- [152] N. H. Turner in *Encyclopedia of Analytical Chemistry*, (Ed.: R. A. Meyers), John Wiley & Sons, Ltd, Chichester, UK, **2006**, DOI 10.1002/9780470027318.a6702.
- [153] J. F. Watts, J. Wolstenholme, *An introduction to surface analysis by XPS and AES*, Wiley, New York and Weinheim, **2003**.
- [154] M. Newville, *Fundamentals of XAFS*, University of Chicago, Chicago, IL, **2004**.
- [155] S. R. Chae, J. Moon, S. Yoon, S. Bae, P. Levitz, R. Winarski, P. J. M. Monteiro, “Advanced Nanoscale Characterization of Cement Based Materials Using X-Ray Synchrotron Radiation: A Review”, *International Journal of Concrete Structures and Materials* **2013**, 7, 95–110, DOI 10.1007/s40069-013-0036-1.
- [156] I. Langmuir, “The Adsorption of Gases on Plane Surface of Glass, Mica and Platinum”, *Journal of the American Chemical Society* **1918**, 40, 1361–1403, DOI 10.1021/ja02242a004.
- [157] K. S. W. Sing, “Reporting physisorption data for gas/solid systems with special reference to the determination of surface area and porosity (Recommendations 1984)”, *Pure and Applied Chemistry* **1985**, 57, 603–619, DOI 10.1351/pac198557040603.
- [158] K. S. W. Sing, D. H. Everett, R. A. W. Haul, L. Moscou, R. A. Pierotti, J. Rouquerol, T. Siemieniowska in *Handbook of Heterogeneous Catalysis*, (Eds.: G. Ertl, H. Knözinger, F. Schüth, J. Weitkamp), Wiley-VCH, Weinheim, DE, **2008**, DOI 10.1002/9783527610044.hetcat0065.
- [159] D. S. Lee, D. J. Min, “A Kinetics of Hydrogen Reduction of Nickel Oxide at Moderate Temperature”, *Metals and Materials International* **2019**, 25, 982–990, DOI 10.1007/S12540-019-00261-Y.

- [160] D. Monti, “Temperature-programmed reduction. Parametric sensitivity and estimation of kinetic parameters”, *Journal of Catalysis* **1983**, 83, 323–335, DOI 10.1016/0021-9517(83)90058-1.
- [161] L. Reimer, *Transmission Electron Microscopy: Physics of Image Formation*, 5th ed., Springer, New York, NY, **2008**.
- [162] *A practical guide to microstructural analysis of cementitious materials*, (Eds.: K. Scrivener, R. Snellings, B. Lothenbach), CRC Press, Boca Raton, FL, **2016**, DOI 10.1201/b19074.
- [163] E. W. Washburn, “The Dynamics of Capillary Flow”, *Physical Review* **1921**, 17, 273–283, DOI 10.1103/PhysRev.17.273.
- [164] D. Staub, S. Meille, V. Le Corre, J. Chevalier, L. Rouleau, “Revisiting the Side Crushing Test Using the Three-Point Bending Test for the Strength Measurement of Catalyst Supports”, *Oil & Gas Science and Technology – Revue d’IFP Energies nouvelles* **2015**, 70, 475–486, DOI 10.2516/ogst/2013214.
- [165] S. Timoshenko, J. N. Goodier, *Theory of Elasticity*, 2nd ed., McGraw-Hill, **1951**.
- [166] N. Guo, M. C. Leu, “Additive manufacturing: technology, applications and research needs”, *Frontiers of Mechanical Engineering* **2013**, 8, 215–243, DOI 10.1007/s11465-013-0248-8.
- [167] D. E. Dunn, L. J. LaFountain, R. E. Jackson, “Porosity dependence and mechanism of brittle fracture in sandstones”, *Journal of Geophysical Research* **1973**, 78, 2403–2417, DOI 10.1029/JB078i014p02403.
- [168] J. A. Gonzalez, J. Mireles, Y. Lin, R. B. Wicker, “Characterization of ceramic components fabricated using binder jetting additive manufacturing technology”, *Ceramics International* **2016**, 42, 10559–10564, DOI 10.1016/j.ceramint.2016.03.079.
- [169] P. Kunchala, K. Kappagantula, “3D printing high density ceramics using binder jetting with nanoparticle densifiers”, *Materials & Design* **2018**, 155, 443–450, DOI 10.1016/j.matdes.2018.06.009.
- [170] S. J. Huang, C. S. Ye, “Preparation and performance of binder jetting porous alumina ceramic”, *IOP Conference Series: Materials Science and Engineering* **2020**, 770, 012057, DOI 10.1088/1757-899X/770/1/012057.
- [171] M. Mariani, R. Beltrami, P. Brusa, C. Galassi, R. Ardito, N. Lecis, “3D printing of fine alumina powders by binder jetting”, *Journal of the European Ceramic Society* **2021**, 41, 5307–5315, DOI 10.1016/j.jeurceramsoc.2021.04.006.
- [172] M. Li, L. Xu, W. Lu, “Nanopore size effect on critical infiltration depth of liquid nanofoam as a reusable energy absorber”, *Journal of Applied Physics* **2019**, 125, 1–7, DOI 10.1063/1.5065485.

- [173] D. R. Coupland, “Catalyst shaped unit and method of its manufacture”, *EP27522-44A1* **2014**.
- [174] N. Kashani-Shirazi, V. Wloka, W. Gerlinger, A. Schmidt, K. Heinen, W. Kollenberg, “Use of shaped bodies having catalytic properties as reactor internals”, *US20100222209A1* **2012**.
- [175] C. Huo, X. Tian, Y. Nan, Z. Qiu, Q. Zhong, X. Huang, S. Yu, D. Li, “Regulation mechanism of the specific surface area of alumina ceramic carriers with hierarchical porosity fabricated by powder bed fusion”, *Ceramics International* **2021**, *47*, 30954–30962, DOI 10.1016/j.ceramint.2021.08.198.
- [176] M. Ziaee, N. B. Crane, “Binder jetting: A review of process, materials, and methods”, *Additive Manufacturing* **2019**, *28*, 781–801, DOI 10.1016/j.addma.2019.05.031.
- [177] S. F. Hulbert, F. A. Young, R. S. Mathews, J. J. Klawitter, C. D. Talbert, F. H. Stelling, “Potential of ceramic materials as permanently implantable skeletal prostheses”, *Journal of Biomedical Materials Research* **1970**, *4*, 433–456, DOI 10.1002/jbm.820040309.
- [178] C. M. Murphy, M. G. Haugh, F. J. O’Brien, “The effect of mean pore size on cell attachment, proliferation and migration in collagen-glycosaminoglycan scaffolds for bone tissue engineering”, *Biomaterials* **2010**, *31*, 461–466, DOI 10.1016/j.biomaterials.2009.09.063.
- [179] K. Shimura, T. Miyazawa, T. Hanaoka, S. Hirata, “Preparation of Co/Al<sub>2</sub>O<sub>3</sub> catalyst for Fischer-Tropsch synthesis: Combination of impregnation method and homogeneous precipitation method”, *Applied Catalysis A: General* **2014**, *475*, 1–9, DOI 10.1016/j.apcata.2014.01.012.
- [180] S. Ewald, O. Hinrichsen, “On the interaction of CO<sub>2</sub> with Ni-Al catalysts”, *Applied Catalysis A: General* **2019**, *580*, 71–80, DOI 10.1016/j.apcata.2019.04.005.
- [181] J. H. Sinfelt, H. Hurwitz, R. A. Shulman, “Kinetics of methylcyclohexane dehydrogenation over Pt-Al<sub>2</sub>O<sub>3</sub>”, *The Journal of Physical Chemistry* **1960**, *64*, 1559–1562, DOI 10.1021/j100839a054.
- [182] P. Euzen, P. Raybaud, X. Krokidis, H. Toulhoat, J.-L. Le Loarer, J.-P. Jolivet, C. Froidefond in *Handbook of porous solids*, **2002**, pp. 1591–1677, DOI 10.1002/9783527618286.ch23b.
- [183] M. Trueba, S. P. Trasatti, “gamma-Alumina as a Support for Catalysts: A Review of Fundamental Aspects”, *European Journal of Inorganic Chemistry* **2005**, *2005*, 3393–3403, DOI 10.1002/ejic.200500348.
- [184] Wolfgang Kollenberg, “Verfahren zur Herstellung eines keramischen Grünkörpers, Grünkörper und keramischer Formkörper”, *DE102008022664B4* **2008**.

- [185] A. M. Elliott, P. Nandwana, D. Siddel, B. G. Compton in *Proceedings of the 27th Annual International Solid Freeform Fabrication Symposium*, Texas, USA, **2016**, pp. 1031–1037.
- [186] DIN EN 623-2:1993-11, Hochleistungskeramik; Monolithische Keramik; Allgemeine und strukturelle Eigenschaften; Teil 2: Bestimmung von Dichte und Porosität, Berlin, **1993**.
- [187] Y.-B. P. Kwan, J. R. Alcock, “The impact of water impregnation method on the accuracy of open porosity measurements”, *Journal of Materials Science* **2002**, *37*, 2557–2561, DOI 10.1023/A:1015460127828.
- [188] J. F. Bredt, S. Clark, G. Gilchrist, “Three dimensional printing material system and method”, *US7087109B2* **2006**.
- [189] E. M. Sachs, M. J. Cima, M. A. Caradonna, J. Grau, J. G. Serdy, P. C. Saxton, S. A. Uhland, J. Moon, “Jetting layers of powder and the formation of fine powder beds thereby”, *US6596224B1* **2003**.
- [190] Y. Bai, G. Wagner, C. B. Williams, “Effect of Particle Size Distribution on Powder Packing and Sintering in Binder Jetting Additive Manufacturing of Metals”, *Journal of Manufacturing Science and Engineering* **2017**, *139*, DOI 10.1115/1.4036640.
- [191] H. Miyanaji, S. Zhang, L. Yang, “A new physics-based model for equilibrium saturation determination in binder jetting additive manufacturing process”, *International Journal of Machine Tools and Manufacture* **2018**, *124*, 1–11, DOI 10.1016/j.ijmachtools.2017.09.001.
- [192] G. D. Martin, S. D. Hoath, I. M. Hutchings, “Inkjet printing - the physics of manipulating liquid jets and drops”, *Journal of Physics: Conference Series* **2008**, *105*, 012001, DOI 10.1088/1742-6596/105/1/012001.
- [193] A. B. Aqeel, M. Mohasan, P. Lv, Y. Yang, H. Duan, “Effects of nozzle and fluid properties on the drop formation dynamics in a drop-on-demand inkjet printing”, *Applied Mathematics and Mechanics* **2019**, *40*, 1239–1254, DOI 10.1007/s10483-019-2514-7.
- [194] V. A. Ivanov, A. Piéplu, J. C. Lavalley, P. Nortier, “Effect of sodium oxide on the morphology and basicity of alumina”, *Applied Catalysis A: General* **1995**, *131*, 323–334, DOI 10.1016/0926-860X(95)00149-2.
- [195] W. El Hotaby, H. H. A. Sherif, B. A. Hemdan, W. A. Khalil, S. K. H. Khalil, “Assessment of in situ-Prepared Polyvinylpyrrolidone-Silver Nanocomposite for Antimicrobial Applications”, *Acta Physica Polonica A* **2017**, *131*, 1554–1560, DOI 10.12693/APhysPolA.131.1554.

- [196] N. Vijaya, S. Selvasekarapandian, S. Karthikeyan, M. Prabu, N. Rajeswari, C. Sanjeeviraja, “Synthesis and characterization of proton conducting polymer electrolyte based on poly(N-vinyl pyrrolidone)”, *Journal of Applied Polymer Science* **2013**, *127*, 1538–1543, DOI 10.1002/app.37765.
- [197] H. C. Stumpf, A. S. Russell, J. W. Newsome, C. M. Tucker, “Thermal Transformations of Aluminas and Alumina Hydrates - Reaction with 44% Technical Acid”, *Industrial & Engineering Chemistry* **1950**, *42*, 1398–1403, DOI 10.1021/ie50487a039.
- [198] S. V. Tsybulya, G. N. Kryukova, “Nanocrystalline transition aluminas: Nanostructure and features of x-ray powder diffraction patterns of low-temperature Al<sub>2</sub>O<sub>3</sub> polymorphs”, *Physical Review B* **2008**, *77*, 024112, DOI 10.1103/PhysRevB.77.024112.
- [199] C. V. Chandran, C. E. A. Kirschhock, S. Radhakrishnan, F. Taulelle, J. A. Martens, E. Breynaert, “Alumina: discriminative analysis using 3D correlation of solid-state NMR parameters”, *Chemical Society Reviews* **2019**, *48*, 134–156, DOI 10.1039/c8cs00321a.
- [200] K. Wefers, C. Misra, *Oxides and hydroxides of aluminum*, 19th ed., Pittsburgh, PA, **1987**.
- [201] I. Levin, D. Brandon, “Metastable Alumina Polymorphs: Crystal Structures and Transition Sequences”, *Journal of the American Ceramic Society* **1998**, *81*, 1995–2012, DOI 10.1111/j.1151-2916.1998.tb02581.x.
- [202] S. Lamouri, M. Hamidouche, N. Bouaouadja, H. Belhouchet, V. Garnier, G. Fantozzi, J. F. Trekat, “Control of the gamma-alumina to  $\alpha$ -alumina phase transformation for an optimized alumina densification”, *Boletín de la Sociedad Española de Cerámica y Vidrio* **2017**, *56*, 47–54, DOI 10.1016/j.bsecv.2016.10.001.
- [203] G. Busca in *Advances in catalysis*, Advances in Catalysis, Academic Press, Amsterdam, **2014**, pp. 319–404.
- [204] A. L. Dragoo, J. J. Diamond, “Transitions in Vapor-Deposited Alumina from 300 degreeC to 1200 degreeC”, *Journal of the American Ceramic Society* **1967**, *50*, 568–574, DOI 10.1111/j.1151-2916.1967.tb15000.x.
- [205] L. H. Chagas, G. de Carvalho, R. San Gil, S. Chiaro, A. A. Leitão, R. Diniz, “Obtaining aluminas from the thermal decomposition of their different precursors: An <sup>27</sup>Al MAS NMR and X-ray powder diffraction studies”, *Materials Research Bulletin* **2014**, *49*, 216–222, DOI 10.1016/j.materresbull.2013.08.072.
- [206] T. Sato, “Thermal transformation of alumina trihydrate, bayerite”, *Journal of Applied Chemistry* **1962**, *12*, 553–556, DOI 10.1002/jctb.5010121206.
- [207] M. N. Rahaman, *Sintering of ceramics*, CRC Press, Boca Raton, FL, **2008**.

- [208] J. Zheng, J. S. Reed, “Effects of Particle Packing Characteristics on Solid-State Sintering”, *Journal of the American Ceramic Society* **1989**, 72, 810–817, DOI 10.1111/j.1151-2916.1989.tb06222.x.
- [209] A. Kumar, Y. Bai, A. Eklund, C. B. Williams, “Effects of Hot Isostatic Pressing on Copper Parts Fabricated via Binder Jetting”, *Procedia Manufacturing* **2017**, 10, 935–944, DOI 10.1016/j.promfg.2017.07.084.
- [210] E. A. Olevsky, R. M. German, “Effect of gravity on dimensional change during sintering—I. Shrinkage anisotropy”, *Acta Materialia* **2000**, 48, 1153–1166, DOI 10.1016/S1359-6454(99)00368-7.
- [211] F. V. Lenel, H. H. Hausner, O. V. Roman, G. S. Ansell, “The influence of gravity in sintering”, *Soviet Powder Metallurgy and Metal Ceramics* **1963**, 2, 379–384, DOI 10.1007/BF01194674.
- [212] I. B. Cutler, R. E. Henrichsen, “Effect of Particle Shape on the Kinetics of Sintering of Glass”, *Journal of the American Ceramic Society* **1968**, 51, 604, DOI 10.1111/j.1151-2916.1968.tb13334.x.
- [213] A. Mostafaei, P. Rodriguez De Vecchis, I. Nettleship, M. Chmielus, “Effect of powder size distribution on densification and microstructural evolution of binder-jet 3D-printed alloy 625”, *Materials & Design* **2019**, 162, 375–383, DOI 10.1016/j.matdes.2018.11.051.
- [214] Y. Zhu, Z. Wu, W. D. Hartley, J. M. Sietins, C. B. Williams, H. Z. Yu, “Unraveling pore evolution in post-processing of binder jetting materials: X-ray computed tomography, computer vision, and machine learning”, *Additive Manufacturing* **2020**, 34, 101183, DOI 10.1016/j.addma.2020.101183.
- [215] I. O. Ozer, E. Suvaci, B. Karademir, J. M. Missiaen, C. P. Carry, D. Bouvard, “Anisotropic Sintering Shrinkage in Alumina Ceramics Containing Oriented Platelets”, *Journal of the American Ceramic Society* **2006**, 89, 1972–1976, DOI 10.1111/j.1551-2916.2006.01039.x.
- [216] A. Heunisch, A. Dellert, A. Roosen, “Effect of powder, binder and process parameters on anisotropic shrinkage in tape cast ceramic products”, *Journal of the European Ceramic Society* **2010**, 30, 3397–3406, DOI 10.1016/j.jeurceramsoc.2010.08.012.
- [217] A. Mostafaei, E. L. Stevens, J. J. Ference, D. E. Schmidt, M. Chmielus, “Binder jetting of a complex-shaped metal partial denture framework”, *Additive Manufacturing* **2018**, 21, 63–68, DOI 10.1016/j.addma.2018.02.014.
- [218] E. Wheat, M. Vlasea, J. Hinebaugh, C. Metcalfe, “Sinter structure analysis of titanium structures fabricated via binder jetting additive manufacturing”, *Materials & Design* **2018**, 156, 167–183, DOI 10.1016/j.matdes.2018.06.038.

- [219] S. Cao, F. Xie, X. He, C. Zhang, M. Wu, “Postprocessing Study for the Controllable Structures of Ceramic Green Parts Realized by a Flexible Binder Jetting Printing (BJP) Solution”, *Advances in Materials Science and Engineering* **2020**, 2020, DOI 10.1155/2020/3865752.
- [220] S. Maleksaedi, H. Eng, F. E. Wiria, T. Ha, Z. He, “Property enhancement of 3D-printed alumina ceramics using vacuum infiltration”, *Journal of Materials Processing Technology* **2014**, 214, 1301–1306, DOI 10.1016/j.jmatprotec.2014.01.019.
- [221] W. Si, Y. Zhang, J. Sha, Y. Chen, “Mechanisms of pressure-induced water infiltration process through graphene nanopores”, *Molecular Simulation* **2019**, 45, 518–524, DOI 10.1080/08927022.2018.1559310.
- [222] M. E. Suk, N. R. Aluru, “Water Transport through Ultrathin Graphene”, *The Journal of Physical Chemistry Letters* **2010**, 1, 1590–1594, DOI 10.1021/jz100240r.
- [223] F. Granados-Correa, J. Jiménez-Becerril, “The effect of the calcination temperature of boehmite on its Co(II) adsorption properties”, *Journal of Ceramic Processing Research* **2012**, 13, 142–148.
- [224] P. K. Kiyohara, H. Souza Santos, A. C. Vieira-Coelho, P. de Souza Santos, “Structure, surface area and morphology of aluminas from thermal decomposition of  $\text{Al}(\text{OH})(\text{CH}_3\text{COO})_2$  crystals”, *Anais da Academia Brasileira de Ciências* **2000**, 72, 471–495, DOI 10.1590/S0001-37652000000400003.
- [225] B. C. Lippens, Doctoral thesis, Delft University of Technology, Delft, **1961**.
- [226] D. R. Ceratti, M. Faustini, C. Sinturel, M. Vayer, V. Dahirel, M. Jardat, D. Grosso, “Critical effect of pore characteristics on capillary infiltration in mesoporous films”, *Nanoscale* **2015**, 7, 5371–5382, DOI 10.1039/c4nr03021d.
- [227] D. Sergi, L. Grossi, T. Leidi, A. Ortona, “Simulation of capillary infiltration into packing structures for the optimization of ceramic materials using the lattice Boltzmann method”, *Engineering Applications of Computational Fluid Mechanics* **2016**, 10, 485–499, DOI 10.1080/19942060.2016.1189361.
- [228] M. Thommes, K. Kaneko, A. V. Neimark, J. P. Olivier, F. Rodriguez-Reinoso, J. Rouquerol, K. S. W. Sing, “Physisorption of gases, with special reference to the evaluation of surface area and pore size distribution (IUPAC Technical Report)”, *Pure and Applied Chemistry* **2015**, 87, 1051–1069, DOI 10.1515/pac-2014-1117.
- [229] M. Alava, M. Dubé, M. Rost, “Imbibition in disordered media”, *Advances in Physics* **2004**, 53, 83–175, DOI 10.1080/00018730410001687363.
- [230] Mark G. Bernadiner, “A Capillary Microstructure of the Wetting Front”, *Transport in Porous Media* **1998**, 30, 251–265, DOI 10.1023/A:1006571720867.

- [231] S.-Y. Chun, T. Kim, B. Ye, B. Jeong, M.-j. Lee, D. H. Lee, E.-S. Kim, H. Lee, H.-D. Kim, “Capillary pressure and saturation of pore-controlled granules for powder bed binder jetting”, *Applied Surface Science* **2020**, *515*, 1459–1479, DOI 10.1016/j.apsusc.2020.145979.
- [232] A. Ertas, A. Stroud, “Additive Manufacturing Research and Applications”, *Metals* **2022**, *12*, 634, DOI 10.3390/met12040634.
- [233] A. Alammari, J. C. Kois, M. Revilla-León, W. Att, “Additive Manufacturing Technologies: Current Status and Future Perspectives”, *Journal of Prosthodontics* **2022**, *31*, 4–12, DOI 10.1111/jopr.13477.
- [234] R. Kumar, M. Kumar, J. S. Chohan, “The role of additive manufacturing for biomedical applications: A critical review”, *Journal of Manufacturing Processes* **2021**, *64*, 828–850, DOI 10.1016/j.jmapro.2021.02.022.
- [235] S. Nayar, S. Bhuminathan, W. M. Bhat, “Rapid prototyping and stereolithography in dentistry”, *Journal of Pharmacy & Bioallied Sciences* **2015**, *7*, S216–9, DOI 10.4103/0975-7406.155913.
- [236] S. Salifu, D. Desai, O. Ogunbiyi, K. Mwale, “Recent development in the additive manufacturing of polymer-based composites for automotive structures - a review”, *The International Journal of Advanced Manufacturing Technology* **2022**, *119*, 6877–6891, DOI 10.1007/s00170-021-08569-z.
- [237] B. Blakey-Milner, P. Gradl, G. Snedden, M. Brooks, J. Pitot, E. Lopez, M. Leary, F. Berto, A. Du Plessis, “Metal additive manufacturing in aerospace: A review”, *Materials & Design* **2021**, *209*, 110008, DOI 10.1016/j.matdes.2021.110008.
- [238] M. Khorasani, A. Ghasemi, B. Rolfe, I. Gibson, “Additive manufacturing a powerful tool for the aerospace industry”, *Rapid Prototyping Journal* **2022**, *28*, 87–100, DOI 10.1108/RPJ-01-2021-0009.
- [239] H. Thakkar, S. Eastman, Q. Al-Naddaf, A. A. Rownaghi, F. Rezaei, “3D-Printed Metal-Organic Framework Monoliths for Gas Adsorption Processes”, *ACS Applied Materials & Interfaces* **2017**, *9*, 35908–35916, DOI 10.1021/acsami.7b11626.
- [240] G. Vega, A. Quintanilla, N. Menendez, M. Belmonte, J. A. Casas, “3D honeycomb monoliths with interconnected channels for the sustainable production of dihydroxybenzenes: towards the intensification of selective oxidation processes”, *Chemical Engineering and Processing - Process Intensification* **2021**, *165*, 108437, DOI 10.1016/j.cep.2021.108437.

- [241] S. M. Sajadi, L. Vásárhelyi, R. Mousavi, A. H. Rahmati, Z. Kónya, Á. Kukovecz, T. Arif, T. Filleter, R. Vajtai, P. Boul, Z. Pang, T. Li, C. S. Tiwary, M. M. Rahman, P. M. Ajayan, “Damage-tolerant 3D-printed ceramics via conformal coating”, *Science Advances* **2021**, 7, DOI 10.1126/sciadv.abc5028.
- [242] A. D. Salazar-Aguilar, A. Quintanilla, P. López, C. Martínez, S. M. Vega-Díaz, J. A. Casas, P. Miranzo, M. I. Osendi, M. Belmonte, “3D-Printed Fe/gamma-Al<sub>2</sub>O<sub>3</sub> Monoliths from MOF-Based Boehmite Inks for the Catalytic Hydroxylation of Phenol”, *ACS Applied Materials & Interfaces* **2022**, 14, 920–932, DOI 10.1021/acsami.1c19755.
- [243] H. M. Bui, P. F. Großmann, T. Gros, M. Blum, A. Berger, R. Fischer, N. Szesni, M. Tonigold, O. Hinrichsen, “3D printed co-precipitated Ni-Al CO<sub>2</sub> methanation catalysts by Binder Jetting: Fabrication, characterization and test in a single pellet string reactor”, *Applied Catalysis A: General* **2022**, 643, 118760, DOI 10.1016/j.apcata.2022.118760.
- [244] ISO/ASTM 52900, *Additive manufacturing - General principles - Terminology*, **2015**.
- [245] J. A. Lewis, “Direct-write assembly of ceramics from colloidal inks”, *Current Opinion in Solid State and Materials Science* **2002**, 6, 245–250, DOI 10.1016/S1359-0286(02)00031-1.
- [246] J. A. Lewis, “Direct Ink Writing of 3D Functional Materials”, *Advanced Functional Materials* **2006**, 16, 2193–2204, DOI 10.1002/adfm.200600434.
- [247] A. Shahzad, I. Lazoglu, “Direct ink writing (DIW) of structural and functional ceramics: Recent achievements and future challenges”, *Composites Part B: Engineering* **2021**, 225, 109249, DOI 10.1016/j.compositesb.2021.109249.
- [248] J. Cesarano, “A Review of Robocasting Technology”, *MRS Proceedings* **1998**, 542, DOI 10.1557/PROC-542-133.
- [249] L. del-Mazo-Barbara, M.-P. Ginebra, “Rheological characterisation of ceramic inks for 3D direct ink writing: A review”, *Journal of the European Ceramic Society* **2021**, 41, 18–33, DOI 10.1016/j.jeurceramsoc.2021.08.031.
- [250] E. Feilden, E. G.-T. Blanca, F. Giuliani, E. Saiz, L. Vandeperre, “Robocasting of structural ceramic parts with hydrogel inks”, *Journal of the European Ceramic Society* **2016**, 36, 2525–2533, DOI 10.1016/j.jeurceramsoc.2016.03.001.
- [251] P. Jiang, Z. Ji, X. Zhang, Z. Liu, X. Wang, “Recent advances in direct ink writing of electronic components and functional devices”, *Progress in Additive Manufacturing* **2018**, 3, 65–86, DOI 10.1007/s40964-017-0035-x.

- [252] J. A. Lewis, J. E. Smay, J. N. Stuecker, J. Cesarano, “Direct Ink Writing of Three-Dimensional Ceramic Structures”, *Journal of the American Ceramic Society* **2006**, *89*, 3599–3609, DOI 10.1111/j.1551-2916.2006.01382.x.
- [253] L. A. Chavez, P. Ibañez, B. Wilburn, D. Alexander, C. Stewart, R. Wicker, Y. Lin, “The Influence of Printing Parameters, Post-Processing, and Testing Conditions on the Properties of Binder Jetting Additive Manufactured Functional Ceramics”, *Ceramics* **2020**, *3*, 65–77, DOI 10.3390/ceramics3010008.
- [254] M. Li, W. Du, A. Elwany, Z. Pei, C. Ma, “Metal Binder Jetting Additive Manufacturing: A Literature Review”, *Journal of Manufacturing Science and Engineering* **2020**, *142*, DOI 10.1115/1.4047430.
- [255] W. Du, G. Miao, L. Liu, Z. Pei, C. Ma in Proceedings of the ASME 14th International Manufacturing Science and Engineering Conference - 2019, the American Society of Mechanical Engineers, New York, N.Y., **2019**, DOI 10.1115/MSEC2019-2983.
- [256] P. M. Modisha, C. N. M. Ouma, R. Garidzirai, P. Wasserscheid, D. Bessarabov, “The Prospect of Hydrogen Storage Using Liquid Organic Hydrogen Carriers”, *Energy & Fuels* **2019**, *33*, 2778–2796, DOI 10.1021/acs.energyfuels.9b00296.
- [257] G. Do, P. Preuster, R. Aslam, A. Bösmann, K. Müller, W. Arlt, P. Wasserscheid, “Hydrogenation of the liquid organic hydrogen carrier compound dibenzyltoluene – reaction pathway determination by  $^1\text{H}$  NMR spectroscopy”, *Reaction Chemistry & Engineering* **2016**, *1*, 313–320, DOI 10.1039/C5RE00080G.
- [258] Y. Sekine, T. Higo, “Recent Trends on the Dehydrogenation Catalysis of Liquid Organic Hydrogen Carrier (LOHC): A Review”, *Topics in Catalysis* **2021**, *64*, 470–480, DOI 10.1007/s11244-021-01452-x.
- [259] N. Brückner, K. Obesser, A. Bösmann, D. Teichmann, W. Arlt, J. Dungs, P. Wasserscheid, “Evaluation of industrially applied heat-transfer fluids as liquid organic hydrogen carrier systems”, *ChemSusChem* **2014**, *7*, 229–235, DOI 10.1002/cssc.201300426.
- [260] P. Preuster, PhD thesis, Friedrich-Alexander-Universität, Erlangen-Nürnberg, **2017**.
- [261] A. Seidel, PhD thesis, Friedrich-Alexander-Universität, Erlangen-Nürnberg, **2019**.
- [262] D. A. Snelling, C. B. Williams, C. T. A. Suchicital, A. P. Druschitz, “Binder jetting advanced ceramics for metal-ceramic composite structures”, *The International Journal of Advanced Manufacturing Technology* **2017**, *92*, 531–545, DOI 10.1007/s00170-017-0139-y.
- [263] C.-L. Huang, J.-J. Wang, C.-Y. Huang, “Sintering behavior and microwave dielectric properties of nano  $\alpha$ -alumina”, *Materials Letters* **2005**, *59*, 3746–3749, DOI 10.1016/j.matlet.2005.06.053.

- [264] D. L. Trimm, A. Stanislaus, “The control of pore size in alumina catalyst supports: A review”, *Applied Catalysis* **1986**, *21*, 215–238, DOI 10.1016/S0166-9834(00)81356-1.
- [265] J. E. Park, B. B. Kim, E. D. Park, “Propane combustion over Pt/Al<sub>2</sub>O<sub>3</sub> catalysts with different crystalline structures of alumina”, *Korean Journal of Chemical Engineering* **2015**, *32*, 2212–2219, DOI 10.1007/s11814-015-0062-6.
- [266] J. Lee, E. J. Jang, D. G. Oh, J. Szanyi, J. H. Kwak, “Morphology and size of Pt on Al<sub>2</sub>O<sub>3</sub>: The role of specific metal-support interactions between Pt and Al<sub>2</sub>O<sub>3</sub>”, *Journal of Catalysis* **2020**, *385*, 204–212, DOI 10.1016/j.jcat.2020.03.019.
- [267] J. H. Kwak, J. Hu, D. Mei, C.-W. Yi, D. H. Kim, C. H. F. Peden, L. F. Allard, J. Szanyi, “Coordinatively unsaturated Al<sup>3+</sup> centers as binding sites for active catalyst phases of platinum on gamma-Al<sub>2</sub>O<sub>3</sub>”, *Science* **2009**, *325*, 1670–1673, DOI 10.1126/science.1176745.
- [268] H. Yao, M. Sieg, H. K. Plummer, Jr., “Surface interactions in the Pt/gamma-Al<sub>2</sub>O<sub>3</sub> system”, *Journal of Catalysis* **1979**, *59*, 365–374, DOI 10.1016/S0021-9517(79)80005-6.
- [269] P. P. Robinson, V. Arun, K. K. A. Rashid, C. U. Aniz, K. K. M. Yusuff, “The active phase (Ni<sup>2+</sup>) distribution in Ni/gamma-Al<sub>2</sub>O<sub>3</sub> catalysts prepared by impregnation of Bis(ethylenediamine)nickel(II) complexes”, *Chemical Engineering Communications* **2012**, *199*, 321–334, DOI 10.1080/00986445.2011.591615.
- [270] X. Liu, J. G. Khinast, B. J. Glasser, “A parametric investigation of impregnation and drying of supported catalysts”, *Chemical Engineering Science* **2008**, *63*, 4517–4530, DOI 10.1016/j.ces.2008.06.013.
- [271] K. Ghaib, F.-Z. Ben-Fares, “Power-to-Methane: A state-of-the-art review”, *Renewable and Sustainable Energy Reviews* **2018**, *81*, 433–446, DOI 10.1016/j.rser.2017.08.004.
- [272] H. Blanco, W. Nijs, J. Ruf, A. Faaij, “Potential of Power-to-Methane in the EU energy transition to a low carbon system using cost optimization”, *Applied Energy* **2018**, *232*, 323–340, DOI 10.1016/j.apenergy.2018.08.027.
- [273] R. Daiyan, I. MacGill, R. Amal, “Opportunities and Challenges for Renewable Power-to-X”, *ACS Energy Letters* **2020**, *5*, 3843–3847, DOI 10.1021/acsenenergylett.0c02249.
- [274] A. Bosoaga, O. Masek, J. E. Oakey, “CO<sub>2</sub> Capture Technologies for Cement Industry”, *Energy Procedia* **2009**, *1*, 133–140, DOI 10.1016/j.egypro.2009.01.020.

- [275] R. Muñoz, L. Meier, I. Diaz, D. Jeison, “A review on the state-of-the-art of physical/chemical and biological technologies for biogas upgrading”, *Reviews in Environmental Science and Bio/Technology* **2015**, *14*, 727–759, DOI 10.1007/s11157-015-9379-1.
- [276] I. Gibson, D. Rosen, B. Stucker, M. Khorasani in *Additive Manufacturing Technologies*, (Eds.: I. Gibson, D. Rosen, B. Stucker), Springer International Publishing, Cham, **2021**, pp. 237–252.
- [277] R. Jiang, L. Monteil, K. Kimes, A. Mostafaei, M. Chmielus, “Influence of powder type and binder saturation on binder jet 3D–printed and sintered Inconel 625 samples”, *The International Journal of Advanced Manufacturing Technology* **2021**, *116*, 3827–3838, DOI 10.1007/s00170-021-07496-3.
- [278] A. S. Díaz-Marta, S. Yáñez, C. R. Tubío, V. L. Barrio, Y. Piñeiro, R. Pedrido, J. Rivas, M. Amorín, F. Guitián, A. Coelho, “Multicatalysis Combining 3D-Printed Devices and Magnetic Nanoparticles in One-Pot Reactions: Steps Forward in Compartmentation and Recyclability of Catalysts”, *ACS Applied Materials & Interfaces* **2019**, *11*, 25283–25294, DOI 10.1021/acsami.9b08119.
- [279] V. Middelkoop, T. Slater, M. Florea, F. Neațu, S. Danaci, V. Onyenkeadi, K. Boonen, B. Saha, I.-A. Baragau, S. Kellici, “Next frontiers in cleaner synthesis: 3D printed graphene-supported CeZrLa mixed-oxide nanocatalyst for CO<sub>2</sub> utilisation and direct propylene carbonate production”, *Journal of Cleaner Production* **2019**, *214*, 606–614, DOI 10.1016/j.jclepro.2018.12.274.
- [280] F. M. Dautzenberg in *ACS Symposium Series*, American Chemical Society, Washington, DC, **1989**, pp. 99–119, DOI 10.1021/bk-1989-0411.ch011.
- [281] J. A. Moulijn, A. Tarfaoui, F. Kapteijn, “General aspects of catalyst testing”, *Catalysis Today* **1991**, *11*, 1–12, DOI 10.1016/0920-5861(91)87002-5.
- [282] H. Heinemann, “Catalyst Performance Testing”, *Catalysis Today* **1994**, *22*, 281–293, DOI 10.1016/0920-5861(94)80105-3.
- [283] D. S. Scott, W. Lee, J. Papa, “The measurement of transport coefficients in gas-solid heterogeneous reactions”, *Chemical Engineering Science* **1974**, *29*, 2155–2167, DOI 10.1016/0009-2509(74)80023-0.
- [284] C. N. Satterfield, A. A. Pelossof, T. K. Sherwood, “Mass transfer limitations in a trickle-bed reactor”, *AIChE Journal* **1969**, *15*, 226–234, DOI 10.1002/aic.690150219.
- [285] R. K. Sharma, D. L. Cresswell, E. J. Newson, “Effective diffusion coefficients and tortuosity factors for commercial catalysts”, *Industrial & Engineering Chemistry Research* **1991**, *30*, 1428–1433, DOI 10.1021/ie00055a004.

- [286] K. Takács, H. P. Calis, A. W. Gerritsen, C. M. van den Bleek, “The selective catalytic reduction of nitric oxide in the bead string reactor”, *Chemical Engineering Science* **1996**, *51*, 1789–1798, DOI 10.1016/0009-2509(96)00037-1.
- [287] O. Šolcová, K. Soukup, P. Schneider, “Diffusion coefficients and other transport characteristics of peculiarly shaped porous materials in the single pellet-string column”, *Microporous and Mesoporous Materials* **2006**, *91*, 100–106, DOI 10.1016/j.micromeso.2005.11.024.
- [288] J. Fernengel, L. Bolton, O. Hinrichsen, “Characterisation and design of single pellet string reactors using numerical simulation”, *Chemical Engineering Journal* **2019**, *373*, 1397–1408, DOI 10.1016/j.cej.2019.03.114.
- [289] J. Fernengel, L. Bolton, O. Hinrichsen, “Numerical Investigation of Pressure Drop in Single Pellet String Reactors”, *Chemical Engineering & Technology* **2020**, *43*, 172–178, DOI 10.1002/ceat.201900372.
- [290] V. Petrazzuoli, M. Rolland, V. Sassanis, V. Ngu, Y. Schuurman, L. Gamet, “Numerical prediction of Peclet number in small-sized fixed bed reactors of spheres”, *Chemical Engineering Science* **2021**, *240*, 116667, DOI 10.1016/j.ces.2021.116667.
- [291] M. Behrens, “Coprecipitation: An excellent tool for the synthesis of supported metal catalysts – From the understanding of the well known recipes to new materials”, *Catalysis Today* **2015**, *246*, 46–54, DOI 10.1016/j.cattod.2014.07.050.
- [292] D. Beierlein, D. Häussermann, M. Pfeifer, T. Schwarz, K. Stöwe, Y. Traa, E. Klemm, “Is the CO<sub>2</sub> methanation on highly loaded Ni-Al<sub>2</sub>O<sub>3</sub> catalysts really structure-sensitive?”, *Applied Catalysis B: Environmental* **2019**, *247*, 200–219, DOI 10.1016/j.apcatb.2018.12.064.
- [293] S. Abelló, C. Berrueco, D. Montané, “High-loaded nickel–alumina catalyst for direct CO<sub>2</sub> hydrogenation into synthetic natural gas (SNG)”, *Fuel* **2013**, *113*, 598–609, DOI 10.1016/j.fuel.2013.06.012.
- [294] F. Koschany, D. Schlereth, O. Hinrichsen, “On the kinetics of the methanation of carbon dioxide on coprecipitated NiAl(O)”, *Applied Catalysis B: Environmental* **2016**, *181*, 504–516, DOI 10.1016/j.apcatb.2015.07.026.
- [295] S. Ewald, S. Standl, O. Hinrichsen, “Characterization of nickel catalysts with transient methods”, *Applied Catalysis A: General* **2018**, *549*, 93–101, DOI 10.1016/j.apcata.2017.09.023.
- [296] P. Scherrer, “Bestimmung der Größe und der inneren Struktur von Kolloidteilchen mittels Röntgenstrahlen”, *Mathematisch-Physikalische Klasse* **1918**, 98–100, DOI 10.1007/978-3-662-33915-2\_7.

- [297] S. Kannan, A. Narayanan, C. S. Swamy, “Effect of composition on the physicochemical properties of nickel aluminium hydrotalcites”, *Journal of Materials Science* **1996**, *31*, 2353–2360, DOI 10.1007/BF01152946.
- [298] M. Gabrovska, R. Edreva-Kardjieva, D. Crişan, P. Tzvetkov, M. Shopska, I. Shtereva, “Ni–Al layered double hydroxides as catalyst precursors for CO<sub>2</sub> removal by methanation”, *Reaction Kinetics, Mechanisms and Catalysis* **2012**, *105*, 79–99, DOI 10.1007/s11144-011-0378-0.
- [299] D. C. Puxley, I. J. Kitchener, C. Komodromos, N. D. Parkyn in *Preparation of catalysts III*, (Eds.: G. Poncelet, P. Grangé, P. A. Jacobs), Studies in Surface Science and Catalysis, Elsevier, Amsterdam and New York, **1983**, pp. 237–271, DOI 10.1016/S0167-2991(09)60025-2.
- [300] F. Cavani, F. Trifirò, A. Vaccari, “Hydrotalcite-type anionic clays: Preparation, properties and applications”, *Catalysis Today* **1991**, *11*, 173–301, DOI 10.1016/0920-5861(91)80068-K.
- [301] G. Li, L. Hu, J. M. Hill, “Comparison of reducibility and stability of alumina-supported Ni catalysts prepared by impregnation and co-precipitation”, *Applied Catalysis A: General* **2006**, *301*, 16–24, DOI 10.1016/j.apcata.2005.11.013.
- [302] D. Guo, Y. Wang, P. Zhao, M. Bai, H. Xin, Z. Guo, J. Li, “Selective Aerobic Oxidation of Benzyl Alcohol Driven by Visible Light on Gold Nanoparticles Supported on Hydrotalcite Modified by Nickel Ion”, *Catalysts* **2016**, *6*, 64, DOI 10.3390/catal6050064.
- [303] F. Koschany, PhD thesis, Technische Universität München, **2016**.
- [304] S. Ewald, PhD thesis, Technische Universität München, **2019**.
- [305] D. S. MacIver, H. H. Tobin, R. T. Barth, “Catalytic aluminas I. Surface chemistry of eta and gamma alumina”, *Journal of Catalysis* **1963**, *2*, 485–497, DOI 10.1016/0021-9517(63)90004-6.
- [306] H. L. Rotgerink, H. Bosch, J. G. van Ommen, J. Ross, “The effect of Ni-Al ratio on the properties of coprecipitated nickel-alumina catalysts with high nickel contents”, *Applied Catalysis* **1986**, *27*, 41–53, DOI 10.1016/S0166-9834(00)81045-3.
- [307] L. E. Alzamora, J. R. H. Ross, E. C. Kruissink, L. L. van Reijen, “Coprecipitated nickel-alumina catalysts for methanation at high temperature. Part 2. Variation of total and metallic areas as a function of sample composition and method of pretreatment”, *Journal of the Chemical Society, Faraday Transactions 1: Physical Chemistry in Condensed Phases* **1981**, *77*, 665, DOI 10.1039/f19817700665.

- [308] P. De Korte, E. Doesburg, C. P. J. de Winter, L. L. van Reijen, “Characterization of the interaction between nickel oxide and aluminium oxide in coprecipitated catalysts”, *Solid State Ionics* **1985**, *16*, 73–80, DOI 10.1016/0167-2738(85)90026-8.
- [309] M. K. Titulaer, “The Quantity of Reduced Nickel in Synthetic Takovite: Effects of Preparation Conditions and Calcination Temperature”, *Clays and Clay Minerals* **1994**, *42*, 249–258, DOI 10.1346/ccmn.1994.0420303.
- [310] S. Abelló, C. Berrueco, F. Gispert-Guirado, D. Montané, “Synthetic natural gas by direct CO<sub>2</sub> hydrogenation on activated takovites: effect of Ni/Al molar ratio”, *Catalysis Science & Technology* **2016**, *6*, 2305–2317, DOI 10.1039/c5cy01200g.
- [311] J. Zieliński, “Effect of alumina on the reduction of surface nickel oxide; morphology of the surfaces of the surfaces of Ni/Al<sub>2</sub>O<sub>3</sub> catalysts”, *Journal of Molecular Catalysis* **1993**, *83*, 197–206, DOI 10.1016/0304-5102(93)87019-5.
- [312] B. Vos, E. Poels, A. Bliet, “Impact of Calcination Conditions on the Structure of Alumina-Supported Nickel Particles”, *Journal of Catalysis* **2001**, *198*, 77–88, DOI 10.1006/jcat.2000.3082.
- [313] R. Darouhegi, F. Meshkani, M. Rezaei, “Enhanced activity of CO<sub>2</sub> methanation over mesoporous nanocrystalline Ni–Al<sub>2</sub>O<sub>3</sub> catalysts prepared by ultrasound-assisted co-precipitation method”, *International Journal of Hydrogen Energy* **2017**, *42*, 15115–15125, DOI 10.1016/j.ijhydene.2017.04.244.
- [314] C. Li, Y.-W. Chen, “Temperature-programmed-reduction studies of nickel oxide/alumina catalysts: effects of the preparation method”, *Thermochimica Acta* **1995**, *256*, 457–465, DOI 10.1016/0040-6031(94)02177-P.
- [315] D. Mustard, C. H. Bartholomew, “Determination of metal crystallite size and morphology in supported nickel catalysts”, *Journal of Catalysis* **1981**, *67*, 186–206, DOI 10.1016/0021-9517(81)90271-2.
- [316] G. Poncelet, M. A. Centeno, R. Molina, “Characterization of reduced  $\alpha$ -alumina-supported nickel catalysts by spectroscopic and chemisorption measurements”, *Applied Catalysis A: General* **2005**, *288*, 232–242, DOI 10.1016/j.apcata.2005.04.052.
- [317] G. Bergeret, P. Gallezot in *Handbook of Heterogeneous Catalysis*, (Eds.: G. Ertl, H. Knözinger, F. Schüth, J. Weitkamp), Wiley-VCH, Weinheim, DE, **2008**, DOI 10.1002/9783527610044.hetc0038.
- [318] P. A. Webb, C. Orr, *Analytical Methods in Fine Particle Technology*, 1. ed., 2. print, Micromeritics Instrument Corp, Norcross, Ga., **1997**.

- [319] L. He, Q. Lin, Y. Liu, Y. Huang, “Unique catalysis of Ni-Al hydrotalcite derived catalyst in CO<sub>2</sub> methanation: cooperative effect between Ni nanoparticles and a basic support”, *Journal of Energy Chemistry* **2014**, *23*, 587–592, DOI 10.1016/S2095-4956(14)60144-3.
- [320] S. Abate, K. Barbera, E. Giglio, F. Deorsola, S. Bensaid, S. Perathoner, R. Pirone, G. Centi, “Synthesis, Characterization, and Activity Pattern of Ni-Al Hydrotalcite Catalysts in CO<sub>2</sub> Methanation”, *Industrial & Engineering Chemistry Research* **2016**, *55*, 8299–8308, DOI 10.1021/acs.iecr.6b01581.
- [321] D. Wierzbicki, R. Baran, R. Debek, M. Motak, T. Grzybek, M. E. Gálvez, P. Da Costa, “The influence of nickel content on the performance of hydrotalcite-derived catalysts in CO<sub>2</sub> methanation reaction”, *International Journal of Hydrogen Energy* **2017**, *42*, 23548–23555, DOI 10.1016/j.ijhydene.2017.02.148.
- [322] C. K. Vance, C. H. Bartholomew, “Hydrogenation of carbon dioxide on group VIII metals”, *Applied Catalysis* **1983**, *7*, 169–177, DOI 10.1016/0166-9834(83)80005-0.
- [323] R. Maatman, “A kinetic study of the methanation of CO<sub>2</sub> over nickel-alumina”, *Journal of Catalysis* **1980**, *62*, 349–356, DOI 10.1016/0021-9517(80)90463-7.
- [324] T. Burger, P. Donaubaue, O. Hinrichsen, “On the kinetics of the co-methanation of CO and CO<sub>2</sub> on a co-precipitated Ni-Al catalyst”, *Applied Catalysis B: Environmental* **2021**, *282*, 119408, DOI 10.1016/j.apcatb.2020.119408.
- [325] M. Komiyama, “Design and Preparation of Impregnated Catalysts”, *Catalysis Reviews* **1985**, *27*, 341–372, DOI 10.1080/01614948508064738.
- [326] A. Afshar Taromi, S. Kaliaguine, “Hydrodeoxygenation of triglycerides over reduced mesostructured Ni/gamma-alumina catalysts prepared via one-pot sol-gel route for green diesel production”, *Applied Catalysis A: General* **2018**, *558*, 140–149, DOI 10.1016/j.apcata.2018.03.030.
- [327] Y.-J. Huang, J. A. Schwarz, J. R. Diehl, J. P. Baltrus, “Effect of Catalyst Preparation on Catalytic Activity”, *Applied Catalysis* **1988**, *36*, 163–175, DOI 10.1016/S0166-9834(00)80112-8.
- [328] M. Romero-Sáez, A. B. Dongil, N. Benito, R. Espinoza-González, N. Escalona, F. Gracia, “CO<sub>2</sub> methanation over nickel-ZrO<sub>2</sub> catalyst supported on carbon nanotubes: A comparison between two impregnation strategies”, *Applied Catalysis B: Environmental* **2018**, *237*, 817–825, DOI 10.1016/j.apcatb.2018.06.045.
- [329] M. Yusuf, A. Salaam Farooqi, M. Azad Alam, L. Kok Keong, K. Hellgardt, B. Abdullah, “Performance of Ni/Al<sub>2</sub>O<sub>3</sub>-MgO catalyst for Dry Reforming of Methane: Effect of preparation routes”, *IOP Conference Series: Materials Science and Engineering* **2021**, *1092*, 012069, DOI 10.1088/1757-899X/1092/1/012069.

- [330] J. Regalbuto, *Catalyst Preparation: Science and Engineering*, Taylor & Francis, Hoboken, NJ, **2007**.
- [331] V. G. Baldovino-Medrano, M. T. Le, I. van Driessche, E. Bruneel, C. Alcázar, M. T. Colomer, R. Moreno, A. Florencie, B. Farin, E. M. Gaigneaux, “Role of shaping in the preparation of heterogeneous catalysts: Tableting and slip-casting of oxidation catalysts”, *Catalysis Today* **2015**, *246*, 81–91, DOI 10.1016/j.cattod.2014.08.030.
- [332] J. M. Asua, B. Delmon, “Theoretical study of the influence of nonuniform active-phase distribution on activity and selectivity of hydrodesulfurization catalysts”, *Industrial & Engineering Chemistry Research* **1987**, *26*, 32–39, DOI 10.1021/ie00061a007.
- [333] E. Assaf, L. Jesus, J. Assaf, “The active phase distribution in Ni/Al<sub>2</sub>O<sub>3</sub> catalysts and mathematical modeling of the impregnation process”, *Chemical Engineering Journal* **2003**, *94*, 93–98, DOI 10.1016/S1385-8947(03)00006-8.
- [334] G. D. Wehinger, “Improving the radial heat transport and heat distribution in catalytic gas-solid reactors”, *Chemical Engineering and Processing - Process Intensification* **2022**, *177*, 108996, DOI 10.1016/j.cep.2022.108996.
- [335] F. Álvarez, A. Cifuentes, I. Serrano, L. Franco, G. Fargas, F. Fenollosa, R. Uceda, L. Llanes, C. Tardivat, J. Llorca, J. J. Roa, “Optimization of the sintering thermal treatment and the ceramic ink used in direct ink writing of  $\alpha$ -Al<sub>2</sub>O<sub>3</sub>: Characterization and catalytic application”, *Journal of the European Ceramic Society* **2022**, *42*, 2921–2930, DOI 10.1016/j.jeurceramsoc.2022.01.032.
- [336] F. Car, G. Brnadić, V. Tomašić, D. Vrsaljko, “Advanced preparation method of monolithic catalyst carriers using 3D-printing technology”, *Progress in Additive Manufacturing* **2022**, *7*, 797–808, DOI 10.1007/s40964-022-00266-x.
- [337] S. Hock, C. Rein, M. Rose, “3D-Printed Acidic Monolithic Catalysts for Liquid-Phase Catalysis with Enhanced Mass Transfer Properties”, *ChemCatChem* **2022**, *14*, DOI 10.1002/cctc.202101947.
- [338] I. Lucentini, G. García Colli, C. Luzi, I. Serrano, L. Soler, N. J. Divins, O. M. Martínez, J. Llorca, “Modelling and simulation of catalytic ammonia decomposition over Ni-Ru deposited on 3D-printed CeO<sub>2</sub>”, *Chemical Engineering Journal* **2022**, *427*, 131756, DOI 10.1016/j.cej.2021.131756.
- [339] Z. Yuan, L. Liu, W. Ru, D. Zhou, Y. Kuang, J. Feng, B. Liu, X. Sun, “3D printed hierarchical spinel monolithic catalysts for highly efficient semi-hydrogenation of acetylene”, *Nano Research* **2022**, *15*, 6010–6018, DOI 10.1007/s12274-022-4291-9.

- [340] T. Li, J. Gonzalez-Gutierrez, I. Raguž, C. Holzer, M. Li, P. Cheng, M. Kitzmantel, L. Shi, L. Huang, “Material extrusion additively manufactured alumina monolithic structures to improve the efficiency of plasma-catalytic oxidation of toluene”, *Additive Manufacturing* **2021**, *37*, 101700, DOI 10.1016/j.addma.2020.101700.
- [341] K. Essa, H. Hassanin, M. M. Attallah, N. J. Adkins, A. J. Musker, G. T. Roberts, N. Tenev, M. Smith, “Development and testing of an additively manufactured monolithic catalyst bed for HTP thruster applications”, *Applied Catalysis A: General* **2017**, *542*, 125–135, DOI 10.1016/j.apcata.2017.05.019.
- [342] J. Liu, Y. Gao, Y. Fan, W. Zhou, “Fabrication of porous metal by selective laser melting as catalyst support for hydrogen production microreactor”, *International Journal of Hydrogen Energy* **2020**, *45*, 10–22, DOI 10.1016/j.ijhydene.2019.10.173.
- [343] B. Ravel, M. Newville, “ATHENA, ARTEMIS, HEPHAESTUS: data analysis for X-ray absorption spectroscopy using IFEFFIT”, *Journal of Synchrotron Radiation* **2005**, *12*, 537–541, DOI 10.1107/S0909049505012719.
- [344] K. Mocala, A. Navrotsky, “Structural and Thermodynamic Variation in Nickel Aluminate Spinel”, *Journal of the American Ceramic Society* **1989**, *72*, 826–832, DOI 10.1111/j.1151-2916.1989.tb06225.x.
- [345] R. Lindner, Å. Åkerström, “Selbstdiffusion und Reaktion in Oxyd- und Spinellsystemen”, *Zeitschrift für Physikalische Chemie* **1956**, *6*, 162–177, DOI 10.1524/zpch.1956.6.3\_4.162.
- [346] F. S. Pettit, E. H. Randklev, E. J. Felten, “Formation of NiAl<sub>2</sub>O<sub>4</sub> by Solid State Reaction”, *Journal of the American Ceramic Society* **1966**, *49*, 199–203, DOI 10.1111/j.1151-2916.1966.tb13233.x.
- [347] T. Burger, H. M. S. Augenstein, F. Hnyk, M. Döblinger, K. Köhler, O. Hinrichsen, “Targeted Fe-Doping of Ni-Al Catalysts via the Surface Redox Reaction Technique for Unravelling its Promoter Effect in the CO<sub>2</sub> Methanation Reaction”, *ChemCatChem* **2020**, *12*, 649–662, DOI 10.1002/cctc.201901331.
- [348] J. H. Kwak, L. Kovarik, J. Szanyi, “CO<sub>2</sub> Reduction on Supported Ru/Al<sub>2</sub>O<sub>3</sub> Catalysts: Cluster Size Dependence of Product Selectivity”, *ACS Catalysis* **2013**, *3*, 2449–2455, DOI 10.1021/cs400381f.
- [349] H. C. Wu, Y. C. Chang, J. H. Wu, J. H. Lin, I. K. Lin, C. S. Chen, “Methanation of CO<sub>2</sub> and reverse water gas shift reactions on Ni/SiO<sub>2</sub> catalysts: the influence of particle size on selectivity and reaction pathway”, *Catalysis Science & Technology* **2015**, *5*, 4154–4163, DOI 10.1039/C5CY00667H.

- [350] J. K. Kesavan, I. Luisetto, S. Tuti, C. Meneghini, G. Iucci, C. Battocchio, S. Mobilio, S. Casciardi, R. Sisto, “Nickel supported on YSZ: The effect of Ni particle size on the catalytic activity for CO<sub>2</sub> methanation”, *Journal of CO<sub>2</sub> Utilization* **2018**, *23*, 200–211, DOI 10.1016/j.jcou.2017.11.015.
- [351] S. Loiha, W. Klysubun, P. Khemthong, S. Prayoonpokarach, J. Wittayakun, “Reducibility of Ni and NiPt supported on zeolite beta investigated by XANES”, *Journal of the Taiwan Institute of Chemical Engineers* **2011**, *42*, 527–532, DOI 10.1016/j.jtice.2010.09.013.
- [352] P. Lu, T. Teranishi, K. Asakura, M. Miyake, N. Toshima, “Polymer-Protected Ni/Pd Bimetallic Nano-Clusters: Preparation, Characterization and Catalysis for Hydrogenation of Nitrobenzene”, *The Journal of Physical Chemistry B* **1999**, *103*, 9673–9682, DOI 10.1021/jp992177p.
- [353] J. Rynkowski, D. Rajski, I. Szyszka, J. R. Grzechowiak, “Effect of platinum on the hydrogenation activity of nickel catalysts”, *Catalysis Today* **2004**, *90*, 159–166, DOI 10.1016/j.cattod.2004.04.022.
- [354] J. Zieliński, “Morphology of nickel/alumina catalysts”, *Journal of Catalysis* **1982**, *76*, 157–163, DOI 10.1016/0021-9517(82)90245-7.
- [355] B. Mile, D. Stirling, M. A. Zammitt, A. Lovell, M. Webb, “The location of nickel oxide and nickel in silica-supported catalysts: Two forms of ‘NiO’ and the assignment of temperature-programmed reduction profiles”, *Journal of Catalysis* **1988**, *114*, 217–229, DOI 10.1016/0021-9517(88)90026-7.
- [356] J. H. Cho, S. H. An, T.-S. Chang, C.-H. Shin, “Effect of an Alumina Phase on the Reductive Amination of 2-Propanol to Monoisopropylamine Over Ni/Al<sub>2</sub>O<sub>3</sub>”, *Catalysis Letters* **2016**, *146*, 811–819, DOI 10.1007/s10562-016-1695-8.
- [357] A. Morales-Marín, J. L. Ayastuy, U. Iriarte-Velasco, M. A. Gutiérrez-Ortiz, “Nickel aluminate spinel-derived catalysts for the aqueous phase reforming of glycerol: Effect of reduction temperature”, *Applied Catalysis B: Environmental* **2019**, *244*, 931–945, DOI 10.1016/j.apcatb.2018.12.020.
- [358] J. L. Rogers, M. C. Mangarella, A. D. D’Amico, J. R. Gallagher, M. R. Dutzer, E. Stavitski, J. T. Miller, C. Sievers, “Differences in the Nature of Active Sites for Methane Dry Reforming and Methane Steam Reforming over Nickel Aluminate Catalysts”, *ACS Catalysis* **2016**, *6*, 5873–5886, DOI 10.1021/acscatal.6b01133.
- [359] L. Zhou, L. Li, N. Wei, J. Li, J.-M. Basset, “Effect of NiAl<sub>2</sub>O<sub>4</sub> Formation on Ni/Al<sub>2</sub>O<sub>3</sub> Stability during Dry Reforming of Methane”, *ChemCatChem* **2015**, *7*, 2508–2516, DOI 10.1002/cctc.201500379.

- [360] Y. Cesteros, P. Salagre, F. Medina, J. E. Sueiras, "Preparation and Characterization of Several High-Area NiAl<sub>2</sub>O<sub>4</sub> Spinels. Study of Their Reducibility", *Chemistry of Materials* **2000**, *12*, 331–335, DOI 10.1021/cm990154h.

# Nomenclature

## Latin Symbols

$A$	Area	$\text{m}^2$
$c$	Concentration	$\text{mol}/\text{m}^3$
$d$	d-spacing	$\text{m}$
$d$	Diameter	$\text{m}$
$d$	Crystallite size	$\text{m}$
$C$	Curvature of meniscus	$\text{m}^{-1}$
$C$	BET Constant	-
$D$	Dispersion	-
$D$	Diffusion coefficient	$\text{m}^2/\text{s}$
$d_{\text{pen}}$	Penetration depth	$\text{m}$
$d_{\text{red}}$	Degree of reduction	-
$F$	Force	$\text{N}$
$h$	Height	$\text{m}$
$h, k, l$	Miller indices	-
$I$	Intensity	a.u.
$k$	Reaction rate constant (1st order)	$\text{s}^{-1}$
$K$	Shape factor	-
$l$	Length	$\text{m}$
$m$	Mass	$\text{kg}$
$M$	Molar mass	$\text{kg}/\text{mol}$
$n$	Molar amount	$\text{mol}$
$N_{\text{A}}$	Avogadro constant	$6.022 \cdot 10^{23}$
$Oh$	Ohnesorge number	-
$p$	Pressure	$\text{Pa}$
$P$	Platinum productivity	$\text{g}_{\text{H}_2} \text{g}_{\text{Pt}}^{-1} \text{min}^{-1}$
$p_i$	Partial pressure of species $i$	$\text{Pa}$
$Re$	Reynolds number	-
$S$	Stoichiometry	-
$S$	Mass-specific surface area	$\text{m}^2/\text{kg}$

$T$	Temperature	K / °C
$t$	Time	s
$t_{\text{imp}}$	Duration of impregnation	s
$u$	Velocity	m/s
$U$	Adsorption uptake	mol/g <sub>cat</sub>
$\dot{V}$	Volume	m <sup>3</sup>
$\dot{V}$	Volumetric flow rate	m <sup>3</sup> /s
$w$	Loading	wt. %
$We$	Weber number	-
$Z$	Characteristic number for stable drop formation, $1/Oh$	-

### Greek Symbols

$\gamma$	Surface tension	N/m
$\varepsilon$	Porosity	-
$\eta$	Dynamic viscosity	Pa s
$\eta$	Effectiveness factor	-
$\theta$	Diffraction angle	°
$\lambda$	Wavelength	nm
$\rho$	Density	g/m <sup>3</sup>
$\sigma$	Surface tension	N/m
$\sigma_{\text{comp}}$	Compressive/ side crushing strength	Pa
$\sigma$	Molecular cross-sectional	m <sup>2</sup>
$\phi$	Thiele modulus	-
$\phi$	Work function	eV

### Subscript

app	apparent
b	bulk
c	determined by chemisorption
C	crystal
calc	calcination
cat	catalyst
debind	debindered
eff	effective

i1c, i2c, i3c	one, two, three times infiltrated
imp	impregnation
kin	kinetic
m	molar
M	metal
ML	monolayer
p	pore, particle
red	reduction
s	solid

### Abbreviations

3D	Three-dimensional
$\mu$ CT	X-ray microtomography
AAS	Atom Absorption Spectroscopy
AM	Additive Manufacturing
BET	Brunauer-Emmett-Teller
BJ	Binder jetting
BJH	Barrett-Joyner-Halenda
bNiO	Bulk nickel oxide species
CAD	Computer-aided design
DFT	Discrete fourier transform
DIW	Direct ink writing
DLP	Digital Light Processing
DOD	Drop-on-demand
DoD	Degree of dehydrogenation
EXAFS	Extended X-ray absorption fine structure
FBR	Fixed-bed reactor
FCC	Fluid catalytic cracking
FFF	Fused Filament Fabrication
FWHM	Full width at half maximum
GHSV	Gas hourly space velocity
GP	Green part
H0-DBT	Dibenzyltoluene
H18-DBT	Perhydro-dibenzyltoluene
HDS	Hydrodesulfurization
ICP-OES	Inductively coupled plasma atomic emission spectroscopy
LOHC	Liquid organic hydrogen carrier
MIP	Mercury intrusion porosimetry

NI	Prepared by 3D printing via nickel ink deposition
PIPS	Passivated Implanted Planar Silicon
poreSD	Pore size distribution
PSD	Particle size distribution
PtG	Power-to-Gas
PtX	Power-to-X
PVP	Polyvinylpyrrolidone
PZC	Point of zero charge
SLA	Stereolithography
sNiO	surface nickel oxide species
SPSR	Single pellet string reactor
STL	Standard tessellation language
TCD	Thermal conductivity detector
TEM	Transmission electron microscopy
TGA	Thermogravimetric analysis
TPR	Temperature programmed reduction
UHV	Ultra-high vacuum
WI	Prepared by wet impregnation
XANES	X-ray absorption near edge structure
XAS	X-ray absorption spectroscopy
XPS	X-ray photoelectron spectroscopy
XRD	X-ray diffraction

# List of Figures

2.1	General concept of additive manufacturing, adapted from [18]. . . . .	5
2.2	Classification of additive manufacturing technologies. . . . .	6
2.3	Main components of a binder jetting printer. . . . .	7
2.4	Binder penetration steps into the powder bed. . . . .	8
2.5	Regimes of droplet ejectability for a drop on demand printhead, adapted from [26]. . . . .	9
2.6	Temporal evolution and milestones of heterogeneous catalysis. . . . .	10
2.7	Development of number of scientific publications and citations for the combined topics of additive manufacturing and catalysis over time (Source: Web of Science [39]). . . . .	11
2.8	Different active phase distributions across a spherical catalyst pellet. . . . .	17
2.9	Catalyst selection in dependence of the Thiele moduli of the main reaction $\phi_{\text{main}}$ and of the poisoning reaction $\phi_{\text{poison}}$ where the criterion is the longest catalyst life (effectiveness factor $\eta \geq 0.4$ ). Based on Becker and Wei [90]. . . . .	18
2.10	Schematic overview of the power-to-gas concept. . . . .	19
2.11	Schematic LOHC infrastructure using the pair perhydro-dibenzyltoluene / dibenzyltoluene. . . . .	22
3.1	General scheme of the binder jetting setup with its main components. 1: Excess powder collector, 2: Build platform, 3: Powder supply chamber, 4: Printhead, 5: Spreading roller, 6: Ink supply. . . . .	27
3.2	Diagram of the ejection of a photoelectron from a carbon atom. Reprinted with permission from John Wiley and Sons [152]. . . . .	29
3.3	Exemplary XAS spectrum depicting the XANES and EXAFS regions as well as the pre- and post-absorption edge regions [155]. . . . .	30
3.4	Gas adsorption data evaluation according to the IUPAC classification. Reprinted with permission from John Wiley & Sons [158]. . . . .	33
4.1	Flowchart of the process chain for generating a catalyst support via binder jetting. . . . .	46

---

4.2	Debindered alumina cylinders placed on a stainless steel grid before post-processing. . . . .	46
4.3	Temperature program for debinding as well as calcination. . . . .	47
4.4	PSD of the printing powder (PP) and its single components, measured with laser diffraction. The vertical line marks the layer thickness of 40 $\mu\text{m}$ . . . . .	53
4.5	PSD of fresh PP powder blend (blue, solid) and recycled powder after 3 print cycles (blue, dotted). . . . .	54
4.6	PSD of the dispersed boehmite particles Dispal 14N4-80 in the water-based ink, measured by laser diffraction. . . . .	55
4.7	TGA curves for pure PVP powder (blue) and a green body (dotted) under synthetic air. . . . .	57
4.8	XRD patterns of a debinded part, heated until 600 $^{\circ}\text{C}$ , held for 1 h (blue) and 2 h (orange). The vertical dashed lines correspond to the reference pattern of pure PVP. . . . .	57
4.9	Comparison of the XRD pattern of a debinded part, heated until 600 $^{\circ}\text{C}$ and held for 1 h with a reference pattern for $\text{Al}_2\text{O}_3$ (ICDD 04-0875). . . . .	58
4.10	Side crushing strengths of printed parts at different process stages. . . . .	63
4.11	Coordinate system used for $\mu\text{CT}$ analysis with colors for easier visualization. $y$ is the printing direction. Gray cross-sections in Fig. 4.12 are perpendicular to the cylinder axis. Blue and red cross-sections in Fig. 4.14 go through loose and dense planes, respectively, parallel to the cylinder axis. Green cross-sections run through the cylindrical center of rotation and perpendicular to the red and blue slices. . . . .	64
4.12	Cross-sectional views of $\mu\text{CT}$ scans of printed cylinders perpendicular to the $z$ -axis of the green body, i1c and i2c samples (top row). The bottom row shows the respective averaged pixels over 1000 slices. The orientation corresponds to the gray cross-section in Fig. 4.11. The horizontal direction is along the $x$ , the vertical direction is along the $y$ axis depicted in Fig. 4.11. . . . .	65
4.13	Gray value profiles along $x$ -direction through the averaged cross-sectional views of Fig. 4.12, bottom row. The number of density maxima within a distance of 7 mm are 49, 54 and 52 for GP, i1c and i2c, respectively. . . . .	66
4.14	Cross-sectional views with identical grayscaleing of the green body, i1c and i2c. Green frame (top row) = $xz$ -plane, red (middle row) = slice of dense $yz$ -plane, blue (bottom row) = slice of loose $yz$ -plane. The colors correspond to the cross-sections depicted in Fig. 4.11. The vertical direction of all 9 images is along the $z$ -direction. . . . .	67

4.15	Bulk density $\rho_{\text{bulk}}$ and specific surface area $S_{\text{BET}}$ at various stages of catalyst support fabrication via binder jetting. $\rho_{\text{bulk}}$ could not be determined for the debinding stage but is assumed to decrease due to burnout of the in-bed binder. . . . .	68
4.16	Pore size distribution of one to three times infiltrated samples compared to the debinded (calcined) part. . . . .	70
4.17	Pore size distribution of a one time calcined green part (according to normal preparation procedure) and a three times calcined specimen. . . .	70
4.18	$\text{N}_2$ physisorption isotherms of the sample i2c. . . . .	71
5.1	Schematic representation of the H18-DBT dehydrogenation. . . . .	78
5.2	Overview of the experimental outline. . . . .	79
5.3	Front (left) and isometric view (right) of the monolith CAD file. . . . .	79
5.4	General schemes of the printing techniques used in this study. . . . .	80
5.5	Photos of monolithic alumina supports (first row) and reduced $\text{Pt}/\text{Al}_2\text{O}_3$ catalysts (second row) fabricated by DIW (first column) and BJ (second column). . . . .	85
5.6	Size change of BJ and DIW printed alumina test cylinders in dependence of calcination temperature. . . . .	86
5.7	Comparison of DIW and BJ compression strengths of printed alumina supports calcined with varying calcination temperatures. . . . .	87
5.8	Pore size distribution of the 3D printed alumina supports from (a) DIW and (b) BJ calcined at varying calcination temperatures, determined by $\text{N}_2$ physisorption. . . . .	89
5.9	Pore size distribution of 3D printed alumina supports calcined at $1100\text{ }^\circ\text{C}$ , determined by MIP. . . . .	91
5.10	Pt loading and penetration depth in dependence of the wet impregnation duration $t_{\text{imp}}$ . Supports were calcined at $1100\text{ }^\circ\text{C}$ and impregnated with a target Pt loading of 0.30 wt.%. . . . .	92
5.11	Light microscopic images of printed $\text{Pt}/\text{Al}_2\text{O}_3$ catalysts used for Pt penetration depth analysis in dependence of the wet impregnation times $t_{\text{imp}}$ for BJ and DIW printed supports calcined at $1100\text{ }^\circ\text{C}$ . Target Pt loading $w_{\text{Pt,target}} = 0.3\text{ wt.}\%$ . . . . .	95
5.12	TEM images of the ground $\text{Pt}/\text{Al}_2\text{O}_3$ monoliths used for catalytic testing, calcined at $1100\text{ }^\circ\text{C}$ and wet impregnated for 3 h, including respective metal particle size distribution. . . . .	97
5.13	H18-DBT dehydrogenation over BJ and DIW printed $\text{Pt}/\text{Al}_2\text{O}_3$ catalysts in a semi-batch reactor setup, tested with monolithic and powder catalysts, respectively. For each reaction, two monoliths were used. . . . .	98

---

5.14	XRD diffraction pattern of alumina supports, printed by BJ (blue) and DIW (black). (Reference patterns: $\alpha$ -Al <sub>2</sub> O <sub>3</sub> : ICSD 01-075-1862, $\theta$ -Al <sub>2</sub> O <sub>3</sub> : PDF 00-023-1009). . . . .	101
5.15	Particle size distribution of powder used for LOHC dehydrogenation, prepared by grinding of whole monoliths. . . . .	102
5.16	Pt particle size distribution by TEM of BJ printed Pt/Al <sub>2</sub> O <sub>3</sub> catalysts which were wet impregnated for varying durations. . . . .	103
5.17	Pt particle size distribution by TEM of DIW printed Pt/Al <sub>2</sub> O <sub>3</sub> catalysts which were wet impregnated for varying durations. . . . .	104
6.1	Catalyst manufacturing scheme for Ni-Al catalysts via Binder Jetting. . .	111
6.2	Scheme of the SPSR setup, packed with 12 printed spherical Ni-Al catalyst pellets. . . . .	114
6.3	PSD of the co-precipitated Ni-Al precursor powder (red, dashed), alumina and binder powder (blue, dashdotted), and final printing powder material (black, solid line). . . . .	115
6.4	XRD pattern of the as-synthesized Ni-Al precursors with varying Ni/Al molar ratio. (Reference pattern: Takovite, JCPDS 015-0087.) Reflexes are shifted to smaller angles with increasing Ni loading due to lattice expansion. . . . .	118
6.5	XRD pattern of the 3D printed and calcined Ni-Al catalysts with varying Ni/Al molar ratio. (Reference patterns: $\eta$ -Al <sub>2</sub> O <sub>3</sub> : JCPDS 04-0875, NiO: 01-078-0429, NiAl <sub>2</sub> O <sub>4</sub> : 10-0339) . . . . .	119
6.6	XRD pattern of the 3D printed and reduced Ni-Al catalysts with varying Ni/Al molar ratio. (Reference patterns: $\eta$ -Al <sub>2</sub> O <sub>3</sub> : JCPDS 04-0875, NiO: 01-078-0429, NiAl <sub>2</sub> O <sub>4</sub> : 10-0339, Ni: 01-087-0712.) . . . . .	120
6.7	XRD pattern of the 3D printed and reduced Ni-Al catalysts with varying amounts of admixed Ni-Al precursor. (Reference patterns: $\eta$ -Al <sub>2</sub> O <sub>3</sub> : JCPDS 04-0875, NiO: 01-078-0429, NiAl <sub>2</sub> O <sub>4</sub> : 10-0339, Ni: 01-087-0712.)	121
6.8	Calculated degrees of reduction $d_{red}$ from TG analysis for 3D printed Ni-Al catalysts. . . . .	122
6.9	TEM images of 3D printed and reduced Ni-Al catalysts. . . . .	124
6.10	Compressive strength $\sigma_{comp}$ of green and calcined printed Ni-Al catalysts.	128
6.11	Pore size distribution of 3D printed Ni-Al catalysts, determined by N <sub>2</sub> physisorption using the BJH method on the desorption branch. . . . .	130
6.12	Pore size distribution of calcined Ni-Al catalysts, determined by MIP. . .	131
6.13	Comparison of pore size distributions obtained by gas adsorption (black) and mercury porosimetry (blue) for the calcined sample NiAl11-20. . . .	131

6.14	Results of the catalytic tests of the Binder Jet 3D printed Ni-Al catalyst NiAl11-20, NiAl21-20 and NiAl51-20. Reaction conditions: $\text{CO}_2/\text{H}_2/\text{Ar}/\text{N}_2 = 2/8/9/1$ , total pressure $p_{\text{tot}} = 9$ bar. . . . .	133
6.15	Exemplary XRD patterns of NiAl11-20_c, NiAl31-20_c and NiAl51-20_c. The spherical 3D printed catalysts were used where the outer shell layer material (manually removed with a scalpel) was measured. The inner core material was measured separately. . . . .	136
6.16	Particle size distributions of all Ni-Al catalysts determined by TEM analysis. Measurement of at least 100 particles per sample. . . . .	137
6.17	Comparison of pore size distributions obtained by gas adsorption and MIP for all 3D printed Ni-Al catalysts. . . . .	138
7.1	Schematic of the binder jetting printer used in this study. . . . .	142
7.2	Test cylinders at different processing stages printed by Ni ink deposition. . . . .	142
7.3	Compressive strength $\sigma_{\text{comp}}$ of debindered (blue) and calcined (gray) test cylinders for varying pH values of the Ni ink (see Table 7.2). . . . .	147
7.4	XPS Ni 2p spectra of NI_d (debindered), NI_i (infiltrated), and WI samples, calcined at 450 °C (c450) and 600 °C (c600, solid line) and reduced at 400 °C (r400, dotted line). . . . .	148
7.5	Ni 2p intensities of calcined and reduced samples. . . . .	149
7.6	Quadrupol mass spectrometry signal intensities of the $\text{CO}_2$ hydrogenation reaction products methane and carbon monoxide. Feed gas composition: $\text{CO}_2/\text{H}_2/\text{Ar} = 2/8/1$ . . . . .	151
7.7	Ni K-edge XANES spectrum of (a) NI_i_c600 (infiltrated, calcined at 600 °C) and references $\text{NiAl}_2\text{O}_4$ and NiO and (b) NI_i_c600_r480 (reduced at 480 °C) and corresponding references NI_i_c600 and Ni foil. . . . .	153
7.8	Comparison of $k^2$ -weighted Fourier-transformed EXAFS of different NI prepared samples at the Ni K-edge. Bottom: Debindered samples reduced at 480 °C and 600 °C. Middle: Infiltrated samples, calcined and reduced. Top: References. . . . .	154
7.9	TPR profiles with normalized $\text{H}_2$ consumption of (a) catalysts printed by nickel ink deposition (NI) after infiltration/debinder (i/d) and calcination at different temperatures (c450/c600), and (b) wet impregnation (WI), calcined at different temperatures (c450/c600). . . . .	155
7.10	Ni K-edge XANES of calcined samples, including reference samples $\text{NiAl}_2\text{O}_4$ and NiO. . . . .	159
7.11	Ni K-edge XANES of reduced samples, including Ni foil and the respective calcined sample as reference. . . . .	160
7.12	$\text{H}_2$ consumption of $\text{NiAl}_2\text{O}_4$ and co-precipitated Ni-Al catalyst (calcined at 450 °C). . . . .	161

7.13 Quadrupole mass spectrometry signal intensities of the CO<sub>2</sub> hydrogenation reaction products methane and carbon monoxide. Feed gas composition: CO<sub>2</sub>/H<sub>2</sub>/Ar = 2/8/1. . . . . 163

# List of Tables

2.1	Literature research of the state of the art on additive manufacturing of heterogeneous catalysts. . . . .	14
2.2	The three most commonly used industrial catalyst shaping methods [83–85].	16
4.1	Physical parameters for used printing liquid. . . . .	48
4.2	Composition of used powder blend. . . . .	49
4.3	Overview of methods used for material characterization and analysis. . .	49
4.4	PSD ( $d_{50}$ and $d_{90}$ ) of the starting materials and the fresh powder blend PP.	55
4.5	Deviation of cylinder height and radius from the target value of 8 mm. For the infiltrated parts (i1c, i2c and i3c) the deviation as compared to the de-binded part is shown additionally. Sample number for each measurement $n \geq 7$ . . . . .	59
4.6	Measured bulk density $\rho_{\text{bulk}}$ , apparent solid density $\rho_{\text{app,s}}$ and open void fraction $\epsilon_{\text{open}}$ for the powder bed and post-processed specimens. . . . .	61
4.7	Mass increase of all stages between part debinding and third infiltration step. $\Delta m_{\text{debind-i3c}}$ denotes the total mass increase achieved by slurry infiltration. . . . .	62
4.8	Calculated values for periods per inch according to the DFT and gray value methods and resulting shrinkage, compared to measured radial shrinkage. . . . .	66
5.1	Specific surface area $S_{\text{BET}}$ of 3D printed alumina supports calcined at varying calcination temperatures. . . . .	88
5.2	Overview of characterization data for monoliths calcined at 1100 °C: Pt loading $w_{\text{Pt}}$ , average particle size $d_{\text{Pt}}$ , resulting Pt dispersion $D_{\text{Pt}}$ and Pt penetration depth $d_{\text{pen}}$ of BJ and DIW printed samples depending on the impregnation time $t_{\text{imp}}$ . . . . .	94
5.3	Characterization data for Pt catalysts fabricated with DIW and BJ which were used for the catalytic tests. Impregnation time $t_{\text{imp}} = 3$ h. . . . .	96
5.4	Platinum productivities of powder ( $P_{\text{powder}}$ ) and monolithic catalysts ( $P_{\text{monolith}}$ ), determined for the dehydrogenation reaction between DoD = 10 to 60%. . . . .	99

---

6.1	Prepared catalysts and their printing powder composition. $w_{\text{Alumina}}$ is the total amount of bayerite and boehmite powder in the mixture. . . . .	110
6.2	Elemental compositions ( $w_{\text{Al}}$ , $w_{\text{Ni}}$ ) and Ni/Al ratios $n_{\text{Ni}}/n_{\text{Al}}$ of prepared Ni-Al precipitates as well as Ni loading $w_{\text{Ni}}$ of the 3D printed catalysts in their debinded and calcined states, all values determined by AAS. . . . .	116
6.3	Nickel particle size $d_{\text{Ni}}$ determined by TEM, XRD line broadening analysis and $\text{H}_2$ chemisorption. . . . .	124
6.4	Active metal surface area $S_{\text{Ni}}$ , metal dispersion $D_{\text{Ni}}$ of reduced samples and specific surface area $S_{\text{BET}}$ of printed Ni-Al catalysts at varying process stages. . . . .	126
7.1	Sample nomenclature of catalysts prepared by Ni ink deosition (NI) and wet impregnation (WI) with respective nickel loading $w_{\text{Ni}}$ , calcination $T_{\text{calc}}$ and reduction Temperature $T_{\text{red}}$ . . . . .	143
7.2	Molar nickel nitrate concentration $c_{\text{Ni}(\text{NO}_3)_2}$ of used ink, its pH, resulting Ni loading of the catalyst $w_{\text{Ni}}$ and sample densities $\rho$ after final post-processing. . . . .	146
7.3	Ni loading $w_{\text{Ni}}$ , degree of reduction $d_{\text{red,TPR}}$ of NI and WI samples determined by TPR analysis weight percentage of nickel oxide (surface NiO: sNiO, bulk NiO: bNiO) and Ni aluminate determined by peak fitting of $\text{H}_2$ consumption determined by TPR. . . . .	156
7.4	Specific surface area $S_{\text{BET}}$ determined by $\text{N}_2$ physisorption. . . . .	158

# List of Publications

## Journal Publications

- H. M. Bui, R. Fischer, N. Szesni, M. Tonigold, K. Achterhold, F. Pfeiffer, O. Hinrichsen, "Development of a Manufacturing Process for Binder Jet 3D Printed Porous Al<sub>2</sub>O<sub>3</sub> Supports Used in Heterogeneous Catalysis", *Additive Manufacturing*, **2021**, 50, 102498, DOI 10.1016/j.addma.2021.102498.
- H. M. Bui, P. F. Großmann, T. Gros, M. Blum, A. Berger, R. Fischer, N. Szesni, M. Tonigold, O. Hinrichsen, "3D Printed Co-Precipitated Ni-Al CO<sub>2</sub> Methanation Catalysts by Binder Jetting: Fabrication, Characterization and Test in a Single Pellet String Reactor", *Applied Catalysis A: General*, **2022**, 643, 118760, DOI 10.1016/j.apcata.2022.118760.
- H. M. Bui<sup>1</sup>, P. F. Großmann<sup>1</sup>, A. Berger, A. Seidel, M. Tonigold, N. Szesni, R. Fischer, B. Rieger, O. Hinrichsen, "Comparison of Direct Ink Writing and Binder Jetting for additive manufacturing of Pt/Al<sub>2</sub>O<sub>3</sub> catalysts for the dehydrogenation of perhydro-dibenzyltoluene", *Chemical Engineering Journal*, **2023**, 458, 141361, DOI 10.1016/j.cej.2023.141361.
- H. M. Bui, T. Kratky, I. Lee, R. Khare, M. Hiller, S. Wedig, S. Günther, O. Hinrichsen, "In Situ Impregnated Ni/Al<sub>2</sub>O<sub>3</sub> Catalysts Prepared by Binder Jet 3D printing Using Nickel Nitrate-containing Ink", *Catalysis Communications*, **2023**, 106738, DOI 10.1016/j.catcom.2023.106738.

---

<sup>1</sup> These authors equally contributed to this work.

## Oral Presentations

- H. M. Bui, O. Hinrichsen, "Challenges for Binder Jetting of Packings and Monoliths for Heterogeneous Catalysis", Conference for Young Scientists in Ceramics, **2019**, Novi Sad, Serbia.
- H. M. Bui, P. F. Großmann, M. Tonigold, R. Fischer, N. Szesni, O. Hinrichsen, "Manufacturing Strategies for Active Alumina-based Heterogeneous Catalysts by Binder Jetting", 8th Shaping Conference, **2022**, Dübendorf/Zürich, Switzerland.

## Poster Presentations

- H. M. Bui, P. F. Großmann, M. Tonigold, R. Fischer, B. Rieger, O. Hinrichsen, "Binder Jetting of Ceramic Powders for Use in Heterogeneous Catalysis", Young Ceramists Additive Manufacturing Forum, **2020** (online event).
- H. M. Bui, P. F. Großmann, M. Tonigold, R. Fischer, B. Rieger, O. Hinrichsen, "Powder-based Additive Manufacturing of Al<sub>2</sub>O<sub>3</sub> Catalyst Supports", 54. Jahrestreffen deutscher Katalytiker, **2021**, Weimar, Germany (online event).
- P. F. Großmann, H. M. Bui, C. Troll, M. Tonigold, R. Fischer, O. Hinrichsen, B. Rieger, "Improving Catalytic Activity by Direct Ink Writing of Heterogeneous Catalysts", International Chemical Congress of Pacific Basin Societies, **2021**, Honolulu, USA (online event).
- C. Bauer, H. M. Bui, T. Gros, O. Hinrichsen, "Modelling of Single Pellet String Reactors by CFD Simulations coupled with detailed Surface Chemistry", The 27th North American Catalysis Society Meeting, **2022**, New York, USA.
- H. M. Bui, T. Gros, M. Blum, M. Tonigold, R. Fischer, N. Szesni, O. Hinrichsen, "Powder-based Additive Manufacturing of Ni-Al Catalysts via Binder Jetting", The 27th North American Catalysis Society Meeting, **2022**, New York, USA.
- P. F. Großmann, H. M. Bui, M. Tonigold, R. Fischer, B. Rieger, O. Hinrichsen, "Binder Jetting and Direct Ink Writing: Advantages and Disadvantages of Two Additive Manufacturing Techniques in Heterogeneous Catalysis", 55. Jahrestreffen deutscher Katalytiker, **2022**, Weimar, Germany.

- C. Bauer, H. M. Bui, T. Gros, O. Hinrichsen, "Comparison of Reactive CFD Modelling with Experimental Data for CO<sub>2</sub> Methanation in Single Pellet String Reactors", Jahrestreffen Reaktionstechnik, **2022**, Würzburg, Germany.
- H. M. Bui, P. F. Großmann, M. Tonigold, R. Fischer, N. Szesni, O. Hinrichsen, "Powder-based Additive Manufacturing of Pt/Al<sub>2</sub>O<sub>3</sub> Catalysts for Liquid Organic Hydrogen Carrier Dehydrogenation", 12th Energy Colloquium, **2022**, München, Germany.
- H. M. Bui, T. Kratky, I. Lee, M. Hiller, S. Wedig, O. Hinrichsen, "A Novel Catalyst Preparation Method for Supported Ni Catalysts via Binder Jetting 3D Printing Using Nickel Ink", 56. Jahrestreffen deutscher Katalytiker, **2023**, Weimar, Germany.

